



# Rôle of interfaces on the magnetic properties of ferromagnetic metal/organic heterostructures : exchange bias and interlayer exchange coupling in cobalt/metal tetra-phenyl porphyrin

Garen Avedissian

## ► To cite this version:

Garen Avedissian. Rôle of interfaces on the magnetic properties of ferromagnetic metal/organic heterostructures : exchange bias and interlayer exchange coupling in cobalt/metal tetra-phenyl porphyrin. Physics [physics]. Université de Strasbourg, 2020. English. NNT : 2020STRAE022 . tel-03253039

**HAL Id: tel-03253039**

**<https://theses.hal.science/tel-03253039>**

Submitted on 8 Jun 2021

**HAL** is a multi-disciplinary open access archive for the deposit and dissemination of scientific research documents, whether they are published or not. The documents may come from teaching and research institutions in France or abroad, or from public or private research centers.

L'archive ouverte pluridisciplinaire **HAL**, est destinée au dépôt et à la diffusion de documents scientifiques de niveau recherche, publiés ou non, émanant des établissements d'enseignement et de recherche français ou étrangers, des laboratoires publics ou privés.

**UNIVERSITÉ DE STRASBOURG**  
**ÉCOLE DOCTORALE de Physique et Chimie-Physique**  
**Institute de Physique et Chimie des Matériaux de Strasbourg**

**Role of interfaces on the magnetic properties of  
ferromagnetic metal/organic heterostructures:  
Exchange bias and interlayer exchange coupling in  
Co/metal tetra-phenyl porphyrin**

**THÈSE** présentée par :  
**Garen Avedissian**

pour obtenir le grade de : **Docteur de l'université de Strasbourg**

Discipline/Spécialité : **Physique**

17 novembre 2020

**THÈSE dirigée par :**  
**Mr. Christian Meny**

Director of research CNRS, Université de Strasbourg

**RAPPORTEURS :**  
**Mr. Jean-Phillipe Ansermet**  
**Mme. Agnes Barthelemy**

Professor, École polytechnique fédérale de Lausanne  
Professor, Unité Mixte de Physique CNRS/Thales

**Examineur :**  
**Mr. Jean Weiss**

Professor, Institut de Chimie de Strasbourg







# Acknowledgment

## **To Strasbourg, thank you for the memories....**

“We must accept finite disappointment, but we must never lose infinite hope.” Martin Luther King, Jr.

October 13, 2016 saw the first foot-step towards one of the most interesting and beautiful journeys I have had encountered in my relatively young and vivid life. Adventure of a lifetime, the maturity and experience gained, both on scientific and personal level is priceless. The journey was rich in obstacles, difficulties, problems, and complications yet it lifted me up intellectually and spiritually.

Throughout this journey, I had the chance to meet interesting individuals which deserve recognition. First, my sincere gratitude goes to Dr. Eric Beaurepaire for his significant efforts in convincing the doctoral school to make an exception and postpone the audition date for the “Initiative d’Excellence (Idex)” funding campaign, which the current Ph. D. thesis project is funded with. If it were not for his efforts, this manuscript would have not been in your hands. I would like to thank him for giving me the opportunity to conduct and have first experience of research at Institute de physique et chimie des Materiaux de Strasbourg (IPCMS). Unfortunately, tragic events of life did not allow me to benefit from his knowledge and expertise, nevertheless that truly short period of time of contact was enough to know his scientific excellence and humble character. To Dr. Eric, this manuscript goes in your honor.

I would like to thank the jury members: Prof. Agnes Barthelemy, Prof. Jean-Philippe Ansermet, and Prof. Jean Weiss. Thank you for reading the manuscript in uncertain and unprecedented times. It is an honor and privilege to have such elite members, as you, in the thesis jury commission.

Of course, Dr. Christian Meny. I would like to acknowledge with deep gratitude his act on stepping up and accepting the responsibility of supervising my thesis, after almost passing more than half of the period. I know it was not easy, but I think we came so far and had a noteworthy ending. There might be so many things which I am grateful to and writing them here might cost pages and patience but there are two things which I would like to highlight. First, his “old school” and fundamental approach to research which I will carry it on with me no matter where I end up and second, the presence of sense of “respect” through thick and thin.

With no doubt, my profound gratitude goes to Mr. Jacek Arabski, our senior research engineer who is now on retirement and whom I would like to refer as “the man behind all curtains”. I feel very fortunate to be part of the last group of Ph. D. students who had the chance to benefit from his scientific, technical, and experimental expertise. With no hesitation he provided all his knowledge of experimental research, UHV systems, and instrumentation and showed us where to look and how to solve problems with big UHV systems. You might guess his age as he is now retired nevertheless his soul and approach to life


is energetic and forever young. I truly value his encouragement, support, and entrust in every single step then and now. I appreciate and enjoyed every discussion with him whether science or life. His life expertise, discussions about socio-political issues, philosophy, adventure, travel, and cuisine are priceless. I am forever grateful and will cherish the moments with him in and out of the laboratory peripheries.

Hope I do not miss anyone. Dr. Victor Da Costa, thank you. His gentle approach to research, attention to minor but important details, special care for the UHV chambers and instruments are invaluable. I would like to thank him for his time and availability at the beginning of the thesis work, for teaching and training me on using microscopy techniques (AFM, STM etc.).

Whoever have spent some time at IPCMS, short or long, would definitely remember Mr. Guy Schmerber. His contribution to science and life in IPCMS in general is remarkable. I would like to thank him for his assistance throughout the thesis especially with the measurements related to X-ray reflectometry, X-ray diffraction and UV-vis spectroscopy. I really appreciate his support throughout the entire period, even after his retirement, his support emails are something to hold on. His joyfulness and positive energy all over the corridors of the institute is something that will be remembered for a long time.

I would like to thank Dr. Martin Bowen for his support and discussion whenever it was necessary, his enthusiasm and grind are like no other. Further recognition goes to Mr. Christophe Kieber for his technical assistance and his time in taking care and making modifications to the systems whenever needed. Special thanks to Mr. Romain Bernard for responding to our calls and providing, in a rapid way, all the necessary substrates from clean room, that were extensively used within this thesis work. Also, to Dr. Wolfgang Weber, thank you for your kindness and patience in explaining in detail every single element of an experimental set-up, the experiment and even the physics behind it. Big thanks go to Corinne Bouillet for all the assist and help in performing TEM measurements on the hybrid samples. It was a long shot, but I am glad we went for it and she were always there to listen and share her expertise. Within her overloaded schedule, she always invested time in our interest, and it was worth it, thank you. Next, I would like to recognize Dr. Silviu Colis's efforts for training me on AGFM and SQUID magnetometers, his door was always open for questions and further explanations. For sure, I cannot go by SQUID and not mention Dr. Guillaume Rogez. My sincere appreciation to him, for his time in training me on SQUID, his constant care to the magnetometer. I am truly thankful for entrusting me to work even on critical times (well, they were so many). Monday morning SQUID meetings were definitely something positive to start the week with and you made it even more enjoyable. Next on the list come Prof. Jean Weiss and Dr. Jennifer A. Wytke from Institut de Chimie de Strasbourg. All the thankfulness to them for their unconditional support and their time invested to my questions, meetings. Without hesitation, they always responded to my calls for meetings regardless their overloaded schedule

and their own work. Oh, yes for sure, all the organic molecules used within this thesis are synthesized by them, thank you.

Indeed, special thanks goes to the secretary of our department (Departement de magnetism des objets nanostructures “DMONS”  ) Mme. Veronique Wernher. Well, she is more of a super-secretary, you just need to say the “a” and then she would complete the mission to “z”. The constant care she puts in all the administrative work of the department is unparalleled.

To my colleagues and friends at IPCMS, thank you. You are numerous but I would like to mention Sambit Mohapatra, Kostantine Katcko, Franck Ngassam Nyakam, Khaled Rassoul, Lalit-Mohan Kandpal, Gladice Magnifouet, Bhavishya Chowrira and formerly present in the institute Beata Taudul and Filip Schleicher. You guys made life at IPCMS more pleasurable and entertaining.

On a personal front,

Dear people of tomorrow land, friends from all over the world, thank you. With no exception, you are all special and have big place in my story book. Big shout out to you for making Strasbourg a beautiful portrait which I will carry it all the way from Earth to outer space and treasure it forever.

At last, my foremost gratitude to my entire family. Father, Mother, and Brother words will not be enough to express my appreciation towards you. You are the main pillar and the backbone of everything I am today. You raised me as a dreamer and here we are, accomplishing together the baby steps of what is going to be the best ride, ever. Looking forward to the future with you, salute.





# Contents

INTRODUCTION .....	1
--------------------	---

## PART I SCIENTIFIC CONTEXT

Chapter 1: Introduction to organic spintronics .....	7
1.1 Electronics with spins.....	7
1.2 Organic Spintronics .....	11
Chapter 2: Organic/inorganic hybrid interface interactions .....	14
2.1 Isolated organic molecules and metallic ferromagnets .....	14
2.2 Hybrid organic/inorganic interface .....	15
2.2.1 Physisorption regime .....	15
2.2.2 Chemisorption regime .....	16
2.2.3 Partial conclusion.....	18
Chapter 3: Magnetic properties at the hybrid organic/inorganic interface .....	19
3.1 Magnetic exchange interactions .....	19
3.2 Magnetic properties at the interface of the hybrid systems.....	21
3.3 Exchange bias in organic hybrid systems.....	24
3.3.1 Phenomenology of exchange bias.....	24
3.3.2 Molecular exchange bias .....	27
3.4 Partial summary .....	28
Chapter 4: Porphyrins and porphyrin-based metal complexes.....	29
4.1 Porphyrin.....	29
4.2 Metal complexes of tetra phenyl porphyrin.....	30
4.3 MTPP molecules on metallic surfaces .....	33
4.4 TPP/MTPP molecules in hybrid nanostructures.....	34
4.5 Partial summary .....	35
4.6 Conclusion.....	35

## PART II EXPERIMENTAL METHODS

Chapter 5: Experimental setups, growth, and characterization techniques .....	39
5.1 Ultra-high vacuum deposition systems .....	39
5.1.1 Molecular beam epitaxy (MBE) chamber.....	39

5.1.2 The “Hybrid” system .....	40
5.2 Substrate cleaning and sample preparation conditions .....	43
5.3 Characterization techniques.....	45
5.3.1 Super conducting quantum interface device .....	46
5.3.2 Atomic Force microscopy .....	48
5.3.3 X-ray photoelectron spectroscopy .....	49
5.3.4 Transmission electron microscopy .....	50
5.3.4.1 TEM sample preparation.....	53
5.3.5 Ferromagnetic nuclear resonance .....	54
5.3.5.1 Zero-external field .....	55
5.3.5.2 Local restoring field and magnetic analysis .....	55
5.3.5.3 Structural analysis.....	58
5.3.5.4 Hybrid heterostructures for FNR .....	60
5.3.5.5 FNR experimental conditions .....	61

### **PART III IS MOLECULAR EXCHANGE BIAS A SPINTERFACE EFFECT?**

Chapter 6: Investigating the molecular exchange bias in Co/organic systems.....	67
6.1 Sample optimization and sample architecture.....	67
6.2 Reference sample and checking the contamination-free character of the deposition chambers.....	70
6.3 Exchange bias in Co/ZnTPP.....	71
6.3.1. Discussion and analysis.....	73
6.4 Exchange bias in Co/NiTPP and Co/CoTPP.....	74
6.5 Partial conclusions.....	77
6.6 Exchange bias in Co/CoPc.....	77
6.7 Summary and conclusion.....	79
Chapter 7: Chemical composition and morphological characterization of Co/MTPP hybrid systems .....	80
7.1 XPS measurements.....	80
7.1.1 Co 2p-edge of CoTPP and Co/ZnTPP hybrid sample.....	80
7.1.2 N 1s and Zn 2p edges of Co/ZnTPP hybrid sample .....	81
7.1.3 Discussion and conclusion .....	83
7.2 AFM measurements .....	84
7.2.1 Surface morphology of Au capping layer .....	84
7.2.2 The “freshly deposited” and the ageing of the free ZnTPP molecular surface .....	86
7.2.3 The “freshly deposited” and the ageing of the free NiTPP molecular surface .....	89
7.2.4 Partial discussion and conclusion .....	90
7.3 Conclusions .....	92

## **PART IV PROBING THE PHYSICAL PROPERTIES OF ORGANIC HYBRID HETEROSTRUCTURES AND OF THEIR EMBEDDED INTERFACES BY FNR AND TEM**

<b>GENERAL INTRODUCTION.....</b>	<b>97</b>
<b>Chapter 8: Optimization of the Heterostructures.....</b>	<b>99</b>
8.1 Optimization of the buffer layer .....	99
8.2 Optimization of the capping layer.....	100
8.3 Partial conclusion .....	101
<b>Chapter 9: The FNR approach in organic/metallic heterostructures.....</b>	<b>102</b>
9.1 Probing the continuity of molecular films embedded in-between Co and Fe electrodes.....	102
9.1.1 Results and discussion .....	102
9.1.2 Quantitative analysis .....	106
9.2. Phenomenological analysis: Growth models.....	107
9.3 Partial conclusion .....	110
<b>Chapter 10: Probing the interfaces of hybrid heterostructures with FNR.....</b>	<b>112</b>
10.1 Hybrid interfaces embedded within organic/Co/organic heterostructure .....	112
10.1.1 Results and discussion .....	113
10.1.2 Analysis of FNR integral intensities .....	115
10.1.3 Partial conclusion.....	116
10.2 Morphology of the single Co/ZnTPP and ZnTPP/Co interfaces .....	117
10.2.1 Building up the single interface .....	117
10.2.2 Results and discussions.....	117
10.2.3 Partial conclusion.....	119
<b>Chapter 11: Revealing the hybrid interfaces: TEM in organic hybrid heterostructures.....</b>	<b>120</b>
11.1 STEM images and EELS spectra : results and discussion.....	120
11.1.1 Co/ZnTPP/Fe heterostructure .....	120
11.1.2 Fe/ZnTPP/Co/ZnTPP/Fe heterostructure.....	125
11.1.3 Cu/ZnTPP/Co/Fe heterostructure .....	129
11.2 Partial conclusion .....	132
11.3 General conclusions.....	133
<b>PART V: GENERAL DISCUSSION, CONCLUSIONS, AND OUTLOOK.....</b>	<b>139</b>
<b>BIBLIOGRAPHY .....</b>	<b>155</b>





## Résumé in French

Les innovations technologiques actuelles peuvent se constater au travers des appareils électroniques utilisés quotidiennement. Ces progrès se traduisent par l'augmentation de leur capacité de stockage et de leur puissance de calcul et sont accompagnés par la réduction en taille de leurs composants. Cependant, cette miniaturisation augmentera encore la complexité des appareils et entraînera des limitations technologiques si aucuns matériaux alternatifs ne sont mis en œuvre. Les matériaux à base de molécules organiques sont des matériaux de choix parmi les matériaux alternatifs envisagés. Avec l'intégration de molécules organiques dans l'électronique, une nouvelle activité de recherche est née : l'électronique organique qui vise en particulier à utiliser ces molécules pour le transport de spin en raison de leur faible mécanisme de relaxation de spin [1]. Avec ces couches organiques plusieurs effets typiques de l'électronique de spin ont déjà été obtenus : vanne de spin [2,3,4] jonction tunnel magnétique [5,6] et magnétorésistance inverse [7,8]. Leur rôle sur la modification de la polarisation de spin des interfaces de films ferromagnétiques [9] a également été révélé. Ces activités relèvent de ce qu'on peut appeler la science des interfaces [10] (ou « spinterface »). Ces travaux pionniers ont suscité une importante activité scientifique et plusieurs nouveaux phénomènes interfaciaux ont été rapportés [11,12,13]. Ces travaux posent néanmoins de nouvelles questions sur l'origine physique des propriétés développées aux interfaces entre le matériau organique et son environnement. C'est pourquoi, corrélérer les propriétés physiques observées aux morphologies associées des interfaces molécules/ferromagnétiques est d'une grande importance.

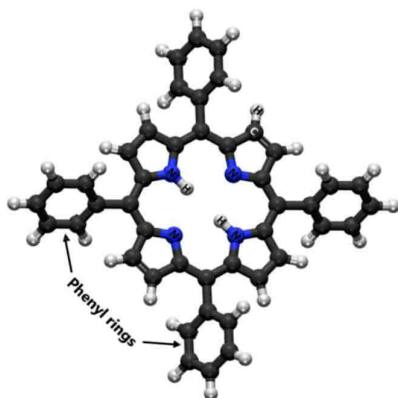


**Figure 1:** Structure chimique du tetra-phényle porphyrine ( $H_2TTP$ ). Sphères bleues : atomes d'azote ; sphères grises : atomes d'hydrogène ; sphères noires : atomes de carbone. Les groupements phényle présentent un angle de rotation par rapport au macrocycle de porphyrine. Dans les complexes métalliques l'ion est au centre du macrocycle. Cambridge Structural Database.

Dans ce cadre, ce travail se concentre sur l'étude des interfaces entre un métal ferromagnétique et un matériau organique le métal tétra phényle porphyrine (MTPP) (figure 1). Il tente en particulier d'étudier les corrélations entre les propriétés magnétiques de ces hétérostructures et la morphologie de leurs interfaces. Cette étude a été rendue très complexe en raison du comportement non conventionnel des molécules au contact des ferromagnétiques métalliques. Cela nous a conduit à développer une méthodologie originale d'étude par Résonance Nucléaire Ferromagnétique (FNR, c'est-à-dire la Résonance Magnétique Nucléaire dans les ferromagnétiques) permettant en particulier d'étudier des interfaces métal/organique individuelles au sein des hétérostructures. Cette nouvelle méthodologie est combinée à d'autres techniques de caractérisation (AFM, SQUID, XPS, TEM) ce qui a permis de réaliser des études détaillées de ces interfaces hybrides et ensuite de corréler les informations obtenues sur leurs morphologies à leurs propriétés magnétiques.

L'un des effets interfaciaux qui est plus spécifiquement abordé dans ce travail est le blocage par couplage d'échange de la direction de l'aimantation d'un métal ferromagnétique par une couche organique moléculaire (effet appelé « molecular exchange bias »). L'« exchange bias » est bien connu dans les systèmes ferromagnétique/inorganique, mais il est plutôt surprenant de l'observer dans des hétérostructures métal ferromagnétique/organique. Cet effet est expliqué en considérant qu'un moment magnétique est induit dans la molécule à l'interface avec le matériau ferromagnétique et qu'en conséquence l'aimantation stabilisée dans la molécule induit à son tour un champ d'échange sur le ferromagnétique. C'est ce champ d'échange qui est à l'origine du « molecular exchange bias ». Les premiers résultats qui ont décrit cet effet ont été obtenus avec des couches formées de molécules de phtalocyanine (Pc) dans des hétérostructures de Co/MnPc [14]. Des observations similaires ont ensuite été faites pour des couches moléculaires de Pc incluant d'autres ions métalliques [15].

C'est dans ce cadre que la première partie de ce travail est dédiée à l'étude de l'existence du « molecular exchange bias » dans des bicouches hybrides Au/Co/MTPP/Au ( $M = \text{Co, Zn et Ni}$ ). Les molécules de MTPP ont été choisies dans ce travail en raison de leur morphologie non-planaire, contrairement aux molécules de phtalocyanines. Par conséquent, ces molécules devraient avoir un comportement différent aux interfaces et donc des interactions différentes avec les couches ferromagnétiques sous-jacentes. En outre, MTPP peut être fonctionnalisé par des ligands supplémentaires greffés sur les groupements phényles, permettant d'envisager l'étude de différentes propriétés physiques en appliquant les stimuli externes appropriés. Enfin, pour le choix des complexes métalliques nous avons considéré la nature magnétique ou non de l'ion métallique inclus dans la molécule (Zn, Ni et Co). Dans les 3 complexes, les molécules ont une symétrie  $D_{4h}$  et en conséquence le Co(II)TPP est paramagnétique ( $S = 1/2$ ) mais Zn(II)TPP et Ni(II)TPP sont diamagnétiques, cependant, la nature magnétique de l'ion nickel (contrairement au zinc) pourrait faciliter l'apparition d'un moment magnétique aux interfaces en raison de la rupture de symétrie aux interfaces. Enfin, Ni(II)TPP est chimiquement plus stable que Zn(II)TPP.



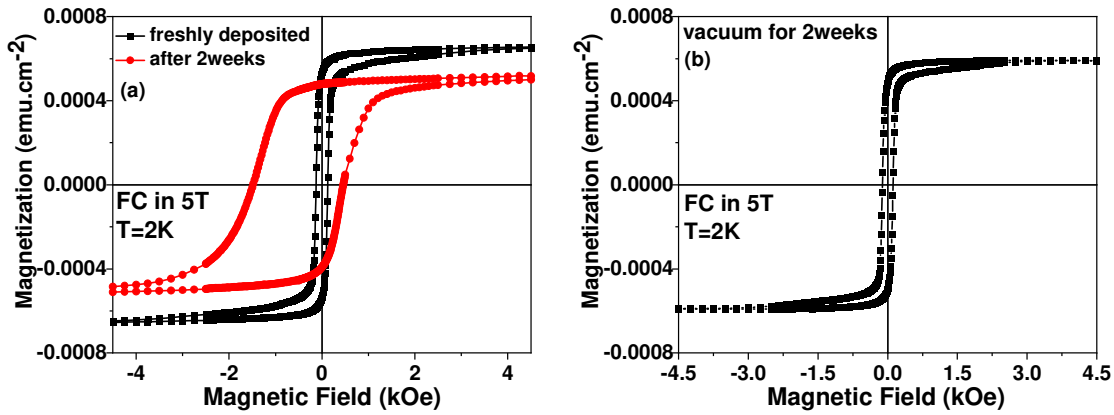


**Figure 2:** Courbes d'aimantation a) échantillon Co(6nm)/ZnTPP(10nm)/Au(50nm) fraîchement préparé (en noir) et remesuré deux semaines plus tard (en rouge) (b) échantillon Co(6nm)/ZnTPP(10nm)/Au(50nm) vieilli pendant deux semaines en UHV mesuré directement après sa sortie du vide.

Des bicouches Co/ZnTPP ont été fabriquées par évaporation sous ultra vide (UHV). Ces échantillons ont montrés des courbes d'aimantation présentant un champ d'« exchange bias » ( $H_{EB}$ ) important et accompagné d'une réduction importante de leur aimantation à saturation par rapport à celle estimée à partir de l'épaisseur des couches ferromagnétiques. Ces premiers résultats sont en accord avec les travaux déjà publiés sur des systèmes similaires, néanmoins, de façon surprenante, avec le temps, il a été observé une augmentation spectaculaire de  $H_{EB}$  accompagnée d'une baisse supplémentaire de leur aimantation à saturation. Ces résultats nous ont fait douter de la nature intrinsèque de l'« exchange bias » dans ces systèmes. Pour tester cette hypothèse, les échantillons pouvant avoir été contaminés par exposition à l'air, l'épaisseur de la couche de protection (10 nm d'Au) a été augmentée. Les échantillons avec une couche de protection d'Au de 50 nm ont révélé l'absence d'« exchange bias » lorsqu'ils ont été mesurés directement (figure 2) après leur élaboration (mesurés moins de 15 min après avoir prélevé les échantillons de la chambre UHV), cependant, l'« exchange bias » est à nouveau apparu après quelques semaines. L'hypothèse la plus plausible est donc que l'« exchange bias » provient de la contamination par l'air des couches de cobalt ce qui conduit à la croissance d'un oxyde de Co qui est bien connu pour produire un effet d'« exchange bias ».

Néanmoins il est tout de même surprenant que 50 nm de couche de protection d'or ne soit pas suffisant pour protéger des couches bien moins épaisses de cobalt (6 nm) et de ZnTPP (NiTPP) (10 nm). À titre de vérification définitive, les mêmes hétérostructures, ont été préparées et conservées dans la chambre UHV pendant plusieurs semaines avant mesure. Les courbes d'aimantation des échantillons maintenus plusieurs semaines en UHV mais fraîchement sortis de la chambre UHV n'ont montré, encore une fois, aucun signe d'« exchange bias ». Ce résultat a confirmé que l'oxydation par exposition à l'air des échantillons est à l'origine de l'« exchange bias » observé. Les mêmes effets ont été observés pour les hétérostructures Co/NiTPP et Co/CoTPP ; une fois correctement protégés aucun de ces systèmes n'a présenté d'« exchange bias » si les échantillons sont mesurés rapidement après leur fabrication.

Pour mieux comprendre le processus de contamination, des mesures AFM et XPS ont été effectuées. La morphologie de la couche d'or de protection de 10 nm présente une surface composée de grains circulaires non coalescés, qui forment des îlots plus grands, déconnectés et séparés par des fissures très profondes (figure 3). Ces fissures profondes pourraient être à l'origine des propriétés des échantillons en facilitant la contamination par exposition à l'air. De plus, les spectres  $2p_{3/2}$  du Zn et 1s de N dans les échantillons Au/Co/ZnTPP/Au n'a montré aucune trace de distorsion de ZnTPP lorsqu'il est adsorbé sur la surface métallique. Par contre le spectre  $2p_{3/2}$  du Co de l'échantillon avec « exchange bias » a montré clairement la présence de cobalt oxydé.

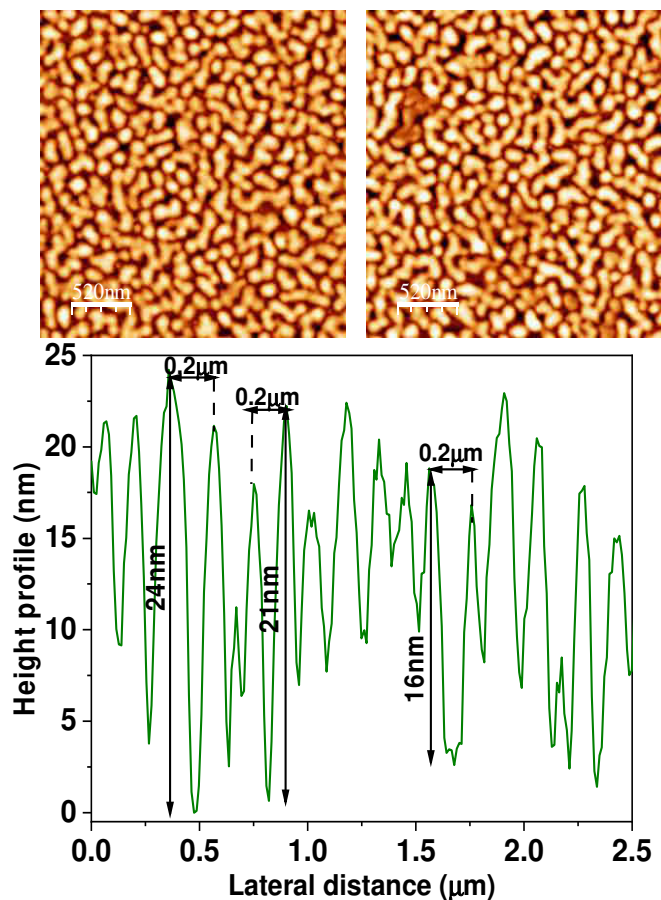


**Figure 3:** panneau supérieur: image AFM de la surface d'un échantillon protégé par 10nm d'Au. Panneau inférieur : profil de la surface ; la rugosité est très élevée, d'une profondeur de 20 nm.

De cette première partie, il a été conclu que l'« exchange bias » dans les bicouches Co/MTPP ( $M = \text{Co, Ni, Zn}$ ) et Co/CoPc n'est pas un effet moléculaire induit par l'interface. Cependant, ces résultats n'excluent pas que d'autres phénomènes interfaciaux puissent exister à ces interfaces hybrides organique/ferromagnétique. Pour pouvoir poursuivre l'étude de ces effets sur des échantillons structuralement contrôlés, la deuxième partie de la thèse est consacrée à une étude approfondie de la morphologie de ces films moléculaires lorsqu'ils sont déposés sur différents films métalliques ferromagnétiques.

Avant de nous engager dans des investigations aussi délicates, nous avons d'abord résolu le problème de la couche de protection inefficace, qui ne parvient pas à éviter l'oxydation du Co. La couche de protection en or a été remplacée par 100 nm de chrome ce qui permet de protéger efficacement les échantillons de la contamination, au moins à échelle de temps de l'étude. La couche tampon d'or initialement choisie car elle avait été utilisée dans de précédents travaux n'était pas non plus satisfaisante. En effet, bien qu'elle forme de grandes terrasses plates, ces terrasses sont séparées par de profondes fissures qui ne conviennent pas aux mesures macroscopiques. Par conséquent, la couche tampon d'or a été substituée par 25 nm de cuivre déposée par pulvérisé magnétron et qui montre une surface beaucoup plus plate à grande échelle.

Dans un premier temps, nous nous sommes intéressés à la morphologie de surface de films MTPP épais. Les mesures AFM ont plus particulièrement révélé que la morphologie des films change rapidement sur une échelle de temps assez courte. Un travail plus approfondi est nécessaire pour comprendre si la modification de la morphologie est déclenchée alors que les échantillons sont exposés à l'air ou si l'effet apparaît déjà in situ pendant le processus de croissance. Néanmoins, ces observations suggèrent qu'étudier les premières étapes de croissance des couches avec des techniques comme la microscopie à effet tunnel n'est pas forcément pertinente dans le cadre de notre travail. En effet, l'évolution des couches pendant la croissance pourrait ne pas refléter correctement la structure et la morphologie des couches dans les hétérostructures finales.

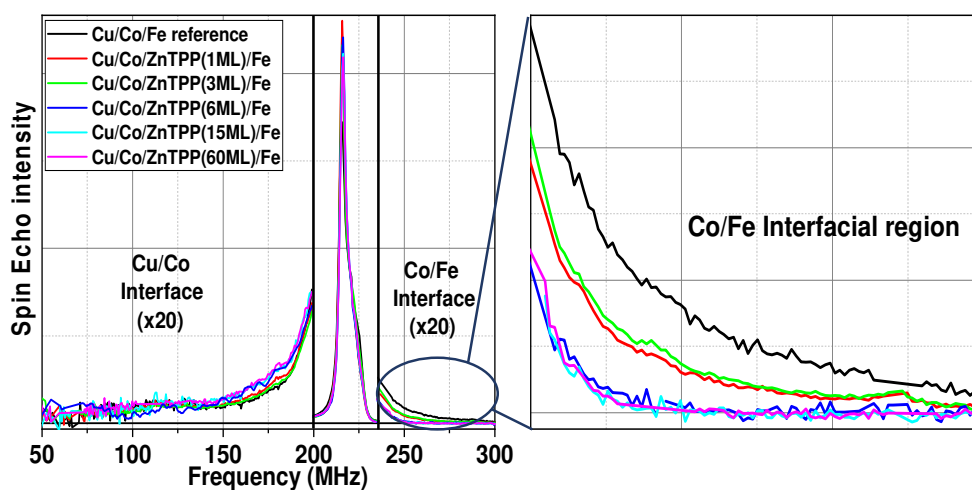


**Figure 4:** Evolution des spectres FNR avec augmentation de l'épaisseur de la couche de ZnTPP. La partie haute fréquence (>240 MHz) diminue avec l'augmentation de l'épaisseur et disparaît à partir de 15 ML.

Une approche plus appropriée est d'encapsuler efficacement les hétérostructures pour ralentir la cinétique des molécules et d'étudier la structure et la morphologie des échantillons achevés. Par contre peu de techniques expérimentales permettent d'effectuer ce genre d'étude. C'est pourquoi nous avons développé une nouvelle méthodologie d'étude faisant appel à la Résonance Nucléaire Ferromagnétique.

À cette fin, deux types d'hétérostructures ont été préparées. Les couches de ZnTPP (allant de 1ML à 60ML ;  $1\text{ML} \approx 3.3\text{\AA}$ ) sont prises en sandwich entre deux couches ferromagnétiques métalliques différentes (Cobalt et Fer) dont l'ordre de croissance est inversé : i.e. Co/ZnTPP(t)/Fe et Fe/ZnTPP(t)/Co. L'intérêt de cette architecture est le suivant. Un spectre FNR présente un nombre d'atomes en fonction de la fréquence du champ radiofréquence appliqué à l'échantillon. Dans une architecture de couche Cu/Co/Fe, le spectre FNR peut être divisé en 3 gammes de fréquences distinctes : la première pour les atomes de Co qui se trouvent dans le cœur des couches de Co (atomes de Co uniquement entourés d'autres atomes de Co, entre 200 et 240 MHz), une région pour l'interface Cu/Co ( $<200$  MHz) et une troisième région pour l'interface Co/Fe ( $> 240$  MHz) (figure 4). Par conséquent, si une couche organique est insérée entre la couche de Co et de Fe, il est simple de mettre en évidence si les atomes de Fe ou de Co migrent (quel qu'en soit le processus) à travers la couche organique. En effet, lorsque la couche organique isolera complètement les deux électrodes ferromagnétiques les contributions haute fréquence ( $> 240$  MHz) dans le spectre FNR disparaîtront (figure 4).

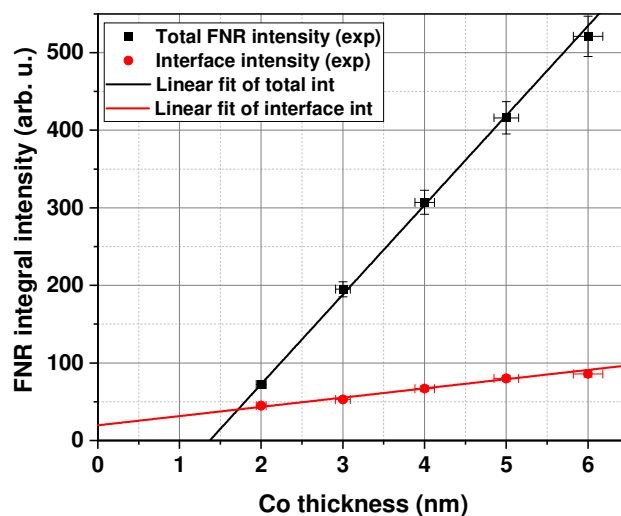


**Figure 5:** Intensité totale des spectres FNR des échantillons ZnTPP/Co/ZnTPP en fonction de l'épaisseur de Co (en noir). Intensité de la partie du spectre basse fréquence ( $<200$  MHz ; en rouge).

En utilisant cette méthodologie originale, il a été démontré qu'au moins 15 couches moléculaires de ZnTPP sont nécessaires pour séparer complètement les deux couches ferromagnétiques. En outre, l'analyse détaillée de l'intensité des spectres FNR haute fréquence a révélé des modes de croissance différents pour les deux types d'hétérostructures. Cela suggère que la croissance du ZnTPP dépend fortement de la structure et de la morphologie de la couche métallique ferromagnétique initiale. Une fois que l'épaisseur seuil de ZnTPP (au moins 15 ML) nécessaire pour séparer les deux couches ferromagnétiques métalliques a été déterminée, les caractéristiques des interfaces Co/ZnTPP et ZnTPP/Co ont été étudiées. Aucun signal FNR n'a pu être clairement identifié comme provenant d'atomes de Co avec une liaison chimique avec un élément organique. L'interface Co/organique est caractérisée par une large contribution non structurée à basse fréquences (50 à 200 MHz). Enfin l'analyse FNR a montré que lorsque ZnTPP est déposé au-dessus d'un film de cobalt (Cu/Fe/Co/ZnTPP) l'interface Co/ZnTPP a une structure complètement différente de celle obtenue lorsque le film de cobalt est déposé au-dessus de la molécule (Cu/ZnTPP/Co/Fe). L'interface Co/ZnTPP est plus plate, par rapport à l'interface ZnTPP/Co. Cette différence peut être attribuée aux atomes de Co qui peuvent migrer dans le film moléculaire lorsqu'ils sont déposés sur celle-ci et/ou à la morphologie « ondulée » de la surface de la couche organique qui laisse des zones poreuses qui doivent d'abord être remplies par les atomes de cobalt avant de finalement constituer un film métallique continu.

Dans le but d'affiner l'étude des interfaces Co/ZnTPP le travail s'est poursuivi par l'étude d'échantillons dans lesquels la couche de Co est complètement prise en sandwich entre les films organiques. De façon similaire à l'étape précédente, des films de Fe supérieurs et inférieurs supplémentaires ont été ajoutés dans l'architecture pour garantir que les films organiques isolent complètement la couche de Co (Fe/ZnTPP/Co/ZnTPP/Fe). Dans ces échantillons, encore une fois, aucun environnement n'a pu être identifié comme provenant d'une liaison chimique entre des atomes de Co et l'organique. Seule une large contribution interfaciale non structurée a été observée. Cette étude a également montré qu'une quantité significative d'atomes de cobalt ferromagnétique sont absents des spectres FNR. Il manque près de 1.4 nm de cobalt par rapport aux épaisseurs déposées (figure 5). Cette perte peut s'expliquer par la diffusion/migration des atomes de cobalt dans le film moléculaire. Ces atomes de Co ne seraient plus ferromagnétiques et disparaîtraient du spectre FNR.

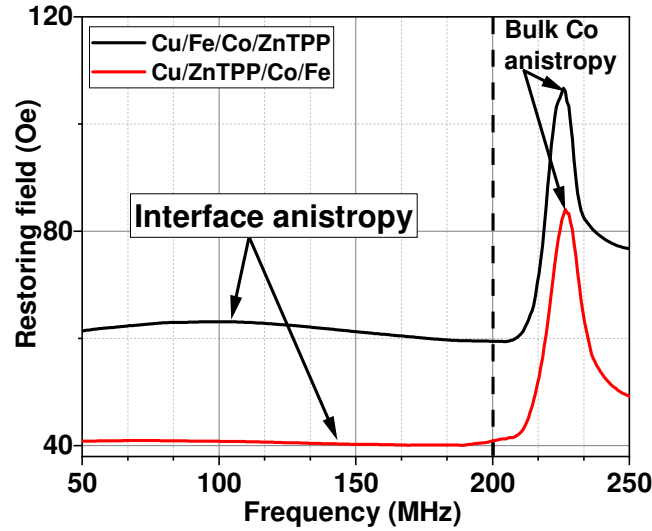


**Figure 6:** Anisotropie magnétique de la couche de Co des hétérostructures en fonction de la fréquence. L'anisotropie des interfaces (< 200 MHz) est toujours plus faible que celle du centre des couches (> 200 MHz).

Enfin, l'étude FNR a également permis de sonder si un effet de durcissement d'interface est induit à l'interface ferromagnétique/organique. Le champ de rappel [16] sondé par la FNR aux interfaces Co/Organique n'a révélé aucune augmentation de l'anisotropie aux d'interfaces (figure 6). Au contraire, les interfaces sont systématiquement plus douces magnétiquement que la partie massive des couches de Co.

Une dernière contribution importante à cette thèse a été la mise en œuvre de la Microscopie Electronique à Transmission (MET) dans des hétérostructures qui contiennent des couches moléculaires organiques fragiles (figure 7). Le TEM a été utilisé pour appuyer les interprétations des résultats obtenus à partir des mesures FNR. Alors que la FNR fournit des informations macroscopiques sur les échantillons, le TEM permet d'avoir un aperçu local de la morphologie des films. La combinaison des deux types d'informations permet de mieux comprendre la structure et la morphologie des interfaces hybrides. Tous Les résultats TEM sont en bon accord avec les interprétations FNR.

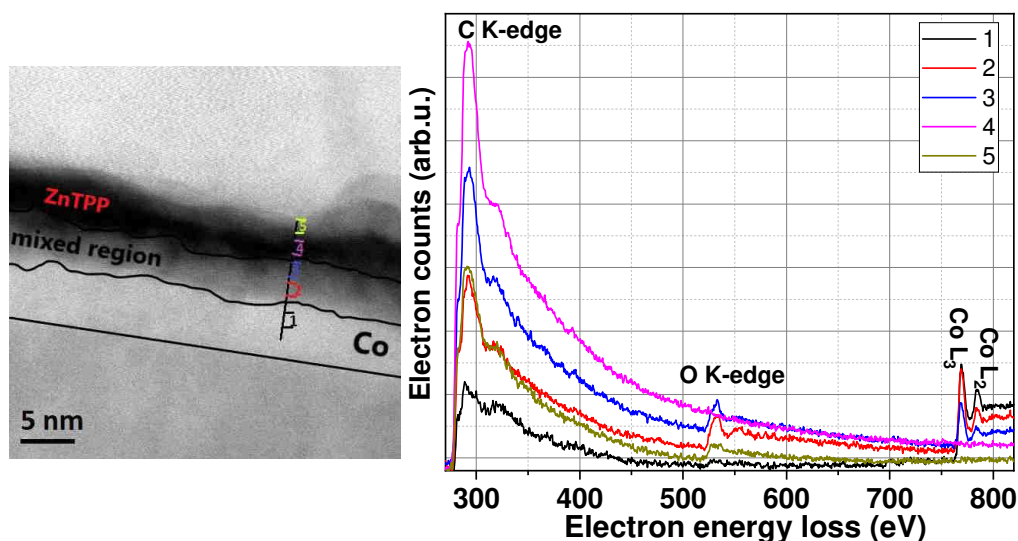


**Figure 7:** A gauche : champ sombre d’une hétérostructure dont les spectres EELS sont donnés à droite. Chaque spectre est représenté avec la même couleur que le numéro correspondant dans la le champ sombre.

Grâce à la connaissance détaillée acquise sur la croissance et la morphologie de ce système métal ferromagnétique/organique, il est désormais possible d’étudier si de nouvelles propriétés physiques intrinsèques peuvent être mises en évidence. Bien qu’il ait été démontré que l’« exchange bias » n’est pas un effet d’interface intrinsèque, cela n’exclut pas la possibilité que d’autres effets de couplage d’échange magnétique se produisent entre les électrodes ferromagnétiques à travers la couche organique. Pour étudier cet effet, les courbes d’aimantation des hétérostructures multicouches ont été mesurées (figure 8). Leur retournement d’aimantation s’effectue en plusieurs étapes pour différentes plages de champs magnétique. Chaque étape peut être attribuée aux différentes couches ferromagnétiques présentes dans le système. Les cycles mineurs obtenus pour chaque retournement ont montré un décalage vers l’axe positif du champ magnétique. Ce décalage positif est la conséquence d’un couplage antiferromagnétique entre les couches ferromagnétiques adjacentes au travers de la couche organique. Il s’agit d’un résultat prometteur qui nécessitera des investigations plus approfondies.



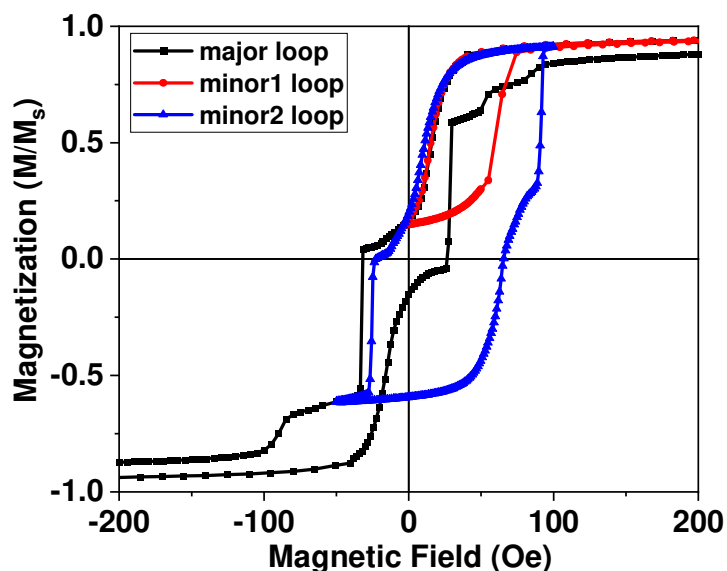


**Figure 8:** Courbe d'aimantation et cycles mineurs d'un échantillon Fe(30nm)/ZnTPP(20ML)/Co(5nm)/ZnTPP(20ML)/Fe(30nm). Les cycles mineurs sont tous les deux décalés dans le sens positif ce qui traduit la présence d'un couplage antiferromagnétique.

Nos travaux ont permis de résoudre la controverse sur l'existence de l'« exchange bias » dans les systèmes hybrides ferromagnétique/organique : l'« exchange bias » n'est pas un effet d'interface mais provient de l'oxydation partielle de la couche de Co entraînée par l'exposition à l'air. De plus, la mise en œuvre de techniques de caractérisation standards (par exemple XPS, SQUID, TEM etc.) Ce travail montre que l'élaboration de composants électroniques à base d'hétérostructures métal/organique sera très complexe. Néanmoins, les propriétés magnétiques d'échantillons structurellement maîtrisés suggèrent qu'il existe un couplage d'échange antiferromagnétique entre couches ferromagnétiques séparées par des couches organiques MTPP.

Ces résultats sont prometteurs et conduisent à envisager de nombreuses perspectives à ce travail. Un couplage magnétique antiferromagnétique a été mis en évidence pour une épaisseur organique de 15ML. Nous ignorons si ce couplage peut changer de signe ; Il faudra donc étudier cet effet en détail pour des épaisseurs de couche supérieures à l'épaisseur seuil de 15 ML. Le fait d'avoir des couches magnétiques avec des champs coercitifs différents rend possible des études de transport afin de mettre en évidence des effets de TMR et/ou GMR au travers de MTPP. Le vieillissement des échantillons reste un point critique et il serait intéressant de comprendre l'origine de celui-ci.

Des études de croissance in situ sous UHV et en température pourraient permettre de comprendre si ce vieillissement est induit par l'exposition à l'air ou pas. Le vieillissement ainsi que le désordre aux interfaces sont probablement liés à la mobilité des éléments qui constituent les hétérostructures. Elle pourrait être limitée en effectuant des dépôts à très basse température. Enfin la méthodologie d'étude développée pendant ce travail pourra être appliquée à d'autres systèmes métal/organique. Il serait particulièrement intéressant de l'utiliser dans un cas où une forte interaction chimique se produit entre le métal et le matériau organique.

- [1] V. A. Dediu, L. E. Hueso, I. Bergenti and C. Taliani, *Nat. Mater.* **8**, 707–716 (2009).
- [2] R. Geng, H. M. Luong, T. T. Daugherty, L. Hornak and T. D. Nguyen, *J. Sci.* **1**, 256–272 (2016).
- [3] X. Sun, M. Gobbi, A. Bedoya-Pinto, O. Txoperena, F. Golmar, R. Llopis, A. Chuvilin, F. Casanova and L.E. Hueso, *Nat. Commun.* **4**, 2794 (2013).
- [4] M. Gobbi, F. Golmar, R. Llopis, F. Casanova and L. E. Hueso, *Adv. Mater* **23**, 1609–1613 (2011).
- [5] M. Grünwald, M. Wahler, F. Schumann, M. Michelfeit, C. Gould, R. Schmidt, F. Wurthner, G. Schmidt, and L.W. Molenkamp, *Phys. Rev. B* **84**, 125208 (2011).
- [6] J. J. H. M. Schoonus, P. G. E. Lumens, W. Wagemans, J. T. Kohlhepp, P. A. Bobbert, H. J. M. Swagten, and B. Koopmans, *Phys. Rev. Lett.* **103**, 146601 (2009).
- [7] H. Vinzelberg, J. Schumann, D. Elefant, R. B. Gangineni, J. Thomas, and B. Buchner, *J. Appl. Phys.* **103**, 093720 (2008).
- [8] D. Ciudad, M. Gobbi, C. J. Kinane, M. Eich, J. S. Moodera, and L. E. Hueso, *Adv. Mater.* **26**, 7561–7567 (2014).
- [9] C. Barraud, P. Seneor, R. Mattana, S. Fusil, K. Bouzehouane, C. Deranlot, P. Graziosi, L. Hueso, I. Bergenti, V. Dediu, F. Petroff, and A. Fert, *Nat. Phys.* **6**, 615–620 (2010).
- [10] S. Sanvito, *Nat. Phys.* **6**, 562–564 (2010).
- [11] K. V. Raman, *Appl. Phys. Rev.* **1**, 031101 (2014).
- [12] K. V. Raman, A. M. Kamerbeek, A. Mukherjee, N. Atodiresei, T. K. Sen, P. Lazic, V. Caciuc, R. Michel, D. Stalke, S. K. Mandal, S. Blugel, M. Munzenberg and J. S. Moodera, *Nature* **493**, 509–513 (2013).
- [13] P. K. J. Wong, W. Zhang, G. van der Laan and de Jong, M. P., *Org. Elec.* **29**, 39–43 (2016).
- [14] M. Gruber, F. Ibrahim, S. Boukari, H. Isshiki, L. Joly, M. Peter, M. Studniarek, V. Da Costa, H. Jabbar, V. Davesne, U. Halisdemir, J. Chen, J. Arabski, E. Otero, F. Choueikani, K. Chen, P. Ohresser, W. Wulfhekel, F. Scheurer, M. Alouani, E. Beaurepaire, and M. Bowen, *Nat. Mater.* **14**, 981-984 (2015).
- [15] S. Boukari, H. Jabbar, F. Schleicher, M. Gruber, G. Avedissian, J. Arabski, V. Da Costa, G. Schmerber, P. Rengasamy, B. Vilen, W. Weber, M. Bowen, and E. Beaurepaire, *Nano Lett.* **18**, 4659-4663 (2018).
- [16] P. Panissod and C. Meny, *Magn. Reson.* **19**, 447-460 (2000).



# Introduction

At the end of the 20<sup>th</sup> century, the scientific community experienced a great revolution which influenced the technological world and the computer industrial sector. This revolution came within the field of electronics and led to the rise of spintronics. Spintronics has its origins in the discovery of anti-ferromagnetic exchange coupling and giant magnetoresistance (GMR) in iron-chromium metallic super-lattices. Spintronics gave a whole new approach on how to carry the spin of an electron for memory and logic applications in electronic devices. Although it has been almost more than three decades since the discovery of GMR and TMR (tunnel magneto-resistance), spintronics is still an active research field and to date, commercialized spintronics based devices (e.g. hard disc read heads, sensors, memories...) are used in many applications .

To feel the impact of this revolution on the tech world, one good example would be to translate the increase of data storage into numerical figures. The first ever computer to use magnetic data storage was the “ERA Atlas” built in 1950s. This computer had a density of about 400 bits per square inch. In 2012, Seagate technology one of the leading tech firms in data storage demonstrated the first ever 1 terra bit per square inch hard drive with the possibility of scaling it up to 60 terra bits in the coming decades! Within 70 years, there has been enormous increase in the data density. This increase significantly tells us that the magnetic storage technology is growing even faster than the exponential trend that Gordon Moore predicted for the silicon-based technology.

Like the materials used for the discovery of GMR, early stages of research in the field of spintronics concentrated on using metallic materials (magnetic, non-magnetic). However, pure metallic systems have some drawbacks as the order of magnitude of their electrical resistance is small which makes their integration into regular microelectronic devices difficult. So, with the progress of spintronics there has been massive efforts to find new materials that could replace the conventional metallic materials used in the devices. Among these alternatives, half-metals or semiconductor materials appeared as ideal candidates. Half metallic materials show 100% spin polarization and the charge carriers in semiconductors have longer spin lifetime compared to metallic materials. Nevertheless, these materials also have some major drawbacks like the defects at the metal/semiconductor interfaces which often lead to structural and chemical disorder hence reflect poorly on the performance of the device. More importantly, there exists a difference in the density of states between a metal and a semiconductor that results into the resistivity mismatch.

More recently a new class of alternative materials has been considered: carbon-based compounds. Therefore organic molecules were integrated into spintronic devices which led to the birth of a new research field known as organic spintronics. In theory, organic molecules with low molecular weights

are promising agents not only because of their strong electron-phonon coupling and long spin coherence length but also because different chemical functionalities can be grafted on their ligands. In addition, organic molecules can serve as cheap, mechanically flexible, and chemically interactive entities to fabricate bottom-up electronic devices. All these characteristics make organic molecules a good candidate for spintronics devices.

The path from new concepts to experimental data in organic spintronics was first explored at the turn of the 21<sup>st</sup> century. Several groups reported the experimental evidence of spin polarized injection and magnetoresistance in planar hybrid junctions using hexa-thienyl ( $T_6$ ) derivatives as well as low temperature GMR effects in vertical spin valve structure using  $\pi$  conjugated 8-hydroxy-quinoline aluminum ( $Alq_3$ ) molecules. Following these promising results, several spintronic effects were investigated in organic materials including the inverse spin-valve effect, tunneling magnetoresistance, magneto-transport, and other phenomena which all mimicked the conventional spintronics.

Organic spintronics showed a strong synergy between various research fields and combined the efforts of theoretical and experimental physicists, chemists, engineers, surface scientists etc. Such multi-disciplinary research field led to promising results and introduced a new science recognized as the science of “spinterface”. In organic spintronics, science of “spinterface” is very important as it is expected to help to tailor and understand the fundamental mechanisms occurring at the organic/inorganic hybrid interfaces. However, even if the concept of “spinterface” is very attractive there are still many open questions since most of the effects originating from the organic/inorganic hybrid interfaces are poorly understood.

As the main mechanisms of organic spintronics, ranging from spin injection to detection occurs at the contact of the organic molecule with the inorganic metallic electrode, the quality and the nature of the hybrid interfaces is of great importance. Therefore, it is especially important to have well-defined hybrid systems and interfaces allowing a detailed understanding of the physics occurring at the level of the hybrid interfaces.

To this end, this thesis focuses on studying the interdependence between the structural and the magnetic properties of organic heterostructures and interfaces. It addressed several of the most debatable “spinterface” effects in organic/inorganic hybrid systems like the molecular exchange bias. In addition, through novel experimental methodologies it provided important insights into the morphological characteristics of the organic/inorganic heterostructures which led to a better understanding of their physical properties.

The first part of the current manuscript discusses the scientific context within which this work has been done. It provides a broad knowledge on organic molecules, emphasizing on metal tetra-phenyl porphyrin (MTPP) molecules that has been particularly studied in this work. The actual knowledge

of their on-surface physical properties has also been discussed. Furthermore, it focuses on explaining the interactions occurring at the hybrid interfaces and their accompanied effects in organic/inorganic heterostructures. Finally, it presents the scientific motivations of the thesis.

The second part describes the experimental deposition techniques and the conditions necessary for the growth of the organic/inorganic hybrid heterostructures. It presents the conventional experimental characterization techniques (AFM, SQUID, TEM, XPS) and introduces the novel methodology developed with ferromagnetic nuclear resonance (FNR) spectroscopy technique. These techniques are then used in part III and part IV to probe the morphology, the magnetic, and the chemical properties of the organic/inorganic heterostructures and of the hybrid interfaces embedded in them.

Part three concentrates on investigating the origin of exchange bias in cobalt/organic hybrid systems. The experimental evidences of this part provided by SQUID, XPS and AFM solve the controversy about the existence of the molecular exchange bias in cobalt/MTPP and cobalt/MPc (metal phthalocyanine) hybrid systems. The experimental proofs show that exchange bias in these systems is not an intrinsic “spinterface” effect. In addition, it reveals the mechanical instability of the molecular films.

The most important and novel contributions of this thesis are presented in part IV. The chapters of this part describe for the first time the application of FNR to study the interfaces of organic/inorganic hybrid heterostructures. After a first chapter devoted to the optimization of the organic heterostructures, chapters 9 and 10 provide important information on the morphology of ZnTPP molecular films on top of the ferromagnetic electrodes and deliver valuable insights into the structure and the chemical nature of the hybrid interfaces embedded in cobalt-ZnTPP heterostructures. The second important asset of this part is represented in the last chapter. It describes the direct visualization of the cross-sectional organic/inorganic hybrid heterostructures via TEM. TEM clarifies and provides local insights into the morphology and the chemical composition of the layers and of the interfaces of the heterostructures.

Finally, the manuscript ends with a general discussion on the experimental observations of the work conducted throughout the thesis. It highlights the conclusions and provides some ideas for future potential work in the thesis’s direction.



# **Part I**

## **Scientific context**





The introductory part of this manuscript discusses the general scientific context related to this Ph.D. thesis work. It provides a broad overview on spintronics and discusses the research field of organic spintronics. Moreover, it concentrates on explaining the interactions occurring at the organic/inorganic interfaces and discusses the different possible magnetic effects occurring at these hybrid interfaces. Finally, it presents the metal tetra-phenyl porphyrin (MTPP) organic compounds as they are the organic molecules mostly studied in this work.

## Chapter 1: Introduction to organic spintronics

Silicon-based technology and classical electronics saw an additional contributor to the field of electronics with the rise of spintronics. Spintronics allowed a significant improvement in the performance of many electronic devices. For example, through-out the years and thanks to spintronics, the magnetic recording head technology evolved from bulk inductive heads with wire-wound coils to giant magnetoresistance (GMR) and then to tunnel magnetoresistance (TMR) type of magnetic read heads. This allowed big increase of the read heads' sensitivity and in consequence a big increase in the recording density. As this Ph.D. work is focused on the study of a new class of heterostructures for applications in spintronics, the aim of this chapter is to briefly present the evolution of spintronics from the discovery of the GMR effect to the more recent developments that have motivated this work.

### 1.1 Electronics with spins

In addition to the charge of the electron, when an electronic device uses the electron spin to process and transfer information, the device will no longer belong to conventional electronics category, but rather will be considered belonging to spin-based electronics, commonly known as spintronics. Spintronics is one of the relatively young research fields in nano-technology which involves nano-magnetism too. It is well known and accepted that spintronics came to light with the discovery of the giant magnetoresistance (GMR) effect in iron/chromium magnetic superlattices [1,2]. The authors studied two ferromagnetic iron layers that were anti-ferromagnetically coupled through a chromium spacer. They observed change in the resistance of the superlattices when varying the in-plane external magnetic field. However, spintronics and GMR have their origins from previous works on the influence of the spin on the electron mobility in ferromagnetic (FM) metals. This phenomenon was first suggested by Nevill F. Mott [3] and then expanded experimentally and theoretically by other groups [4,5,6].

GMR, as indicated by its name is based on the phenomenon of magnetoresistance (MR) effect. MR represents the change in the resistance of a system on the application of an external magnetic field. A typical GMR device, referred to a spin-valve (SV) device consists of two FM layers separated by a conductive but non-magnetic (NM) spacer. Following A. Fert's arguments of MR effect in multilayered systems [1,7] the mechanism of GMR can be described as follows: When an electric current passes through the SV device the electrons with one spin direction (the spin-up electrons in the case of the

Fe/Cr system) will experience more scattering compared to the electrons with the other spin direction (spin-down electrons for Fe/Cr system). This is called spin dependent scattering and depends on the nature of the ferromagnetic/non ferromagnetic metals involved in the structure.

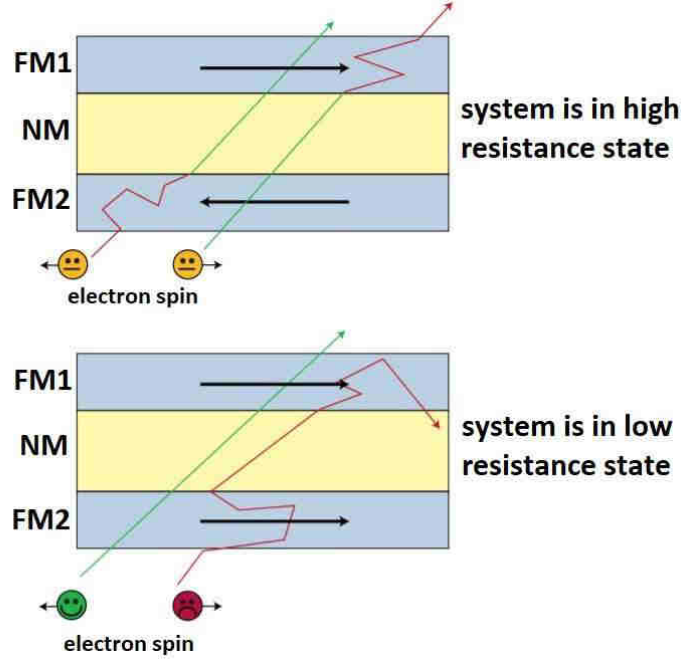


**Figure 1:** General schematic of a spin-valve device illustrating the GMR effect. The two FM layers are separated by non-magnetic (NM) metal spacer. In the upper sketch, when the FM electrodes have anti-parallel configuration, both spin-up and spin-down electrons undergo strong scattering in either of the FM electrodes thus the overall resistance of the multilayer system will be high. In the lower sketch, when the FM electrodes are in parallel state the electrons of one of the spin directions can go easily through all the magnetic layers and the overall resistance of the multilayer system is small. The solid lines represent the trajectory of the conduction electron in the metallic layers of the system. The figure is reproduced from ref. [8].

Considering now that the two FM electrodes of the SV device have different coercive fields (figure 1), they can show parallel or anti-parallel alignments of their magnetization upon changing the strength of the external magnetic field. So, when the two FM electrodes are in parallel configuration the electrons of one of the spin directions experience small scattering only through the whole system while the others experience large scattering. Since one of the spin direction experiences only weak scattering, it results in a system with a low overall resistance denoted as  $R_p$ . On the contrary, when the electrodes are aligned as anti-parallel the spin-up electrons will experience strong scattering in one of the electrodes while the spin-down electrons will have strong scattering in the other electrode. As a result, the overall system

shows high resistance state represented as  $R_{AP}$ . Hence, GMR can be written as a function of these two resistance states:

$$GMR = \frac{R_{AP} - R_P}{R_P} \quad (1)$$

GMR is an interesting and important example that illustrates how artificially structured materials at the nanoscale can give birth to fundamental effects that provide new functionalities.

From this starting point tremendous research work took place in order to increase the MR ratio. The next step towards enhancing the MR ratio of an SV device came when the non-magnetic spacer was replaced by a thin layer of insulator. As a result, magnetic tunnel junctions (MTJ) were created. In MTJ kind of structure, the MR effect arises from spin-conserved tunneling across the thin insulator spacer and is reported as tunneling magnetoresistance (TMR). Like GMR, the resistance of a TMR device depends on the relative magnetic orientation of the metallic electrodes. Since the metallic electrodes are FM, the DOS of the electrodes are spin dependent due to the exchange interactions. DOS at the fermi energy ( $E_F$ ) level for the spin-up electrons are different than that of the spin-down electrons. The difference between the electronic DOS is at the origin of TMR. Figure 2 represents an illustration of the TMR effect in MTJ. As mentioned, during the tunneling process the electron spin is conserved. An electron can only tunnel through the thin barrier to the spin sub-band of the same spin orientation. Consequently, the conduction will be proportional to the product of DOS of the two FM electrodes of the same spin orientation. Moreover, a change from parallel to anti-parallel magnetization configuration for the two FM electrodes will result in an exchange between the two sub-bands of one of the electrodes for the tunneling process. As a result, a change in the conductance will be observed. Using this explanation, the TMR ratio can now be expressed in terms of the polarizations of the FM electrodes that are denoted as  $P_1$  and  $P_2$  respectively.

$$TMR = \frac{R_{AP} - R_P}{R_P} = \frac{2P_1P_2}{1 - P_1P_2} \quad (2)$$

It was Julliere who first demonstrated this explanation of TMR and observed experimentally small values of TMR at low temperature [9]. However, only after decades reproducible and higher values of TMR were obtained using amorphous  $AlO_x$  tunnel barrier [10,11]. Soon after, extensive research work was dedicated in this direction and higher TMR values were reached using both amorphous  $AlO_x$  and epitaxial MgO tunnel barriers [12,13,14,15,16,17]. Using high quality epitaxial layers as tunnel barrier allows additionally to filter the symmetry of the wave function of the electrons tunneling through the barrier. In this case, the TMR depends only on the spin polarization of that selected symmetry. In a different report, significantly higher TMR values were noted when half-metals (100% spin polarized) were used as the electrodes [18]. Among the commercial technological applications, MTJ devices based on TMR effects had important contribution in the read head of hard disk drives (HDD) and in magnetic

random-access memories (MRAM). Seeing operational MTJ structures in MRAM devices is promising since MRAM could be a dream-like memory that can combine the functionalities of static and dynamic access memories together on a single electronic chip. With SV and MTJ based devices, research had made important progress in the field of spintronics leading to important technological advances. After exploring spintronics with metallic and insulating spacer layers, the possibility of using semiconducting spacers have also been investigated.

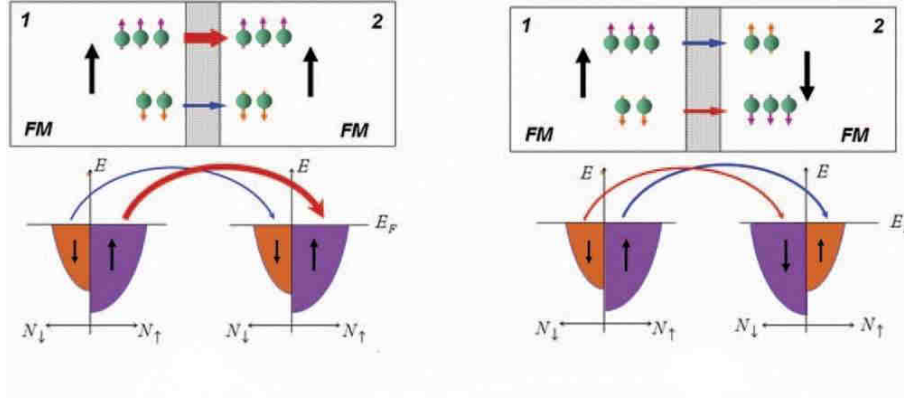


**Figure 2:** Schematic of TMR effect in an MTJ. The tunnel barrier (light grey) is thin enough so an electron in its evanescent wave will have enough energy to pass through the barrier and reach the second electrode (FM2). Left sketch: in parallel magnetization configuration spin-up electrons can only pass to spin-up sub-band (represent as red arrow) and spin-down electrons to spin-down sub-band (orange). Right sketch: in anti-parallel configuration the tunneling scenario is the same as the parallel, however there is an exchange in the sub-bands, as now the majority of the electrons in FM2 are of spin-down configuration (seen in the upper right configuration). This exchange will lead change in the conductance of the device. The figure is taken from ref. [19].

Considering spintronic devices with semiconductor materials is an interesting approach as it combines the potentials of semiconductors and FM metals. Combining FM metals and semiconductors could offer a possibility to develop a device that could perform information processing, communication, and storage all in single material electronic chip. Such devices had hypothetical advantages but revealed some major disadvantages. One of the first advantages is that semiconductor materials, in general, are more versatile than metals since their electronic properties can be modified by doping. Second, the spin-relaxation time is usually longer in semiconductors than in metals. In semiconductors the spin lifetime is of the order of  $\approx 100$  picoseconds while in metals it is of the order of femtoseconds. On the other hand, one of the first drawbacks is found in the difficulty of growing a semiconductor material in contact with FM metallic layers. More often, this kind of growth gives rise to complicated structural and

chemical properties at the semiconductor/metal interface. In addition, a more fundamental problem is related to the difference in the DOS between a metal and a semiconductor resulting in the so-called conductivity mismatch. Due to such mismatch spin-relaxation occurs mainly in the metallic part, in the spin accumulation region at the interfaces. However, some solutions have been proposed [20,21] and the mismatch problem was solved by creating a spin-dependent interface resistance (tunnel junction). Another interesting approach for solving the conductivity mismatch and the interfacial complication was the fabrication of ferromagnetic semiconductors like the  $Ga_{1-x}Mn_xAs$  [22] that showed large values of TMR [23] but low Curie temperature (170K). The low Curie temperature ruled out practical room temperature applications. Semiconductor spintronics brought several advantages yet showed some serious obstacles that are difficult to overcome.

After using metallic, insulating, and semi-conducting spacers, a new kind of material had been considered: Organic molecular layers. Organic molecules have the potentiality to show long spin lifetime and are therefore very promising.

## 1.2 Organic Spintronics

Organic molecules are mainly composed of light weight carbon atoms. Therefore, they have the potentiality to show exceptionally long spin lifetimes; in the order of micro or milli seconds. Indeed, the mechanism reducing spin lifetime is driven by strong spin-orbit coupling while small spin-orbit coupling is expected in molecules since it is proportional to the atomic number of the carbon ( $Z^4$ ,  $Z = 6$  for C). Consequently, organic based spintronic devices are expected to show large GMR and TMR like effects.

In addition to the expected long spin lifetime, organic molecules have other interesting properties. They are mechanically flexible, chemically tunable, are of low cost and can be used in large area fabrication. Combining these properties, researchers expect that organic molecules will have the potential to contribute strongly in the field of spintronics, thus allowing them to design and develop multifunctional spintronic devices.

With organic molecular layers, new device structures were formed. These structures can be of two types: organic spin valves (OSV) or organic magnetic tunnel junctions (OMTJ). OSV devices have thick organic spacer layer, typically tens of nanometers. In general, the transport of charge carriers in OSV devices begins with injection in the organic layer, in which there will be a net flow of spin-polarized carriers through the organic molecules. The conduction across this thick organic layer occurs by hopping of the electrons, followed by electron capture in the magnetic counter electrode [24]. As mentioned, organic molecules are well known for their long spin-relaxation time which ranges from  $10^{-6}$  to  $10^{-3}$ s [25,26]. Therefore, it is expected that organic based SV devices will offer interesting opportunities for spin manipulation.

The first experimental result in organic based spintronic devices was reported almost two decades ago [27]. Lateral devices were fabricated by lithography techniques and the two ferromagnetic manganite electrodes (LSMO) were separated by 100-500nm of hexa-thienyl ( $T_6$ ) derivatives. This device showed strong MR behavior up to 200nm of organic spacer. MR disappeared for thicker organic spacers. As a result, spin diffusion length ( $\lambda_s$ ) (at room temperature) was concluded to be of 200nm and spin-relaxation time ( $\tau_s$ ) for an  $10^{-4} \text{ cm}^2 \text{ V}^{-1} \text{ s}^{-1}$  mobility ( $\mu_s$ ) to be 1 $\mu\text{s}$  (the relation  $\tau_s = \frac{e\lambda_s}{KT\mu}$  has been used to compute the spin relaxation). Soon after, vertical devices were fabricated using LSMO as first electrode, cobalt as counter electrode and 8-hydroxy-quinoline aluminum ( $\text{Alq}_3$ ) molecules as the organic barrier. This kind of devices showed strong negative MR behavior at low temperatures i.e. resistance decreased when the magnetization of the two electrodes was switched from parallel to anti-parallel states [28,29].

In contrast to OSV, the thickness of the organic spacer in an organic magnetic tunnel junction (OMTJ) has to be very thin, of the order of 5nm and less. As in any tunneling phenomena, the probability of the electrons to tunnel across the barrier scales exponentially with the thickness of the potential barrier. In an OMTJ device, the tunneling spins are not injected to the electronic energy level of the organic molecules, but the spin transport properties are dominated by the electronic and magnetic properties of the interface formed at the organic-ferromagnetic metallic contact. Traditional technological tools utilized in inorganic spintronic devices has been applied to the fabrication of organic devices and led to important breakthroughs in the field of organic spintronics. For example, standard shadow masking techniques were used to build  $\text{Alq}_3$ /aluminum oxide ( $\text{Al}_2\text{O}_3$ ) and rubrene/ $\text{Al}_2\text{O}_3$  hybrid structures. In these devices, small MR was observed at room temperature [30,31]. Significant progress in this direction has been made by C. Barraud et. al, where the authors had fabricated nanometer-scale LSMO/ $\text{Alq}_3$ /Co MTJ device, that exhibits giant tunneling magnetoresistance, reaching up to 300% at 2K [32].

However, many controversies arise when talking about OSV and OMTJ. First puzzling factor of an OSV device is the appearance of MR for organic spacer thickness ranging from 100nm and above. This is surprising because organic materials have short spin-diffusion length [33] and low electron mobility. For example, Rubrene, one of the best organic semiconductor has around  $10 \text{ cm}^2 \text{ V}^{-1} \text{ s}^{-1}$  hole mobility which is much lower than p-type silicon that has  $400 \text{ cm}^2 \text{ V}^{-1} \text{ s}^{-1}$  mobility. On the other hand, in MTJ the barrier spacer separating the two metallic electrodes should be insulator. Organic molecules are closer to semiconductor type of materials rather than to insulators. So, the transport of the charge carriers between the electrodes will not solely be governed by tunneling mechanism but hoping conduction mechanism through the molecule might also contribute. Second, the required thickness of the organic spacer in OMTJ is of 5nm and less. Since organic molecules are light weighted compounds, this thickness will be more complicated to control with organic layers than with metallic or insulating

---

layers. Third, in any device there is always a counter electrode on top of the spacer layer. Therefore, if the organic spacer layer is thin then it might not guarantee the pin-hole free character of the spacer. If the thin organic spacer is rich in pin-holes, the two electrodes will be in contact and the device will be shorted. At last, like in the case of semiconductor spacer layers, metal/molecule interface will lead to structural and chemical complications that could lead to serious misconceptions in the transport mechanisms.

Over a short period of time, spintronics did revolutionize the traditional concept of electrons in the field of electronics and its applications. For the first time, spintronics opened new ways to efficiently use the spin of the electron, to control the motion of the electrons in ferromagnetic systems through the orientation of their magnetization. Spintronics is at the origin of important scientific breakthroughs and led to a giant leap in technological applications. Even though organic device structures might not be eligible for commercial use in near future, already organic light-emitting diodes exist commercially. This gives hope that organic molecules integrated in spintronic devices could be a good solution for future faster and denser information processing and storage.



---

## Chapter 2: Organic/inorganic hybrid interface interactions

To understand the properties of organic based spintronic devices a fundamental insight into their different components is required. One of the main factors governing their physical properties is the hybrid organic/inorganic interface. Therefore, it is very important to identify and understand the nature of these hybrid interfaces. For this purpose, the current chapter briefly describes the electronic structure of the FM metals and the molecular orbitals of an isolated organic molecule and then, it discusses the different types of interactions occurring at the hybrid interface when organic molecules are at the vicinity of inorganic metallic layers.

### 2.1 Isolated organic molecules and metallic ferromagnets

Before engaging into the much complex hybrid system, it is worth to briefly remind the electronic structure of an isolated FM metal and the molecular orbitals of an organic molecule in the gas phase. FM metals act differently from normal metals. Namely, the 3*d*-transition metal ferromagnets show exchange interactions between their *d*-electrons that leads to the exchange splitting of the two *d*-spin bands and therefore to ferromagnetism.

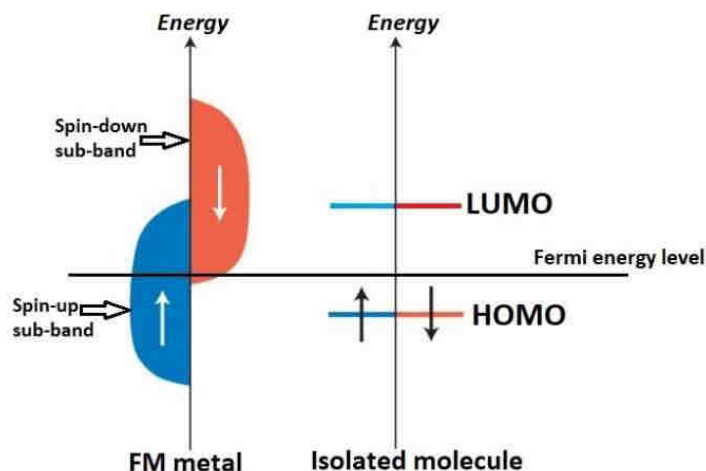


**Figure 3:** General scheme representing the energy level alignment of a ferromagnetic (FM) metal and the molecular orbitals of an isolated organic molecule. The figure is partially reproduced from ref. [34].

As seen in figure 3, the electronic structure of the FM is characterized by a spin-split DOS corresponding to majority and minority spin sub-bands. On the other hand, organic molecules in their gas phase have discrete molecular energy levels, that are spin independent. The orbital occupation is

characterized by the frontier orbitals: the highest occupied molecular orbital (HOMO) and the lowest unoccupied molecular orbital (LUMO). If there is no interaction between the magnetic layer and the organic molecule, the electronic properties of the interface will be nothing but the superposition of the electronic energy levels of each component.

## 2.2 Hybrid organic/inorganic interface

The deeply buried, truly hidden yet most important part of any spintronic device is the interface. This is the place of many interesting physical phenomena and can be considered a crucial region for creating new spin effects. However, it is challenging to understand the physics beneath these interfacial phenomena. This is already true for inorganic interfaces, and it becomes even more interesting yet overly complex when soft, and light materials like organic molecules are in contact with the inorganic metallic electrode.

At early stages of research, the focus was only on understanding the charge transport at the FM metal/organic interface. So, the main modification taken into consideration was the energy level alignment at the interface [35]. With time, more advanced understanding of the modification of the molecular orbitals was presented which took into consideration the concept of energy level broadening [36]. In general, the metal/molecule interactions are divided into two different categories. First, the physisorption regime where the dominant interaction is the long-range, weak van der Waals (vdW) forces while the second is defined as chemisorption. In chemisorption, molecules have strong chemical bonds with the underneath substrate. In real organic/metallic systems, these two distinct regimes probably co-exist however when chemisorption is involved, it will be the dominant one as its energy exceeds vdW interaction energy by orders of magnitudes.

### 2.2.1 Physisorption regime

A quantitative description of the strength of molecule-substrate interactions can be described via adsorption energy  $E_{ads}$  which can be represented as:

$$E_{ads} = E_{system} - (E_{surface} + E_{molecule}) \quad (3)$$

$E_{system}$  represents the total energy of the adsorbed system i.e. molecule-substrate system,  $E_{surface}$  is the total energy of the clean FM substrate surface and  $E_{molecule}$  is the energy of the isolated molecule in gas phase. In the physisorption regime,  $E_{ads}$  is usually very small, less than 0.1 eV. In this case, the molecule-FM substrate equilibrium distance exceeds 3 Å [37]. As a result, little charge transfer will be present at the interface and weak orbital overlap will occur between the adsorbed molecule and the FM metallic substrate, with no chemical bonds.

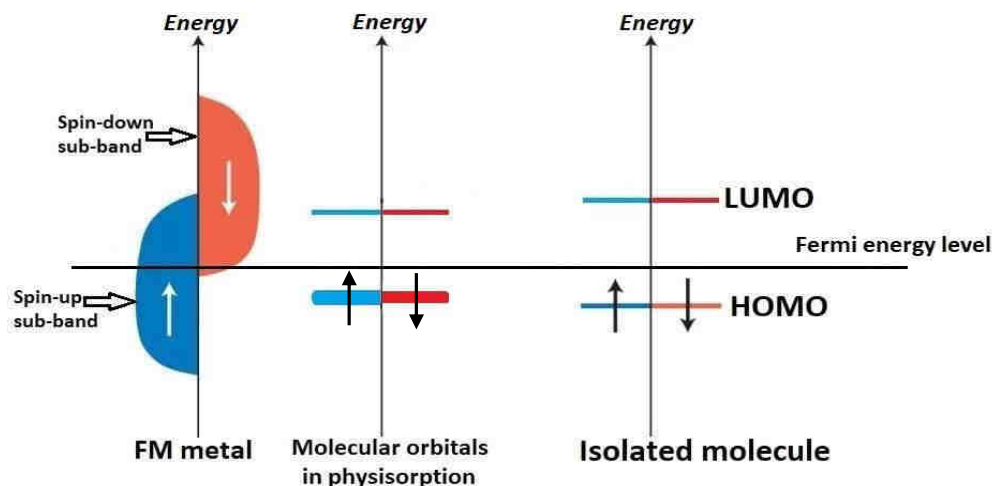


**Figure 4:** General scheme representing the energy level alignment of metals, isolated molecule, and molecule when in physisorption regime. Due to weak interactions, only slight change in the electronic energy levels occurs (very weak broadening and very weak energy shift). The figure is partially reproduced from ref. [34].

Nevertheless, the weak molecule-substrate interactions will lead to a re-distribution of molecular orbitals and a re-normalization of HOMO-LUMO gap of the molecules of the first molecular layer that are close to the substrate [38,39]. This re-normalization is most often negligible, and the resulting molecular orbital energies are only slightly different from those of the isolated molecule. In this case, the molecular orbitals can still be used to define the electronic structure of the molecules. Further from the interface, the molecules of the second molecular layer are completely isolated from the metallic surface thus fully retain their gas phase electronic properties. HOMO and LUMO of these molecules will have the same energy levels as the energy levels of molecules in the gas phase.

### 2.2.2 Chemisorption regime

When the adsorbed molecules are close enough to the substrate with an equilibrium distance of less than  $2.5 \text{ \AA}$ , they generate an adsorption energy ( $E_{ads}$ ) typically larger than  $0.5 \text{ eV}$  [40]. This is commonly recognized as the chemisorption regime. In this case, the molecules will have strong chemical bonds with the substrate. These bonds can be ionic and/or covalent in nature.

Due to these strong bonds, two phenomena can occur at the interface between the energy bands of surface atoms and the molecular orbitals of the molecules: charge transfer and/or hybridization [41]. The latter will lead to the broadening of the molecular states and create new ones with mixed metal-molecular character while the former will redistribute the charge occupation in the bands, thus

renormalize the electronic energy levels. These newly formed spin-polarized hybrid interface states will have mixed character of metal and molecule and might not correspond to any of the band features of a free FM surface or of the orbitals of an isolated molecule [42].

According to the strength of the chemical bonds a chemisorption can be divided into two different regimes: weak chemisorption or strong chemisorption [43]. A strong chemisorption ( $E_{ads} > 1\text{eV}$ ) usually occurs between the FM metallic substrate and the molecules of the first molecular layer that are in direct and close contact with the substrate. In this case, the molecular states split into bonding and anti-bonding states. This is due to the strong hybridization of the molecular orbitals with the  $d$ -bands of the FM. The hybridization can broaden up the molecular orbitals near the Fermi energy level. As seen in the left panel of figure 5, this broadening is spin-dependent as it depends on how strongly a particular molecular orbital interacts with the spin-split bands of the FM electrode. For example, if the molecular orbital interacts strongly with spin-down sub-band of the FM, the broadening of the molecular orbital at the Fermi level will be larger for the spin-down direction than that of the spin-up direction. Second effect arising from the strong interactions is the shift of the molecular orbitals with respect to the Fermi energy level of the FM. This shift can also be spin-dependent and may create new spin-polarized molecular orbitals at the Fermi level.

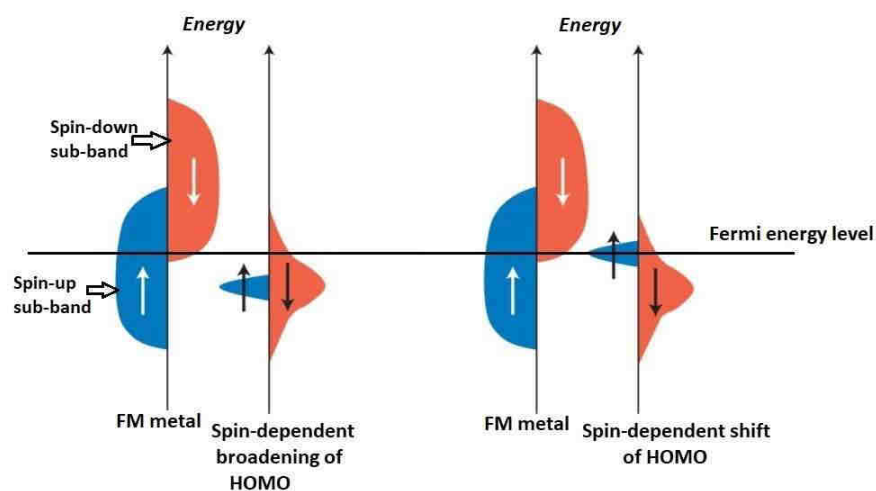


**Figure 5:** General scheme representing the energy level alignment of metals and molecular orbitals of the molecule when the system is in chemisorption regime. Due to strong interactions, the initial discrete molecular orbitals hybridize with the atomic orbital of the FM and lead to spin dependent broadening of the molecular orbital (left scheme) and spin-dependent energy shift of the molecular orbital (right scheme). The figure is partially reproduced from ref. [34].

---

On the contrary, a weak chemisorption ( $E_{ads} < 1\text{eV}$ ) is usually characterized by weak broadening of the new interface states. Weak chemisorption best describes the interactions of the molecules of the second molecular layer with the FM substrate. In this case, the molecules are not in close contact with the FM substrate hence they do not show any strong interactions with the surface. As a result, the molecules experience weak broadening in their molecular orbitals. Generally, the hybridization effects experienced by the molecules decreases with the increase in the number of the molecular layer i.e. the distance to the FM. As a consequence, the molecules of the third molecular layer (and above) will be almost free of hybridization effects and will retain their gas phase electronic properties.

### **2.2.3 Partial conclusion**

From the previous paragraphs one can conclude that the spin behavior in molecular systems is highly dependent on the nature of the chemical bonds between the FM metallic substrate and the organic molecule. The physisorption type of bonding interaction is characterized by weak, long-range van der Waals (vdW) forces that occur between the first molecular layer and the substrate surface. In this regime, the modification of the molecular orbitals is negligible thus the molecules are characterized by their gas phase electronic properties. On the contrary, molecules in the chemisorption regime experience strong chemical bonds with the substrate which leads to new hybrid interface electronic states with strong overlapping between DOS of the metallic electrode and the molecular orbitals of the molecule.

---

## Chapter 3: Magnetic properties at the hybrid organic/inorganic interface

The versatility of organic molecules and their various interactions with FM metallic surfaces excited researchers of various fields to further dig into the hybrid interfaces for better knowledge of already existing “spinterface” effects and to search for new interfacial phenomena. Interface-assisted magnetism is an interesting effect which can influence and modify the magnetic properties of the hybrid interfaces hence the magnetic properties of the organic hybrid system. This chapter gives an overview about such “spinterface” magnetic effects in the hybrid organic/inorganic systems and ends by concentrating on the so-called molecular exchange bias effect.

### 3.1 Magnetic exchange interactions

Magnetism, in magnetic materials exists due to the coupling between local magnetic moments thus forming magnetically ordered systems. This coupling, quantum mechanical in nature is known as exchange interaction. The exchange interaction between magnetic atoms makes the neighboring moments to align in parallel or anti-parallel configuration. Generally, this configuration is estimated with the exchange integral  $J$ . For ferromagnetic type of coupling,  $J$  will result into positive value while for antiferromagnetic coupling,  $J$  is negative. Within the exchange interaction, there exist several scenarios where neighboring magnetic moments do couple. First, strong but short-range coupling. This is called direct exchange [44] where the moments are close enough to have significant overlap between their wavefunctions. In contrary, indirect exchange interactions couple moments over relatively long distances where little or no direct overlap occurs between the neighboring electrons. Therefore, an intermediate conduction electron is needed to achieve this interaction. The indirect exchange is often recognized as RKKY [45,46,47] interaction named after Ruderman, Kittel, Kasuya and Yoshida. Third scenario is the super exchange [44,48]. In this case, neighboring moments are too far to interact via direct exchange, so they are coupled over long distances through a non-magnetic entity such as oxygen. The interaction of the cations'  $d$ -orbitals intermediated by the anions' (e.g. oxygen)  $p$ -orbital is the super exchange.

For example, nickel oxide (NiO) compound represents a typical anti-ferromagnetic super exchange type of interaction. In NiO, the 2 nickel ions ( $Ni^{2+}$  as cations) have eight valence electrons in the  $3d$ -orbital and are separated by the non-magnetic oxygen anion. Moreover, the nickel atoms in the compound are in octahedral coordination symmetry thus  $d$ -orbitals are split into  $d_{x^2-y^2}$  and  $d_{z^2}$  energy levels. These energy levels will then have one unpaired electron. The coupling between the nickel ions is related to the exchange interactions between the  $Ni^{2+}$  and  $O^{2-}$  ions. As represented in figure 6, the

unpaired  $3d_{x^2-y^2}$  electron of nickel ion can undergo covalent interactions with the electron of the  $p$ -orbital of oxygen if and only if the neighboring spins in these two orbitals are of opposite sign (respecting Pauli's exclusion principle). So, the spin-up electron of the  $d$ -orbital of nickel will interact with the spin-down electron of the  $p$ -orbital of oxygen. Same kind of interactions will happen in the opposing nickel ion. As a result, the two nickel ions will couple anti-ferromagnetically via super exchange interactions.

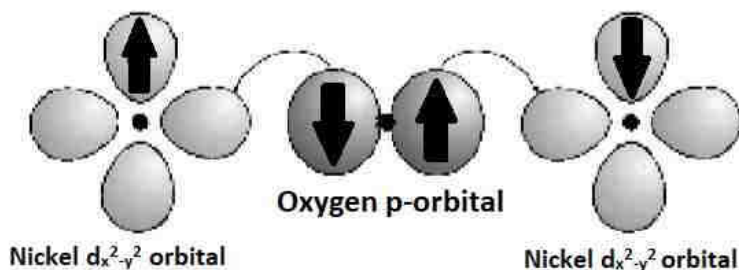


**Figure 6:** Representation of a super exchange interactions with anti-ferromagnetic kind of coupling. In this case oxygen is in-between the nickel ions and shows  $180^\circ$  geometry. The figure is partially reproduced from ref. [48].

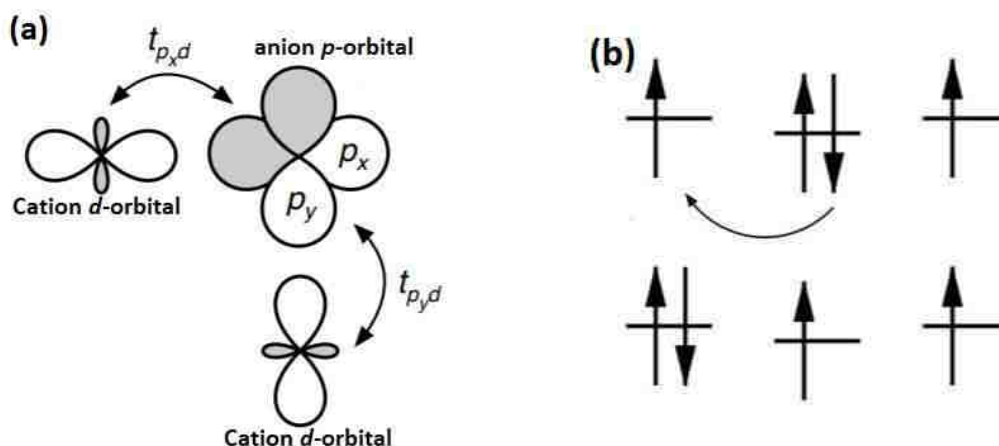


**Figure 7:** (a) Orbital representation for  $90^\circ$  super exchange, where  $d$ -orbitals couple orthogonally to the opposite  $p$ -orbital. In this case the super exchange will be mediated by Coulomb exchange as well. (b) sketch of the only possible hopping process for parallel spin alignment in the cations while the second is suppressed by the Pauli principle. The figure is taken from ref. [44].

Besides anti-ferromagnetic type of super exchange, when the oxygen anion makes a  $90^\circ$  bridge between the two  $d$ -orbitals of the nitrogen cations, the situation is different and will result into a ferromagnetic super exchange interaction. This scenario is represented in figure 7a. Respecting Pauli's exclusion principle, there exists only one way for electron hopping between the  $d$ -orbitals of the cations and anions'  $p$ -orbitals that point towards each other. The  $d$ -orbitals couple to the orthogonal  $p$ -orbital making it impossible for one  $d$ -orbital electron from one cation to reach to the second cations'  $d$ -orbital. This is illustrated in figure 7b with a simple sketch.

Super exchange interactions have been considered in hybrid organic/inorganic systems, namely in cobalt/metal tetra-phenyl porphyrin hybrid systems to explain the complicated coupling mechanism between the molecular spin i.e. spin of the unpaired electron of the molecules' central ion, and the spins of cobalt atoms at the interface. Such exchange interactions are considered in the next section among other magnetic effects that might occur at the hybrid interfaces.

### 3.2 Magnetic properties at the interface of the hybrid systems

Magnetic exchange coupling interactions at the hybrid interface occurs between the localized moments of the organic molecules and the magnetic moments of the ferromagnetic substrates. This kind of investigations are often accomplished experimentally via synchrotron based spectroscopical techniques and also theoretically by ab-initio calculations.

For example, it has been shown that the Mn-porphyrin (MnP) exhibits a  $90^\circ$  indirect exchange coupling with the cobalt films [49]. This indirect exchange coupling occurs between the metallic site of the molecule (Mn) and the cobalt substrate atom via an intermediate nitrogen atom. Another case of indirect super exchange coupling has been observed in Fe-octaethylporphyrin (FeOEP) molecules when adsorbed on cobalt and nickel films [50]. With computational methods and X-ray spectroscopy experimental techniques it is shown that due to the super exchange coupling, the FeOEP molecules can be made to order ferromagnetically. This means that the magnetic moments of the FeOEP molecules are aligned parallel with respect to the magnetization direction of the metallic films.

On the contrary, the spin of the Cr(II) ion in the paramagnetic chromium tetra-phenyl porphyrin (CrTPP) molecule revealed an anti-parallel orientation with respect to the bare cobalt substrate magnetization [51]. This was observed experimentally and confirmed theoretically. In addition, DFT calculations showed that the Cr ion is at a distance of  $3.1 \text{ \AA}$  from the cobalt substrate. This suggests that CrTPP molecules on the cobalt substrate are adsorbed in physisorption regime and Cr(II) ion cannot have any direct coupling interactions with the metallic surface. Moreover, it was observed that when an intermediate chlorine layer/atom is inserted in-between the cobalt film and CrTPP molecules, the Cr(II) ion's spin did not show any magnetic exchange coupling with the cobalt surface. Therefore, the



exchange interactions between the spin of the Cr(II) ion and the spin of the Co surface atom is attributed to be an anti-ferromagnetic indirect  $90^\circ$  exchange coupling.

The above-mentioned exchange coupling interactions are observed in bi-layer hybrid systems where the organic molecular layer is on top of a single FM metallic electrode. Now, if a third layer is present on top of the organic layer as the counter electrode, it would be possible to study interlayer exchange coupling phenomenon between the two electrodes via the organic molecular spacer. This kind of investigation can be performed both theoretically and experimentally. Theoretically, *ab initio* calculations are performed to calculate the exchange energies and the sign of the coupling between neighboring spins. Experimentally, the interlayer exchange coupling mechanism is detected by studying the magnetization curves of the tri-layer hybrid systems.

Such kind of exchange coupling has been reported in  $\text{Fe}_3\text{O}_4/\alpha$ -sexithiophene (6T)/Co and  $\text{Fe}_3\text{O}_4$ /paraseixiphenyl (P6P)/Co magnetic tunnel junction type of hybrid structures [52,53]. The ferrimagnet  $\text{Fe}_3\text{O}_4$  is prepared on top of  $\text{CoFe}_2\text{O}_4$ . This procedure results in an increase of the coercive field of the  $\text{Fe}_3\text{O}_4$  layer by almost one order of magnitude. Consequently, the in-plane major magnetic hysteresis loop (at 50K) reveals a two-step magnetization reversal. The high-field reversal corresponds to that of the magnetically blocked ferrite  $\text{Fe}_3\text{O}_4$  magnetization while the low-field reversal corresponds to the switching of the soft Co layer. In addition, the minor magnetization loops show a shift towards the positive side of the field axis. This shift indicates the presence of an anti-ferromagnetic exchange coupling between the two electrodes mediated by the thin layer of  $\alpha$ -sexithiophene (6T) (and paraseixiphenyl P6P) organic molecule.

It is interesting to see such interlayer exchange coupling effects in hybrid heterostructures where an organic molecular film serves as the spacer layer in-between the electrodes. This interlayer exchange coupling suggests that there is a transfer of net polarization from one electrode to the other electrode through the molecular layer. First, there has to be an induced polarization created at the interfaces and secondly this polarization has to propagate through the molecular layer which needs unbalanced charge carriers that are delocalized over the entire molecule. However, this process is surprising as the molecules have discrete energy levels, and the transport of the charge carriers are governed by hopping mechanism. Hopping mechanism might not guarantee to keep the polarization of the carriers intact over the molecular layer. Furthermore, in such tri-layer heterostructures the integrity of the molecular layer in-between the two electrodes is a critical point that should be considered. If the molecular layer is not continuous enough to ensure the pin-hole free character to the organic layer, then all the observed effects in such structures might be governed by the metallic impurities; which are provided by the metallic electrodes, found in the organic molecular layer.

In addition to magnetic exchange interactions, several other magnetic effects have been evidenced at the hybrid interfaces: the magnetic hardening effect, induced magnetization of a non-magnetic metallic substrate and even molecular exchange bias effect.

Some remarkable modification in the properties of the non-magnetic metallic layer has been observed in hybrid organic/inorganic system. Precisely, a  $C_{60}$  molecular film on top of copper and manganese thin films [54] was shown to modify the electronic density of states of the metals near Fermi energy level. As a result, an emerging magnetization was detected in the metallic film and the non-magnetic elements became ferromagnetic at room temperature. This emerging magnetic effect is obtained at the interface between the layer of  $C_{60}$  and the atoms of the Cu metal and extends through several layers in the metal. Nonetheless, such results are unexpected for several reasons: First,  $C_{60}$  molecules are not spin-polarized, they are diamagnetic molecules. Therefore, it is not expected for such a diamagnetic molecule to induce magnetism in metallic films especially in copper which has closed  $3d$  shell. Second, in contrast to flat and planar molecules (e.g. porphyrins or phthalocyanines)  $C_{60}$  molecules have spherical geometry. This will limit the fraction of carbon atoms that bond directly with the metallic substrate atoms. Hence less hybridization should occur between the molecular orbitals of the molecule and the atomic energy levels of the metallic substrate.

Another kind of magnetic effect has been evidenced with spin-polarized first-principle theoretical calculations. It revealed that the adsorption of a non-magnetic paracyclophane (PCP) organic molecule chemisorbed on a Fe magnetic substrate locally increases the strength of the magnetic exchange interaction between the magnetic atoms attached directly to the molecule. This strong interaction thus induces a magnetic hardening effect [55].

Actually, here and in any study in general, the choice of the organic molecule is of great importance. In this case, PCP molecule consists of two benzene-like rings that form columnar  $\pi$ -conjugated electronic structure. These benzene rings are connected by two pairs of two  $sp^3$  hybridized carbon atoms (note:  $sp^3$  hybridization means that the  $2s$  and the  $3\ 2p$  orbitals of the carbon atom combine together and form four identical orbitals, each occupying a spin-up electron). Therefore, when adsorbed on a metallic surface one benzene ring will interact strongly with the surface while the other ring will point outwards with no contact with the metallic surface. This means that the lower benzene ring will have hybrid metallic-molecule bands due to the strong hybridization with the metallic surface while the upper benzene ring will have sharp spin-split electronic states. The hybrid metallic-molecule interface states will play an important role for the magnetic properties of the hybrid interface, as seen from the example above where magnetic hardening effect was observed. On the other hand, the spin-split electronic bands are key factor for spin-polarized current injection from the hybrid interface. The presence of these two properties in a single molecule can be of a great advantage and can serve as an important magnetic building block integrated in molecular spintronic devices.

Furthermore, thickness-dependence magnetic hardening effect has been observed in Co/C<sub>60</sub> interface [56]. This magnetic hardening is effective up to 200nm of C<sub>60</sub> molecular film. In addition, C<sub>60</sub> molecules are shown to become ferromagnetic as the result of transmission of net spin polarization from cobalt atoms to the molecules. Consequently, C<sub>60</sub> molecules showed induced magnetic moment of 1.2  $\mu_B$  while a fraction of magnetic moments of the cobalt FM film was suppressed. This magnetic suppression is reflected in the corresponding magnetic hysteresis loop of the Co/C<sub>60</sub>, where constant loss in saturation magnetization has been observed.

From these examples of magnetic effects, it is clear that hybrid interfaces are very important in tailoring the properties of the hybrid organic systems. Nevertheless, much of the phenomena occurring at these hybrid interfaces are poorly understood. Indeed, detailed comprehensive studies of organic/inorganic interfaces are further required to understand the mechanism of charge transfer and transmission of spin-polarized currents at the hybrid interface.

Among all these interface-assisted magnetic effects, one of the most surprising effect observed in hybrid organic systems is the so-called molecular exchange bias. This effect will be discussed in the coming section.

### 3.3 Exchange bias in organic hybrid systems

When exchange coupling interactions between neighboring spins occur at the interface of a ferromagnetic layer with an anti-ferromagnetic film it can lead to exchange bias (EB) effects. Exchange bias plays an important role in spintronics since it allows pinning the magnetization direction of one of the FM layers involved in devices. Exchange bias has been thoroughly studied between inorganic anti-ferromagnets and metallic FM layers but only recently and rather surprisingly, similar exchange bias effect has been reported between metallic FM and organic molecular layers. In this case, EB is considered to be a “spinterface” magnetic effect and could play big role in the next generation of environment-friendly electronic devices. To this end, the following section starts with the phenomenological picture of exchange bias effect and then concentrates on the molecular exchange bias effect i.e. exchange bias in organic hybrid systems.

#### 3.3.1 Phenomenology of exchange bias

Exchange bias was first discovered in core-shell fine particles of cobalt and cobalt oxide [57]. Since then, exchange bias was observed in many different systems and is being used to build functional elements like pinning heterostructures which are embedded in devices such as storage media and magnetic random-access memory (MRAM) [58,59,60].

To explain the onset of exchange bias one have to consider the two characteristic temperatures of the FM and AFM. The FM material's characteristic temperature is known as the Curie temperature  $T_c$  and for temperatures below  $T_c$ , the FM layer is magnetically ordered. Likewise, the AFM material's

characteristic temperature is called the Néel temperature  $T_N$  and for temperatures below  $T_N$ , the AFM layer is anti-ferromagnetically ordered. Taken individually, the two kinds of ferromagnetic materials have completely different magnetization curves. When a static magnetic field is applied to the FM material the spins align along the direction of the applied magnetic field and when the magnetic field is cycled the FM magnetization presents a hysteresis loop typical for FM materials. In the case of the AFM, below  $T_N$  the magnetization of the AFM can hardly become aligned with respect to the magnetic field because in this case the magnetic field has to overcome the antiferromagnetic exchange interaction that is very large.

In order to observe exchange bias effect a field cooling (FC) procedure has to be applied on the FM/AFM system. Field cooling (FC) procedure can be described as follows: From a temperature  $T$  satisfying  $T_N < T < T_C$  i.e. in state 0 of figure 8, an external magnetic field is applied to the system to saturate the FM layer. Then, the system is cooled down through and below  $T_N$  while maintaining the magnetic field. After field cooling (FC), the system is schematically described by the state 1 in figure 8 and the AFM will be magnetically ordered. In this state, the interfacial magnetic moments of the AFM layer will point either parallel or anti-parallel with respect to the spins of the FM layer. The alignment of the spins at the AFM and FM interface depends on the exchange coupling interactions of the interfacial spins. Ideally, the neighboring spins in the AFM layer follow the interfacial spin pattern so that the resulting net bulk magnetization of the AFM is zero.

When the applied magnetic field is cycled from positive to negative fields, the FM spins will start to reverse but the AFM spins remain intact because of their large anisotropy. Due to the exchange interaction between the FM and AFM interfacial spins, the FM spins experience additional torque from AFM spins contributing to maintain them in the direction of the original FC field direction (as seen in state 2 of figure 8). Eventually, when the negative applied field ( $H_{c1}$ ) is large enough compared to the exchange interaction, the magnetic moments of the FM will reverse while the spin configuration of the AFM layer stays unchanged. This is represented in state 3 of figure 8, where the FM spins have opposite direction to that of the FM spins in state 1.

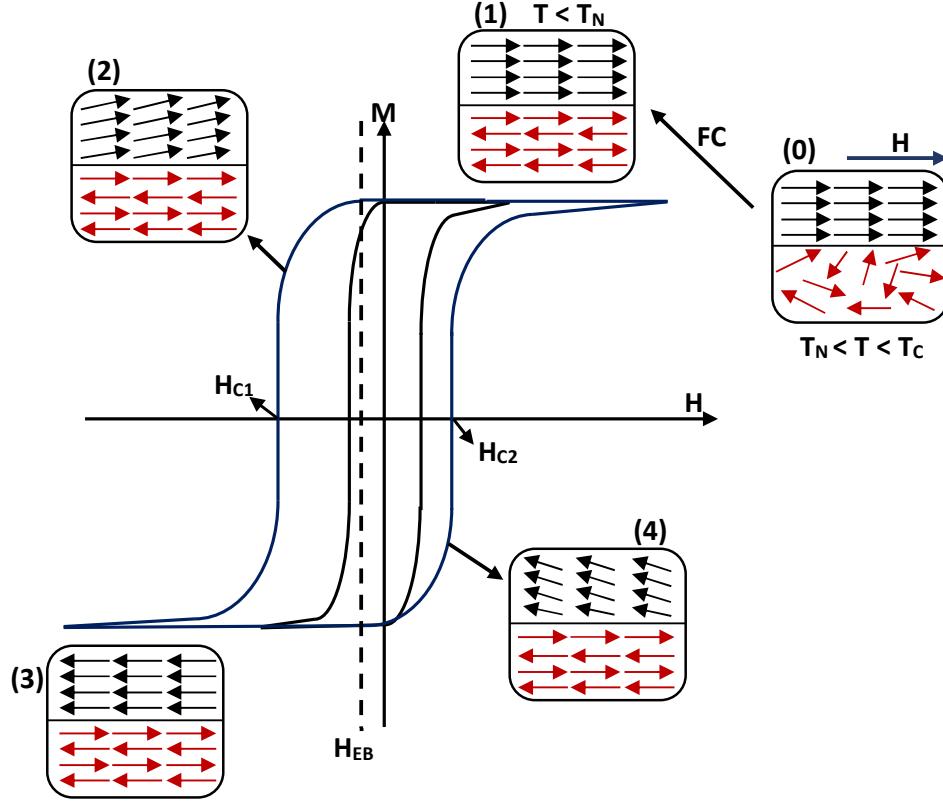


**Figure 8:** Schematic illustration of shifted hysteresis in an exchange bias system. Black scheme indicates the hysteresis loop of the FM showing symmetrical magnetization loop. Blue scheme is the hysteresis loop for the exchange biased FM/AFM system when FC. States 0, 1, 2, 3 and 4 corresponds to the spin configurations of the FM and AFM at different stages.  $H_{C1}$  and  $H_{C2}$  are the coercivities while  $H_{EB}$  represents the exchange bias field.

When increasing again the field to positive values, the second reversal ( $H_{C2}$ ) will occur for a smaller positive field since the spin interactions now favor the initial spin-configuration of the system as in state 1. The shift of the magnetization curve resulting from this process corresponds to the exchange bias field ( $H_{EB}$ ). Exchange bias field ( $H_{EB}$ ) and the coercivity ( $H_c$ ) are calculated from the coercive fields  $H_{C1}$  and  $H_{C2}$  of the hysteresis loop as:

$$H_{EB} = \frac{H_{C2} + H_{C1}}{2} \quad (4)$$

$$H_c = \frac{H_{C2} - H_{C1}}{2} \quad (5)$$

In exchange biased systems the temperature where exchange bias sets in, is generally lower than the  $T_N$  of the AFM layer. This temperature is called the blocking temperature  $T_B$ . Moreover, it should be taken into consideration that the schematics of figure 8 represent a case of perfect interface. This ideal case is

rare to be found in real systems, and many factors affect and modify the structure and morphology of the AFM/FM interface hence affect the exchange bias phenomenon.

#### 3.3.2 Molecular exchange bias

One of the most surprising and debatable “breakthroughs” achieved because of an interface-assisted magnetism in hybrid organic/inorganic systems is the molecular exchange bias. In this effect the molecular spin is used to pin the spins of the FM atoms within the metallic electrode of the device.

The molecular exchange bias has been observed in different organic/inorganic systems. In 2015, and for the first time in a letter to nature materials [61], M. Gruber et. al. showed how a paramagnetic manganese phthalocyanine (MnPc) molecular film can induce exchange bias to the adjacent cobalt FM metallic electrode. The effect is attributed to the strong hybridization between the MnPc molecules and the cobalt which creates robust magnetism at the hybrid organic/inorganic interface that stabilizes an anti-ferromagnetic ordering inside the molecules. Furthermore, it has been shown that this induced magnetism is effective up to 3 molecular layers after which the molecules retain their paramagnetic gas phase properties.

Moreover, taking advantage of this induced AFM ordering it has been shown that the Co/MnPc hybrid system exerts a molecular exchange bias field on the ferromagnetic layer. The exchange bias field has a magnitude of 60 milli tesla at 14K. The exchange bias field is observed up to a blocking temperature  $T_B = 100K$ . After observing exchange bias in Co/MnPc hybrid bi-layer, the work on molecular exchange has been expanded to different metal phthalocyanine molecules (MPc, M=Co, Zn, and Fe). These molecules too showed the onset of molecular exchange bias when deposited on cobalt film [62] with blocking temperatures  $T_B \approx 100K$ . The magnitude of exchange bias field was the highest for the Co/MnPc system and it decreased to lower magnitudes in Co/CoPc, Co/FePc and Co/ZnPc systems. However, in Co/ZnPc the origin of the unidirectional anisotropy is unlikely to be explained by the exchange interaction between FM cobalt film and the organic molecular layer since ZnPc molecules are diamagnetic.

In addition to MPc molecules, different family of organic molecules such as the paramagnetic metal octa-ethyl porphyrin (MOEP; M = Zn, Cu, Ni and Co) molecules have been used to study the molecular exchange bias [63,64]. Similar to MPc molecules, the MOEP molecules are planar. When the MOEP molecules are deposited on cobalt, iron, nickel, and permalloy ferromagnetic substrates the magnetization cycles of the different hybrid systems showed shift along the field axis hence, the presence of molecular exchange bias. However, the observed magnitudes of the exchange bias field on nickel and permalloy are around 1.5 milli tesla. Such small fields might be questionable to be considered as exchange bias fields.

---

### 3.4 Partial summary

As illustrated in this chapter, the organic/metallic interface is a rich platform that holds several interesting magnetic effects. These effects can modify the magnetic properties of the metal, of the organic molecules hence of the hybrid system. In the molecular side, these modifications are recognized as induced magnetic moments at different atomic entities of the molecule and as enhanced magnetic ordering due to the magnetic exchange interactions between the molecular spin and the spin of metallic surface atoms. In the inorganic side, the magnetic modifications occur because of strong local hybridizations between the molecular orbitals and *d*-orbitals of the metal and because of the change in the electronic density of states of the metal near Fermi level. At last, controlling the degree of these hybridization and manipulating intentionally the spin-dependent effects occurring at the organic/inorganic interface could be the key factor in achieving multi-functional organic/molecular spintronic devices. That is the role of the science of “spinterface” [34].

---

## Chapter 4: Porphyrins and porphyrin-based metal complexes

Among the organic molecules that can be thermally evaporated, porphyrin and phthalocyanine compounds stand out from other  $\pi$ -conjugated molecules because of their remarkable stability at elevated temperatures. They are one of the most interesting molecular classes to be investigated and often grabbed the attention of wide range of scientists. Porphyrins and phthalocyanines attracted especially the physics community because of their tremendous versatility and their accompanied metal complexes. Indeed, metal atoms can be inserted in these molecules and depending on the nature of the metal center enormous variations of electronic and magnetic functionalities can be obtained. This chapter particularly focuses on metal tetra-phenyl porphyrin (MTPP) molecules, their on-surface properties, and their functionalities as they have been used extensively in this thesis work.

### 4.1 Porphyrin

Porphyrins are important biological molecules with a broad range of natural activities. Hemes, the oxygen-binding groups in red blood cells that are responsible for oxygen transport, are Fe(II) porphyrin complexes [65], whereas chlorophylls, the biochemical responsible for photosynthesis [66], have a Mg(II) porphyrin as their active site. These biomolecules have also paved their path in various technological applications such as thin film organic light-emitting diodes (OLED) [67,68,69,70] and nanodevices [71,72,73]. The parent structure of all porphyrins is porphin ( $H_2P$ ) (figure 9a) that has a chemical formula of  $C_{20}H_{14}N_4$ . A porphin consists of four pyrrole moieties bridged via methine ( $=CH-$ ) groups at their alpha positions [74] and two pyrrolic hydrogen atoms ( $-NH-$ ) which can undergo tautomerization based on proton transfer [75,76]. The porphin core is a planar,  $\pi$ -conjugated system, i.e. atoms of the macrocycle are connected through  $p$ -orbitals, with 18 delocalized electrons, which satisfies the  $4n + 2$  Hückel rule for aromatic systems. The symmetry group of porphin is  $D_{2h}$  due to the two delocalized hydrogen atoms on diagonally opposite pyrrolic nitrogen atoms. Moreover, the porphin molecule crystallizes with a monoclinic crystal structure.

One of the most studied porphyrin ligands is the tetra-phenyl porphyrin (TPP) in which phenyl rings are added at the 4 meso positions of the porphin core (figure 9b). This compound is also called the free base tetra-phenyl porphyrin ( $H_2TPP$ ). The free base TPP molecule has a square planar  $D_{4h}$  symmetry and crystallizes with a triclinic crystal structure. In the equilibrium crystal structure of the free base TPP, the phenyl rings are not co-planar with the macrocycle. This non co-planarity results from the intramolecular sterical repulsive forces between the ortho-positioned hydrogen atoms of the phenyl rings and the adjacent hydrogen atoms of the porphin core [77]. However, these phenyl rings can exhibit



rotational motion that may lead to a transient co-planar orientation of the rings and the porphyrin macrocycle. In this case, the  $\pi$ -conjugation reaches its maximum [78].

Because of their large  $\pi$ -conjugated system, porphyrins have an intense absorption band, called the Soret band in the visible range, in the 400-450 nm region ( $\pi$ - $\pi^*$  transition) and several less intense bands, called Q bands in the 500-700 nm region. This characteristic makes porphyrins and porphyrin-based compounds good candidates for dye sensitized solar cells (DSSC) [79,80,81] and organic solar cells (OSC) [81,82].

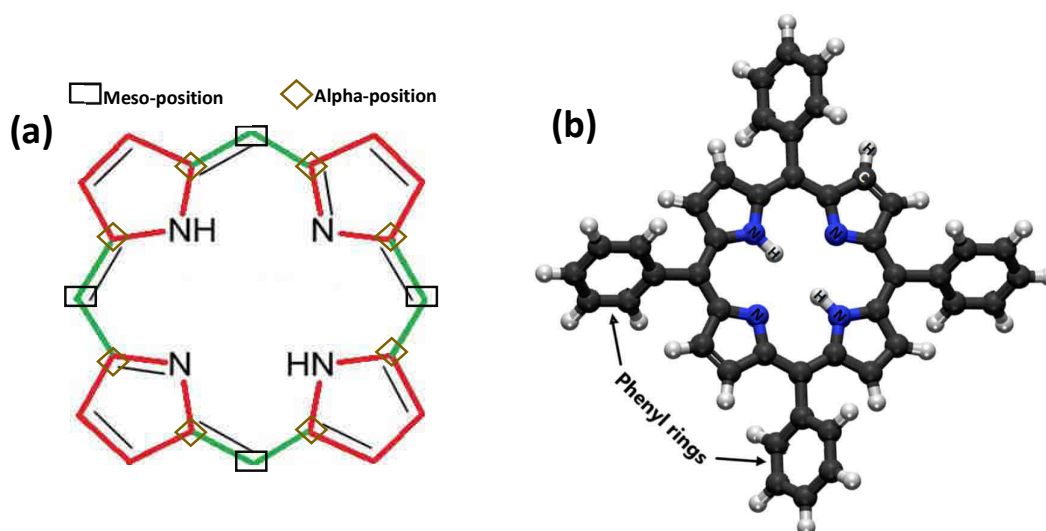


**Figure 9:** Chemical structure of (a) porphyrin with indicated meso and alpha positions (b) free base tetra-phenyl porphyrin (H<sub>2</sub>TTP) blue balls: nitrogen atoms, light grey balls: hydrogen atoms, dark grey balls: carbon atoms. The phenyl rings show a rotational angle with respect the porphyrin macrocycle. The chemical diagrams are generated from Cambridge Structural Database.

## 4.2 Metal complexes of tetra phenyl porphyrin

The size of the porphyrin macrocycle is large enough to host a large variety of metal ions; thus metal complexes of tetra-phenyl porphyrin (MTPP) can be synthesized for almost all elements of the periodic table. Because of the dibasic nature of porphyrins, the central ion in the complex is found to be in its +2-oxidation state, unless further axial ligands are added to the metal site of the macrocycle. The metalation of a TPP can be achieved in two different ways. First, in solutions as an ion exchange [83], where the protons are replaced by a metal ion. The second method occurs on metallic surfaces, followed by a redox reaction, which results in oxidation of the metal atom to its cation +2 state and further

reduction of the protons to two hydrogen atoms [84]. In addition, similar to a free base TPP molecule ( $H_2TPP$ ), MTPP molecules are also non-planar compounds. Their four phenyl rings are not co-planar with the porphyrin macrocycle i.e. the phenyl rings show a rotational angle with respect to the porphyrin macrocycle.

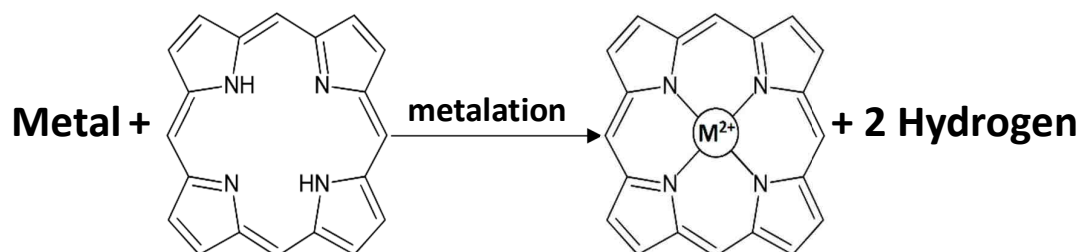


**Figure 10:** Metalation of simple free base porphyrin. If in solvent, then the two hydrogens will be ionic, if on surfaces then they will form  $H_2$ .

The first row 3d transition metals (e.g. Zn, Co, Ni, Fe etc.) have ionic radii that are smaller than 80-85 picometers. Therefore, inserting these transition metals into the porphyrin will result in metalloporphyrin molecules where the metal center will be located within the plane of the porphyrin macrocycle (figure 10). The fact that there will be no distortion in the macrocycle upon adding these 3d transition metals is important since the planar character of the macrocycle will make the metal center to be accessible from both side of the molecular plane. Even though the porphyrin macrocycle will be planar nevertheless the phenyl rings of the MTPP molecule will still have the rotational angle with respect to the macrocycle.

On surfaces, the planar character of the macrocycle is expected to result in strong interactions with the substrate, thus modifying the electronic and magnetic properties of the metal ion and opening wide areas for further investigations. MTPP molecules exhibit important electronic and magnetic properties, which are highly dependent on the nature of the metal incorporated within the porphyrin macrocycle and on inter-molecular interactions.

The intrinsic magnetic properties of MTPP molecules are determined by the spin state of the 3d transition metal ion within the porphyrin macrocycle. The overlap between the metallic orbitals and the molecular orbitals of the porphyrin ligand leads to redistribution of the spins in the energy levels. The redistribution also plays a role in defining the final magnetic state of the MTPP molecules.

When a transition metal is placed inside the TPP molecule, the degeneracy of the 3d transition metal orbitals is lifted which results in the splitting of the metal orbitals (figure 11). The splitting occurs

because the degenerate  $3d$  bands of the free transition metal atom are subjected to a strong ligand field in the TPP molecule. Depending on the symmetry of the surrounding molecule, in this case  $D_{4h}$  symmetry, the  $3d$  metallic orbital can be transformed to irreducible molecular orbitals, and can be written as  $b_{1g}(d_{x^2-y^2})$ ,  $a_{1g}(d_{z^2})$ ,  $e_g(d_{xz}$  and  $d_{yz})$  and  $b_{2g}(d_{xy})$ . In the isolated TPP molecule, the  $D_{4h}$  symmetry transforms the degenerate  $3d$  orbitals of the metal into three singlet states  $a_{1g}$ ,  $b_{1g}$  and  $b_{2g}$ , and one doublet state  $e_g$ . The energetic order of the orbitals depends on the strength and the type of the distortion and on the hybridization effects of the metal  $3d$  orbitals with the ligand orbitals.

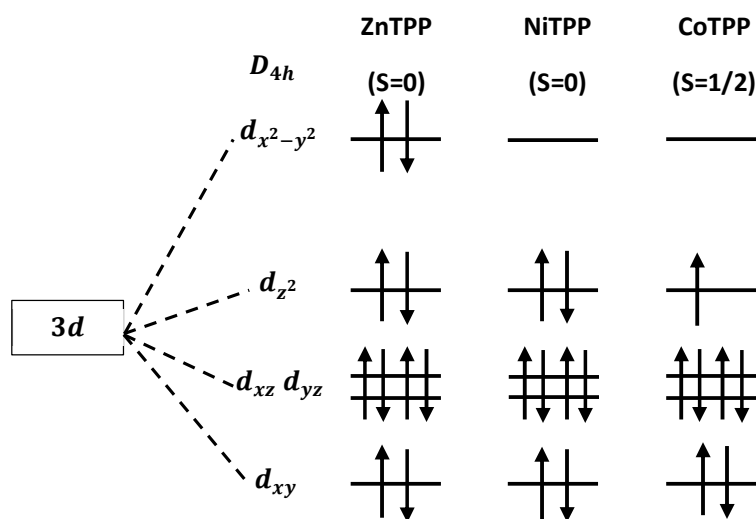


**Figure 11:** Sketch of the energy splitting of the different  $3d$  levels embedded in  $D_{4h}$  square planar crystal field and the electron filling scheme for Zn(II)TPP, Ni(II)TPP and Co(II)TPP. “S” represents the total spin due to the unpaired electrons. Black arrows represent spin-up and spin-down configurations.

Figure 11 represents the electron filling scheme of the MTPP molecules that has been used in this thesis work. It is the metal that provides electrons to fill up the molecular orbitals. For example, Zn(II)TPP is a diamagnetic molecule. This can be explained as follows. A zinc metal atom has an electronic configuration that is written as  $[Ar] 3d^{10}4s^2$ . When Zn is inserted in the TPP molecule, it will lose two electrons hence Zn will become an ion with +2 oxidation state. Now, the electron configuration of the Zn ion will be written as  $[Ar] 3d^{10}$ . The Zn ion is in a closed shell configuration with no unpaired electrons in the  $3d$  orbital thus, no net spin. This is represented in figure 11, where Zn(II)TPP has its  $3d$  metallic orbitals completely full resulting in a diamagnetic molecule with  $S = 0$ .

On the other hand, a Ni ion is magnetic and the distribution of the spins in its atomic orbitals  $[Ar] 3d^8$ , leaves two unpaired electrons, resulting in a net spin of  $S = 1$ . Yet, this is not the case when Ni is included in the TPP molecule. Ni(II)TPP, in its ground state has no net spin and is diamagnetic. This is because the  $b_{1g}(d_{x^2-y^2})$  orbital falls in the energy range of the porphyrin molecular orbitals which are high enough in energy to be occupied by an electron provided by the Ni ion. This configuration is represented in figure 11 where the Ni ion in the molecule has a closed shell configuration with no net spin.

In contrast to Zn(II)TPP and Ni(II)TPP molecules, Co(II)TPP has one unpaired electron ( $S = 1/2$ ) and is paramagnetic with effective magnetic moment of  $1.92 \mu_B$ . Nevertheless, the correct recognition of these molecular orbitals experimentally is quite difficult and indeed much of the assignment of the electronic orbitals is achieved theoretically. Further detailed explanation of the electronic structure of different metal-tetra phenyl porphyrin (MTPP) molecules can be found elsewhere [85].

As observed, the central ion of the molecule plays a significant role in defining the magnetic properties of the free MTPP molecule. However, the magnetic and electronic properties of MTPP molecules could be modified because of the interactions that the molecule undergoes with the surface substrate. Such modifications are illustrated in the next section.

### 4.3 MTPP molecules on metallic surfaces

When MTPP molecules are in contact with metallic surfaces, they experience modifications in their electronic structure, magnetic, and structural properties. Like any other organic molecule, the degree of these modifications strongly depends on the type of interactions between the MTPP molecules and the metallic surface.

For example, when Co(II)TPP is adsorbed on Cu (111) the molecules undergo saddle-shape deformation with one pair of opposite pyrrole rings tilting upwards while the other pair bending downwards [86]. On the other hand, when Co(II)TPP molecules are adsorbed on Ag (111) a new valence state is observed at 0.6 eV below the fermi level [87]. In addition, when Co(II)TPP molecules are adsorbed on the same kind of Ag (111) surface the oxidation state of the Co ion in the Co(II)TPP molecule is reduced [88]. These modifications appear because of the transfer of electron from the substrate to the cobalt ion due to the strong interaction of Co  $3d_{z^2}$  orbital with the metallic surfaces.

Contrary to CoTPP molecules, Ni(II)TPP has much weaker coupling with metallic substrates because of its fully occupied  $3d$  orbitals [89]. The nickel ion shows no surface-induced energy level reduction when Ni(II)TPP is adsorbed on Au (111) surface [90]. Even on strongly reactive metallic surfaces like Ag (111), Ni(II)TPP has very weak coupling interactions with the metallic atoms, as shown via scanning tunneling spectroscopy (STS) measurements [91].

Moreover, when Zn(II)TPP molecules are adsorbed on Ag (111) metallic surfaces the molecule shows inert character for Zn(II) ion and no indication of covalent bonds with the metallic substrate. The Zn(II) ion does not contribute to any of the electronic interactions between the Zn(II)TPP and the substrate [88]. In addition, when Zn(II)TPP molecules are adsorbed on Ag (110) it is observed that the molecules lie flat on the metallic surface. Both the macrocycle and the phenyl rings show planar character on the surface [92]. This on-surface geometry of the phenyl rings is opposite to that of the Zn(II)TPP in gas phase since the phenyl rings of the Zn(II)TPP in gas phase are almost orthogonal to the macrocycle plane. One explanation for this could be that the orbitals of the phenyl rings strongly overlap with the atomic orbitals of the Ag surface i.e. there exists significant charge transfer between the orbitals of the metal surface atoms and the  $\pi$ -orbitals of the phenyl rings.

Indeed, there is extensive research work ongoing towards studying organic layers on top of metallic surfaces. These studies are done especially by near field techniques. Such techniques become more difficult to implement when the molecular thickness exceeds the few mono layers and when a counter electrode is deposited on top of the molecular layer.

### 4.4 TPP/MTPP molecules in hybrid nanostructures

As discussed in the above section, MTPP molecules experience modifications in their electronic and magnetic properties when adsorbed on metallic surfaces. In addition to these modifications, there has been few reports on magnetoresistance (MR) effects in porphyrin-based organic devices. For example, in the work of Xu et al. [93], -15% of MR has been observed in organic based spintronic device where the organic spacer layer is tetra-phenyl porphyrin (TPP) and has a thickness in the order of 15-20 nm. The observed negative MR means that the resistance of the device decreases when the magnetization of the two electrodes is switched from parallel to anti-parallel states. Moreover, the fit of the I-V curve using the Simmons model [94] shows barrier height of 0.72 eV and a barrier width of the order of 2nm.

The observed tunneling magnetoresistance in this organic tunnel junction device is controversial since the determined effective barrier thickness by the Simmons model is an order of magnitude thinner than the actual deposited TPP thickness; 15-20 nm. This suggest that the TPP organic layer is not uniform and has discontinuous morphology. From this point, one can conclude that the fabrication of organic based spintronic devices is problematic. This is because it is difficult to control the homogeneity of the organic films when deposited on metallic surfaces. More importantly, the system becomes even more complex when a counter electrode is being deposited on top of the organic layer. These uncertainties raise doubts on the potentiality of using TPP molecules and organic molecules in general, in spintronic devices.

More recently, there has been reports on asymmetrical magneto-transport characteristics in planar metal octa-ethyl porphyrin/cobalt hybrid systems [63,64].

### 4.5 Partial summary

Porphyrin compounds embody an interesting family of molecules with remarkable chemical and physical properties. Their incredible thermal and chemical stability makes them the perfect candidate to be included in physical vapor deposition techniques. In this context, porphyrin molecules and their metal complexes are considered to be interesting functional materials to implement different electronic functions in nano-hybrid devices. Even though organic based spintronic devices are not likely to be implemented in significant electronic applications in near future, extensive efforts are being put in this direction to explore new functionalities and to further understand the fundamental properties of these molecules when adsorbed on inorganic surfaces and when included in devices.

### 4.6 Conclusion

Spintronics is a multidisciplinary research field that relies on the effective manipulation of the spin degree of freedom in solid-state systems. Spintronics took its first steps with the discovery of GMR effect in ferromagnetic/non-magnetic metallic multilayers. Metallic spintronics had its own challenges and in order to improve its performances alternates to metallic materials were investigated. Therefore semiconductor materials had been integrated into the spintronic devices. These materials have several advantages that can be stated as: Semiconductor materials can be doped with different dopants to tailor their properties; semiconductor materials show longer spin lifetimes compared to metallic layers. Nonetheless, semiconductor spintronics showed major drawbacks mainly the conductivity mismatch.

Figures of merit in spintronics are spin diffusion length and spin lifetime. Organic molecules are compounds that show much longer relaxation time than metallic systems, due to their light-weight character. Consequently, research activities towards organic spintronics started and many of the effects in organic based spintronic devices mimicked the conventional inorganic spintronics. Soon after, the concept of “spinterface” science shed light on the importance of the hybrid interfaces and their comprehension in pursuit of understanding the physical properties of organic hybrid nanostructures and for creating better functional organic spintronic devices. However, organic spintronics is a complicated research field and most of the effects are poorly understood still.

Indeed, massive research activities were oriented towards hybrid interface-related mechanisms that included structural, chemical, and magnetic studies. Because of their versatility and high thermal and chemical stability, porphyrin molecules and their metal compounds are extensively used in this kind of research work. Moreover, the possibility of MTPP molecules to be further functionalized by additional ligands motivated the researchers as these newly synthesized molecules could combine different properties in a single organic compound. Consequently, they tend to be a good candidate for on-surface fundamental investigations and for multifunctional organic spintronic devices.



# **Part II**

## **Experimental Methods**





---

## Chapter 5: Experimental setups, growth, and characterization techniques

The work of this thesis is divided into two parts. The first part investigates the molecular exchange bias in hybrid bilayers composed of metal tetra-phenyl porphyrin (MTPP) and cobalt phthalocyanine (CoPc) molecules in proximity to Co film. The second part concentrates on studying the morphology and structural properties of the hybrid interfaces when ZnTPP molecules are in contact with FM metallic electrodes. Here after, this chapter describes the UHV preparation techniques and explains how they are used to build the hybrid organic heterostructures. In addition, this part explains the different characterization techniques that have been used to analyze the physical properties of the hybrid systems.

### 5.1 Ultra-high vacuum deposition systems

For this work, two of the IPCMS's UHV systems have been used. First one is the MBE chamber that is a stand-alone UHV system while the second one is the so-called "Hybrid" system that consists of a cluster of UHV chambers. The coming sections will describe these two UHV systems.

#### 5.1.1 Molecular beam epitaxy (MBE) chamber

Molecular beam epitaxy (MBE) is a physical vapor deposition (PVD) technique that uses UHV environment alongside slow deposition rates to grow epitaxial layers of thin films. A typical MBE growth chamber, as the MBE of DMONS-IPCMS, consists of Knudsen effusion cells and electron-beam guns for material evaporation, and reflection high-energy electron diffraction (RHEED) setup for structural surface analyses. Generally, Knudsen effusion cells and electron-beam guns are placed at the bottom of the UHV chamber and aligned towards the sample holder where the substrate is located. On the other hand, RHEED is located at the level of the sample holder and allows the in-situ characterization of the crystallinity and morphology of the surface of the grown layers.

Electron-beam deposition is a physical vapor (PVD) deposition technique in which a target is bombarded with a high energy electron beam ejected from an electron gun. The main component of an electron-beam deposition technique is the electron beam source i.e. the electron gun. The electron gun uses tungsten (W) or tantalum (Ta) materials as the filament. A power supply is connected to the gun and a high current passes through the filament thus heating the filament to high temperatures. As a result, stream of electrons is emitted from the filament surface. The generated electron beam is then accelerated to high kinetic energy, focused, and directed towards the target. Once the electron beam hits the surface of the target, the high kinetic energy of the electrons is converted to thermal energy that heats up the target and consequently, melts and evaporates the target. With adequate UHV conditions, the evaporated target atoms will then migrate and coat the surface of the substrate forming the required

metallic films. Generally, the substrate is continuously rotated at a low rotation speed for more uniform material growth. Moreover, the target material is held in a water-cooled crucible to keep the material outer surface in solid form. In this way, the target will less likely react with the crucible than in the molten form and will stay pure.

### 5.1.2 The “Hybrid” system

The “Hybrid” of DMONS-IPCMS is a multi-chamber, thin-film deposition UHV system composed of a load lock and different deposition chambers namely thermal evaporation chamber, organic molecular beam epitaxy (OMBE) chamber and sputtering chamber. All the chambers are inter-connected with an UHV robot arm chamber that ensures the transfer of the samples between the chambers of the “Hybrid”, without breaking the UHV environment. The “Hybrid” system has been used extensively for the growth of the hybrid organic heterostructures. A brief description of each chamber is given. First, all the chambers are equipped with primary and turbo-molecular pumps. The primary pumps are common rotary pumps that provide medium vacuum environment ( $10^{-3}$  mbar) to the chamber which is also necessary for the operation of the turbo-molecular pumps. Once the  $10^{-3}$  mbar limit is reached, the turbo-molecular pumps are activated to further pump the chamber, to create and maintain the required UHV conditions. In addition to these pumping systems, the thermal evaporation chamber is equipped with ionic pump and titanium sublimation apparatus that further enhance the UHV conditions of the evaporation chamber. Moreover, each deposition chamber is equipped with a baking system. It is important to have a baking system since after the UHV chambers are vented to atmosphere (e.g. for maintenance, changing targets, etc.), moisture and other gaseous impurities will find their way into the chambers thus contaminate them. Therefore, the UHV chamber’s interior surfaces must be heated to elevated temperatures i.e. around 150-200°C, for a time period sufficient enough to desorb the moisture and other contaminants. This procedure allows to attain better base pressure after the chambers are exposed to air. Generally, the base pressure of the evaporation chamber is  $3 \times 10^{-10}$  mbar, the OMBE chamber has a base pressure of  $1 \times 10^{-9}$  mbar, the base pressure of the sputtering chamber is  $6 \times 10^{-9}$  mbar and the robot chamber has a base pressure of  $2 \times 10^{-9}$  mbar.

The evaporation chamber, as shown by its name is equipped with thermal evaporation deposition technique. Thermal evaporation is a physical vapor deposition (PVD) technique where solid source materials are placed inside tantalum or ceramic crucibles of a high temperature effusion cell. These source materials are heated up beyond their sublimation temperature. The heating process is done slowly by gradually increasing the voltage/current of the electrical power supply that is connected to the effusion cell. Consequently, the electric current through the conductive wires around the crucible will heat up the conductive wires hence heat up the crucible. As in MBE, due to UHV environment of the chamber the sublimed or evaporated atoms will have enough energy to travel and reach the substrate. Consequently, the evaporated atoms coat the substrate surface and form the desired layer. Note, the

evaporation chamber is further equipped with quartz microbalance monitor and temperature regulator. The latter allows to control, regulate, and read the temperature of the effusion cells while the former allows to read the time and units of the deposited material i.e. the deposition rate.

Next in turn comes the organic molecular beam epitaxy (OMBE) chamber. OMBE is a different thermal evaporation chamber dedicated solely to deposit organic molecules. The OMBE chamber consists of four different Knudsen cells which can hold four different molecules. The Knudsen cells of the OMBE is of hot-lip type effusion cell (figure 1). The hot-lip effusion cell is particularly important for the deposition of organic molecules, since a hot-lip source maintains uniform temperature distribution over the entire length of the crucible. This feature will prevent condensation of the organic molecules on the lip of the crucible while the molecules are being evaporated.

In OMBE, the molecular deposition is done via thermal evaporation technique which has the same principles as the evaporation technique explained above. When the temperature of the cell exceeds the molecule's sublimation temperature but is still below decomposition temperature, the molecules start to sublime. The sublimed molecules will migrate through the UHV environment inside the chamber and coat the substrate surface thus forming the molecular layer. In OMBE, during deposition the substrate sample is rotated at a low rotation speed to obtain more uniform molecular layer.

An important step required for the OMBE chamber is the outgassing of the newly introduced molecules prior to their deposition. The outgassing procedure is done slowly and gradually till the temperature reaches the sublimation point, while maintaining the chamber's UHV condition. During the process, longer hours of outgassing is concentrated around 100°C of cell temperature at which moisture and water molecules evaporate. With this process, the molecules will be free of contaminants and ready to be sublimated. Finally, the OMBE is supplied with quartz monitor and temperature regulators to monitor the deposition rate and cell temperature, respectively.

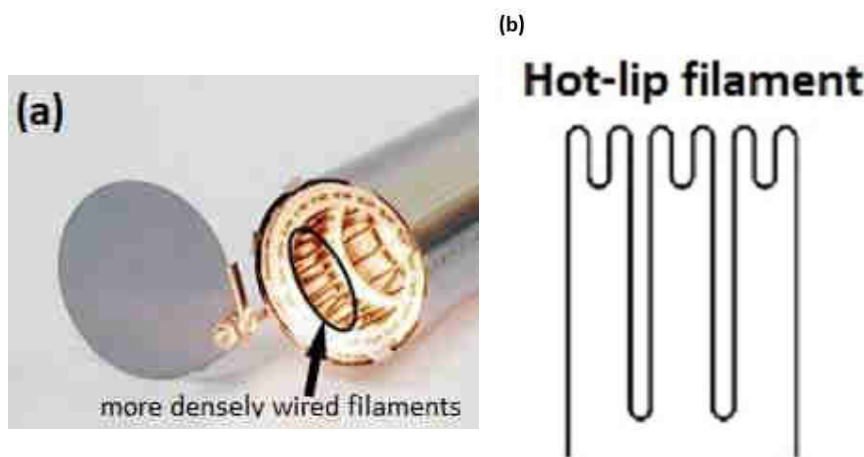


**Figure 1:** (a) view onto the hot lip filaments of the effusion cell. The filaments are more densely wired near the crucible leap (b) a schematic of a hot-lip filament showing the high density of wired filaments at the top compared to the lower regions. The higher density filament winding at the tip of the effusion cell will compensate the large amount of heat loss occurring at the front opening of the cell. Consequently, a uniform temperature gradient will be present over the entire crucible length. The figures are partially reproduced from ref. [95].

The third deposition chamber of the “Hybrid” system is the sputtering chamber. In the “Hybrid”, the equipped sputtering technique is magnetron sputtering. In magnetron sputtering, the target holder is a cathode that includes magnets. The idea behind magnetron sputtering is to enhance the ionization of the injected process argon gas, so that the rate of the sputtered material is increased. This is achieved by the presence of magnetic stray fields created by the permanent magnets on which the target is fixed. A brief description on how the ionization is enhanced is explained in the following manner. Rare earth gas typically argon is introduced to the sputtering chamber after which a high voltage is applied to the magnetron. Due to this high voltage, the ionization of argon will occur creating the plasma where ions and electrons are separated. The presence of magnetic field that is oriented parallel to the target surface in a circular form, will trap the electrons above the target surface. These trapped electrons are capable of ionizing additional amount of argon gas thus create the “dark space” generally observed near the target. Once the ionization of the argon gas has started, the positively charged argon ions are accelerated to the negatively charged target, thus giving rise to sputtering of the target material. The sputtered material will thereafter be transported and deposited onto the substrate. In the current sputtering chamber, all the targets are metallic (copper, iron, chromium, and cobalt) therefore direct current (DC) sputtering mode has been used. In DC mode, the deposition rate is controlled by regulating the applied bias voltage to the magnetrons. In addition, the distance between the target and the sample holder is of

the order of 0.25 m. This ensures that the samples are not affected by the plasma. Finally, the sputtering chamber is equipped with quartz microbalance to monitor the flux of the sputtered materials.

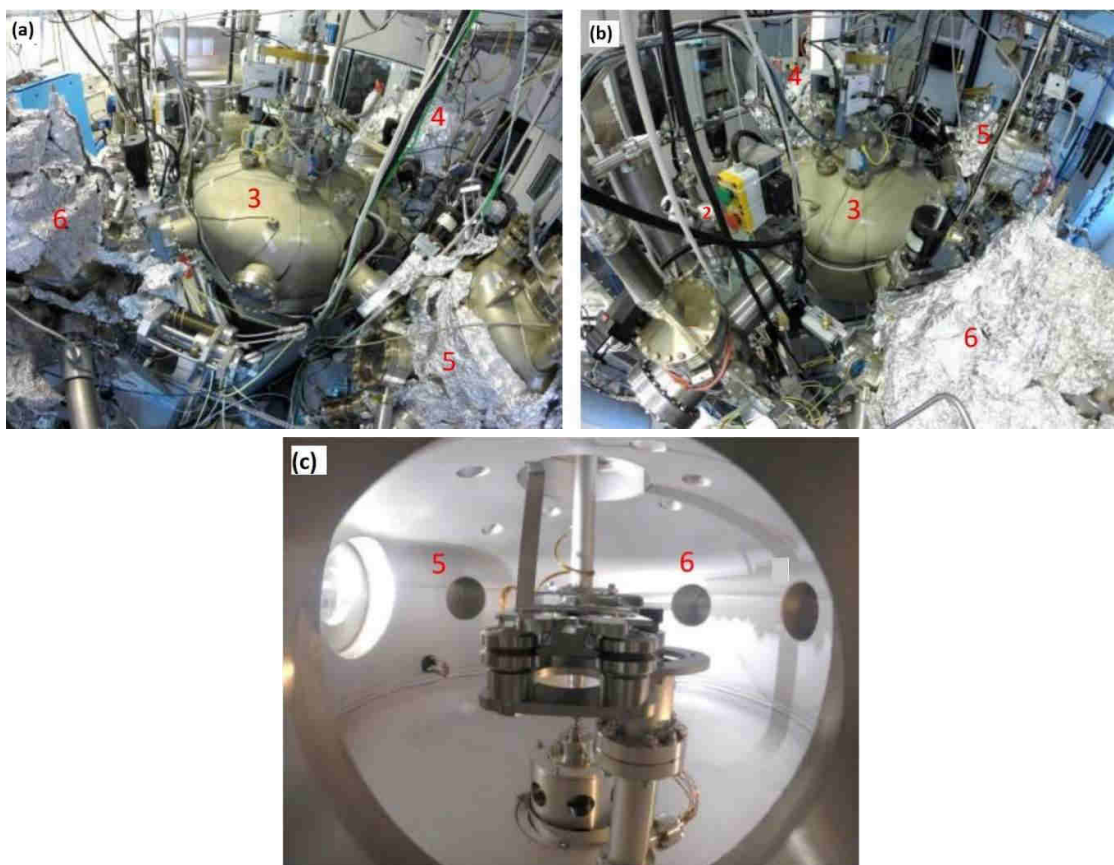


**Figure 2:** (a) and (b) top view picture of the “Hybrid” system. 2- load lock chamber, 3- robot-arm chamber, 4- sputtering chamber, 5- evaporation chamber, 6- OMBE chamber. (c) the interior of the robot-arm chamber with the valve gates of the evaporation (5) and OMBE (6) chambers. The pictures are taken from ref. [96].

## 5.2 Substrate cleaning and sample preparation conditions

In this thesis work, wide variety of organic hybrid heterostructures have been prepared to study their magnetic, structural, chemical, and morphological properties. Thanks to MBE and to the versatility of the “Hybrid” system all the metallic and organic molecular layers were grown under UHV environment. In this work, the metals that have been used are: gold (Au), copper (Cu), iron (Fe), cobalt (Co), and chromium (Cr) whereas the deposited organic molecules are: metal tetra-phenyl porphyrin (MTPP; M= Co, Ni and Zn) and cobalt phthalocyanine (CoPc). A brief overview of their deposition parameters are represented in table 1.

For the deposition of the films, it is essential to note the importance of the chamber base pressure. Generally, at atmospheric pressure the time required for a contamination adsorbate layer to be formed is of the order of nanoseconds (following the relation  $t \approx \frac{1}{P} \times 10^{-6}$ ). Therefore, at  $10^{-10}$  mbar a monolayer of contamination will be formed on the substrate in approximately 2-3 hours which is much slower compared to the deposition time of the films (few minutes). This feature leads to the preparation of pure films with no impurities.

Material	Deposition technique	Base pressure (mbar)	Deposition rate
Co	Thermal evaporation	$3 \times 10^{-10}$	0.16 Å/s
Au	Thermal evaporation	$3 \times 10^{-10}$	0.07 Å/s
	Electron beam	$1 \times 10^{-9}$	1.2 Å/s
Cu	Magnetron sputtering	$2.5 \times 10^{-8}$	0.6 Å/s
Fe	Magnetron sputtering	$2.5 \times 10^{-8}$	0.25 Å/s
Cr	Magnetron sputtering	$2.5 \times 10^{-8}$	0.5 Å/s
MTPP	Thermal evaporation	$1 \times 10^{-9}$	0.055 ML/sec
CoPc	Thermal evaporation	$1 \times 10^{-9}$	0.0025 ML/sec

**Table 1 :** Deposition techniques and the different deposition parameters for the different materials used in preparing the hybrid heterostructures.

The organic molecules are deposited at room temperature. To check if the deposited molecules are not damaged by the process, the molecular films have been measured by UV-Visible optical spectroscopy. Figures 3a and 3b show that the spectra are constituted by B-bands and Q-bands expected for the MTPP and CoPc films.

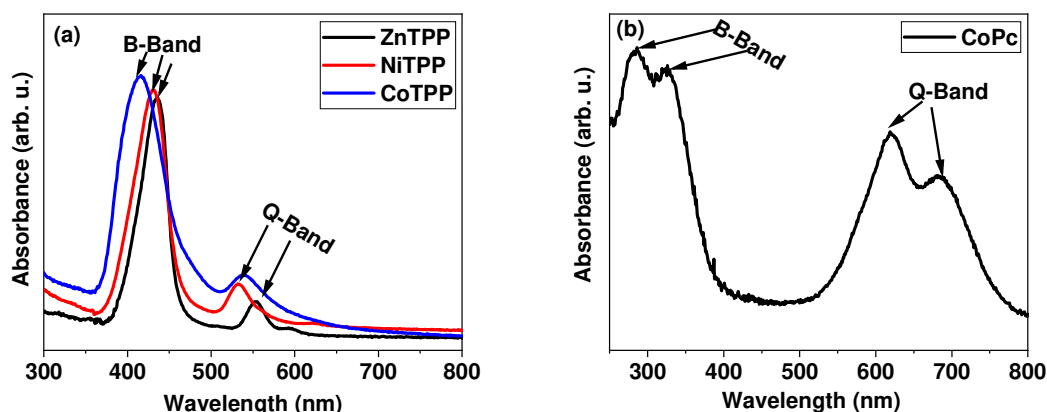


**Figure 3:** UV-Visible spectrum of (a) Zn(II)TPP, Ni(II)TPP and Co(II)TPP molecular films (b) CoPc molecular film. All molecular films are 10nm and are deposited on quartz glass substrate.

It must be noted that Fe has been often used as the second FM electrode of the hybrid heterostructures and is therefore deposited on top of the organic layers. Since sputtering might be more harmful to the organic layers than thermal evaporation, the deposition rate of the sputtered Fe atoms has been chosen to be in the lower limit rate for sputtering techniques. The large target-to-sample distance ( $\approx 0.25\text{m}$ ) and the slow deposition rate of Fe minimize the energy of the sputtered atoms reaching the molecular film. This should avoid damaging the molecular film. In addition, for all of the metallic layers (Cu, Cr, and Fe) prepared by sputtering the substrate sample is rotated at a low rotation speed to obtain more uniform metallic layer coverage.

At last, throughout this thesis work special care has been put in obtaining clean substrate surfaces. Prior to any deposition the commercially bought Si/SiO<sub>2</sub> (500nm) substrates are cleaned with an ultra-sonic resonator in three different stages using ethanol, acetone, and isopropanol solvents to ensure the high quality of the films. This cleaning process results in smooth substrate surfaces with a root mean square roughness of 0.18nm, which is typical for SiO<sub>2</sub> surface morphology.

After the growth process, the hybrid heterostructures are taken out of the “Hybrid” system to conduct different measurements. For this purpose, several characterization techniques have been used which are explained in the next section.

### 5.3 Characterization techniques

Several characterization techniques have been used to investigate the physical properties of the hybrid organic/inorganic systems. Some are conventional techniques typical for studying inorganic and organic



thin films, yet others are more original as it will be illustrated in part IV. The following sections will give brief overview to the characterization techniques used during this thesis.

### 5.3.1 Super conducting quantum interference device

The superconducting quantum interference device (SQUID) magnetometer technique is designed to detect the magnetic flux originating from a sample. The SQUID utilizes solenoids of superconducting wires to subject the samples to magnetic fields. The sample is then vibrated through detection coils. The SQUID sensor consisting of superconducting rings operating via a Josephson junction, detects the current in these rings and transform it to output voltage. This output voltage is proportional to the magnetic moments of the studied sample.

SQUID magnetometer has been used extensively to study the magnetic behavior of the different hybrid organic heterostructures prepared in this thesis work. The prepared samples are  $3\text{mm} \times 4\text{mm}$  of size, so it can properly fit in the plastic straw sample holder. A plastic straw is used as it does not add any magnetic contribution to the sample signal. The straw holder containing the sample is then introduced to the magnetometer to fine tune the signal. As shown in figure 4, the sample is positioned in a way that during vibration, the sample does not exceed the distance of the pick-up coils. In this way, maximum SQUID output voltage will be detected hence all the magnetic moments in the sample.

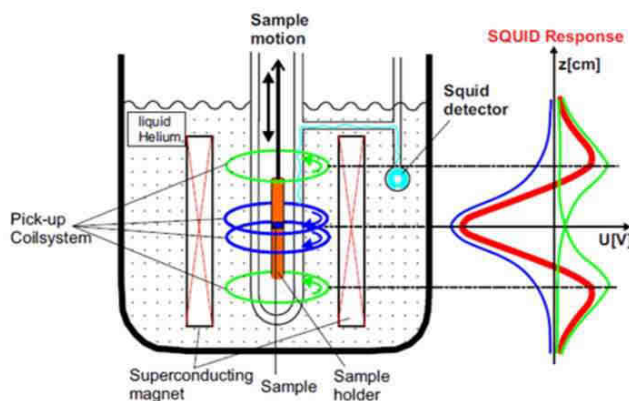


**Figure 4:** The interior components of SQUID magnetometer. The maximum/optimum SQUID output voltage signal is detected when the sample is well situated in-between the blue pick-up coils. The figure is taken from ref. [97].

For the exchange bias measurements field cooling (FC) procedure is performed during which samples are cooled down from 300K to the low target temperatures in an applied external magnetic field. The principle of FC measurements has been described in the previous part within the chapter about exchange bias.

In addition, for all the magnetic measurements conducted by SQUID a remnant field correction is performed. This is because even when the external magnetic field of the SQUID is set to zero there will be still some remnant current in its superconducting solenoids which will create a remnant magnetic flux. This trapped flux (the residual fields) leads to discrepancies between true and reported magnetic field values, especially at low fields. To determine the true magnetic field values applied to the investigated samples, paramagnetic samples are used e.g. erbium-doped yttrium aluminum garnet (Er:YAG). The Er:YAG is measured using exactly the same sequence used to measure the investigated samples. This measurement can be done at 300K since it is the characteristics of the magnets that is checked, it is not correlated to the sample measurement temperature.

Since the Er:YAG is perfectly paramagnetic its magnetization curve is a straight line passing through the origin of the magnetic field axes. However, this is not the case in the experimental measurements. As observed in the black curve of figure 5a, the measured magnetic curve of the Er:YAG sample shows hysteretic response with low remnant magnetization and small coercive fields (35 Oe). These features are due to the remnant field in the SQUID. Therefore, a linear fit (with y-intercept set to 0) is conducted. The slope of this linear fit is then used to compute the field correction in order to recover the paramagnetic behavior of the test sample. The field correction allows to find the residual fields trapped in the SQUID using the following formula:

$$H_{res} = (M \times a) - H_{rep} \quad (1)$$

Where  $H_{res}$  is the residual fields,  $M$  is the reported magnetization of the Er:YAG sample,  $a$  is the evaluated slope from the linear fit and  $H_{rep}$  is the reported magnetic fields of the Er:YAG sample.

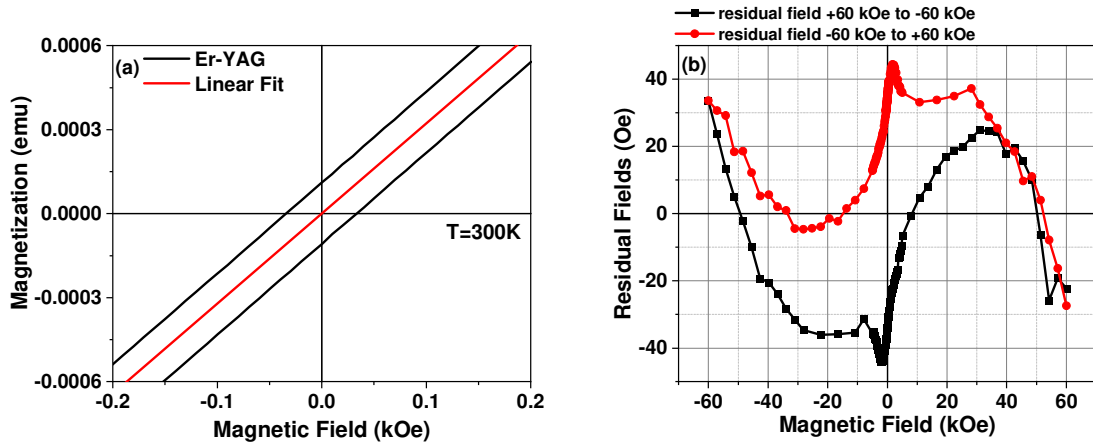


**Figure 5:** (a) black: magnetization curve of the Er:YAG sample, red: linear fit of the measured magnetization curve. The graph is scaled at [200 Oe, -200 Oe] for the details of the low field region. (b) Evolution of the residual fields of the SQUID as a function of applied magnetic field.

An example of such residual fields is plotted in figure 5b as a function of the applied magnetic field. As observed, the residual field curves show symmetrical behavior while cycling the applied magnetic field from +6T to -6T and back. These calculated residual fields are then subtracted from the recorded magnetic fields of the investigated organic samples to obtain their true magnetic field values.

The remnant field correction procedure is especially used for the indirect magnetic exchange coupling measurements that will be discussed in the last part of the manuscript. Such field correction allowed to confirm that the small exchange fields observed in the investigated samples are not experimental artifacts.

In this work, the SQUID is used in DC mode where static magnetic field is applied to study the macroscopic magnetic properties of the hybrid organic samples (Co/MTPP and Co/CoPc). The measurements are conducted in IPCMS using the commercial MPMS3 SQUID (Quantum Design Inc) magnetometer. This SQUID operates with an applied magnetic field of  $\pm 7T$  (*Tesla*) and a temperature range of 400K down to a low limit of 1.8K. The sensitivity is  $\leq 10^{-8}emu$  (*electromagnetic units*).

### 5.3.2 Atomic Force microscopy

Atomic Force microscopy (AFM) is a relatively new technique yet extensively used for surface characterizations. AFM is one the most versatile and powerful microscopy technique for studying sample's surface at nanoscale and can generate images with atomic resolution (vertical resolution). The general principle of AFM is based on the assembly of cantilever-tip (probe), that is brought near a surface at an interatomic distance. As the tip approaches a surface, the closed-range repulsive forces, force the cantilever to bounce back and forth depending on the nature of the surface. AFM can perform several tasks: force measurements, topographic imaging, and surface manipulation. Within this work, topographic imaging was used extensively. For this task, the response of the probe to the surface atomic forces is detected using a laser and monitor detector. Consequently, a three-dimensional image can be processed at high resolution. As a result, the topography of the surface is extracted.

The AFM images presented in this manuscript are acquired by scanning the samples in ambient conditions (in air), using the tapping mode operation. Since organic molecules are soft compounds, the tapping mode is chosen because it is less destructive compared to contact mode. In tapping mode, the probe is attached to a holder that contains a piezo material. This piezo material oscillates the cantilever near/at its resonance frequency that typically ranges 100 Hz to 2 MHz. In a tapping mode operation, the amplitude of the cantilever's oscillation is maintained constant when there is no interaction with the surface. As the tip approaches closer to the surface, it makes contact for a short time during each oscillation, and the acting forces (van der Waals, electrostatic etc.) will alter the amplitude of the oscillation (because the resonance frequency is modified). Thus, this modified oscillation amplitude will be directly proportional to the surface contour. Finally, using a feedback mechanism the topography of a surface can be mapped.

In addition to the topography imaging, in tapping mode the phase of the cantilever's oscillation can be recorded. This phase scan can be a particularly important kind of data when the sample surface is composed of regions with different adhesion properties and/or zones because the surface material is not the same. Often a topographic image cannot distinguish these differences, but the phase signal that is proportional to the energy dissipated by the cantilever during its oscillation, provides this kind of information. In this work, all AFM images are processed with WSxM 4.0 Beta 9.3 [98].

### 5.3.3 X-ray photoelectron spectroscopy

Any spectroscopy technique based on the use of photoelectric effect [99,100] can be referred as photoelectron spectroscopy. The fundamental mechanism of this technique is the following: when light is incident on a sample, it interacts with atoms near the surface region hence an electron absorbs the photon and is emitted out of the sample. The kinetic energy of the emitted electron can be represented as  $E_K = h\nu - E_B - e\phi$ ; where  $\nu$  is the photon frequency,  $E_B$  electron binding energy and  $e\phi$  electron work function. Therefore, when soft X-rays (200 to 1500 eV) are used to examine the core-level electrons of the probed atoms of the sample the spectroscopy technique will be called X-ray photoelectron spectroscopy (XPS).

XPS is a semi-quantitative analysis technique used for studying the chemical elemental composition of the sample from the binding energies of the elements. In XPS, the surface sample is irradiated by mono-energetic, soft X-rays that penetrate into the sample and ejects electrons of inner atomic energy levels. Each ejected electron, that initially occupies discrete energy levels, contribute differently to the final XPS spectra depending on their different binding energies. In general, the electrons which leave the surface without energy loss i.e. electrons originating from few tens of angstroms ( $\text{\AA}$ ) below the irradiated surface, contribute the most to the final XPS spectra. The XPS spectrum represents the electron counts versus electron binding energy.

A typical XPS setup consists of a UHV chamber, an X-ray source, and an electron energy analyzer. UHV chamber is important to ensure longest possible mean free path for the photoemitted electrons and to avoid contamination. The energy analyzer of the chamber acts as an electron energy filter. It allows only electrons of a given energy to pass through it. These are the photoelectrons that will be detected by the spectrometer.

For this thesis, all X-ray photoelectron spectroscopy (XPS) measurements are performed in an UHV chamber spectrometer equipped with a RESOLVE 120 MCD5 hemispherical electron analyzer.  $Al K_{\alpha}$ ;  $h\nu = 1486.6 \text{ eV}$  dual anode X-ray source is used as an incident radiation. Constant pass energy mode is used to record both survey and high-resolution spectra, with pass energies of 50 and 20 eV, respectively.

### 5.3.4 Transmission electron microscopy

Microscopes allow to get real-time and direct images of macro, micro, and nanoscopic structures that are not visible by naked eyes. Therefore, microscopy techniques are important experimental tools to have insight into such structures and study their chemical and morphological properties. In this thesis, transmission electron microscope (TEM) microscopy technique is used to have local insights into the morphology and the chemical environment of the hybrid organic/inorganic nanostructures. TEM provides several information related to the sample under investigation. First, TEM gives direct visualization to the layers inside the sample and allows to observe/study the quality and the texture of the interfaces. Second, TEM allows to get the crystal structure of the layers by studying the diffraction patterns. Finally, TEM allows to conduct chemical analysis to investigate the different chemical species within the layers of the sample.

The structure of a TEM experimental set up is similar to light microscopes. However, in a TEM microscope the source beam is electrons, the lenses are of electromagnetic/electrostatic in nature and the imaging device is fluorescent film. The electrons in a TEM can be produced by thermionic emission. In a thermionic emission process, an electron gun produces the electrons and ensure their acceleration. Fine tip of tungsten filament, lanthanum hexaboride ( $\text{LaB}_6$ ) single crystal or a ZrO/W Schottky emitter is heated by an electrical current flowing through the electron gun allowing the extraction of electrons. The extracted electrons are of low energy and need to be accelerated to a certain speed so that they can continue their path towards the specimen. Therefore, a high voltage is applied between the electron gun (cathode) and an anode plate to create an electrostatic field through which the extracted electrons are accelerated. For higher imaging resolution and better performance, it is important for the extracted electrons to stay intact along their path to the specimen. Therefore, high vacuum environment is needed. First, high vacuum is necessary in the area of the electron gun to prevent oxidation or burning of the filament from which the electrons are extracted. Second, high vacuum conditions in the sample region will result in long mean free path allowing the electrons to have long distances without colliding with residual gas particles.

After extracting and accelerating the electrons, different electromagnetic lenses are used to focus and guide the incident electron beam. The electromagnetic lenses are usually made of solenoid coils surrounded by ferromagnetic materials to direct the coil's magnetic field. One important advantage of an electromagnetic lens is the ability to modify the focusing power by adjusting the current passing through the solenoid.

The TEM has three different electromagnetic lenses listed as the condenser lens, objective lens, and projector lens. The condenser lens collects all the extracted electrons, packs and guides the primary incident beam to the sample (TEM grid). This incident beam passes through the sample and reaches the objective lens which focuses the transmitted beam thus form the primary image. Finally, at the last stage

the projector lens projects the image on the fluorescent screen and the result will be the final TEM image. In this process, the electron incident beam often suffers from asymmetrical beam distortions known as astigmatism which is caused by the inhomogeneities or the contamination of the lenses. For high resolution images, additional stigmators are present to correct this astigmatism.

Depending on the users' needs the TEM microscope can operate either in imaging mode or diffraction mode. Within this work, TEM has mainly been operated in imaging mode to extract images of the different hybrid nanostructures. The basic mechanism behind retrieving the images results from the interactions of the incident electron beam with the sample. To achieve this, it is important for the sample to be ultra-thin, so that beams can transmit through it. When the primary beam hits the thin sample, it will result into backscattered electrons, elastically and/or inelastically scattered electrons (diffracted electrons) and unscattered electrons.

The scattered and unscattered electrons are collected by the objective lens to form the primary images of the specimen. According to the type of collected electrons, bright field or dark field images can be obtained. If the objective lens is set to collect the transmitted electrons only, then one may create the so-called bright field image. In a bright field image, the strongly scattered electrons resulting from the heavier/thicker areas of the specimen are completely blocked hence these regions appear to be darker compared to lighter areas (layers of lower atomic number). In the contrary, if the objective lens collects the scattered/diffracted electrons then one may obtain a dark field image. Dark field images can be used to study the crystal lattices of a crystalline layer which may be too small to be observed by the bright field imaging.

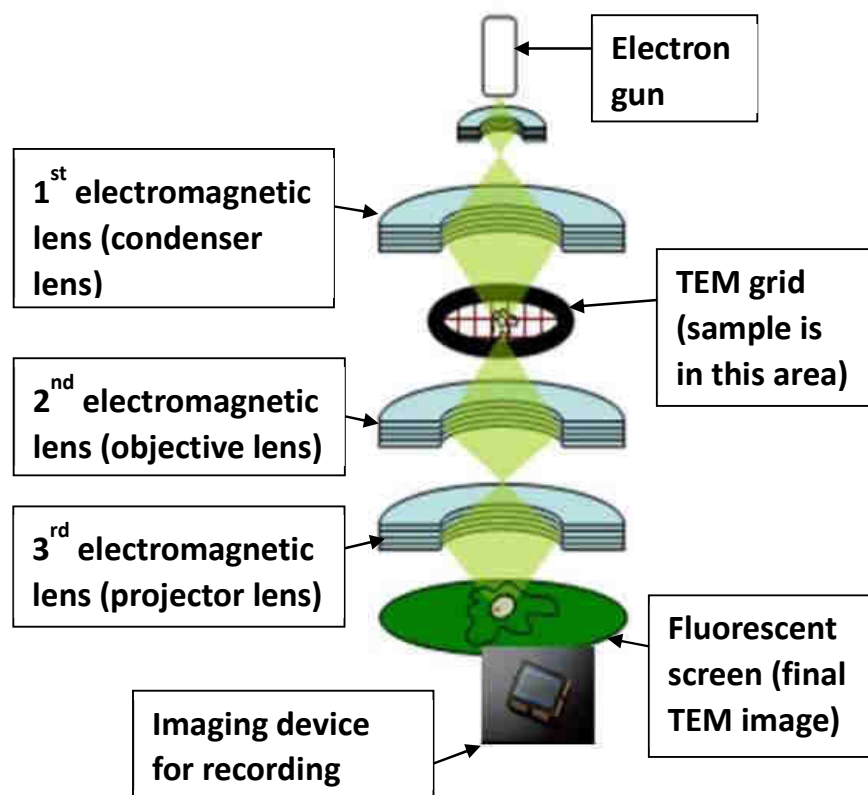


**Figure 6:** Sketch representing the design of basic operational parts of transmission electron microscopy (TEM). The figure is taken from ref. [101].

The original purpose of TEM was to extract structural information about a specimen via magnified images or diffraction patterns. With the progress of science and technology, energy dispersive detectors and electron spectrometers were attached to TEM setups to perform element specific characterization. Such characterizations allowed the analysis and quantification of different chemical species of the specimen. Frequently used spectrometry is the electron energy loss spectroscopy (EELS). EELS records the energy distribution of the electrons passing through the thin specimen. Consequently, EELS allows to form images with unique element specific signatures.

In general, an EELS spectrum consists of zero-loss peak, plasmonic excitation peak, and ionization peak edges. The zero-loss peak found at zero energy of the EELS spectrum results from the elastically scattered electrons that experience small energy exchange when interacting with the atoms of the specimen. The zero-loss peak contains no useful information therefore it is often excluded during the spectrum collection. On the other hand, the plasmonic excitation peak is typically observed below 100 eV in the EELS spectrum. It results from the inelastic interaction of the incident electron with the outer-shell electron of the specimen atom. The outer-shell electrons are delocalized. Therefore, the incident electrons with high kinetic energy experience Coulomb interactions with them hence excite the outer-

shell electron and leave positively charged holes. The attractive forces between these holes will result into energy loss of the incident electrons. As the result of these inelastic interactions, an energy loss peak will be observed in the spectrum, that is known as plasmonic excitation peak.

In contrast to outer-shell electrons, the core-shell electrons have strong binding energies. If the incident electrons have sufficient energy, they will excite the core-shell electrons from their original state to an unoccupied state above fermi energy level. This type of excitation appears in the EELS spectrum as ionization edges. Ionization edges will be present at energies higher than 100 eV in the EELS spectrum. The binding energies of core-shell electrons (K, L, M, N... shells) are dependent on different shells and different elements, so the ionization edges in the EELS spectrum can be used to identify and study the chemical species of the specimen. In this work, EELS spectrometer has been efficiently used to probe the chemical specific elements of the hybrid organic/inorganic nanostructures and interfaces.

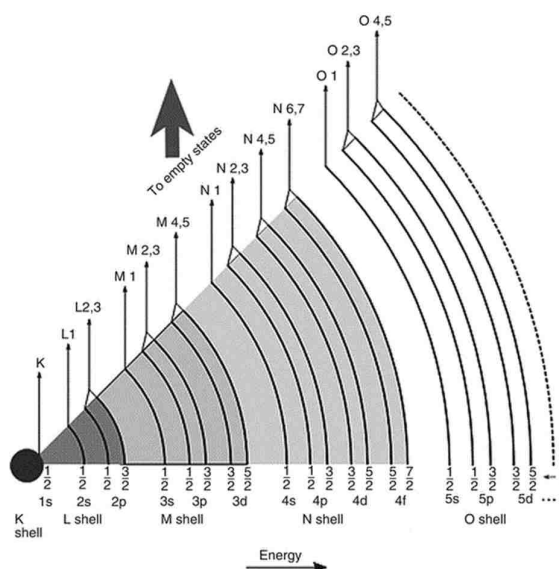


**Figure 7:** Possible ionization edges in an EELS spectrum due to core-shell electron excitation. The figure is taken from ref. [102].

The TEM imaging and EELS spectroscopy measurements for this work are conducted in IPCMS using a Jeol 2100F microscope. The microscope has an electron acceleration voltage of around 200 kV, an image resolution in TEM of 0.2 nm, and energy resolution in EELS of 0.7 eV. The microscope can be operated in high-resolution imaging, electron diffraction, electron energy loss spectroscopy, and electron tomography

#### 5.3.4.1 TEM sample preparation

As mentioned above, ultra-thin samples are required for TEM to allow transmission of electrons. Several techniques can prepare such samples among them are conventional polishing method, cutting



thin samples with ultramicrotome knife and subsequent thinning [103,104], cleaving with minimum mechanical and chemical treatments [105] and focus ion beam (FIB). All the mentioned techniques often require certain expertise even for stable inorganic samples. So, when these techniques are applied to organic hybrid nanostructures that are potentially less stable due to organic molecules, the procedure could become even more complicated and needs additional care.

For the samples under investigation in this thesis, conventional polishing methods are excluded as they require several steps of gluing, polishing and heat treatments that can destroy the organic films. However, several previous works reported the implementation of cross-sectional FIB preparation technique in organic hybrid samples [106,107,108] which led to high resolution TEM images. So, in this work too, FIB technique has been employed for TEM sample preparation. Focus ion beam (FIB) technique uses finely focused beam of gallium ions ( $Ga^+$ ) operating at high beam currents.

These focused ion beams can etch and prepare very localized patterns in solid samples. The preparation process of a FIB sample can be described as follows: First, a platinum layer is deposited on the area of interest for protection, then gallium ions are accelerated on that region to start the etching process. Once the FIB etched zone is ready, a cross section can be produced that is liberated from the rest of the sample surface. This process is done by further etching along the edges of that specific etched area. Then this small area is attached to a micromanipulator needle with platinum spray and transported to a TEM copper grid where again platinum spray is used to stick the small piece on the grid. Finally, the needle is detached from the grid by FIB etching the initial platinum bonds. The FIB section that is now on the copper grid is further thinned with low intensity grazing ion beams. With these steps, ultra-thin specimen can be prepared out of a micrometer big sample. One drawback of FIB technique in hybrid organic/inorganic samples is the high energy incident ion beam that might degrade the crystallinity of the molecular films. Therefore, it is important to optimize the energy of the initial ion beam and the beam current for the final thinning process. In this work, FIB prepared samples are placed parallel to the incident electron beam so clear visualization of the layers and the interfaces is obtained.

### 5.3.5 Ferromagnetic nuclear resonance

Nuclear magnetic resonance (NMR) spectroscopy is a non-destructive spectroscopic technique which has been developed to be one of the most powerful and successful analytical methods to investigate atoms and molecules not only in solution but also in solid state. NMR spectroscopy's basic principle relies on applying an external static magnetic field to the sample to lift the degeneracy of the nuclear spins. This energy split is known as the Zeeman effect. Zeeman effect leads to an energy gap  $\Delta E$  between the energy levels where excitation of nuclear spins is possible. The excitation occurs by applying a radiofrequency (RF) fields and if and only if  $\Delta E = h\nu$ ; where  $\nu$  is the resonance radiofrequency.

This thesis concentrates on investigating by NMR the correlation between magnetic and structural properties of Co/MTPP/FM (with FM= Co or Fe) heterostructures. When NMR is used to investigate ferromagnetic systems, we favor using the term ferromagnetic nuclear resonance (FNR) [109] but it is also often called zero field NMR or internal field NMR. In this thesis, a new FNR methodology has been developed. It is based on the design of specific sample architecture allowing to split the different interface contributions into specific FNR frequency ranges. In the section below, the basic concepts and particularities of FNR will be illustrated.

### 5.3.5.1 Zero-external field

Like any NMR spectroscopic technique, the basic principle of FNR is to lift the degeneracy of the nuclear spin energy levels of the probed nuclei by the presence of a magnetic field. As the samples under investigation are ferromagnetic, a magnetic field already exists at the nuclei sites therefore an additional externally applied magnetic field is not required. Although in some cases adding an external field can provide additional information. This is the first distinctive characteristics of the NMR in ferromagnets and the reason why it is also called zero field NMR. The main magnetic field contribution at the nuclei site is called the Hyperfine field (HF) and can be very large (tenths of Tesla) [110]. However, working in zero field means that to probe the resonance frequency of the nuclei spins, one needs a broadband spectrometer covering a wide range of frequencies i.e. a wide distribution of hyperfine fields. The equipment developed in DMONS-IPCMS laboratory allows such measurements with frequency ranging from 20 to 700 MHz [111].

The hyperfine field of the probed nuclei will essentially depend on the local chemical environment and on the local symmetry of their first neighbors. Therefore, the local structure and the local chemical environment will correspond to specific FNR radiofrequency ranges in the FNR spectra that represents the number of nuclei (atoms) versus their resonance radiofrequencies.

### 5.3.5.2 Local restoring field and magnetic analysis

Besides the possibility of working with zero-external magnetic field, FNR has a second unique characteristics that is related to the excitation process of the applied radiofrequency field  $H_1$ . This feature is represented in figure 8. The magnitude of the radiofrequency  $H_1^*$  sensed by the probed nuclei is in fact not the same as the magnitude of the radiofrequency  $H_1$  applied externally on the sample. Actually, the applied  $H_1$  field is enhanced by a factor  $\eta$  to the local field  $H_1^*$ . This enhancement factor is related to the local permeability of the atoms. The enhancement process can be explained the following way: when applying the radiofrequency field  $H_1$ , it leads to the oscillation of the electronic magnetization  $\mu_e$  of the probed atom; the oscillation of the electronic magnetization  $\mu_e$  will result in the oscillation of the hyperfine field  $H_{HF}$ ; the oscillating  $H_{HF}$  is the field responsible for the excitation of the probed nuclei. Since the oscillations of  $H_{HF}$  are very small, they can be described by a quasi-static longitudinal contribution equal to  $H_{HF}$  and an oscillating transverse contribution  $H_1^*$  that is the

radiofrequency field experienced by the nuclei. The enhancement factor  $\eta$  is the ratio  $\frac{H_1^*}{H_1}$ . Therefore the amplitude of  $H_1^*$  will depend on the local magnetic stiffness at the probed atom sites (the easiness or difficulty with which the local magnetization will follow  $H_1$ ). The magnetic stiffness is characterized by the restoring field  $H_r$ . Considering the scheme in figure 8, the field  $H_1^*$  can be written as:

$$H_1^* = H_{HF} \times \frac{H_1}{H_r} \quad (2)$$

The above-mentioned restoring field  $H_r$  can be translated as the field required to bring back the electronic moment to its equilibrium state i.e. the rest position of the electronic moment. For a given applied field  $H_1$ , in soft ferromagnetic materials the restoring field  $H_r$  will be weak therefore the electronic magnetization  $\mu_e$  will deviate largely from its equilibrium position hence leading to strong radiofrequency field  $H_1^*$ . On the contrary, a stiff ferromagnetic material will have a large restoring fields  $H_r$  hence weak radiofrequency field  $H_1^*$  (figure 8).

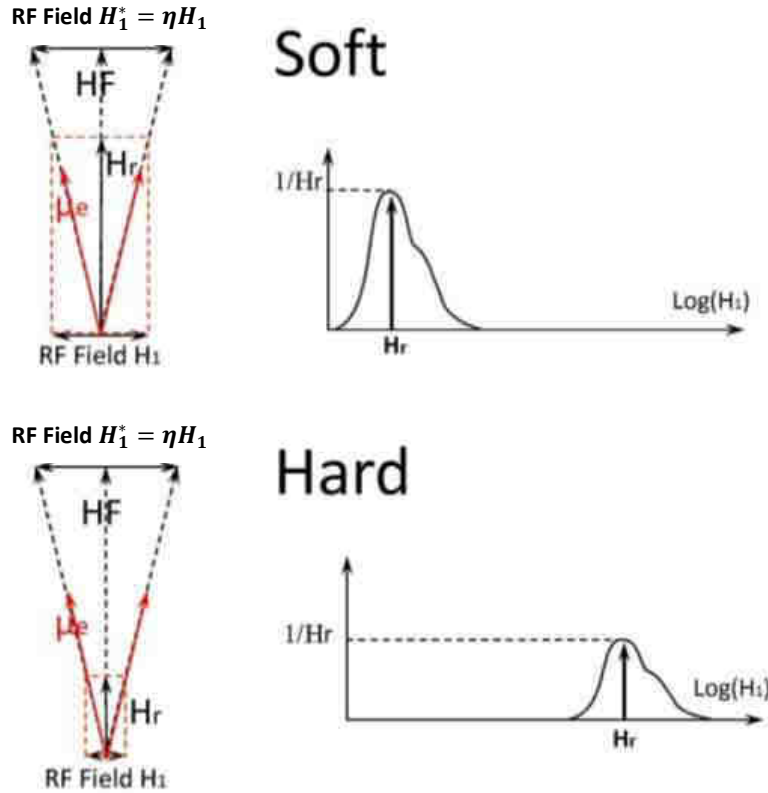


**Figure 8:** A schematic representation of the rf field enhancement process: applying the radiofrequency field  $H_1$  results in the oscillation of the electronic magnetization  $\mu_e$  which in turn results in the oscillation of the  $H_{HF}$ . The oscillation of  $H_{HF}$  then leads to the resulting radiofrequency  $H_1^*$  that is sensed by the probed nuclei. The figure is taken from ref. [111].

During the FNR signal recovery the process is the opposite to what happens during excitation. This time, the transverse nuclear magnetization will exert a torque on the electronic magnetization  $\mu_e$  which is then forced to oscillate. Since the signal in the probe coil of FNR is mostly originating from the electronic magnetization  $\mu_e$ , the received signal is enhanced by the same enhancement factor  $\eta$ .

In a pulsed FNR experiment, like the one used in this thesis the FNR signal is maximum when the nuclear spins experience an effective radiofrequency field  $H_1^*$  strength such that after the pulse sequence, the nuclear magnetization is perpendicular to the hyperfine field  $H_{HF}$  direction. This happens when the radiofrequency field  $H_1^*$  reaches an optimum value  $H_{1(opt)}^*$ , such that for a first pulse of duration  $\tau$ , the following relation is satisfied:

$$\gamma H_{1(opt)}^* \tau = \frac{\pi}{2} \quad (3)$$

Where  $\gamma$  is the gyromagnetic ratio of the probed nuclei, and  $\tau$  is the pulse-duration. The relation in equation (2) means that for a given nucleus and a fixed pulse duration  $\tau$ , the required radiofrequency  $H_{1(opt)}^*$  which is necessary to obtain the maximum FNR signal, must have the same value regardless the magnetic stiffness of the sample. Precisely, since the radiofrequency field applied to the sample is  $H_1$  and not  $H_1^*$ , for magnetically stiff samples it is necessary to apply strong  $H_1$ , so that the probed nucleus feels the sufficient  $H_1^*$  strength to produce the maximum FNR signal. While for magnetically soft samples, it is sufficient to apply weak  $H_1$  field to obtain the necessary  $H_1^*$  strength on the probed nucleus to produce the maximum FNR signal (figure 8). Therefore, determining  $H_{1(opt)}^*$  allows measuring directly the restoring field  $H_r$ . This is one of the main difficulties when applying NMR to ferromagnetic systems especially when the magnetic stiffness differs from one environment to another within the same sample.

Indeed, often there exists an interdependence between the magnetic and structural responses of the sample. Such interdependence causes complications in processing and analyzing the obtained information. To overcome this, a unique methodology has been developed in IPCMS. This methodology includes measuring the same sample for several different values of the applied radiofrequency field  $H_1$ . Consequently, the raw data result in a 3D FNR spectrum where the FNR signal intensity is represented as a function of resonance frequency and the applied radiofrequency field  $H_1$  strength.

A typical 3D FNR spectrum is represented in figure 9a. It can be observed that the FNR maximum signal is reached for different RF field strengths in different frequency ranges: at high frequencies (around 225 MHz) it is obtained for small field values, while at low frequencies the FNR signal hardly reaches its maximum for the maximum field strength used. This shows that the sample is inhomogeneous structurally and magnetically. The structural information is extracted by looking at the FNR signal along the frequency axis, while the magnetic analysis is done by looking at the FNR signal along the radiofrequency (RF) field axis. Actually, tracking down (as a function of frequency) the

amplitude of the radiofrequency (RF) field for which the maximum FNR signal is obtained, allows studying the magnetic inhomogeneity inside the sample. This is represented in figure 9b; it is the frequency dependent restoring field of the sample. The high frequency region at 225 MHz has a restoring field of 200 Oe, which is much lower than the restoring field (1100 Oe) of the low frequency region at 217 MHz. This means that the high frequency region is magnetically softer than the low frequency region.

Depending on the nature of the studied samples the restoring field can be identified to specific magnetic entities like exchange coupling fields or effective magnetic anisotropies.

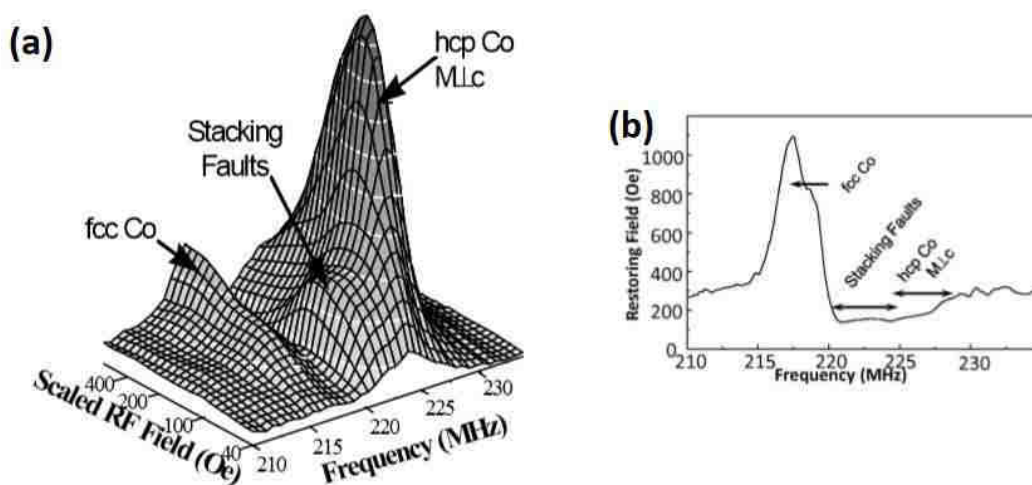


**Figure 9:** (a) 3D FNR spectrum in a hcp cobalt single crystal. The FNR signal intensity is represented as a function of frequency and scaled radiofrequency field  $H_1$  (b) The plot representing the restoring field as a function of resonance frequency. The figures are taken from ref. [111].

### 5.3.5.3 Structural analysis

The FNR spectroscopy technique allows a quantitative analysis of the structural and of the chemical properties of the probed magnetic samples. It provides insights into the structure, site symmetries and the chemical order of the investigated samples. This is explained by representing some archetypical examples.

Figure 10 shows typical FNR spectra of metallic Co. Figure 10a shows the spectrum of Co in the dominant face-centered cubic (fcc) crystal structure. At 217 MHz, a strong sharp peak can be observed corresponding to fcc Co and a very weak peak at higher frequency (225 MHz) which is the fingerprint of hexagonal closed pack (hcp) Co. The intensity of the peak is nothing but the counts of occurrence probability of that atomic configuration. Furthermore, in figure 10a there exists two weaker peaks in between the fcc (217 MHz) and hcp lines (225 MHz) which corresponds to the stacking faults in the

crystal. These stacking faults contributions are visible in the spectrum because of the sensitivity of FNR to the nearest neighbors (NN) of the probed Co atoms. On the other hand, the spectrum in figure 10b is of dominant hexagonal closed pack (hcp) Co. The spectrum shows a main peak at 225 MHz corresponding to Co in hcp structure, weak peak at 217 MHz corresponding to fcc Co, and satellite peaks in-between 217 and 225 MHz due to the stacking faults of the crystal.

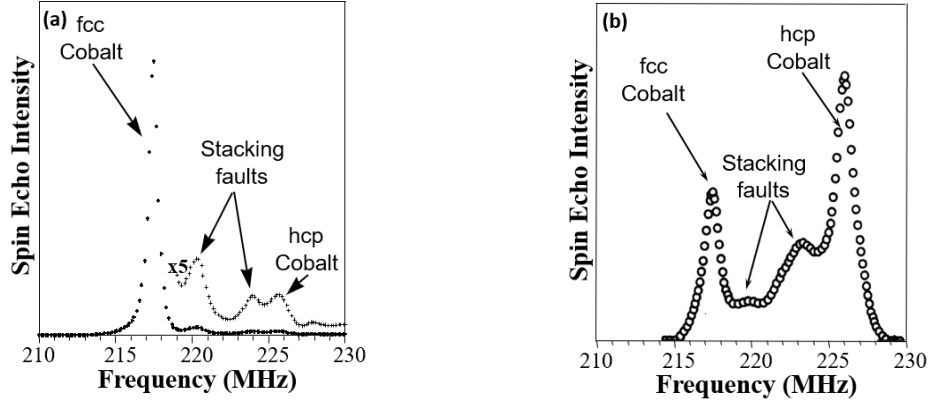


**Figure 10:** FNR spectrum of (a) Dominant fcc cobalt structure, with weaker hcp contribution at higher frequency and peaks corresponding to the stacking faults in-between. The spectrum above 219 MHz is magnified (x5) for visual clarity. (b) Dominant hcp cobalt with fcc and stacking fault contributions observed at lower radiofrequency range. The figures are taken from ref. [111].

In the next examples, influence on the FNR frequency of the chemical environment of the probed Co atoms are represented. In figure 11a, the spectrum of a  $Co_{0.9}Cu_{0.1}$  alloy is shown. As observed, there exists a main peak at around 217 MHz corresponding to Co atoms seeing only other Co atoms in their nearest neighbors. Then, at lower frequencies satellite lines appear as the consequence of the copper (Cu) foreign atoms in the Co environment. These peaks can be explained as follows. In hcp and fcc Co crystal structures, a Co atom sees 12 nearest neighbor atoms. In addition, the hyperfine field is dependent on the nature of the first nearest neighbor atoms. Since the Cu atoms are non-magnetic their contributions decrease the hyperfine field of the neighboring Co atoms thus decrease their resonance frequency [112]. Following these considerations, the first satellite peak right after the main peak towards lower frequencies can be attributed to Co atoms with 1 Cu foreign atom in its environment while the second satellite peak can be ascribed to Co atoms having 2 Cu foreign atoms. In figure 11b, the spectrum of  $Co_{0.9}Fe_{0.1}$  is presented. The peak observed at around 220 MHz corresponds to pure Co chemical environment with no impurities, while the satellite peaks at higher frequencies corresponds to the presence of 1, 2 and 3 Fe atoms respectively, within the nearest neighbors of the probed Co atom. However, it is important to note here that a magnetic atom with a higher magnetic moment (Fe) than

Co increases the hyperfine field of the investigated atom and as a result the resonance frequency of the corresponding chemical environment will increase [113]. In short, the observed resonance frequencies reflect the crystal structure of the investigated atoms in pure systems, while in mixed systems it mirrors the different chemical environments present within.

These unique characteristics make of FNR a powerful and sensitive spectroscopic technique which allows to investigate the atomic distribution, the chemical configuration, and also the local magnetic properties of the probed environment. Owing to the sensitivity of FNR to the nearest neighbors of the probed atoms and considering its unique outputs, FNR has been deployed (for the first time) to extract the physical properties of Co/MTPP hybrid heterostructures. The newly developed methodology is described briefly in the next section, explaining the motivation behind the architecture of the investigated samples.

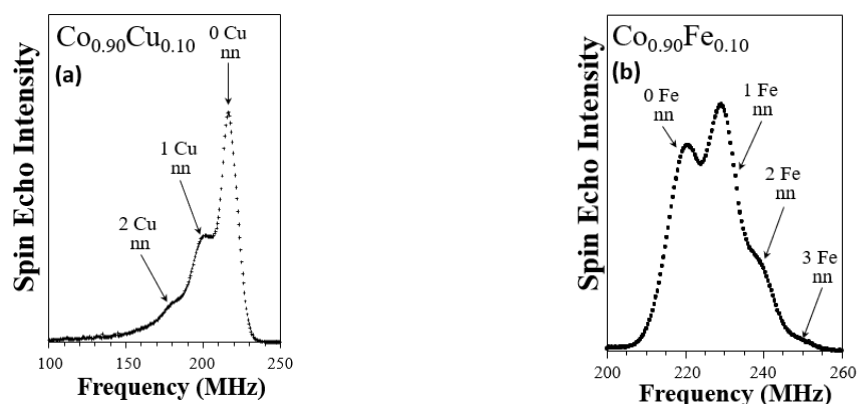


**Figure 11:** FNR spectrum of (a) Co-Cu (b) Co-Fe. In all spectra, 0 X nn (X = Cu or Fe) means no alien metal atom within the 12 NN cell of cobalt i.e. cobalt sees only cobalt atoms in its environment. 1, 2, ... X nn (X = Cu or Fe) corresponds to the replacement of 1,2... Co atoms in the NN cell by alien elements. The figures are taken from ref. [111].

#### 5.3.5.4 Hybrid heterostructures for FNR

One of the main factors governing the properties of the hybrid organic/inorganic systems is the interface of the molecule with the metallic layer. Therefore, a new FNR methodology has been developed to address the specific problematics of the organic/inorganic hybrid interfaces. To this end, different samples with particular architectures have been build which allowed to conduct such studies. The idea behind these specific hybrid samples is to separate in different radiofrequency ranges of the FNR spectrum, the contributions of the interfaces of interest.

To better understand the methodology, let us recall that Cu alien atoms (and in general non-magnetic atoms) in pure Co environment decrease the resonance frequencies of Co (figure 11a) hence, Cu/Co

interface contributions are found at low frequencies (< 200 MHz). On the contrary, Fe atoms close to Co increase the Co resonance frequencies (figure 11b) hence, Co/Fe interface contributions appear at high frequencies (> 240 MHz) of the FNR spectrum. This is shown in figure 12 where the spectrum of an archetypal Cu/Co/Fe sample is displayed. As observed the Cu/Co interface contribution is found at the low radiofrequency range while the Co/Fe interface contribution is at high radiofrequency range. Therefore, inserting new spacer layers in-between these metallic layers will allow to spectrally separate the interfacial contributions of interest and study the contributions of the newly formed interfaces to the FNR spectrum. This method allows to get a unique insight into the morphology of the hybrid heterostructures and will be explained in detail in part IV.

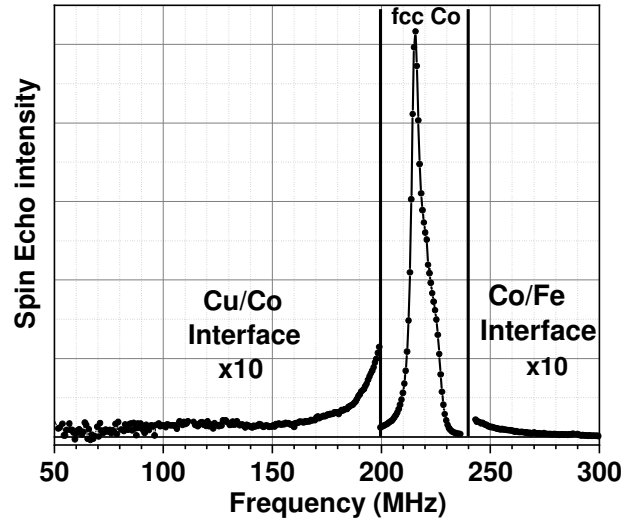


**Figure 12:** FNR spectrum of a typical Cu/Co/Fe sample. Low radiofrequency (< 200MHz) range corresponds to the Cu/Co interfacial contribution. High frequency range (> 240 MHz) corresponds to the Co/Fe interface contribution.

#### 5.3.5.5 FNR experimental conditions

All the FNR measurements are performed in a home-made state of the art FNR set up. The integrated spin-echo intensity is recorded using a broadband un-tuned pulsed spectrometer with phase-sensitive detection and automated frequency scanning (pulse length: 3.2  $\mu$ s, delay: 3  $\mu$ s). The FNR spectra are taken for at least five different values of the excitation radiofrequency field power, covering a range of over more than one order of magnitude. Such a procedure allows the determination of the optimum excitation field power at each frequency and corrects the variation of the local electronic susceptibility, thus the FNR enhancement factor as a function of frequency [129]. After this, a further correction for the regular ( $1/\omega^2$ ) frequency dependence of the FNR signal is applied. The obtained FNR amplitudes



represent the true distribution of the metallic atoms (nuclei) versus the radiofrequency field frequency. The FNR measurements are performed at 2K and the samples' surface area is of the order of  $3\text{cm}^2$ . All the spectra have been averaged for 12 hours. As the thickness of the samples is much thinner than the RF penetration length, several micrometers for the considered frequency range, the full stack FNR signal contribution is retrieved. With these experimental conditions the set-up sensitivity is better than 0.1 atomic layer of Co and in integral form it is better than 0.01 atomic layers of Co (integrated over 100 significant data points). All the spectra have been normalized to the sample surface area.





## **Part III**

**Is molecular exchange bias a  
spinterface effect?**



---

## Chapter 6: Investigating the molecular exchange bias in Co/organic systems

Metal phthalocyanine and metal octa-ethyl porphyrin compounds which showed the onset of molecular exchange bias are planar molecules. Following these works [59,60] and to verify the role of the molecules' planar character on exchange bias effect, the initial purpose of this Ph.D. work was to investigate if the effect can be extended to a new non-planar molecular family namely to metal tetraphenyl porphyrin (MTPP) molecules. Because of their non-planar character, when MTPP molecules are adsorbed on the FM metallic surface one could expect different behavior compared to metal phthalocyanine and metal octa-ethyl porphyrin molecules. Different behaviors will show the presence of different kind of interactions at the interface. Furthermore, MTPP compounds can further be chemically functionalized by additional ligands at different positions of the molecule. These newly functionalized molecules could combine multiple characteristics in a single material compound. As a result, it would be possible to study the influence of the hybrid interfaces on the overall response of device-like nanostructures upon applying different external stimuli. However, the results presented in this part revealed that the molecular exchange bias question was more complicated to answer and resulted in reconsidering our approach.

### 6.1 Sample optimization and sample architecture

As mentioned above, the initial steps of this thesis work was motivated by previous results of molecular exchange bias in Co/MPc hybrid systems. In addition, the author of a previous Ph.D. thesis work [94] observed that when Co/MPc bilayers are prepared on top of an Au buffer layer, the exchange bias field is enhanced showing higher magnitudes than for bilayers with no Au buffer. Therefore, a series of Co/MTPP bilayers were assigned to be prepared on top of Au buffer layer for studying the molecular exchange bias in Co/MTPP systems.

Consequently, a 25nm of Au seed layer was thermally evaporated on Si/SiO<sub>2</sub> substrates in the evaporation chamber of the "Hybrid" system following exactly the same procedure given in the Ph.D. thesis [94]. However, before continuing with the growth process the sample has been taken out of the "Hybrid" system to check the surface morphology of the Au buffer layer with AFM. AFM showed that the surface of the thermally evaporated Au layer has discontinuous morphology with high root mean square roughness;  $\sigma_{RMS} = 3.2nm$ . As observed in figure 1a, the surface is composed of big, disconnected islands. The crack openings in-between the islands are of 15-20nm wide and 8-10nm deep. This kind of buffer morphology is not desired if one wants to obtain smooth and well-defined adlayers when deposited on top of the buffer layer.

For this reason, an alternative deposition technique was to be considered to get smooth and flat surface for the buffer layer. Electron-beam deposition technique of the MBE chamber was chosen to provide smoother buffer layer. As seen in figure 1b, with this technique the surface of Au was improved leading to a smoother surface morphology with  $\sigma_{RMS} = 0.7nm$ . This difference is observed clearly in the height profile of the Au surfaces that are prepared by the two different techniques (figure 1c).

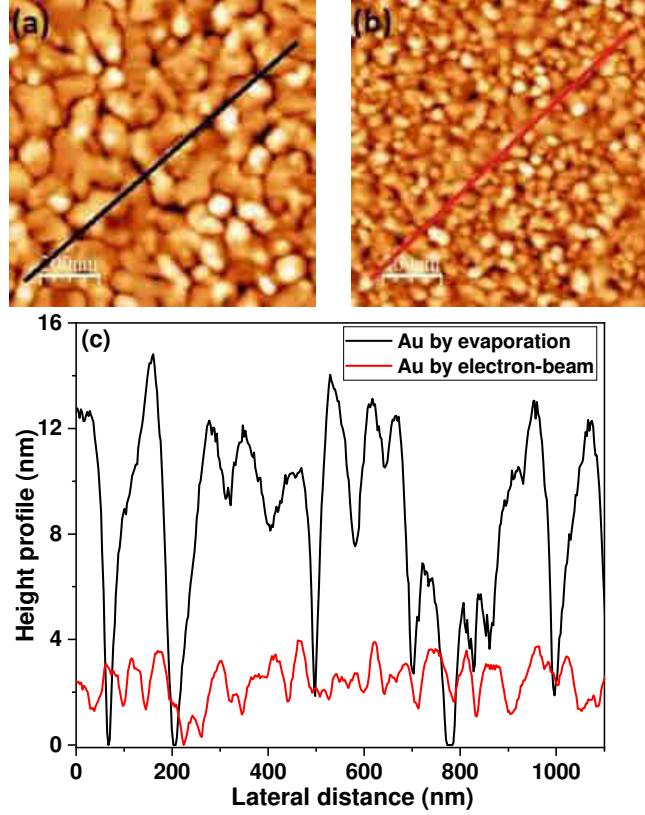


**Figure 1:** Surface image of Au buffer layer prepared by (a) thermal evaporation (b) electron-beam. Scan area is of  $1\mu m^2$ . (c) Height profile of the respective lines (color codes on the images) extracted from the AFM images.

To check the effect of this optimization on the Co adlayer, two different test samples have been prepared for magnetic measurements. In the first sample, 10nm of Co is thermally evaporated on Au buffer layer which is prepared in the “Hybrid” system, while the second sample has 10nm of Co deposited on top of Au buffer layer that is prepared by MBE. The latter is labeled as Au(e-beam)/Co while the former is labeled as Au(evap)/Co. Both samples are capped with 10nm of Au layer that is deposited in the evaporation chamber of the “Hybrid” system. The magnetization loops of these samples were measured by alternating gradient field magnetometer (AGMF) and are represented in figure 2. As observed, Au(evap)/Co sample has high coercive fields with  $|H_{c1}| = |H_{c2}| = 220 Oe$ . On the contrary, Au(e-

beam)/Co sample has low coercive fields  $|H_{c1}| = |H_{c2}| = 30 \text{ Oe}$ . Since these Co films have a [0001] growth direction and are thick enough to have an in-plane easy magnetization direction they are expected to have small coercive fields. The stiffness of Co layer in Au(evap)/Co can be due to the increase in the interface roughness that is caused by the discontinuous and the rough surface of the Au(evap) buffer layer.

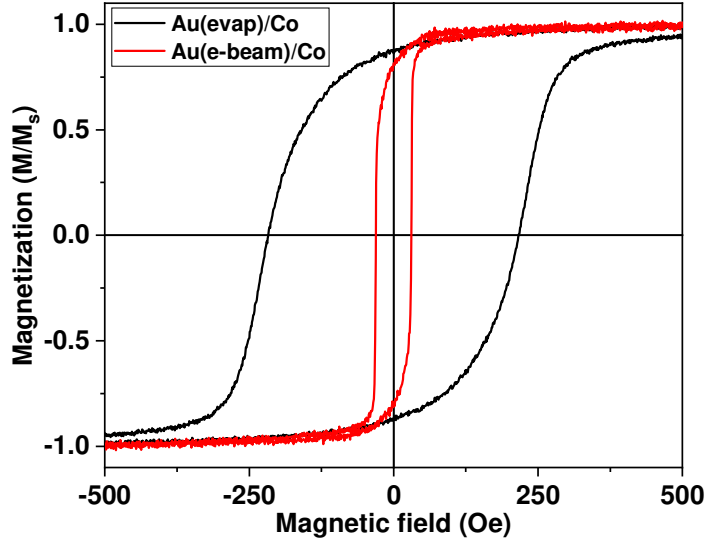


**Figure 2:** Magnetization loops of Au(evap)/Co(10nm)/Au(10nm) (black hysteresis) and Au(e-beam)/Co(10nm)/Au(10nm) (red hysteresis) measured with AGFM at room temperature in an external magnetic field of 1000 Oe.

Following these test samples, all the Au buffer layers were prepared by electron-beam technique in the MBE chamber. After preparing the Au buffer layers in MBE the samples were taken out of the MBE chamber and introduced to the “Hybrid” system to proceed with the growth of the remaining stack. This ex-situ transfer process was synchronized in a way that the removal of the samples from MBE and their introduction to the “Hybrid” is back-to-back with 2-3 minutes of delay in-between.

For studying the molecular exchange bias effect, different Co/organic bilayers have been prepared with the following stacks:

- Si/SiO<sub>2</sub>/Au(25nm)/Co(6nm)/MTPP(10nm)/Au capping layer ; with MTPP being Zn(II)TPP, Ni(II)TPP, and Co(II)TPP.
- Si/SiO<sub>2</sub>/Co(6nm)/CoPc(10nm)/Au capping layer



All the layers of the samples have been prepared using their respective parameters mentioned in the table 1, chapter 5, part II. The results of molecular exchange bias in these systems are discussed in detail in the coming parts.

### 6.2 Reference sample and checking the contamination-free character of the deposition chambers

SQUID magnetometer has been used to study the magnetic properties of Co/MTPP/Au ( $M = \text{Zn, Ni}$  and  $\text{Co}$ ) and Co/CoPc/Au hybrid systems. As mentioned, the probed samples are of hybrid structure therefore it is important to have a control sample that serves as a reference. In this part, the reference sample is Co film sandwiched between two Au layers i.e. Au (25nm)/Co(6nm)/Au(10nm). As of the hybrid samples, the Au buffer layer is prepared by electron beam deposition technique in the MBE while Co and the Au capping layers are thermally evaporated in the evaporation chamber of the “Hybrid” system.

The magnetic response of the sample is acquired after field cooling (FC) in static external magnetic field (+3T) from room temperature to 2K. As seen in figure 3a, the reference sample shows well-defined, symmetrical hysteresis loop with  $|H_{c1}| = |H_{c2}| = 100 \text{ oersted (Oe)}$ . This magnetization loop is stable with time, which shows that a 10nm of Au capping layer is thick enough to protect the FM metallic Co film from surface oxidation.

To check even further that the full deposition process is free of contaminations in the chambers of the “Hybrid” system a simple methodology has been followed. After depositing the Co layer in the evaporation chamber of the “Hybrid”, the sample is taken out from the chamber by the robot-arm and kept in the robot-arm chamber for several minutes. After, the sample is introduced again to the evaporation chamber to cap it with 10nm of Au layer. The magnetic behavior of this sample showed similar behavior to that of the one presented in figure 3a. This means that robot-arm chamber is contamination free, and no impurities are induced in the sample while the sample is being transferred from one chamber to the another in the “Hybrid” system.

Next in turn comes the OMBE chamber where similar process is followed to check for the cleanness of the chamber. After preparing the Co film, the Au/Co sample is introduced to the OMBE chamber via the robot-arm. In the OMBE chamber, the effusion cell which holds the organic molecule has been heated up to the molecules’ sublimation temperature, but the shutter of the cell has been kept closed. This means that the organic molecule will be in the evaporation state, but no deposition will occur because the cell shutter is closed. This step would allow to check whether the evaporation of the organic molecules could introduce impurities to the OMBE chamber thus contaminate the surface of the Co sample, before depositing the molecular layer. After keeping the Au/Co sample in the OMBE chamber for several minutes it is taken out and introduced again to the evaporation chamber and capped with 10nm of Au protective layer. This sample too showed a magnetic response similar to the one presented

in figure 3a. This means that the organic molecules are pure, and their evaporation does not introduce contaminants to the chamber. Therefore, no impurities will be induced to the sample while the organic molecules are being deposited.

With these simple yet fundamental steps one can be confident that all the chambers of the UHV deposition system are contamination free. The resulting samples would be free of impurities and ready for further characterizations.

### 6.3 Exchange bias in Co/ZnTPP

The first hybrid samples investigated have zinc metallated TPP molecules (ZnTPP) with a thickness of 30ML corresponding to  $\approx 10\text{nm}$  of ZnTPP molecular film ( $1\text{ML} \approx 3.3\text{\AA}$ ). ZnTPP is a diamagnetic molecule with a Zn(II) ion of closed shell configuration ( $[\text{Ar}] 3d^{10}$ ). In addition, ZnTPP molecule's interaction with metallic surfaces are believed to belong to physisorption regime dominated by weak van der Waal forces. Therefore, the behavior of ZnTPP layers is expected to be easier to investigate compared to CoTPP and NiTPP molecular films and actually no molecular exchange bias is expected with ZnTPP molecules. The magnetization curves obtained for the Co(6nm)/ZnTPP(10nm) hybrid sample capped with 10nm of Au are shown in figure 3b. These curves are obtained at 2K after FC in +5T external magnetic field. Freshly prepared and directly measured Co(6nm)/ZnTPP(10nm)/Au(10nm) hybrid sample showed exchange bias as observed from the shift of the hysteresis loop towards negative field axis, opposing the direction of the applied field during FC process. The magnitude of this shift is  $H_{EB} = -260\text{ Oe}$  and is close to the magnitude of the exchange bias field observed in Co/ZnPc/Au hybrid system [59]. In addition to exchange bias, the saturation magnetization shows a significant decrease when compared to the saturation magnetization value of the reference sample. It is 33% smaller than the one of the reference sample.

Accidentally, when the same sample was measured again 2 months later, it showed a different response. During those 2 months, the sample was kept in a desiccator which was opened and closed repetitively during working days. This magnetization loop is represented in figure 3b (red loop) in comparison to the magnetization loop of the “freshly deposited” hybrid sample. Further loss in saturation magnetization has been observed with a strong increase in both coercive fields.  $H_{c1}$  increases from -980 Oe for the “freshly deposited” sample to -1695 Oe resulting in larger exchange bias field  $H_{EB} = -600\text{ Oe}$ . As mentioned in the introduction, exchange bias in molecular hybrid systems is considered to be an intrinsic “spinterface” effect therefore it was not expected to observe an increase in the exchange bias field with time. However, to be sure that the observed exchange bias and its increase are indeed intrinsic “spinterface” effects, a new sample with modified Au capping layer has been prepared.

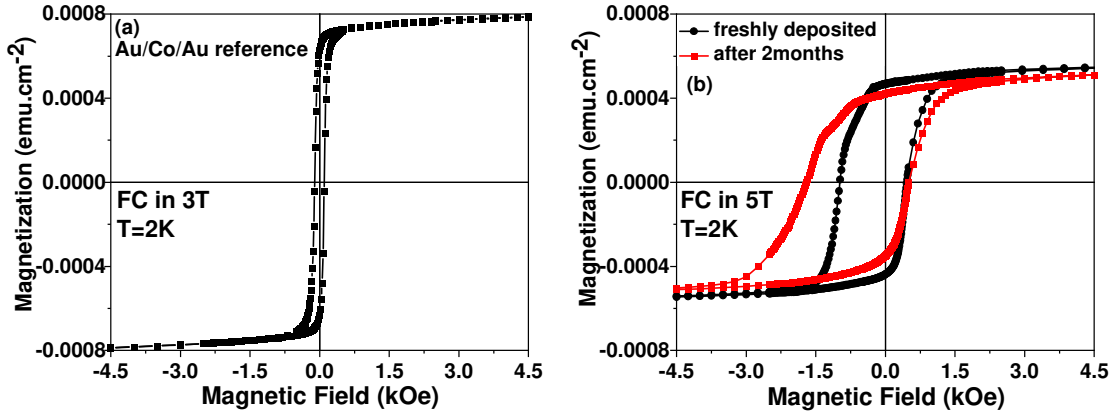


**Figure 3:** Magnetization loop of (a) 10nm capped Au/Co(6nm) reference sample, FC in +3T (b) “freshly deposited” Co(6nm)/ZnTPP(10nm)/Au(10nm) hybrid sample (black loop) and the same sample measured again after 2 months (red loop). Hybrid samples’ loops are acquired at 2K after FC in +5T.

To test the efficiency of the top Au layer whose goal is to encapsulate and protect the sample from extrinsic impurities, the capping Au layer was increased to 50nm without modifying any other part of the sample’s architecture: Si/SiO<sub>2</sub>/Au(25nm)/Co(6nm)/ZnTPP(10nm)/Au(50nm). The magnetization loop of these 50nm Au capped samples is presented in figure 4a. Remarkably, the “freshly deposited” 50nm Au capped hybrid sample (figure 4a, black curve) showed perfectly symmetrical hysteresis loop ( $|H_{c1}| = |H_{c2}| = 127 \text{ Oe}$ ) with respect to zero field, and no evidence of molecular exchange bias. Nevertheless, the saturation magnetization still shows a decrease when compared to the saturation magnetization of the reference sample. It is around 15% smaller than for the reference sample.

The same 50nm capped hybrid sample was measured again after 2 weeks under the same measurement conditions. In those 2 weeks, the sample was kept in a desiccator which was opened and closed constantly during working days. Now, the same sample showed a shift in its hysteresis loop (figure 4a, red curve) with a magnitude of  $H_{EB} = -510 \text{ Oe}$ . This observed shift is rather surprising since the 50nm capping Au layer is much thicker than the 6nm Co film and the 10nm ZnTPP molecular layer. These results strongly suggest that extrinsic impurities are having significant contribution to the observed magnetic response of the hybrid sample and has to be investigated in more details.

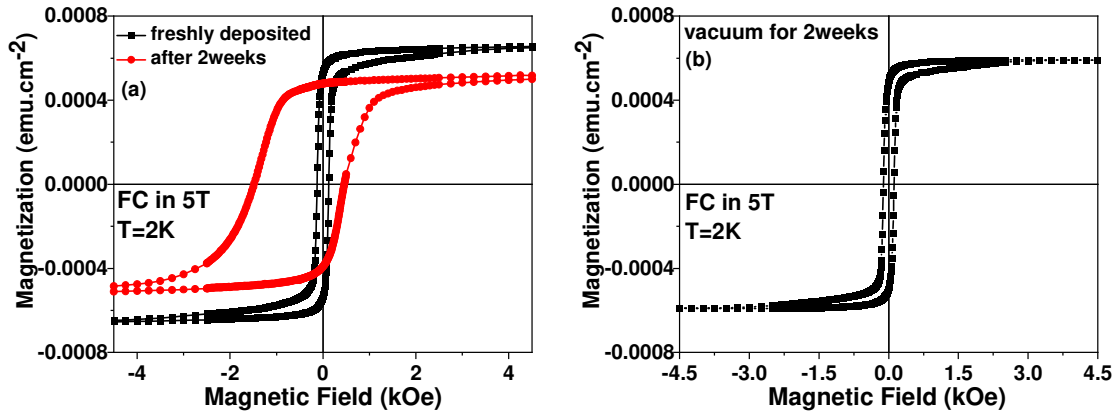


**Figure 4:** Magnetization loop of (a) “freshly deposited” Co(6nm)/ZnTPP(10nm)/Au(50nm) hybrid sample (black loop) and the same sample measured again after 2 weeks (red loop) (b) “fresh but old” Co(6nm)/ZnTPP(10nm)/Au(50nm) sample, kept in UHV for 2 week. The magnetization loops are acquired at 2K after FC in +5T external magnetic field.

Up to this point, the extrinsic contributions and possibly air-driven Co oxidation seems to be at the origin of the observed exchange bias. As an ultimate check, a new Au(25nm)/Co(6nm)/ZnTPP(10nm)/Au(50nm) hybrid sample was prepared but stored in an UHV chamber with a pressure of  $3 \times 10^{-8}$  mbar for complete 2 weeks. This sample has not been exposed to air until the time of the measurements. The magnetic behavior of this “fresh but old” hybrid sample has similar response as the “freshly deposited” 50nm Au capped sample. The magnetization curve of this sample is represented in figure 4b. It has a well-defined hysteretic response with slow and high saturation field, but no shift is observed, no hints of molecular exchange bias. This experimental evidence strongly suggests that indeed the onset of molecular exchange bias in Co/ZnTPP/Au samples is triggered by extrinsic effects and cannot be considered as an intrinsic magnetic effect.

### 6.3.1. Discussion and analysis

All the experimental evidences presented above clearly show that exchange bias in Co/ZnTPP/Au hybrid system is not an intrinsic “spinterface” effect. Actually, these results are not surprising if one recalls the fact that ZnTPP molecules are not spin-polarized, they are diamagnetic molecules. The Zn(II) ion in the ZnTPP molecule has closed shell configuration with no net spin. This means that Zn(II) ion does not have any free unpaired spin that can undergo exchange coupling interactions with the interfacial Co spins.

In addition, ZnTPP molecules belong to physisorption regime [114,88]. In this regime, the equilibrium distance of the ZnTPP from the substrate surface is of the order of  $3\text{\AA}$ . Therefore, the interaction

between the molecules and the Co surface will be very weak, almost negligible. These weak interactions will not induce any magnetic moments on the ZnTPP molecules nor change the spin-configuration of the molecule. Consequently, ZnTPP molecules will remain inert on the surface. As a result, there should be no magnetic effects induced at the hybrid Co/ZnTPP interface.

Therefore, and more trivially, although it has been shown that the 10nm of Au capping layer is thick enough to protect the reference sample (figure 3a), it is highly possible that this same capping layer is not thick enough to protect the hybrid bilayers. If the capping layer is not protecting the sample, it is probable that the sample is being contaminated when exposed to air after removing the samples from the UHV system. This air-exposure might lead to partial oxidation of the Co film transforming part of the metallic Co film into cobalt oxide  $CoO_x$ , that is well known to produce exchange bias effects. Furthermore, with the increase of the samples' exposure time to air the extent of the oxidation inside the FM metallic Co film might simply increase, thus increasing the observed coercivity and exchange bias field.

The same explanations can be used for the 50nm Au capped hybrid samples. The “freshly deposited” samples did not show the onset of exchange bias, but exchange bias appeared only after the samples were exposed to air a time long enough. Therefore, it is most likely that the exchange bias in these hybrid organic systems is the result of air-driven Co oxidation due to the poor efficiency of the capping layers.

From these investigations, it looks clear that exchange bias cannot be generated by diamagnetic ZnTPP molecules. Now, the next question is the following: is it possible to induce exchange bias on the FM Co film in hybrid molecular systems with organic molecules containing a magnetic metal ion? This is answered in the section below.

### 6.4 Exchange bias in Co/NiTPP and Co/CoTPP

To study the dependence of molecular exchange bias on the nature of the molecule's magnet ion, new MTPP molecules have been assigned namely, NiTPP and CoTPP. In NiTPP molecule, the Ni(II) ion has an open shell configuration ( $[Ar] 3d^8$ ) and is magnetic. Although the Ni ion site of NiTPP lies in a  $D_{4h}$  symmetry and results in a diamagnetic molecule, the interactions of NiTPP with the FM metallic Co surface might distort the four-fold square symmetry of the molecules. This break of symmetry might more easily induce a magnetic moment in the molecules at the vicinity of the hybrid organic/inorganic interface. Additional advantage of NiTPP when compared to the ZnTPP, is its higher stability. NiTPP molecules are more stable than ZnTPP. This increase in stability arises from the atomic radius of the Ni metal atom (163 pm) compared to Zn (139 pm). Since the metallic ion of the porphyrin macrocycle is bridged to 4 aminic nitrogen atoms via single chemical bond, a bigger metallic ion will result into shorter bond distance between the nitrogen and the metal thus stronger chemical bonds.

The magnetic measurements were conducted using the same methodology as for Co/ZnTPP/Au samples. The first set of investigated samples are capped with 10nm of Au layer. The magnetization curves of Co (6nm)/NiTPP(10nm)/Au(10nm) system are shown in figure 5a.

Strikingly, the “freshly deposited” sample (figure 5a, back loop) showed no sign of exchange bias. It has a symmetrical hysteresis loop with slightly higher coercive fields ( $|H_{c1}| = |H_{c2}| = 215 \text{ Oe}$ ) compared to the reference sample. After the first measurement, the sample has been stored in vacuum; in a properly pumped desiccator that was kept closed for the entire period and the sample was not exposed to air. After 1 week, the sample has been measured again and the magnetic response of the sample was the same as before i.e. no exchange bias (figure 5a, red loop).

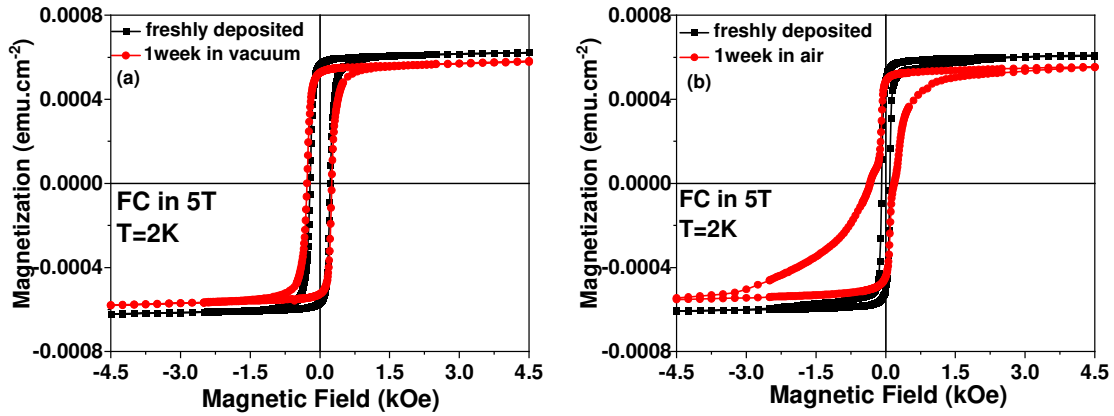


**Figure 5:** Magnetization loop of (a) “freshly deposited” Co(6nm)/NiTPP(10nm)/Au(10nm) hybrid sample (black loop) and the same sample measured again after 1 week, while kept in vacuum (red loop) (b) “freshly deposited” Co(6nm)/NiTPP(10nm)/Au(50nm) hybrid sample (black loop) and the same sample measured again after 1 week, while exposed to air (red loop). Magnetization loops are acquired at 2K after FC in +5T external magnetic field.

However, the sample’s coercive field being slightly larger than for the reference sample and following the same logic as before, a second set of samples was grown with the thicker Au capping layer Si/SiO<sub>2</sub>/Au(25nm)/Co(6nm)/NiTPP(10nm)/Au(50nm). The magnetization loop of the “freshly deposited” sample has been recorded right after preparation and measured again after 1 week while intentionally exposed to air. Its hysteresis loops are shown in figure 5b. Again, the “freshly deposited” sample (figure 5b, black loop) has a symmetrical magnetization loop with respect to the origin  $H=0$  and zero exchange bias field ( $|H_{c1}| = |H_{c2}| = 80 \text{ Oe}$ ). However, after 1 week of exposure to air a more interesting magnetization loop has been observed (figure 5b, red loop) showing two different reversals for different field ranges. This hints the presence of different magnetic domains with different magnetic

anisotropies. As observed in the hysteresis loop, a part of the sample reverses at small fields ( $|H_{c1}| = |H_{c2}| \approx 89 \text{ Oe}$ ) and shows no sign of exchange bias. A second part shows an asymmetrical reversal at higher fields and with a small shift towards the negative field axis ( $|H_{EB}| \approx 70 \text{ Oe}$ ) in the hysteresis loop. This indicates the onset of exchange bias in these domains.

At last, Co/CoTPP/Au hybrid samples were prepared. CoTPP molecules are paramagnetic with 1 unpaired electron ( $S = 1/2$ ) and have an effective magnetic moment of  $1.92 \mu_B$ . This allows to further study the effect of the molecules' magnetic nature on the onset of exchange bias. The magnetization loop of Co/CoTPP(10nm)/Au(10nm) sample was measured via magneto-optical Kerr effect (MOKE) after field cooling the sample in +1T external magnetic field. (note: MOKE has been used for this sample because of no access to SQUID due to technical problems). Figure 6a represents the magnetization loop of “freshly deposited” Co/CoTPP(10nm)/Au(10nm) hybrid sample. As observed, the sample does not show any hints of exchange bias. It shows symmetrical hysteresis loop with coercive fields  $|H_{c1}| = |H_{c2}| \approx 150 \text{ Oe}$  close to the reference sample.

However, when the same sample was measured again after 2 months it showed different magnetic response. During those 2 months' period, the sample was kept in a desiccator that was opened and closed constantly during working days. The magnetization loop (figure 6b) showed the onset of exchange bias.  $H_{c1}$  increases strongly from -150 Oe for the “freshly deposited” sample to -1230 Oe leading to exchange bias field of - 338 Oe.

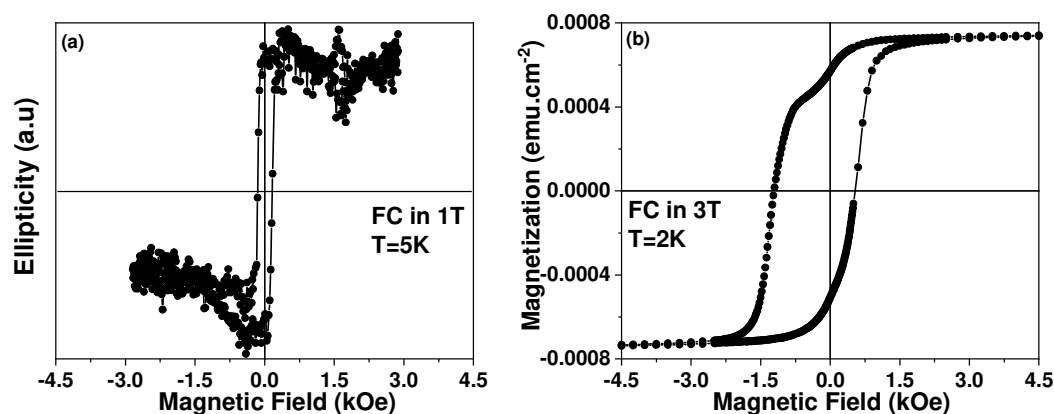


**Figure 6:** Magnetization loop of (a) “freshly deposited” Co(10nm)/CoTPP(10nm)/Au(10nm) hybrid sample measured via MOKE. Loop acquired at 5K after FC in 1T (b) same sample measured again after 2 months this time with SQUID. Loop acquired at 2K after FC in +3T external magnetic field.

## 6.5 Partial conclusions

The above sections showed and explained a detailed magnetic investigation conducted on Co/ZnTPP/Au, Co/NiTPP/Au and Co/CoTPP/Au hybrid samples. By means of SQUID magnetometer, it is concluded that exchange bias in Co/MTPP ( $M = \text{Co, Ni and Zn}$ ) hybrid samples does not originate from “spinterface” effect but is more trivially due to the partial oxidation of the Co film during air exposure resulting in  $\text{CoO}_x$  oxide that is well known to show exchange bias effects. This is true regardless the magnetic nature of the molecule. Properly capped “freshly deposited” samples did not show any sign of exchange bias. The onset of exchange bias is only observed after some time of air exposure. Surprisingly, even Au capping layer as thick as 50nm was not large enough to protect the sample from contamination. These studies raised one important question about the case of the Co/metal phthalocyanine hybrid systems [58], in which the molecular exchange bias has been observed for the first time: does the reported exchange bias really originate from the presence of organic molecules? To answer this question, the magnetic properties of Co/cobalt phthalocyanine (CoPc) hybrid samples have been re-investigated at the light of the gathered knowledge on the Co/MTPP heterostructures.

## 6.6 Exchange bias in Co/CoPc

The Co/CoPc bilayers were grown using exactly the same procedure as in [59]. For this series, two different sets of samples were grown. In the first set, the bilayer was capped with 10nm of Au i.e. Si/SiO<sub>2</sub>/Co(10nm)/CoPc(10nm)/Au(10nm), whereas the second set was protected by 50nm of Au. SQUID measurements were conducted using the same methodology as for Co/MTPP/Au samples and the magnetometry results on Co/CoPc samples are presented in figure 7. Magnetization loop of the “freshly deposited” Co/CoPc hybrid sample capped with 10nm of Au (figure 7a, black loop) has symmetrical loop showing no hints of exchange bias. However, after 5 days of intentional exposure to air (figure 7a, red loop), loss in magnetization has been observed and exchange bias appeared with a magnitude of  $H_{EB} = -352 \text{ Oe}$ . On the other hand, the sample with 50nm of Au capping layer also showed no exchange bias when measured right after sample preparation. However, after 2 and 7 days after the first measurement (sample being kept in the desiccator but not fully under vacuum) the sample has already aged. As observed in figure 7b, the magnetization loop of the sample shows two different reversals at different fields, suggesting the presence of two different magnetic anisotropies. These loops have asymmetrical behavior for the stiffer domain that shows the onset of exchange bias.

Finally, Co (10nm)/CoPc(10nm) hybrid samples capped with 10nm and 50nm of Au showed no onset of molecular exchange bias (figure 8) when kept in UHV chamber for several days before measurement. It has been concluded that exchange bias in Co/CoPc hybrid system that was thought to be a “spinterface” effect is probably also the consequence of partial oxidation of the Co films when the samples are exposed to air for ex-situ measurements.



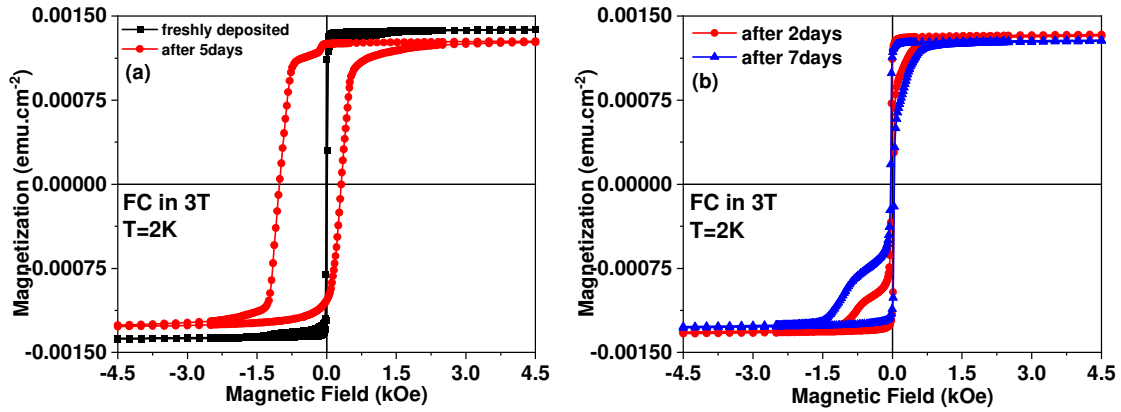


**Figure 7:** Magnetization loop of (a) “freshly deposited” Co (10nm)/CoPc(10nm)/Au(10nm) hybrid sample (black loop) and of the same sample measured again after 5 days (red loop). (b) already aged Co(10nm)/CoPc(10nm)/Au(50nm) hybrid sample measured after 2days (red loop) and measured again after 7days (red loop). Magnetization loops are acquired at 2K after FC in +3T external magnetic field.

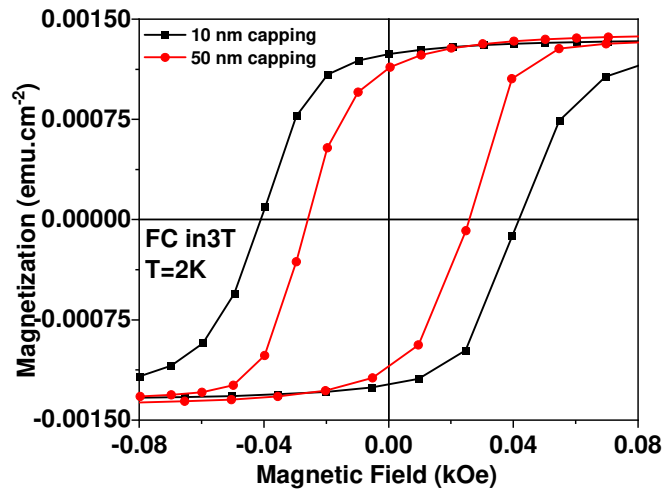


**Figure 8:** Magnetization loops of 10 nm capped Co/CoPc (black curve) and 50 nm capped Co/CoPc (red curve) after being in UHV chamber for 5 days before measurement. The samples are not exposed to atmosphere, until time of measurements. Loops acquired at 2K after FC in +3T.

---

## 6.7 Summary and conclusion

Motivated by previous results on molecular exchange bias induced by planar phthalocyanine molecules, the work was extended to non-planar MTPP molecules ( $M = \text{Co}, \text{Ni}$  and  $\text{Zn}$ ). The non-planar character in addition to the magnetic and non-magnetic nature of the molecules allowed to study the effect of these characters on the molecular exchange bias. At first, it was promising to see diamagnetic ZnTPP molecules inducing exchange bias on Co films. However, this result was a bit doubtful for several reasons. On top of them, is the closed shell configuration of Zn(II) ion which leaves no unpaired spins for exchange interactions. Indeed, by modifying the Au capping layer and measuring several different aging histories, it was confirmed that the observed exchange bias is the result of the air-driven partial oxidation of the Co film when the samples were exposed to air prior to the SQUID measurements. Even 50nm of Au capping layer was not able to protect the hybrid layers from contamination. The same effects were observed regardless the nature of the molecules' metallic ion (Co, Ni or Zn). Finally similar results were observed in newly prepared Co/CoPc samples. These observations allowed to conclude that exchange bias in Co/MTPP/Au ( $M = \text{Co}, \text{Ni}$  and  $\text{Zn}$ ) and Co/CoPc/Au hybrid system is not an intrinsic "spinterface" effect but originates from air-driven, partial oxidation of the Co film. To explore the element-specific chemical composition of the samples and understand the reasons behind the observed contamination, X-ray photoelectron spectroscopy (XPS) and atomic force microscopy (AFM) studies were performed on the samples and the results are discussed in the next chapter.

---

## Chapter 7: Chemical composition and morphological characterization of Co/MTPP hybrid systems

### 7.1 XPS measurements

As seen in the previous chapter, exchange bias in Co/MTPP/Au hybrid systems probably originates from air-driven partial oxidation of the Co film. To confirm this hypothesis, XPS was deployed to study the specific chemical composition of these hybrid samples. The samples investigated with XPS are the following: (i) Co(II)TPP and Zn(II)TPP in their powder form, (ii) Au(25nm)/Co(6nm) reference sample in which the sample is not capped with protective layer to intentionally oxidize the Co film, (iii) Co(6nm)/ZnTPP(10nm)/Au(10nm) and Co(6nm)/ZnTPP(10nm)/Au(50nm) hybrid samples which showed the onset of exchange bias. The measurements were performed at ICPEES-ECPM (CNRS). As the samples were already contaminated, they were transferred under ambient conditions.

#### 7.1.1 Co 2p-edge of CoTPP and Co/ZnTPP hybrid sample

Figure 9 represents the  $Co\ 2p_{3/2}$  XP spectra of CoTPP compound, of the uncapped Au/Co reference sample and of the Co/ZnTPP/Au(10nm) hybrid sample. In figure 9a, the black spectrum represents the  $Co\ 2p_{3/2}$  signal of the uncapped Au/Co reference sample. It shows two main peaks: One peak at binding energy of 778.1 eV which corresponds to Co(0) for metallic Co [115] and a second peak at 781.1 eV attributed to CoO and Co<sub>3</sub>O<sub>4</sub> structures [116,117,118]. Similarly, the red spectrum which represents the  $Co\ 2p_{3/2}$  signal of the Co/ZnTPP/Au(10nm) hybrid sample, exhibits two main peaks: one peak at 778.1 eV corresponding to the metallic Co and a second peak at 781.1 eV corresponding to the cobalt oxide structures. In the two spectra, the presence of these two peaks at the same binding energies suggests that indeed the Co film in Co/ZnTPP/Au(10nm) hybrid sample is oxidized. It must be noted that 10nm is already thick compared to the electron escape length and it was rather surprising that the 10nm Au capped Co/ZnTPP hybrid sample showed  $Co\ 2p_{3/2}$  signals. This is in itself already a proof that the capping layer is not efficient enough to protect the sample. The 50nm capped hybrid sample did not show any signal. This however does not guarantee that the capping layer is thick enough to protect the sample. The escape length of the electron probably also depends on the morphology (roughness) of the films.

The spectrum of the reference CoTPP powder is shown in figure 9b. It shows a sharp main peak at 780.1 eV that is typical for Co(II) peak in the molecule [119,120] and a much broader and weaker shoulder at around 782 eV. This shoulder is a multiplet structure of the signal and is due to the unpaired electrons of the  $d^7$  shell of the Co(II) within the molecule. This shoulder is in good agreement with previously reported experimental and theoretical works [119,121].

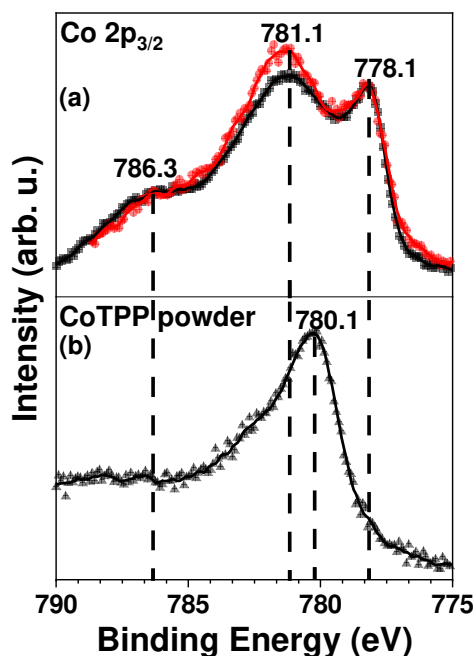


**Figure 9:** Co 2p<sub>3/2</sub> XP spectra of (a) Au(25nm)/Co(6nm) uncapped reference sample (black spectrum) and of Co(6nm)/ZnTPP(10nm)/Au(10nm) hybrid sample (red spectrum), (b) Co(II)TPP compound. Scattered plots are the raw data and the bold lines are the smoothed spectra. The shake-up satellite peak is present at 786.3 eV for all spectra, and it results from the multi electron excitation process during a photoemission mechanism.

It is important to note that no contribution in the range of the peak at 780.1 eV can be observed in the spectrum of the Co/ZnTPP/Au hybrid sample (figure 9a, red spectrum). This suggests that the Zn(II) ion of the molecule is not being replaced by the Co metallic atoms of the Co film when the ZnTPP molecules are adsorbed on the Co surface. To further understand these observed results, the N 1s and Zn 2p<sub>3/2</sub> XP spectra of the samples have been extracted which will be discussed in the next section.

### 7.1.2 N 1s and Zn 2p edges of Co/ZnTPP hybrid sample

Figure 10 shows the N 1s and Zn 2p<sub>3/2</sub> XP spectra of ZnTPP, of CoTPP, and of Co(6nm)/ZnTPP(10nm)/Au(10nm) hybrid sample. First, the dark blue spectrum of figure 10a represents the fitted spectrum of N 1s signal acquired from the Co(6nm)/ZnTPP(10nm)/Au(10nm) hybrid sample. Three different peaks are observed: two main peaks at 399.1 eV and 398.5 eV which lie

in the binding energy range for the 4 aminic nitrogen atoms bonded to the Zn ion within the molecule. The third peak is observed at slightly higher binding energy which is found at 399.95 eV. This peak could result from the nitrogen atom that has a single bond with the hydrogen atom i.e. N-H, which is the pyrrolic nitrogen in a porphyrin compound. However, because the shift is small (0.8 eV) the presence of such peak could also be the result of a final state relaxation mechanism [122] which is considered to be a satellite peak. Within this work, the peak at 399.95 eV is considered to be a satellite peak.

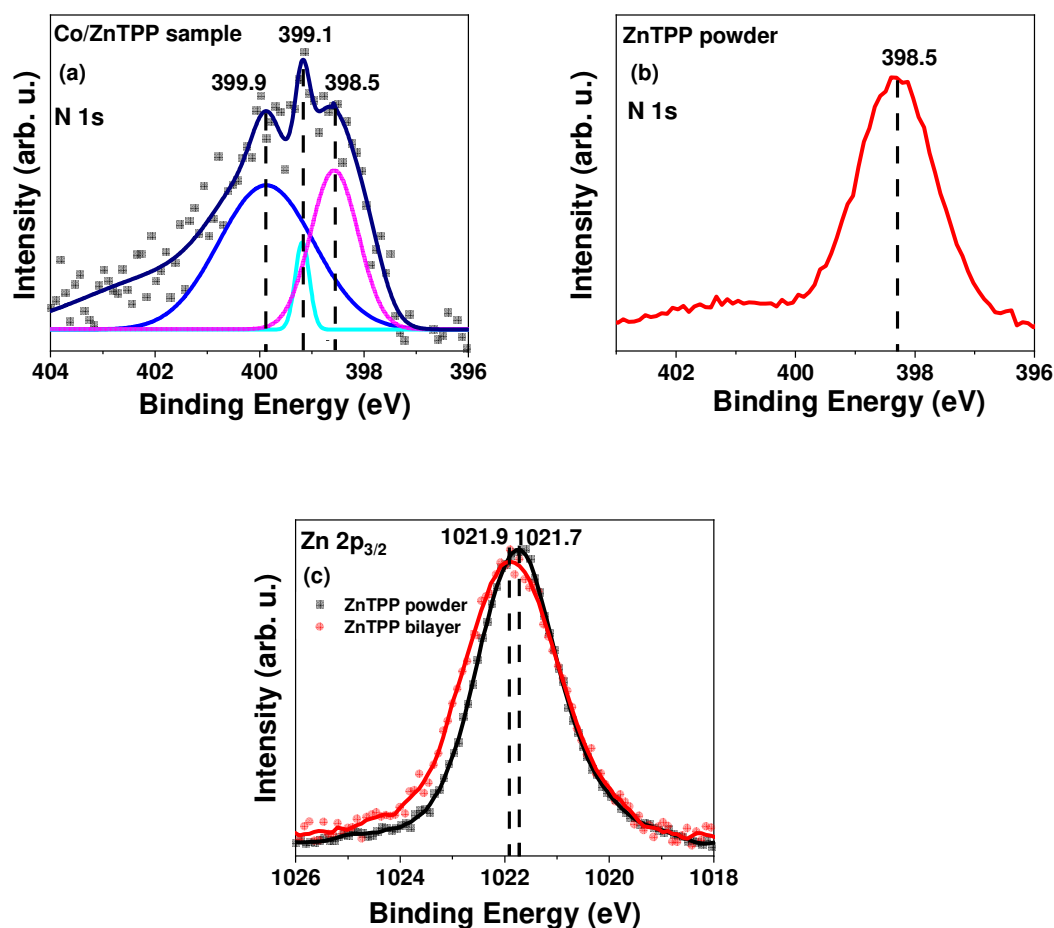


**Figure 10:** (a) *N* 1s XPS spectra of Co(6nm)/ZnTPP(10nm)/Au(10nm) hybrid sample. The dark blue spectrum is the cumulative fitted spectrum from the three other spectra present in the same plot. (b) *N* 1s XPS spectrum for ZnTPP compounds (c) *Zn* 2p<sub>3/2</sub> XPS spectra of ZnTPP compound (black) and Co(6nm)/ZnTPP(10nm)/Au(10nm) hybrid sample (red).

In addition, figure 10b shows the *N* 1s peak of ZnTPP compound at 398.5 eV [123]. This peak is found at the expected binding energy for the aminic nitrogen atoms bonded to the molecule's Zn(II) ion. However, the difference of binding energies between the observed *N* 1s peaks in Co/ZnTPP/Au sample and ZnTPP powder could be due to the molecule's different morphology. In the Co/ZnTPP/Au sample, the molecules are adsorbed on a metallic surface and build the 10nm thick molecular film whereas the ZnTPP compound is measured in the molecule's powder form. Often, such kind of morphology difference can result in small differences in the binding energies.

In figure 10c, the *Zn* 2 $p_{3/2}$  XP spectrum of ZnTPP powder exhibits one sharp peak at 1021.7 eV corresponding to Zn(II) ion within the ZnTPP. Zn is in 2+ oxidation state in the molecule with 3 $d^{10}$  closed shell configuration therefore no satellite peaks are expected to be seen in the spectrum due to the multiplet structure of an unpaired electron. Moreover, the black spectrum of figure 10c shows a similar sharp peak for the *Zn* 2 $p_{3/2}$  signal resulting from the Co(6nm)/ZnTPP(10nm)/Au(10nm) hybrid sample. This peak is positioned at 1021.9 eV, which corresponds to Zn(II) ion of the molecule in a multilayer regime [119,120]. The peak shows a small shift (0.2 eV) in its peak energy with respect to the signal observed from the ZnTPP powder (1021.7 eV). This shift lies in the same range as the *C* 1s and *N* 1s core level shifts and is largely due to the relaxation effect that occurs post photoemission [120].

### **7.1.3 Discussion and conclusion**

To have insight into the chemical atomic species of the contaminated samples XPS was used as it is a surface sensitive spectroscopic technique which allows to investigate metallic atoms and their respective oxides. CoTPP and ZnTPP compounds showed typical *Co* 2 $p_{3/2}$  and *Zn* 2 $p_{3/2}$  edges which suggests that these molecules in their powder form were stable whilst measurement.

Moreover, the *Zn* 2 $p_{3/2}$  edge of the Co/ZnTPP/Au(10nm) sample showed binding energies corresponding to Zn(II) ion within ZnTPP, what suggested that ZnTPP molecules did not experience any structural deformation on the Co surface. Also, a change in the oxidation state of the metal ion within the molecule would result to a shift in binding energies of approximately 1.8 eV which was not observed in this case. This is an additional proof which suggests that the molecules do not experience on-surface degradation. Finally, the comparison of *N* 1s peaks of CoTPP compounds and of Co(6nm)/ZnTPP(10nm)/Au(10nm) sample showed that ZnTPP molecules are not distorted nor decomposed once deposited on the Co surface.

All these experimental observations suggest that the peak observed at 781.1 eV in the *Co* 2 $p_{3/2}$  spectrum of Co/ZnTPP/Au(10nm) hybrid sample is the result of air-driven partial oxidation of the Co film. The oxidation of the Co film is at the origin of the exchange bias observed in the hybrid samples.

The hybrid samples used for XPS measurements are capped with 10nm of Au layer. This thickness is already thicker, by an order of magnitude, than the electron escape length. Despite this, XPS was able to detect signals resulting from the buried Co film. To better understand the reasons of these observations, AFM has been deployed to study the surface morphology of the topmost Au layer and further check the morphology of the molecular films. These results are represented here after.

## **2.2 AFM measurements**

Supposedly encapsulated Co/MTPP/Au hybrid samples showed the onset of exchange bias only after the samples were exposed to air and the buried Co films were, at least partially, oxidized. This was further confirmed with XPS measurements. Generally, the electrons originating from few tens of angstroms ( $\text{\AA}$ ) below the irradiated surface contribute the most to the final XPS spectra. In the studied hybrid samples the Co films are buried almost 20nm below the surface. This depth exceeds by far the electron escape length and no signals should be detected from the Co film. This suggests that the layers above the Co film are not really homogenous and/or continuous, and their morphology might be rich in holes and cracks which allowed the excited electrons from the buried Co films to be detected by XPS. To tackle this point, AFM was deployed to study the surface morphology of the layers and understand the reasons of the above-mentioned results.

### **7.2.1 Surface morphology of Au capping layer**

The same Co(6nm)/ZnTPP(10nm)/Au(50nm) hybrid sample that showed the onset of exchange bias due to Co oxidation (figure 4a, red loop) was transferred to the AFM setup to scan its surface. The transfer of the sample to AFM was done ex-situ and all the measurements are conducted in an open air and under ambient conditions. Figure 11 presents the surface morphology images of the 50nm Au capped hybrid sample scanned at  $1\mu\text{m}^2$  surface area. All 3 images corresponding to different scan zones for the same sample showed similar morphology. It is important to have such kind of mappings, since it allows to check that the observed surface morphology is not the consequence of local defects in a specific zone.

As observed, the surface of the Au capping layer is composed of tightly packed, non-coalesced small circular grains with sizes of the order of  $20 \times 3 \text{ nm}^2$ . These grains form bigger, irregular, and disconnected islands separated by darker contrasts typical of deep cracks between islands. Although the overall surface RMS roughness ( $\sigma_{RMS} = 3.5 \text{ nm}$ ) does not seem too large and suggests that 50nm of Au capping layer should be more than sufficient to protect the samples, these deep cracks might be at the origin of the observed properties of the hybrid samples. To have a better knowledge of the observed cracks, the height profile of the surface morphology was extracted and is represented in the bottom panel of figure 11. The height profiles correspond to the lines that are depicted in the middle image of the figure 11. As observed from the profiles, the cracks extend laterally up to 200nm and are at least

15-16nm deep, within the resolution of the AFM setup. This feature suggests that for thinner Au thicknesses the morphology of the Au layer might be even worse, and the thin Au layer would not be large enough to cover and cap the entire surface properly.

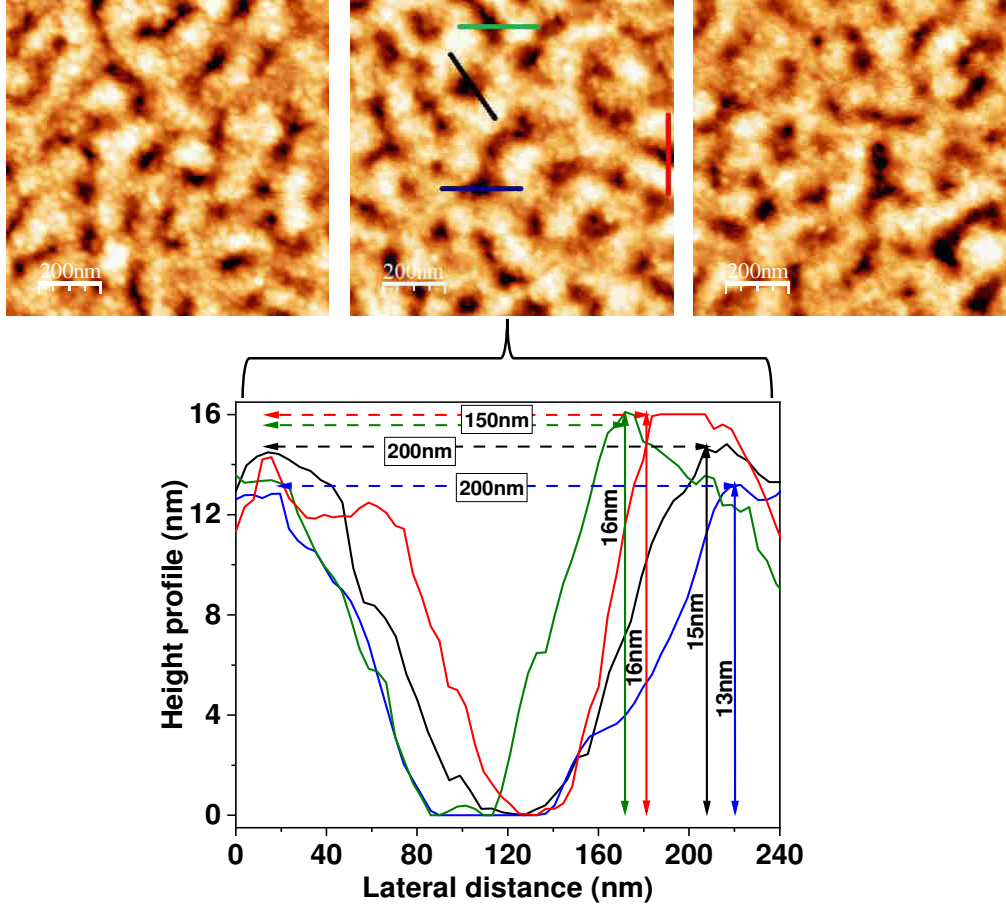


**Figure 11:** Top panel: Surface images of the 50nm Au capping layer on top of Au(25nm)/Co(6nm)/ZnTPP(10nm) stack. The images are acquired with AFM using tapping mode in ambient condition. The 3 images correspond to different zones of the same sample. Scan area is of  $1\mu m^2$ . Bottom panel represents the height profiles of the respective line profiles (color codes on the image) extracted from the middle image.

To check this, the surface of 10nm Au capped Co(6nm)/ZnTPP(10nm) sample has been scanned and its respective images are shown in figure 12. As observed, the surface has non-continuous morphology. It is composed of un-patterned, elongated worm-like disconnected islands with deep cracks in-between. The surface RMS roughness is  $\sigma_{RMS} \approx 7\text{ nm}$ . The height profile in the bottom panel clearly illustrates that these cracks go as deep as 25nm and are extended over 200nm. The results obtained from these



AFM scans might sound bit surprising especially in the case of the thick 50nm capping Au layer, however this could be explained by the structure and morphology of the molecular film underneath, which will be presented in the next section.

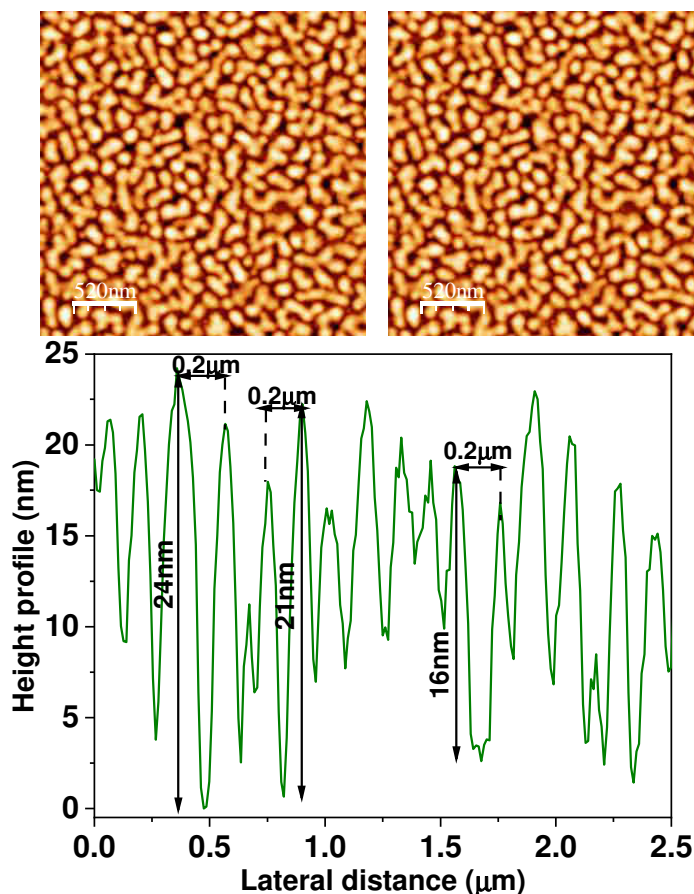


**Figure 12:** Top panel: AFM surface images of the 10nm capping Au layer on top of Au(25nm)/Co(6nm)/ZnTPP(10nm) stack, scanned at 3μm scan size. Bottom panel: The height profile of the surface, extracted from an arbitrary zone. The profile shows the cracks to be 200nm wide and have depth ranges between 16nm to 25nm. Scans are conducted at ambient conditions.

### 7.2.2 The “freshly deposited” and the ageing of the free ZnTPP molecular surface

For studying the free surface molecular films, the organic molecules are deposited in the OMBE chamber of the “Hybrid” system and then taken out of the “Hybrid” system and transferred to an ex-situ AFM setup. Since the AFM scans are all conducted in atmospheric pressure and at room

temperature, they might not really reflect the surface morphology of the molecules during in-situ growth process however it might give some clue about the behavior of the organic films.

When ZnTPP molecules are deposited on top of the metallic Co film the “freshly deposited” ZnTPP molecular film showed a surface morphology with an RMS roughness of 0.8 nm. The roughness is computed as the root mean square average of the scan window displayed in right top panel of figure 13. As seen in the top panel of figure 13, the surface of the free ZnTPP molecular film is composed of mountain-chain-like features separated with crack cliffs which are observed as the darker contrast in the image. These crack openings have depth in the range of 3nm to 5nm. This mountain-like morphology is observed more clearly when looking at the 3D re-construction of the scanned zone.

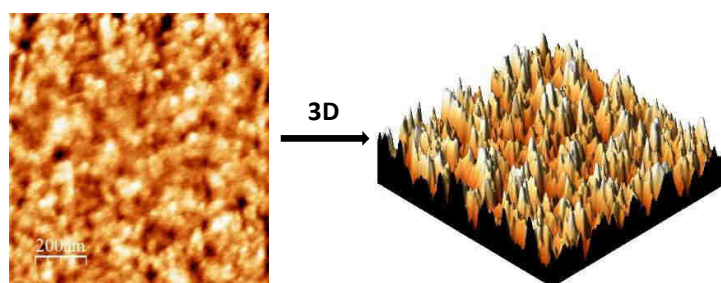


**Figure 13:** The AFM image and the 3D re-construction of the free ZnTPP molecular surface of Au(25nm)/Co(6nm)/ZnTPP(10nm) sample. Scan size is  $1\mu m^2$ .

From the previous chapter it is clear that ageing plays a big role in the properties of the samples, therefore the same molecular layers have been investigated again after several months of air exposure. Ageing can be observed by naked eye.

Figure 14 shows the free surface degraded images of Co/ZnTPP sample captured by the high-resolution camera mounted on the AFM setup. Evidently, there are severe changes in the surface of the ZnTPP molecular film when the samples were kept in contact with air for several months. These modifications are seen in the branch-like features on the sample surface that is present almost all over the surface area. The evolution of the morphology shows molecular aggregation that leads to the leaf-like structures. Going to nanometric scale, these deformed zones were scanned by AFM. Indeed, the AFM images showed exactly the same structural modifications. The surface of ZnTPP has evolved from the morphology described in the previous paragraph to assemblies of molecules, resulting into the branch-like arrangements. These structural defects exhibit heights of 25nm to 30nm on average, whereas the original deposited ZnTPP thickness was 10nm. This feature suggests there is strong molecular aggregations on the surface that leave very wide spacings between one branch structure and the other. An interesting aspect of the image is that underneath the branch-like structures and in-between, no

signature of ZnTPP can be seen. This can be observed in a sharper way when the phase image of the degraded surface is examined. The image shows two different phase contrasts that can be attributed to the assembled ZnTPP molecules (darker contrast) and to the underneath substrate and/or substrate with the Co film (brighter zones). The origin of the ageing process is still not clear. In particular, we do not know if it is air-driven or if it starts during the deposition process itself under vacuum.

In addition to the ageing of the free ZnTPP molecular surface, the free surface of the NiTPP films showed molecular degradations too. These are discussed in the next section.

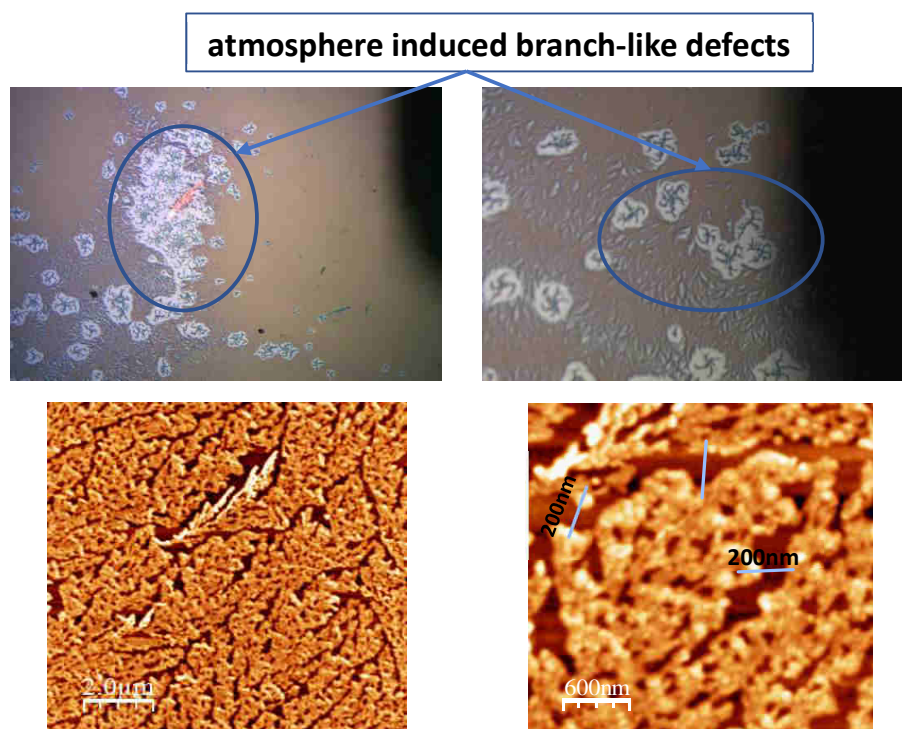


**Figure 14:** Top panel: AFM camera images of the surface defected ZnTPP film of the Au(25nm)/Co(6nm)/ZnTPP(10nm) sample. Branch-like structures are observed and can be differentiated from the intact zones. Bottom panel: AFM scan images at 10 micron (right) and 3 micron (left) of the degraded samples. The spaces between one structure and the other extend up to 200nm (marked by the gray profile on the bottom right image).

### 7.2.3 The “freshly deposited” and the ageing of the free NiTPP molecular surface

The top panel of figure 15 depicts the AFM image of the “freshly deposited” NiTPP molecules on top of the Co film (the AFM scan is conducted in atmospheric pressure and at room temperature). As observed, the surface is composed of potato-like circular grains that are densely packed in a specific pattern leaving no deep crack holes in-between. The average size of these grains is in the order of  $150 \times 1.5 \text{ nm}^2$  and the depth of the holes is in the range of 0.4nm. This depth is much smaller compared to the depth of the crack-holes (4-5nm) observed in the ZnTPP molecular film. Finally, the surface RMS roughness of the NiTPP film is of 0.4nm.

Like in the case of the free ZnTPP molecular film, the free NiTPP molecular film also experienced degradations in its surface morphology when the Co/NiTPP sample was exposed to air for several months. From figure 15 it is clear that the surface morphology of NiTPP shows strong molecule aggregations at the edges. This effect is less strong when closer to the center of the surface. In the central zone of the sample the surface shows almost similar morphology as the surface of the “freshly deposited” sample. Slight modifications were observed where the small circular grains are now merged with one another forming bigger worm-like islands. In this case, the surface morphology is still similar over the surface with densely packed formation. Moving towards the edge, more severe degradations have been observed. The surface scanned over  $1\mu\text{m}^2$  area shows stronger aggregation of molecules that now form much bigger elongated terraces. Each individual island is surprisingly flat with RMS roughness of 0.3nm, but there exist deep cracks (7nm to 8nm deep) in-between. In contrast to these zones, the extreme edge of the surface sample shows the most drastic modifications. In these zones, the surface looks as if the molecules are in their crystal form. Strong accumulation of molecular clusters has been detected with large empty areas in-between the clusters.

In addition, when the empty zones were scanned the AFM images revealed a surface morphology completely different than the surface morphologies which are observed in the AFM images of figure 15 i.e. the molecular surface of the “freshly deposited” samples. The empty zones showed a very small surface roughness with  $\sigma_{RMS} = 0.15\text{nm}$ . These observations suggest that the empty areas are indeed molecular-free zones.

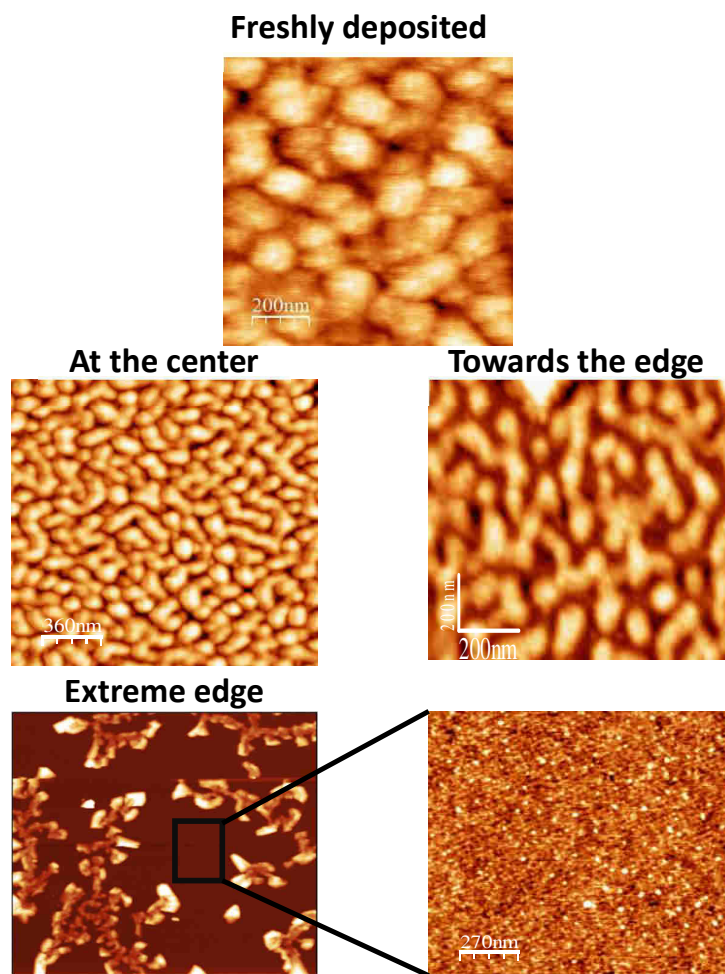


**Figure 15:** Top panel: free surface morphology of NiTPP film of Au(25nm)/Co(6nm)/NiTPP(10nm) sample. Scan size is  $1\mu m^2$ . Middle and bottom panel: AFM scan images of surface degraded Au(25nm)/Co(6nm)/NiTPP(10nm) sample acquired at the center ( $2\mu m^2$ ), towards the edge ( $1\mu m^2$ ) and extreme edge ( $1\mu m^2$ ). Bottom right panel is the image for molecule-free area ( $1\mu m^2$ ), showing a molecule-free surface with  $\sigma_{RMS} = 0.15nm$ .

#### 7.2.4 Partial discussion and conclusion

Even though ZnTPP and NiTPP molecules have similar structures and are prepared on top of a similar Co metallic film with the same molecular deposition rate, the freshly deposited free surface of the NiTPP film showed smoother and more continuous morphology compared to the ZnTPP molecular film. In addition, ZnTPP molecular films showed crack openings with a depth of 5nm which are an order of magnitude higher than the holes observed in the NiTPP surface morphology ( $\approx 0.4nm$ ).

The deep crack openings in the surface of the ZnTPP molecular film could be one of the explanations of why the “freshly deposited” Co/ZnTPP/Au(10nm) hybrid sample showed the onset of exchange bias when measured right after sample preparation whereas the “freshly deposited” Co/NiTPP/Au(10nm) hybrid sample did not. This is because the 5nm deep crack-holes of the ZnTPP molecular film might provide large free space for the counter adatoms, to first fill these voids before making their own continuous metallic layer. Indeed, the surface morphology of the Au capping layer in Co/ZnTPP/Au(10nm) hybrid sample showed a surface morphology that was full of deep holes and cracks with each crack having a depth of 25nm. This means that these cracks are going through the entire sample thickness, since ZnTPP molecular layer is of 10nm and the Co film is 6nm. This kind of deep cracks would simply open a path for atmospheric impurities say oxygen, to migrate and contaminate the Co film even if the sample is exposed to air for a short period of time. As a result, the buried Co film will oxidize with a kinetic that will depend on the capping layer thickness.

In addition, when the free MTPP molecular films were exposed to air their morphology encountered strong modifications over time. For Co/ZnTPP, the surface morphology evolved from mountain chain-like molecular coverage for the “freshly deposited” sample to aggregated branch-like discontinuous structures for the aged sample. For Co/NiTPP, the “freshly deposited” sample had densely packed molecular surface coverage while the aged sample showed very strong degradations and molecular aggregations at the edges of the sample surface. The degradations were much less strong towards the central region of the sample.

Although this study does not prove that the modifications of the film’s morphology is driven by the interaction molecular films with the atmosphere, it is the most probable explanation. This is because MTPP molecules are considered highly reactive agents i.e. they are good donor-acceptor of electrons and can undergo strong redox reactions. Consequently, particles from the atmosphere might interact with the different atomic sites of the molecule. For example, if an oxygen atom is at the metallic site of the molecule its interaction might push the zinc (nickel) metal ion outwards the macrocycle, thus modify the symmetry of ZnTPP (NiTPP) molecules. This modification will result into structural changes in the macrocycle, thus hinder the chemical structure of the molecule. Since molecule-molecule interactions are the dominant forces in the bulk part of the molecular layer, this modification will strongly affect the neighboring molecules too. In another scenario, if the gas particles interact with the aminic nitrogens of the macrocycle the MTPP molecule can experience a saddle-shape deformation. As a result, the phenyl rings of the neighboring molecules will have strong interactions with each other, thus will modify the packing arrangements of the molecules and therefore will cause degradations.

### 7.3 Conclusions

This part described a comprehensive study on the origin of molecular exchange bias in Co/MTPP/Au (M=Co, Ni and Zn) and Co/CoPc/Au hybrid systems. With careful SQUID magnetometer measurements, it was shown that exchange bias is only observed in the “freshly deposited” hybrid samples when the capping layer was too thin (Au 10nm) to protect the samples from oxygen ingress. When the capping layer was increased to larger thickness (50nm), even if the “freshly deposited” samples did not show any hints of exchange bias, the onset of exchange bias always appeared after some time of sample exposure to air. However, when “freshly deposited” hybrid samples were kept under UHV for weeks, the samples did not show any hints of exchange bias when the samples were measured right after removal from the UHV chamber. These features indicate that in Co/MTPP and Co/CoPc hybrid samples, exchange bias is induced by air-driven partial oxidation of the Co film and is not an intrinsic “spinterface” effect.

In addition, AFM showed that the surface morphologies of the thin and thick Au capping layers are discontinuous and are dominated by wide and deep fractured holes with holes depths ranging between 15nm to 25nm. Indeed, it is because of this kind of poor capping morphology that the buried Co films were contaminated and oxidized. XPS showed that the buried Co film is rich in oxygen and its spectra showed profound cobalt oxide edges. These experimental evidences strongly suggest that exchange bias in the investigated FM/organic hybrid systems is not an intrinsic effect but originates from air-driven oxidation of Co films transforming part of the metallic Co into  $CoO_x$ , that is well known to produce the exchange bias effect.

Moreover, this part showed that the organic molecular films have tricky and complicated behavior on top of the FM metallic surfaces. The surface of a “freshly deposited” molecular film evolved from relatively good surface molecular coverage to molecular clusters and aggregates creating disconnected island-like surfaces. The molecular films are not stable and can experience drastic morphological changes with time. These observations further stress the importance of the efficiency of the capping layer since oxygen ingress to the organic film might lead to dramatic modifications into the samples.

In summary, this study ruled out the possibility to achieve molecular exchange bias in FM/organic hybrid systems for two different families of organic molecules: MTPP and MPc. In addition, it showed the complexity of the organic molecules’ structural behavior on top of the FM metallic surfaces. However, the absence of exchange bias does not rule out the fact that other “spinterface” effects, like interface hardening effect or magnetic exchange coupling, can still occur in these hybrid systems.

Finally our observations also suggests that studying the structural properties of these organic molecules via near field techniques might not be completely relevant. Indeed if there is a fast time evolution of the

morphology of the films during the growth process the near field observations might not properly reflect the morphology and the growth of the molecules once embedded into the final stack.

For these reasons, a unique FNR methodology has been developed to probe the physical properties of the FM/organic hybrid heterostructures and interfaces. In addition, TEM was deployed in order to have a direct visualization into the layers and interfaces of these hybrid heterostructures. The next part will be focused on these new contributions.





## **Part IV**

**Probing the physical properties of  
organic hybrid heterostructures and  
of their embedded interfaces with  
FNR and TEM**



## General introduction

Physical properties of magnetic nanostructures and devices strongly depend on the morphological characteristics of their various components. This is especially true and becomes particularly complex in hybrid nanostructures where soft organic molecules are at the vicinity of FM metallic surfaces. One of the main difficulties in studying such organic hybrid nanostructures is the control of the morphology of the organic molecular films on top of the metallic surfaces. This is because organic molecules are light weighted compounds and often show complex structural behavior on the surfaces.

Such complexities have been discussed in the previous part where it was shown that organic molecular films are not stable on the metallic surfaces. The molecular films experienced drastic modifications in their morphology where the initial morphology evolved towards discrete island-like molecular clusters. Moreover, such complex behaviors could mis-lead the interpretation of “spinterface” induced magnetic effects in the organic hybrid heterostructures. For example, in the previous part it was shown that the exchange bias effect in some molecular hybrid systems is nothing but an artefact resulting from the oxidation of the Co film due to the poor efficiency of the capping layers and is not a “spinterface” effect.

We have shown in the previous part that the poor efficiency of the capping layer is, at least partly, attributed to the roughness of the layers. Au buffer layers have been used because of previous works, but even the optimized Au buffer layers are still rather rough. In consequence, the Au buffer layer was replaced by Cu seed layers. In addition, the Au capping layer was changed to Cr encapsulating layer. The surface chromium oxide is expected to act as an oxygen diffusion barrier. The measurements showed that the hybrid samples with Cr capping layers were well protected from extrinsic contaminants within the time scale of the measurements. This is discussed in detail in the upcoming chapter.

To study the physical properties of these optimized organic hybrid heterostructures two different experimental techniques were deployed to investigate the morphology of the organic layers embedded in-between FM electrodes. This did require the development of original experimental methodologies. The first technique that has been used is ferromagnetic nuclear resonance (FNR i.e. NMR in ferromagnets) spectroscopy technique while the second is transmission electron microscopy (TEM) technique.

FNR is a relatively unknown spectroscopy technique. Nevertheless, through time it has been shown that FNR can be a very efficient tool to study the structure and the morphology of interfaces in thin films [124,125,126,127] and multilayers [128,129,130,131,132]. Because of the specific problematics encountered in this work a new FNR methodology has been developed that allowed to probe the magnetic, structural, and chemical properties of the organic hybrid systems. FNR allowed to study the continuity and the thickness dependent morphology of organic molecules embedded in-between FM metallic electrodes. More importantly, FNR gave crucial insights into the morphology of the single

hybrid interfaces buried in the organic heterostructures. It is the first time that such study has been undertaken.

Complimentary to FNR, and despite the difficulties accompanied with TEM sample preparation, TEM has been successfully applied to the study of the organic hybrid heterostructures. TEM allowed to have local insights into the structure and the chemical properties of the layers and more importantly of the organic/metallic hybrid interfaces of the organic heterostructures.

The first chapter of this part will describe how the hybrid heterostructures were optimized to make them proper for macroscopic measurements. Chapters 9 and 10 will discuss in detail the developed FNR methodology and explain how it can be applied to organic hybrid heterostructures. Finally, the last chapter will display the TEM results and show their contribution to this thesis work.

---

## Chapter 8: Optimization of the Heterostructures

Before proceeding with the work it was necessary to optimize the layers within the stack to obtain better defined organic heterostructures. Consequently, the buffer and capping layers of the heterostructures have been modified.

### 8.1 Optimization of the buffer layer

The Au buffer layer has been already optimized by changing its deposition technique from thermal evaporation to electron beam deposition technique. Nevertheless, the buffer layer was still not satisfactory. This is because the surface morphology of the Au(e-beam) buffer layer (figure 1a) was formed of flat terrace-like islands that were separated by deep cracks. Such surface morphology would be satisfactory for near field measurements where microscopy techniques are used to study single molecules but is not suitable for the macroscopic measurement-based investigation of our work.

In order to obtain a buffer surface that is flatter at large length scales as required for macroscopic measurements, the Au buffer layer has been substituted by 25nm of copper (Cu) layer prepared via DC sputtering deposition technique. The surface morphology of a Cu seed layer is depicted in figure 1b. It is composed of compact and small grains leading to continuous and crack-hole free morphology. The surface RMS roughness is of  $\sigma_{RMS} = 0.2 \text{ nm}$ .

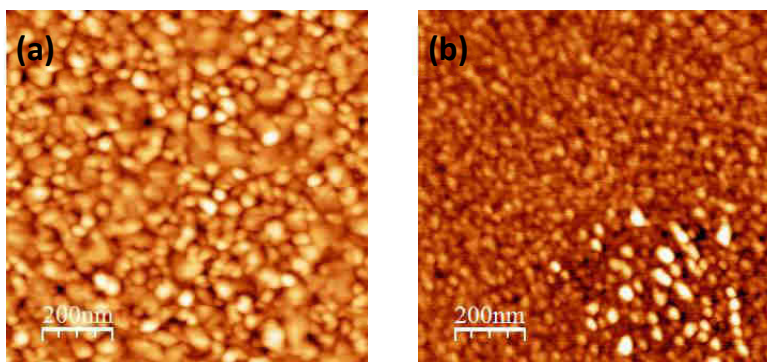


**Figure 1:** Surface morphology of (a) 25nm of Au(e-beam) seed layer (b) 25nm of Cu buffer layer deposited on Si/SiO<sub>2</sub> substrate. Cu buffer layer shows smoother and more uniform surface morphology compared to Au layer.

The difference between Au buffer layers and the Cu seed layer is observed more clearly in the height profile of their respective surfaces in figure 2. As seen in the height profiles, the blue profile of the Cu seed layer is much more continuous over large length scale compared to the Au buffer layers.

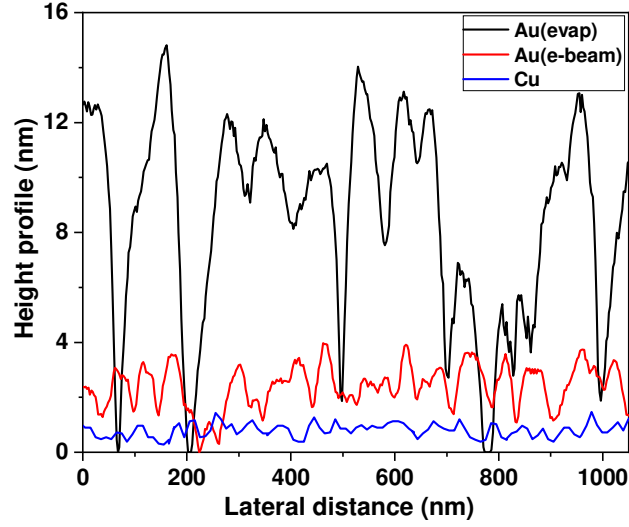


**Figure 2:** The height profiles of the surface for the different buffer layers. Black : Si/SiO<sub>2</sub>/Au(evap), Red : Si/SiO<sub>2</sub>/Au(e-beam), and Blue : Si/SiO<sub>2</sub>/Cu. The thickness of the buffer layers is 25nm for all samples

After optimizing the buffer layer, the capping layer has been also modified. This is discussed in the next section.

## 8.2 Optimization of the capping layer

As shown in the chapters of part III, capping the hybrid samples with Au layer is not efficient. To solve this problem, the top-most Au layer has been replaced by chromium (Cr) which was deposited using DC sputtering technique.

To test the efficiency of this Cr encapsulating layer, a new heterostructure has been prepared with the same stack as the previous samples but capped with 100nm of Cr: Si/SiO<sub>2</sub>/Au(25nm)/Co(6nm)/ZnTPP(10nm)/Cr(100nm). The magnetic response of this sample has been tracked over long period of time and its magnetization loop was measured several times starting from its “freshly deposited” state. Figure 3 represents the magnetic hysteresis loops of the 100nm Cr capped Au/Co/ZnTPP hybrid sample. As observed, the “freshly deposited” sample shows perfectly hysteretic response with no hints of exchange bias. Even measuring the same sample for several times over a 3 months period the heterostructure showed no ageing.

During this period, the sample was kept in the desiccator which was opened and closed regularly on working days. Therefore, the sample has been exposed to air like any other previous sample of this work. The fact that no exchange bias has been observed in the Cr capped sample is another experimental evidence that exchange bias in these investigated organic hybrid systems is not an intrinsic “spinterface” effect.

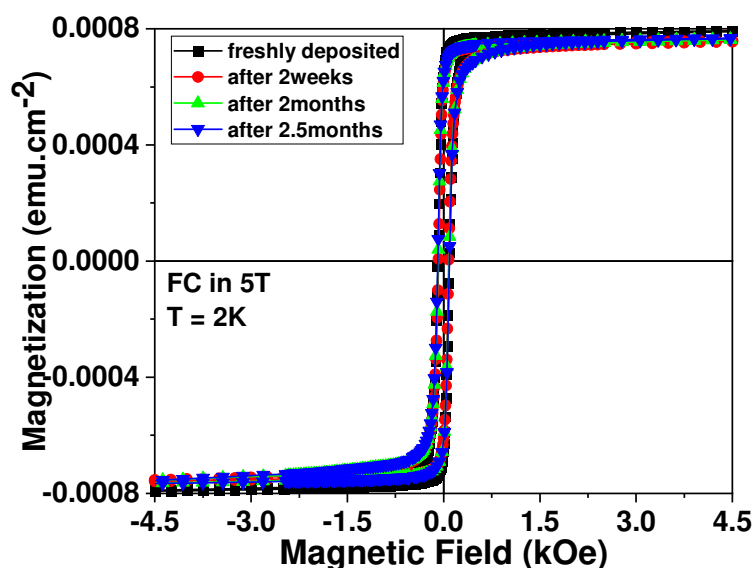


**Figure 3:** Magnetization loops of Au(25nm)/Co(6nm)/ZnTPP(10nm)/Cr(100nm) sample. Same sample has been measured 4 times, over a period of 80 days. Between each measurement, sample is kept in a desiccator. All measurements are done at 2K after field cooling in +5T external magnetic field.

### 8.3 Partial conclusion

Cu buffer layer showed continuous and flat surfaces over the larger length scale while the hybrid samples capped with Cr layers showed no signs of aging for relatively long period of time. Replacing the buffer layer with Cu and the capping layer with Cr led to better-controlled organic hybrid heterostructures which are much more suitable for macroscopic measurement. Using these optimized layers, new hybrid heterostructures with specific architectures have been built to implement the newly developed FNR methodology. The results are discussed in detail in the next chapters.



## Chapter 9: The FNR approach in organic/metallic heterostructures

Investigations conducted on organic/metallic heterostructures have proven to be difficult. This is because the fabrication of organic hybrid heterostructures is not straight forward since organic molecules are soft and light weighted compounds that more often show complex structural behavior on the metallic surfaces. In addition, the organic/metal interface shows structural and chemical defects that could complicate the comprehension of the physical and transport properties of the organic hybrid heterostructures. To properly understand the physical properties of these hybrid heterostructures it was essential to develop a new approach which would allow to conduct the necessary investigations. In consequence, a new FNR methodology has been developed. This chapter introduces and elaborates on the newly developed FNR methodology.

### 9.1 Probing the continuity of molecular films embedded in-between Co and Fe electrodes

Organic/FM hybrid heterostructures can be considered as a basic building block for an organic spintronic device. There is extensive work performed to better understand their physical properties. A key factor essential to reliable experiments is to first ascertain that the organic molecules form continuous films on top of the FM electrodes and once built, prevent the migration of metallic atoms between the FM electrodes embedding the organic molecular film. Here after, this section will explain the original FNR methodology that has been developed to probe the continuity and the morphology of organic molecular films.

#### 9.1.1 Results and discussion

The method is based on the use of two different FM layers on each side of the organic molecular films: Co and Fe. Not only such architecture allows to get an original insight into the morphology and the structure of the hybrid organic heterostructures, but Co and Fe films are also commonly used as FM metallic electrodes for spintronic devices. Therefore, the study of FM<sub>1</sub>/molecular film/FM<sub>2</sub> (FM<sub>1</sub> or FM<sub>2</sub> = Co or Fe) structures could be very interesting for the progress of future devices.

The developed FNR methodology is based on the sensitivity of the Co FNR resonance frequency to its nearest neighbour (NN) cell chemical environment. Indeed, as explained in the experimental section when non-ferromagnetic elements are included in the Co NN cell, the Co resonance frequency is lowered compared to its resonance frequency when surrounded by other Co atoms only [112,133].

In contrast, when Fe atoms are included in the Co NN cell, the Co resonance frequency increases compared to its resonance frequency when surrounded by other Co atoms only [112,133]. Following this logic, figure 4 represents the FNR spectrum of a Cu/Co/Fe sample that can be divided into three radiofrequency ranges. First, the bulk part of the probed metallic Co brings its contribution to the radiofrequency range between 200 MHz and 240 MHz. In this range, the 12 NN of the probed Co atoms are surrounded by other Co atoms only. Moreover, at 216 MHz a main peak is observed that corresponds to bulk Co in face centered cubic (fcc) crystal structure. In addition to the main peak, set of shoulder peaks are observed at 220 MHz and 225 MHz. These peaks correspond to Co in hexagonal closed pack (hcp) structure and its associated stacking faults induced in pure fcc Co. The second range is for the Cu/Co interfacial region which is found at the low radiofrequency range ( $< 200$  MHz) while the third range corresponds to Co/Fe interfacial region and is found at high radiofrequency range ( $> 240$  MHz).

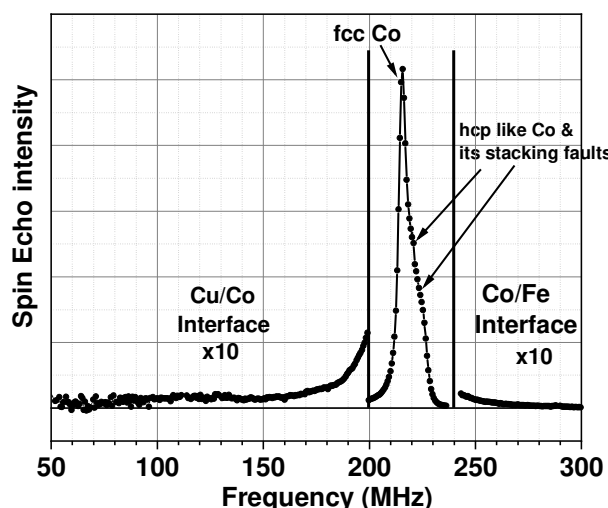


**Figure 4:** FNR spectrum for Cu/Co/Fe reference sample. The spectrum shows three distinct regions separated by the solid lines: the low frequency intensity ( $< 200$  MHz) is attributed to the Cu/Co interfacial contributions, the central region ( $200 < \text{frequency (MHz)} < 240$ ) corresponds to metallic Co atoms inside the Co film, and the high frequency intensity ( $> 240$  MHz) originates from the Co/Fe interface. Spin echo intensities for low and high frequency ranges are magnified 10 times (x10) for clarity. Measurements are conducted at 2K.

Now, when organic molecular films (or any other kind of films: metallic, insulator, semiconductor, etc.) are inserted in-between the Co and Fe films it is straight forward to probe whether the molecular film is continuous and/or if Co or Fe atoms migrate through the organic layer. Indeed, once the molecular film is pin-hole free and builds up a continuous layer it will isolate completely the two FM electrodes thus the high radiofrequency ( $> 240$  MHz) contributions in the FNR spectra will disappear.

This method has been implemented with ZnTPP thickness dependent samples that have the following structure: Cu(25nm)/Co(6nm)/ZnTPP( $t$  in ML)/Fe(30nm)/Cr(100nm) with  $1 \text{ ML} \leq \text{ZnTPP}(t) \leq 60 \text{ ML}$ ;  $1 \text{ ML} = 0.35 \text{ nm}$ . The spectra of these samples are presented in figure 5 and are compared to the Cu(25nm)/Co(6nm)/Fe(30nm) reference sample. In the reference sample, no ZnTPP layer is present in-between Co and Fe electrodes therefore Co and Fe layers are completely in contact with each other.

As expected, in figure 5 the Co/Fe interfacial contributions at high radiofrequency ( $> 240 \text{ MHz}$ ) range decrease with the increase in ZnTPP thickness and eventually vanish for 15 ML of ZnTPP. This means that the ZnTPP molecular film needs at least 15 ML to form continuous and pin-hole free organic layer. It is only after the 15<sup>th</sup> ML of ZnTPP that the Co and Fe electrodes would be fully isolated.

In contrast to the Co/Fe contributions at high radiofrequency range, the low radiofrequency ( $< 200 \text{ MHz}$ ) range contributions increase with the increase in ZnTPP thickness. This increase can be attributed to the additional contribution of Co/ZnTPP hybrid interface to the Cu/Co interfacial signal. This feature suggests that the hybrid interfacial contribution can be found at the low radiofrequency range of the FNR spectrum. This will be further discussed in the next chapter.

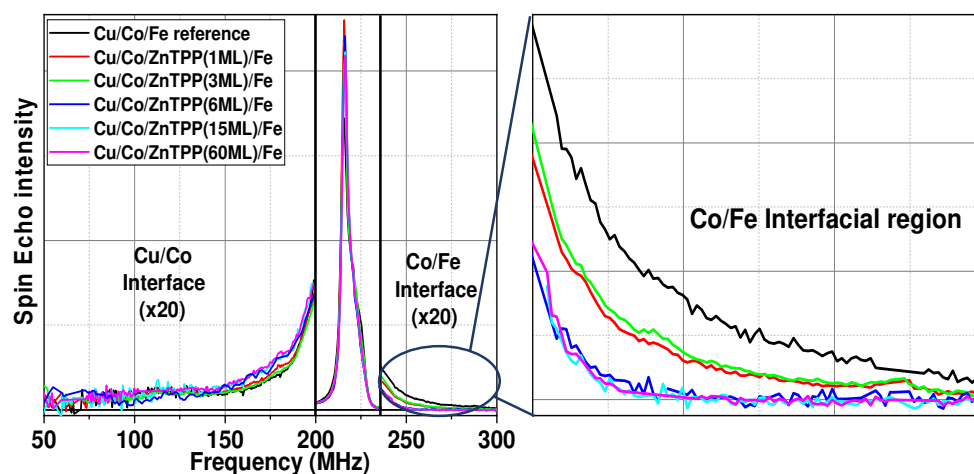


**Figure 5:** Evolution of FNR spectra with increasing thickness of the ZnTPP layers. The high frequency contributions ( $> 240 \text{ MHz}$ ) decrease with the increase in ZnTPP thickness (1 to 60 ML) and vanish from 15 ML and above i.e. no more Fe in contact with Co film. Low frequency ( $< 200 \text{ MHz}$ ) interfacial signature increases with the increase in ZnTPP thickness. Low and high frequency range are magnified by a factor of 20 (x20). Right panel is the re-scaled region of high frequency range for Co/Fe interfacial region. Measurements are done at 2K.

Following the same methodology, the order of the FM electrodes has been reversed to study the continuity of the ZnTPP molecular layers when deposited on top of the Fe films. In this case, the heterostructure has Fe as bottom electrode whereas Co is deposited on top of ZnTPP and serves as the top FM electrode: Cu(25nm)/Fe(30nm)/ZnTPP( $t$  in ML)/Co(6nm)/Cr(100nm) with  $1 \text{ ML} \ll \text{ZnTPP}(t) \ll 15 \text{ ML}$ . Their respective spectra are shown in figure 6 and are compared to the Cu/Co/Fe reference sample. For this case, only the high radiofrequency range is represented.

As observed, the Fe/Co interfacial contributions at high radiofrequency ( $> 240 \text{ MHz}$ ) range show similar behavior as in figure 5 for the previous heterostructures. The FNR spectral intensity in this range decreases as the ZnTPP thickness increases and eventually vanishes above 15 ML of ZnTPP. This feature confirms the validity of the interpretation explained above and shows the effectiveness of the FNR methodology.

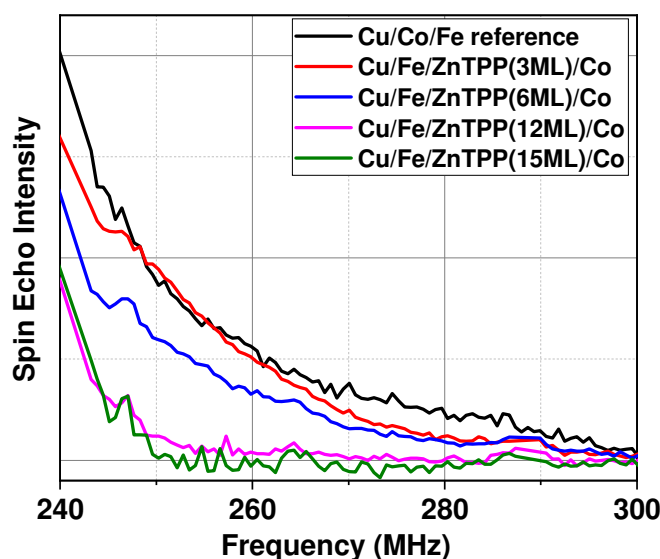


**Figure 6:** Evolution of FNR spectra with increasing thickness of the ZnTPP layers on Fe. The high radiofrequency contributions ( $> 240 \text{ MHz}$ ) decrease with the increase in ZnTPP thickness and vanish at 15 ML. Only high radiofrequency spectral range is represented in the plot. Measurements are at 2K.

However, when comparing the high radiofrequency ranges of the two FNR spectra of figure 5 and 6 one can notice that the detailed spectral behavior is not the same for the two heterostructures. For example, when 3ML of ZnTPP is deposited on top of the Fe electrode (figure 6, red spectrum) its high radiofrequency range shows very small change in the spectral intensity when compared to the Cu/Co/Fe reference sample. Since the high radiofrequency spectral range reflects the remaining Co/Fe interface,

this means that the fraction of Fe electrode in contact with the Co electrode is almost the same as in the Cu/Co/Fe reference sample. On the contrary, when 3ML of ZnTPP is deposited on top of the Co electrode (figure 5, green spectrum) the spectral intensity already decreases significantly when compared to the spectrum of Cu/Co/Fe reference sample. These observed trends suggest that ZnTPP molecules behave very differently when deposited on Co and Fe electrodes. Therefore, one can infer that ZnTPP molecules might have different thickness dependent morphologies depending on the nature of the underneath FM electrode.

### 9.1.2 Quantitative analysis

As illustrated above, ZnTPP molecules behave differently when adsorbed on Co and Fe electrodes. To obtain more quantitative analyses of their behaviour, the coverage ratio (equation (1)) of ZnTPP molecular layers was estimated from the integral intensities of the high radiofrequency range of the FNR spectra.

$$C = \left(1 - \frac{Int_{Co/ZnTPP/Fe}}{Int_{Co/Fe}}\right) \times 100 \quad (1)$$

Where:

- $C$  is the coverage ratio in percentile (%).
- $Int_{Co/ZnTPP/Fe}$  is the integral intensity of the spectra (above 240 MHz) for the Cu/Co(6nm)/ZnTPP( $t$  in ML)/Fe(30nm) and Cu/Co(3nm)/ZnTPP( $t$  in ML)/Fe(30nm) samples.
- $Int_{Co/Fe}$  is the integral intensity of the spectrum (above 240 MHz) for the Cu/Co/Fe reference sample.

The ratio  $\frac{Int_{Co/ZnTPP/Fe}}{Int_{Co/Fe}}$  simply represents the fraction of Co interface area that is in contact with Fe atoms. It is identified as the fraction of Co interface that is not covered by ZnTPP. Subtracting this value from unity it would result into the molecular coverage ratio. The evolution of ZnTPP coverage ratio with the increase in molecular thickness is represented in figure 7. When ZnTPP is deposited on top of the Co films the coverage ratio increases rapidly with the first adsorbed monolayer of ZnTPP. After the first monolayer, the coverage increases much more slowly and shows an asymptotic behaviour that reaches close to full coverage at the 15<sup>th</sup> ML of ZnTPP (figure 7, back symbols). On the contrary, when ZnTPP molecules are deposited on top of Fe film, the molecular coverage ratio increases linearly with the deposited ZnTPP thickness and from a linear fit it shows 14 ML of ZnTPP as the threshold thickness for full surface coverage. These analyses show that the thickness of organic layer required to completely separate the two electrode is quite large: of the order of 14 to 15 ML for both kinds of underlayer.

However, the quantitative analysis also shows that the thickness evolution of the morphology of ZnTPP molecular layers strongly depends on the nature of the underneath FM metallic layer.

To obtain better insights into the evolution of the coverage ratios hence of the morphology of the molecular films one should consider the stacking of the ZnTPP layers on top of the FM metallic layers.

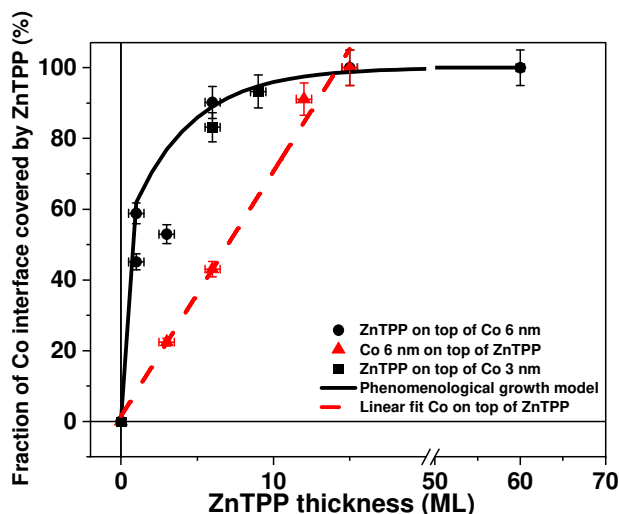


**Figure 7:** The evolution of ZnTPP molecular coverage on top of Co and Fe metallic surfaces, with the increase in ZnTPP thickness. Black square and circle symbols represent the experimental data of ZnTPP coverage ratio when deposited on top of Co. Black line is the fit using phenomenological growth model equation (2) with a filling factor  $f$  of 20%. Red triangles represent ZnTPP coverage ratio when deposited on top of Fe. Red dashed line is the linear fitting of ZnTPP coverage rate on Fe. The coverage rate increase is of 7%.

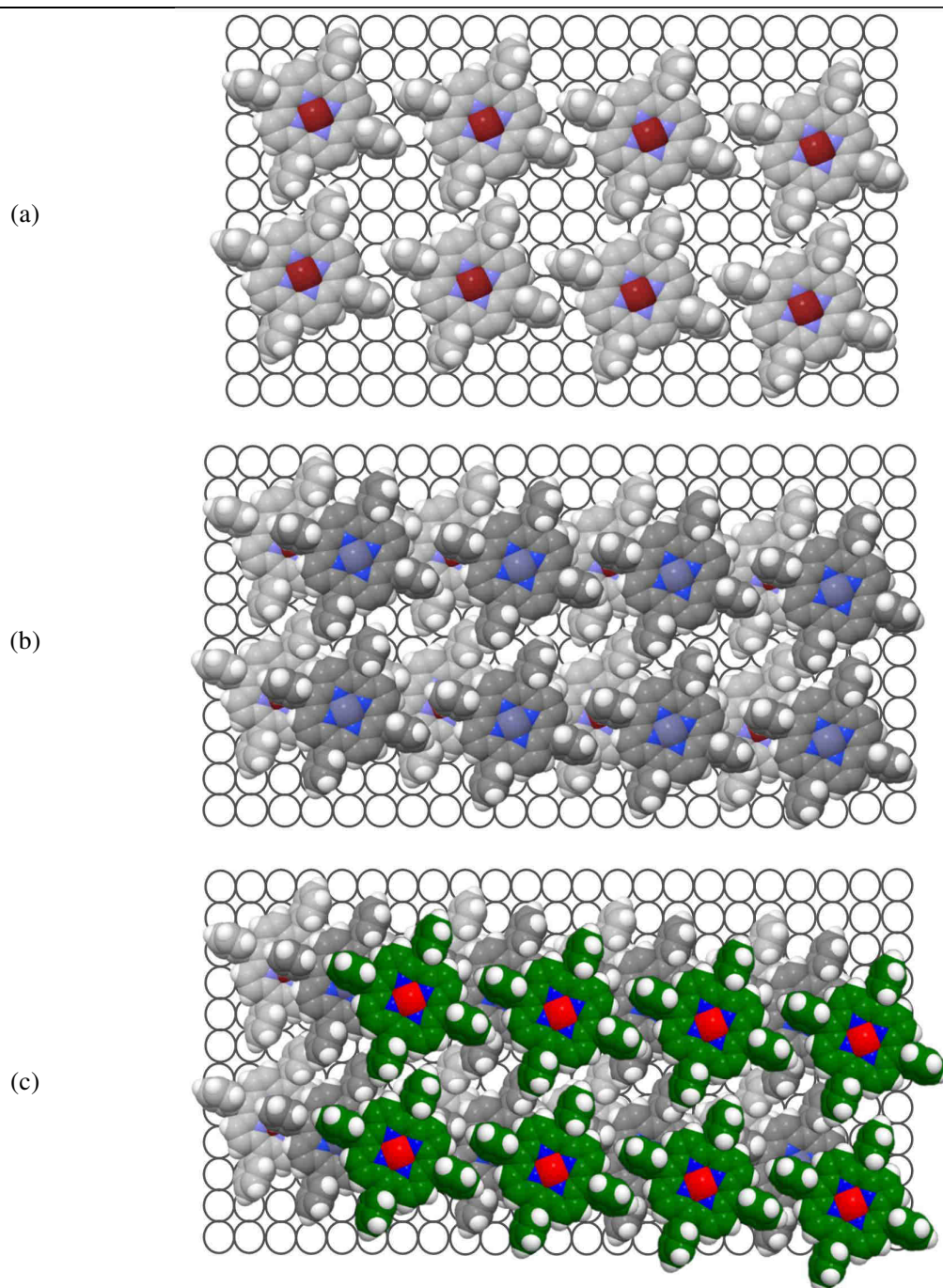
## 9.2. Phenomenological analysis: Growth models

Figure 8a represents a schematic view of molecular arrangement for the first monolayer of ZnTPP adsorbed on a metallic surface. For this scheme, several points are considered which can be listed as:

- (i) Square metal surface, for simplicity.
- (ii) The four phenyl rings are perpendicular to the porphyrin plane hence perpendicular to the surface.
- (iii) The arrangement of the ZnTPP molecules in the monolayers is set in a way that the molecules respect the maximum  $\pi$ -  $\pi$  stacking (neighbouring phenyl groups of the molecule overlap in geometry and lead to parallel phenyl geometry).
- (iv) Small deviations from the crystal structure of ZnTPP, as the molecules are in contact with metallic surface (consequence of weak van der Waals forces).

As observed, one complete monolayer of ZnTPP leaves a large number of metallic atoms (white circles) uncovered. From such a scheme, the area of the uncovered metallic atoms is estimated to be around 38%. In other words, the first monolayer of ZnTPP even if it is ideally adsorbed on the surface, covers only about 62% of the metallic surface. The 62% coverage deduced from the scheme of figure 8a is close to that obtained in the analysis of the coverage ratio in figure 7 for the smallest thickness of ZnTPP deposited on top of the Co film i.e. 1ML of ZnTPP adsorbed on the Co electrode. This suggests that ZnTPP molecules on top of Co film, at least for the first few molecular layers have a layered morphology. On the contrary, when ZnTPP molecules are deposited on top of Fe films, the 1<sup>st</sup> ML of ZnTPP would cover only about 8% of the Fe surface. Then, the coverage ratio increases linearly at a small rate of 7% for the additional coverage per ZnTPP molecular layer. This observation is not compatible with a layered morphology and suggests that when ZnTPP molecules are deposited on top of the Fe electrode the molecules form islands from the initial stages of growth.

On the Co film, once the first molecular layer of ZnTPP is completed the remaining number of voids after the deposition of the subsequent molecular layers will depend on how these molecular layers stack on the first molecular layer. The stackings depicted in figure 8b and 8c represent the additional second and third monolayers of ZnTPP, respectively. The subsequent monolayers are modelled so that ZnTPP molecules respect the offset typically observed in J-aggregate arrangements [134,135]. Consequently, if ZnTPP layers follow this kind of stacking the coverage ratio would increase to 85% with the second monolayer and to almost 100% with the third. These computed values are already larger than that determined experimentally in figure 7 and implies that already for the third layer of ZnTPP, bottom and top electrodes would be fully separated. This is obviously not the case experimentally because, as discussed in the analysis of figure 7 at least 14-15 ML of ZnTPP molecules are required to separate the electrodes. All these observations and analyses suggest that on a Co film the morphology of the ZnTPP films does not show a purely layered stacking when the thickness of the molecule is increased above 1ML. It is most likely that after the 1<sup>st</sup> molecular layer, the morphology of the subsequent molecular layers will exhibit island kind of growth.



**Figure 8:** Proposed schemes for the ZnTPP morphology on a metallic surface. (a) 1ML of ZnTPP (light grey molecules) on top of a square metallic lattice. The ratio of metallic atoms (white circles) which are covered by the molecules is estimated to be of the order of 62%. (b) stacking of the 2<sup>nd</sup> ML (dark grey molecules) which leads to 85% surface coverage. (c) stacking of the 3<sup>rd</sup> ML (green molecules) result in almost full coverage of the metallic surface. In these schemes, the molecules are arranged as such they respect the maximum  $\pi$ - $\pi$  stacking and the offset for a typical J-aggregate.



Considering the complexity of the investigated system, a phenomenological approach has been developed to describe the morphology of the ZnTPP molecules on the Co film. In this approach, it is considered that each subsequent ZnTPP monolayer decreases the number of voids by a constant ratio using the following formula:

$$C_{phenom}(n) = (1 - 0.38 \times (1 - f)^{n-1}) \times 100 ; n > 1 \quad (2)$$

Where:

- $C_{phenom}(n)$  is the coverage ratio in (%) as determined by the phenomenological model.
- 0.38 is the fraction of voids remaining on top of the metallic surface after completion of the first ZnTPP layer, as estimated from figure 7a.
- $f$  is the fraction of voids that are filled in each subsequent layer. It is the only variable in the model.
- $n$  is the number of deposited layers.

Using this formula, the closest simulation has been obtained by considering that the fraction of voids filled with each subsequent ZnTPP monolayer is equal to 0.2 ( $f=0.2$ ). It means that each additional ZnTPP layer will only cover 20% of the remaining empty interface. This simulation is plotted in figure 7 (solid black line) and shows a good agreement with the experimental data. In this model, the full separation of the two FM electrodes is only reached asymptotically. For a deposited ZnTPP thickness of 15 ML, the coverage ratio would reach 98% of the surface of the underlayer. However, this additional coverage ratio of 20% is surprisingly low and can hardly be explained only by the onset of an island kind of morphology after the completion of the first ZnTPP molecular layer. Therefore, it is most likely that the migration of Co and Fe atoms through the organic layers does also take place. Most likely, it is also the case when ZnTPP is deposited on top of the Fe film and would explain the small slope (7%) of the coverage ratio with the increasing thickness of ZnTPP.

### 9.3 Partial conclusion

With an original FNR methodology it was demonstrated that at least 14 molecular layers of ZnTPP are required to obtain organic heterostructures with continuous, pin-hole free molecular layers. In addition, the quantitative analysis of the FNR spectra showed that ZnTPP has distinct thickness dependent morphology when deposited on Fe and on Co films. On Co films, ZnTPP has a layered morphology for the 1<sup>st</sup> adsorbed molecular layer, followed by the onset of island-like morphology in the subsequent molecular layers. On Fe films, the molecule showed island type of morphology from its initial state. The slow increase in the coverage ratios also suggests that atomic diffusion between the metallic electrodes through the organic layers takes place.

After studying the morphology of organic molecular films embedded between FM electrodes, the FNR methodology has been further expanded to specifically probe the morphological properties of the hybrid interfaces. These will be discussed in the next chapter.

---

## Chapter 10: Probing the interfaces of hybrid heterostructures with FNR

Exchange bias, tunnelling magnetoresistance, magnetic hardening, all these phenomena are mainly (if not completely) governed by the mechanisms occurring at the interfaces. Consequently, the comprehension of the nature of the hybrid metallic-organic interfaces are particularly important. Therefore, it is of crucial importance to identify and understand the type of chemical interactions and bonds that organic molecules experience when adsorbed on FM metallic electrodes. This chapter illustrates in detail how the developed FNR methodology has been applied to study the morphology of the hybrid interfaces when organic molecules are in proximity to FM metallic Co films.

### 10.1 Hybrid interfaces embedded within organic/Co/organic heterostructure

From the above discussions, it is clear that FNR can be an efficient tool to probe the continuity and the morphology of organic molecules grown in-between FM electrodes. The fact that no high radiofrequency contribution was observed anymore once the Co and Fe layers are fully separated by the organic layers suggest that the Co/ZnTPP interface contributions are situated at low radiofrequencies compared to the bulk Co resonance frequency. The absence of high radiofrequency contributions up to 300 MHz is clear from the FNR spectra shown above but it has also been checked up to 600 MHz and no FNR contribution was observed.

In the FNR spectra of the previous chapter it has been observed that the low radiofrequency spectral intensity increases with the increase of the ZnTPP coverage. However, the analysis of the spectral intensity of the low radiofrequency range was not possible as it was the result of the superposition of two interfacial contributions: one resulting from Cu/Co interface which is well known to be found at the low radiofrequency range and one resulting from the Co/organic hybrid interface which caused the additional increase in the spectral intensity.

Therefore, in search for a clear fingerprint of the hybrid Co/ZnTPP interface signal in the FNR spectra, a new series of samples have been built in which the Co films are sandwiched between continuous organic molecular films. In such case, the heterostructures contain two Co/organic interfaces, maximizing the Co/ZnTPP interfacial signal in the FNR spectrum. The sample's architecture has the following stack:

- Cu(25nm)/Fe(30nm)/ZnTPP(20ML)/Co(*t* in nm)/ZnTPP(20ML)/Fe(30nm); with Co thickness *t* = 2, 3, 4, 5 and 6 nanometers.

The molecular layers are chosen to be 20ML ( $\approx 7$ nm) as this thickness exceeds by 5ML the threshold thickness for obtaining continuous ZnTPP films which is 15 ML as discussed in the above section.

Depositing 20ML of ZnTPP should ensure the continuity of the molecular films and guarantee their pin-hole free morphology. It should also prevent the migration of the metallic atoms through the organic films. However, to ascertain the continuity of the organic films additional Fe layers have been added in the stack. As explained in the previous chapter any organic layer discontinuity would be revealed by high radiofrequency ( $> 240$  MHz) contribution in the FNR spectra. No high radiofrequency contribution has been observed for any of the samples studied in this chapter. The only interfacial contribution that is expected in such samples is therefore the low radiofrequency ( $< 200$  MHz) spectral line resulting from the contribution of the hybrid interfaces in the ZnTPP/Co/ZnTPP region.

Finally, the samples are chosen to be dependent on the Co thickness with the thickness ranging from 2nm to 6nm. From previous works of FNR in inorganic systems, it has been already demonstrated that studying a series of samples that are dependent on the Co thickness is a very efficient methodology to determine the interface contributions within the FNR spectra [136,137,138]. Consequently, the same methodology has been adapted in organic hybrid systems.

### 10.1.1 Results and discussion

Figure 9 represents the FNR spectra for Cu/Fe/ZnTPP(20ML)/Co(*t in nm*)/ZnTPP(20ML)/Fe/Cr hybrid heterostructures. First, no FNR signal was observed at radiofrequency range above 250 MHz and up to 600 MHz which confirms that indeed the 20 ML of ZnTPP are thick enough to ensure the continuity of the molecular films and also confirms that no Co/ZnTPP interfacial contribution is found in the high radiofrequency range.

In figure 9, all FNR spectra are normalized to the total surface area of the samples. With this normalization procedure the contributions in the FNR spectral range resulting from the ZnTPP/Co and Co/ZnTPP interfaces should show no evolution once the building up of the interfaces is completed. Only the contribution of the bulk part of the Co film, i.e. Co situated far from the interfaces, will increase with the increase in the deposited Co thickness. As observed in figure 9, the shape of the main FNR line becomes sharper and the intensity increases with the deposited thickness of Co. As the Co thickness increases the position of the main line is gradually refined and reaches a position around 224 MHz close to that expected for the Co atoms in an hcp-like crystal structure having a magnetization axis perpendicular to the c-axis of the hcp crystal cell ([0001] growth direction of Co film with in-plane easy magnetisation direction).

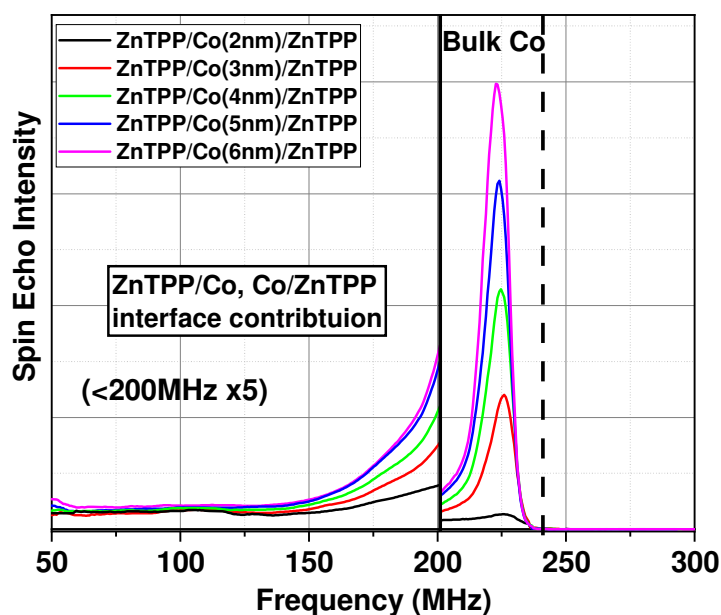


**Figure 9:** Evolution of FNR spectra for Cu/Fe/ZnTPP(20ML)/Co ( $t$  in nm)/ZnTPP(20ML)/Fe samples with the increase of Co thickness from 2nm to 6 nm. Measurements are conducted at 1.8K, sample surface area is of  $3\text{cm}^2$ , spectral intensity below 200 MHz are magnified by a factor of 5 (x5).

The low radiofrequency ( $< 200$  MHz) spectral range is attributed to the interfacial contributions originating from Co/ZnTPP and ZnTPP/Co hybrid interfaces. This low radiofrequency range does not show any well-defined spectral shape that could be ascribed to a specific Co environment near the Co/organic hybrid interfaces. This feature suggests that there are no strong chemical bonds between the interfacial Co atoms and the ZnTPP molecules at the interface. It is most likely that the interactions at the Co/ZnTPP and ZnTPP/Co hybrid interfaces are governed by weak van der Waals (vdW) forces. A closer look at the low radiofrequency region of the spectra revealed that below 120 MHz all spectra are superimposed (within the experimental error bars) but above 120 MHz it is not the case. Between 120 MHz and 200 MHz the spectral lines showed, surprisingly, an increase in their intensities up to Co thickness of 5nm. This is surprising because it shows that even up to 5nm of deposited Co thickness; Co still contributes to building up the hybrid interfaces. This shows a complex interface behaviour and suggests that interface regions are rather extended.

**10.1.2 Analysis of FNR integral intensities**

From the above discussions it was inferred that the Co/organic hybrid interfaces show rather extended morphology. When the interfaces are strongly intermixed, it is not unusual for the interfaces to contain some fraction of Co atoms that are no longer ferromagnetic. These Co atoms would vanish from the FNR spectra. To probe the presence of non-ferromagnetic Co atoms, the total intensity of the FNR spectra as a function of deposited Co thickness is represented in Figure 10. As expected, since the spectra intensity is normalized to the sample surface area the total integral intensity of the FNR spectra increases linearly with the increase in the deposited Co thickness (Figure 10, black symbol). However, the performed linear fit (Figure 10, black solid line) clearly shows that the total FNR intensity does not pass through the origin when extrapolated to zero Co thickness. From the intercept of the fit of the total intensity, one can deduce the amount of Co that is no longer ferromagnetic. About 1.4nm of Co are not ferromagnetic at 1.8 K (temperature of measurements) and hence not detected in the FNR spectra. This suggests that a significant number of Co atoms have diffused deep into the ZnTPP molecular films and take part in forming the two hybrid interfaces.

Figure 10 also represents the plot of the spectra integral intensity below 200 MHz i.e. the spectra integral intensities corresponding to the interfacial region. Since the spectra are normalized to the surface area of the sample, this integral should reach a constant value once the building up of the interfaces is completed. This is obviously not the case in these samples, because the integral intensity continues to increase up to 5nm of Co. Only the samples with 5nm and 6nm of Co thickness show similar intensities. This is of course reflected in the FNR spectra of figure 9 where the spectral line of the samples with 5nm and 6nm Co thickness, do not show significant differences in their respective spectral shapes between 120 MHz and 200 MHz. In addition, the slope of the interface integral intensity is much smaller than that of the total intensity. This confirms that the increase of the interface below 200 MHz does not arise from bulk contributions but from the building up of the interfaces. However, it is rather surprising that this “building up” of the interfaces results in contributions above 120 MHz only and does not affect the whole frequency range. One explanation might be that the top and bottom interfaces i.e. Co/ZnTPP and ZnTPP/Co interfaces, are asymmetrical.

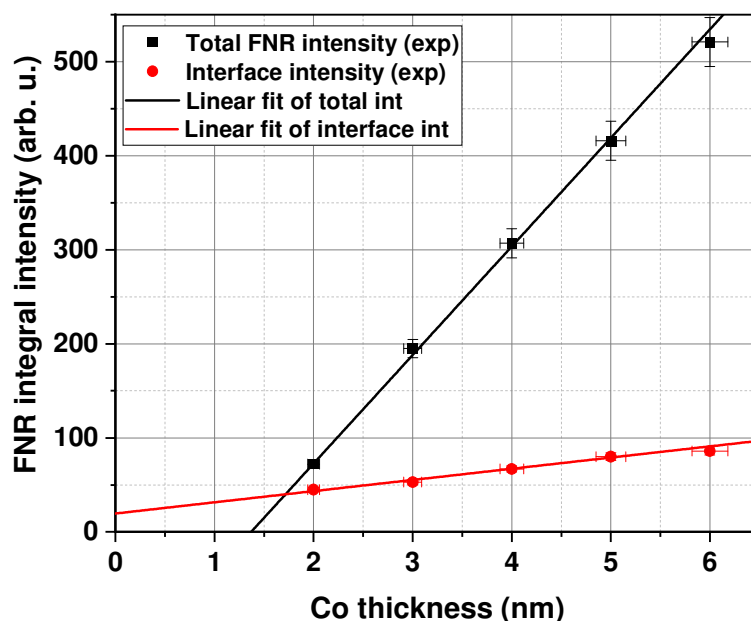


**Figure 10:** Estimated integral intensities of the FNR spectra of figure 5. Red and black symbols are the experimental data obtained for total and bulk part integral intensities and their respective solid lines (red and black) represent the linear fits.

### 10.1.3 Partial conclusion

ZnTPP/Co/ZnTPP hybrid structures have been prepared to have better insight into the hybrid interfacial properties. The spectra of these heterostructures showed no well-defined peaks at low radiofrequency range suggesting that Co atoms at the hybrid interfaces do not show strong chemical bonds with the organic molecular layer. In addition, it was deduced that 5nm of Co is required to complete the interface formation and that approximately 1.4nm of metallic Co atoms were not observed in the FNR spectra. This means probably that a significant number of Co atoms are diffused into the molecular film and lost their ferromagnetic nature. These diffused Co atoms take part in building up the interfaces which has mixed and extended kind of morphology. Finally, the experimental analyses suggested that the hybrid interfaces are highly asymmetrical.

To investigate if the interfaces are asymmetric and to analyze the origin of the extended type of interfaces, exclusive sample architecture has been implemented which allows to measure solely the single Co/ZnTPP and ZnTPP/Co hybrid interfaces. These results are discussed in the next section.

## **10.2 Morphology of the single Co/ZnTPP and ZnTPP/Co interfaces**

To answer to the questions raised in the previous paragraph, specific heterostructures have been built to solely investigate the morphology of the single Co/ZnTPP and ZnTPP/Co embedded interfaces. Again, the method consists in separating in different frequency ranges the contributions of the interfaces inside the heterostructures.

### **10.2.1 Building up the single interface**

Two distinct heterostructures have been built to probe independently Co/ZnTPP and ZnTPP/Co type of single interfaces. The first heterostructure is Cu(25nm)/Fe(30nm)/Co(6nm)/ZnTPP(20ML) while the second sample has Cu(25nm)/ZnTPP(20ML)/Co(6nm)/Fe(30nm) structure. Each layer has been prepared according to its respective method mentioned in the experimental section and both samples are capped with 100nm of Cr.

In the first sample, the role of the Fe film in-between Cu and Co is to fully separate the two layers thus eliminate any Cu/Co interfacial contribution to low radiofrequency ( $< 200$  MHz) range of the FNR spectrum. As a result, any feature at the low radiofrequency would result only from the Co/ZnTPP interface. Of course, the deposited thickness of ZnTPP has been chosen to be 20 ML to ensure the continuous character of the molecular film.

Likewise, in the second sample the presence of 20 ML of ZnTPP in-between Cu and Co would prevent the migration of the metallic atoms and fully separate the two metallic layers thus eliminate Cu/Co interface contribution in the low radiofrequency range ( $< 200$  MHz). The second Co interface is covered by Fe to reject to high frequencies the second interface contributions. So, in the FNR spectrum the only interface acting on the low radiofrequency range will result from the ZnTPP/Co interface contribution.

### **10.2.2 Results and discussions**

Figure 11 shows the spectra of Cu/Fe/Co/ZnTPP and Cu/ZnTPP/Co/Fe heterostructures. As discussed above, the spectra are divided into 3 different regions: the high frequency part of the FNR spectra results only from the Co/Fe and Fe/Co interfacial areas and the low radiofrequency spectral range shows only the Co/ZnTPP and ZnTPP/Co interface contributions. The Co/ZnTPP and ZnTPP/Co interfaces are characterized by unstructured, broad, and tale-like line with no well-resolved peak. There is no resolved interfacial contribution that could be identified to a specific Co environment resulting from the interaction of the Co with the organic molecules at the interface. Therefore, it suggests that Co atoms at the interface do not experience strong interactions with the ZnTPP molecules i.e. Co atoms do not experience ionic and/or covalent chemical bonds with the ZnTPP molecules. Weak interactions like van der Waals (vdW) interactions are most probably involved.



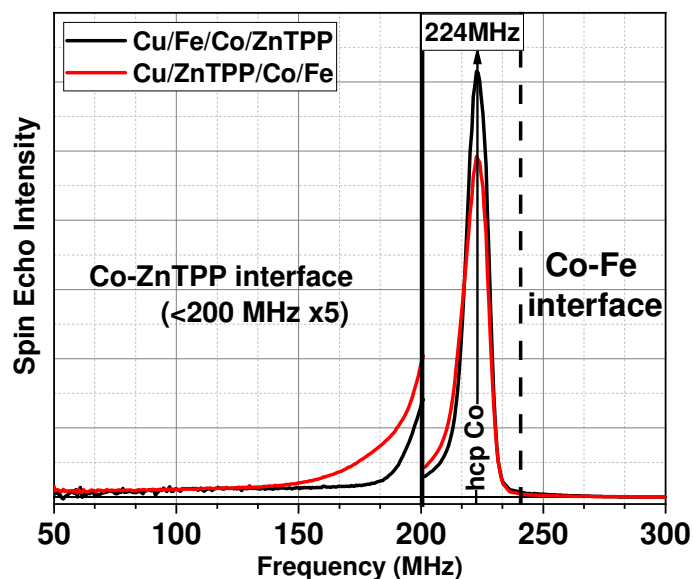


**Figure 11:** Spectra for Cu/Fe/Co/ZnTPP (black) and Cu/ZnTPP/Co/Fe (red) heterostructures. The low frequency spectra region is magnified by a factor of 5 (x5). Co-ZnTPP interface corresponds to the contribution from Co/ZnTPP and ZnTPP/Co type of interfaces.

Although the two heterostructures did not show any specific Co/organic interfacial signature, they do have different morphologies. Indeed, as seen from the spectra of figure 11 between 50 MHz and 140 MHz the two interfaces have identical interfacial contribution where their respective spectra are superimposed. Similar trend was observed in the spectra of ZnTPP/Co(t)/ZnTPP heterostructures. However, between 140 MHz and 200 MHz the spectral shape lines depart from each other. When ZnTPP is on top of the Co film, the Co/ZnTPP contribution (black line) shows, between 140 and 200 MHz, a much smaller intensity than for the ZnTPP/Co interface (Co on top of ZnTPP; red line).

From the integral intensity of the different parts of the spectra it is possible to evaluate the amount of Co atoms involved in the interfacial range. In the Co/ZnTPP interface the fraction of Co atoms involved is of about 0.3nm i.e. 1.5 Co atomic planes, while in the ZnTPP/Co interface the amount of Co is estimated to be around 0.7nm (3.5 atomic planes). In an ideal interface, only one atomic plane of Co (0.2nm) would take part in the interfacial area. Therefore, the 0.3nm interfacial Co estimated for the Co/ZnTPP interface is rather small and close to the ideal case which suggests that when ZnTPP is deposited on top of a Co film it builds smooth and rather sharp interface. On the contrary, the estimated amount of Co (0.7nm) in the ZnTPP/Co interface is much larger than the ideal interface case and reflects a large disorder at the interface.

Following the previous results, it has to be remarked that when Co is deposited on top of the organic film even a small roughness at the organic layer scale would result in a large roughness for the Co film. Indeed, considering that the interlayer distance between the organic planes (0.35nm-0.4 nm) is much larger than that of a metal, a small roughness at the organic layer scale will directly impact a large number of Co atoms. It is thus not so surprising to observe that the amount of Co atoms involved in the interface is much larger when Co is deposited on top of ZnTPP than when ZnTPP is deposited on top of Co. This feature explains the behaviour of the ZnTPP/Co(t)/ZnTPP hybrid sandwich structures and confirms that the interfaces Co/ZnTPP and ZnTPP/Co interface are asymmetrical.

### 10.2.3 Partial conclusion

Probing Co-ZnTPP single interfaces with FNR gave important insights into the morphology and the structural properties of the hybrid interfaces. The hybrid samples consist of interfaces with no strong interactions between the interfacial Co atoms and ZnTPP molecules. The interactions between Co atoms and the ZnTPP molecules are probably governed by weak van der Waals interactions. In addition, the analysis of FNR spectra showed that the hybrid interfaces are asymmetrical with quite different morphologies. When ZnTPP is deposited on top of Co film (Co/ZnTPP) it forms a rather sharp interface. On the contrary, the ZnTPP/Co (Co deposited on top of ZnTPP film) interface is characterized by an extended interface.

To support these results, it is important to have a local insight into the layers of the hybrid nanostructures. For this reason, TEM has been employed and the results are discussed in the next chapter.

---

## **Chapter 11: Revealing the hybrid interfaces: TEM in organic hybrid heterostructures**

TEM applied to organic hybrid systems is a difficult task as it requires post-growth sample thinning preparation that might easily degrade the molecular film. Nevertheless, TEM was successfully applied to investigate the hybrid heterostructures and provided important local information about the morphology of the layers and the structure of the hybrid interfaces.

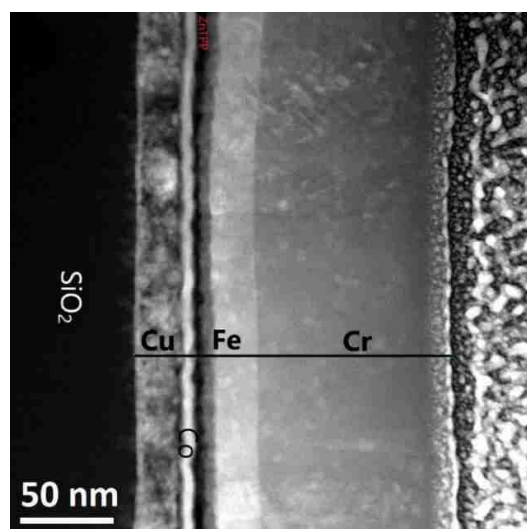
FNR was able to probe the texture and the morphology of the Co/ZnTPP and ZnTPP/Co interfaces at a macroscopic scale. However, FNR cannot probe the morphology of the Fe/ZnTPP and ZnTPP/Fe interfaces since FNR is much less sensitive to probe Fe atoms. In addition, FNR does not provide a direct view into the structure of the samples. In order to have a complete description of the samples and especially of the different FM/organic interfaces it is therefore necessary to compare the FNR interpretations to local observations in the direct space. To this end, transmission electron microscopy (TEM) has been employed to have cross-sectional visualization of the layers and study locally, the texture and the chemical properties of the hybrid interfaces. Consequently 3 different heterostructures were used in the TEM studies: the first one is the Co/ZnTPP/Fe heterostructure which was used to study the continuity of the molecular film with FNR. This sample contains the Co/ZnTPP and the ZnTPP/Fe interfaces. The second heterostructure is Fe/ZnTPP/Co/ZnTPP/Fe which contains all possible kind of hybrid interfaces i.e. the interfaces which are formed when depositing the FM metallic atoms on top of the molecule (ZnTPP/Co and ZnTPP/Fe) and the interfaces which are built when molecules are deposited on top of the FM electrodes (Co/ZnTPP and Fe/ZnTPP). The third sample is Cu/ZnTPP/Co/Fe which includes the single embedded ZnTPP/Co interface. With the following chosen samples, it would be feasible to study locally all kind of possible interfaces that the ZnTPP molecule forms with the Co and Fe metallic films in the organic heterostructures.

### **11.1 STEM images and EELS spectra : results and discussion**

#### **11.1.1 Co/ZnTPP/Fe heterostructure**

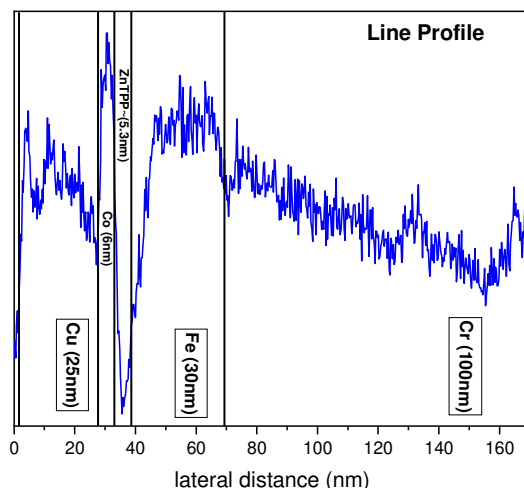
The following section describes the TEM images and the chemical composition of the Cu(25nm)/Co(6nm)/ZnTPP (15ML)/Fe(30nm) tri-layer sample. This sample was chosen as it has 15ML (5.3 nm) of ZnTPP molecular layer which is the threshold thickness, as determined by FNR analyses, to obtain continuous molecular layers. This heterostructure contains the Co/ZnTPP interface where ZnTPP is deposited on top of Co and ZnTPP/Fe interface where the Fe is prepared on top of ZnTPP.

Figure 12 represents the dark field STEM image of the above-mentioned tri-layer sample. As noted on the image, the left-most layer is the Cu seed layer. Next to it, the layer which has brighter color contrast is the 6nm Co film. The black colored layer just right of the Co film is the ZnTPP molecular film. Like the Co film, the top Fe electrode has brighter contrast in the image while the top-most Cr capping layer shows a dark grey contrast. The Cu buffer layer shows different contrasts along its entire film. To be sure of its specific chemical element composition, EELS spectroscopy measurements have been conducted on this layer. The EELS spectrum for this region showed only Cu edges with no other chemical species so it was confirmed that indeed this layer is composed of Cu atomic entities only. In addition to these expected layers, in the image it was also observed that between the ZnTPP and Fe layers there exists a thin region which has a completely different color contrast compared to the light grey color of the Fe electrode and to the all-black color of the ZnTPP molecular film.



**Figure 12:** STEM image of Cu(25nm)/Co(6nm)/ZnTPP (15ML)/Fe(30nm) tri-layer sample.

Figure 13 represents the profile of the line depicted in the above STEM image. From the line profile it was observed that the thickness of each layer in the image is consistent (within error bars) with the deposited thickness of its corresponding layers in the Cu(25nm)/Co(6nm)/ZnTPP(15ML)/Fe(30nm)/Cr(100nm) sample. To better understand the behavior of this sample, the imaging was focused on the interfacial areas to extract and study the morphology of the hybrid interfaces. Furthermore, EELS spectroscopy has been used to conduct chemical analysis on these hybrid interfaces.



**Figure 13:** Profile of the line plot in figure 14. Estimated thicknesses are consistent with the deposited thicknesses.

Figure 14 shows the dark field STEM images of the cross-sectional FIB prepared sample of the Co/ZnTPP(15ML)/Fe heterostructure focused on the interfacial areas of the organic layer. For consistency and reproducibility, different images were extracted from different regions of the sample. All images showed similar features. Fe and Co layers are well distinguished from the rest of the stack and lattice fringes are observed in their respective layers. To extract the distance between the observed fringes, Fast Fourier Transformation (FTT) has been used. For the Fe layer, the distance between the fringes which corresponds to the inter-planar distance was of 0.19nm which is consistent with metallic Fe. Likewise, the inter-planar distance for Co film was computed to be 0.2nm corresponding to the structure of metallic Co.

No well-defined interfaces are observed on both sides of the molecular film. At the ZnTPP/Fe interfacial region there exists a layer of around 6nm thick that has completely different contrast (dark grey) compared to the Fe or ZnTPP film yet it showed lattice fringes which are wider compared to the metallic films. For this layer, the computed distance between the fringes was found to be larger than 0.25nm which is bigger than that of Fe (see figures 14e, 14f and 14g). This suggests that the layer consists of species that do not correspond to metallic Fe and might be an admixture of different chemical species. Nevertheless, the presence of fringes suggests that this layer is crystallized. Since the molecules mainly consist of carbon and zinc atoms it is possible that the fringes could result from Fe-Zn alloy or Fe carbide. On the contrary, the Co/ZnTPP interface shows only a thin interfacial mixed area (0.7nm) and does not show any significant differences compared to the bulk Co film. These observations show that indeed the amount of metallic atoms that are diffused and are involved in the interfaces is larger when the metallic atoms are deposited on top of the molecular film than when the molecule is deposited on top of the metallic film.

Moreover, it was observed that the ZnTPP film is rich in grey dust-like spots/areas. This feature is even stronger and more clearly observed in figures 14c and 14d which show that there are areas where the mixed zone from the top interface is elongated all the way through the molecular film and touches the bottom interfacial areas.

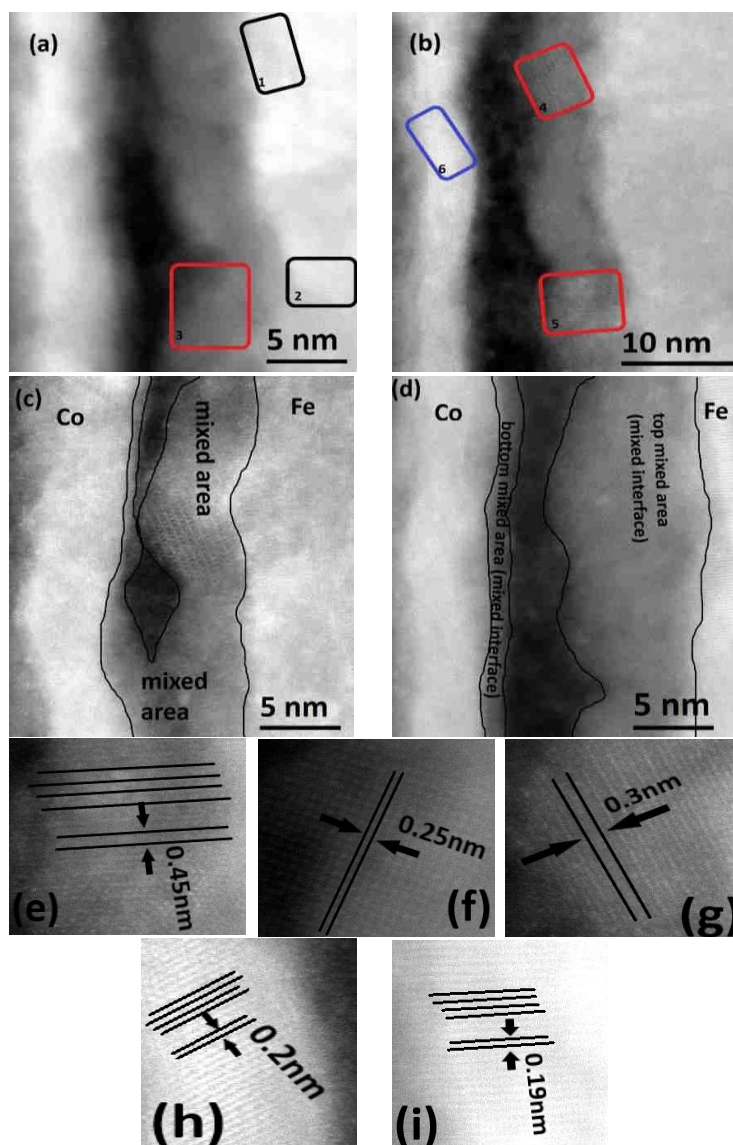


**Figure 14:** (a) (b) (c) (d) STEM images of Co/ZnTPP/Fe tri-layer. Different layers can be identified by the difference of color contrast. In (a) and (b) the black squared region is for the observed fringes in iron, blue is for cobalt's fringe and red is for the fringes in the mixed zones. (c) and (d) show contour at the end of each layer, showing the metallic layers and the mixed interfacial areas. (e) (f) and (g) lattice distances for the mixed zones marked by red square 5, 3, 4 respectively (h) inter-planar distance in Co film (i) inter-planar distance in Fe film.

To go further, EELS spectrometer was employed for insights into the chemical nature of these mixed interfaces and into the grey dust-like areas that were heavily spotted in the ZnTPP film. EELS spectrum represents the electron counts resulting from the ionization of a core shell electron; therefore, it would be possible to precisely check the elements present in these areas. Figure 15 shows the STEM survey image on which EELS was conducted and its respective EELS spectra. The spectra were acquired along the line profile in the image. This line covers a length of 8.5nm, which includes the ZnTPP/Co mixed interfacial area reaching all the way to the bottom Co film. The black spectrum of the ZnTPP/Fe mixed interfacial zone shows profound  $L_{3,2}$  edges of iron and K-edges of oxygen and carbon. Further from this mixed zone towards the molecular film (marked as 2), the intensity of iron and oxygen edges decrease while a small contribution from  $L_3$  cobalt edge starts to appear (red spectrum). Carbon K-edge is still present in this area and is more intense than in the previous zones. In region 3 i.e. deep inside the ZnTPP molecular film, the spectrum indicates Fe  $L_3$  edge, very weak Co  $L_3$  edge and strong carbon K-edge. Further towards the cobalt film and precisely at the Co/ZnTPP mixed interfacial area, the green spectrum still shows iron L-edge and carbon K-edge with strong contribution from the  $L_{3,2}$  edges of cobalt. At last, reaching the cobalt film the spectrum (purple) shows only  $L_{3,2}$  edges of the metallic cobalt.

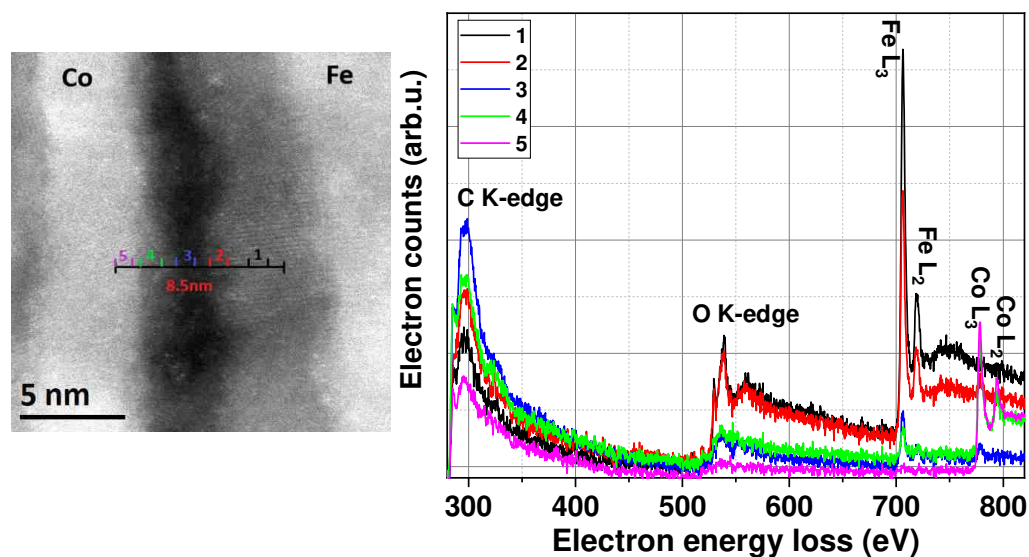


**Figure 15:** (left) Dark field STEM survey image for EELS spectroscopy. (right) EELS spectra acquired from the line profile of the survey image. Each spectrum corresponds to its number and color code, respectively. The integration length to extract the spectrum was of 1nm for each region.

Tracking the evolution of the spectra along the line, it was clearly observed that the ZnTPP/Fe mixed interfacial area is composed of iron, carbon, and oxygen atoms. MTPP molecules are carbon-based compounds (44 carbon atoms), so the observed carbon edge in this area is attributed to ZnTPP molecules. As the “freshly deposited” samples did not show ageing during the FNR and SQUID measurements of this sample, the presence of oxygen is attributed to small contamination post FIB sample preparation. Iron atoms in this mixed region might be dispersed in the form of nano-particles so they will get oxidized much faster when exposed to air hence result in the observed oxygen K-edge. Therefore, it is also possible that the fringes with a large inter-planar distance observed in this mixed area might be the consequence of iron oxide crystal structure. Surprisingly, it was noticed that iron is found in all layers except in the pure metallic cobalt film (bottom most layer). This suggests that iron atoms can diffuse and migrate through the molecular film.

In contrast to the ZnTPP/Fe mixed interfacial area, the Co/ZnTPP interface showed small portion of mixture between cobalt and ZnTPP molecules. Finally, the grey dust-like areas within the ZnTPP film were found to be composed of iron, cobalt and ZnTPP molecules. It suggests that the Co atoms also migrates inside the organic layer. Nevertheless, in these zones there exists more Fe atoms migrated into the molecular film compared to the Co atoms. This is probably because in this heterostructure Fe atoms are deposited on top of the ZnTPP molecular film and might penetrate more easily into the molecular film compared to the Co atoms which are found at the bottom of the ZnTPP film. 15 ML was found to be the threshold thickness required to isolate the ferromagnetic electrodes yet TEM analysis revealed that there exists good portion of diffused metallic atoms into the molecular film.

### **11.1.2 Fe/ZnTPP/Co/ZnTPP/Fe heterostructure**

FIB prepared sample from the Fe(30nm)/ZnTPP(20ML)/Co(5nm)/ZnTPP(20ML)/Fe(30nm) heterostructure was used for morphological and elemental composition studies via TEM imaging and EELS spectroscopy. Figure 16 depicts the cross-sectional view of the sample obtained from dark field STEM images at different scales and regions. From figure 16a, all layers are clearly observed and are consistent with the deposited thicknesses. In addition, it is observed that the bottom Fe layer has a columnar morphology when deposited on Cu which is not the case for the top Fe layer that is grown on top of the ZnTPP films. In fact, the structure of the bottom Fe layer could explain why the FNR analysis of chapter 9 revealed that the ZnTPP molecules have an island kind of morphology when deposited on top of the Fe films. As seen in figure 16c, the Fe layer on the Cu seed layer has columnar growth leading to granular surface morphology with the grain's lateral size of the order of 20nm. Considering the size of the ZnTPP molecules (length=width $\approx$ 1.4nm) it is most likely that when the molecules are deposited on top of this Fe layer they accumulate on the grains as molecular clusters and follow the structure of the Fe film leading to an island kind of morphology from their initial growth state.



It has been observed that the interfacial areas of this sample i.e. Fe/ZnTPP, ZnTPP/Fe and the two interfaces in ZnTPP/Co/ZnTPP region, have a similar behavior as the interfaces of the Co/ZnTPP/Fe heterostructure. The top and bottom mixed interfacial areas at the contact of ZnTPP film with the Fe layers showed lattice fringes with wider spacings (0.27nm and 0.3nm) compared to the inter-planar distance computed for the pure metallic Fe film (0.2nm). These mixed interfacial areas also show different color contrast with respect to the Fe metallic films. The wide spacing and the different contrasts suggest that these interfacial areas are composed of an admixture of different atomic entities that do not follow the structure of pure metallic Fe. These mixed zones can be composed of Fe-Zn alloys or Fe carbide. All the STEM images of this heterostructure revealed that when ZnTPP molecules are deposited on top of the Fe film (Fe/ZnTPP) the mixed interfacial area is around 2.3nm which is relatively thinner compared to the mixed area (3nm-3.5nm) when the Fe atoms are deposited on top of the ZnTPP molecular film (ZnTPP/Fe). This observation looks consistent with the interpretations of the results obtained from the FNR measurements on Co/ZnTPP and ZnTPP/Co interfaces in chapter 10.

On the other hand, the mixed interfacial areas at Co/ZnTPP and ZnTPP/Co interfaces did not show any lattice fringes which means that they are most likely not crystallized. It is still possible that these mixed areas might be an admixture of Co atoms and ZnTPP molecules. This is discussed in detail in the upcoming part of their EELS spectra. Moreover, the mixed regions for both Co/ZnTPP and ZnTPP/Co interfaces are rather thin, in the order of 1nm.

However, one particular feature that should be noted is that when Fe atoms near the ZnTPP molecular films (Fe/ZnTPP and ZnTPP/Fe) they seem to migrate deeper into the molecular films compared to Co atoms. Considering that the two ZnTPP molecular films are of the same thickness (20ML) this difference could result from the different deposition techniques and the deposition rates of the FM metallic atoms. Fe has been prepared using DC sputtering technique with a flux of 0.25Å/sec while Co has been prepared by thermal evaporation with a deposition rate of 0.16Å/sec.

As seen in all the images top and bottom ZnTPP molecular films have the grey dust-like spots like the previous case. These grey spots are attributed to the metallic atoms that are migrated deep into the molecular films. Nevertheless, in this sample the grey spots seem to occur less often than in the ZnTPP film of the above tri-layer sample. This could result from the thicker ZnTPP film in this hybrid sample. For this series, the ZnTPP thickness (20 ML) is 5ML $\approx$ 1.8nm thicker than the threshold thickness (15ML) required to obtain continuous molecular films. Therefore the thickness of the organic layer is large enough to separate completely the two electrodes. Moreover, the additional 1.8nm of molecular film could behave as an additional barrier to prevent the metallic atoms to migrate deep inside the film.

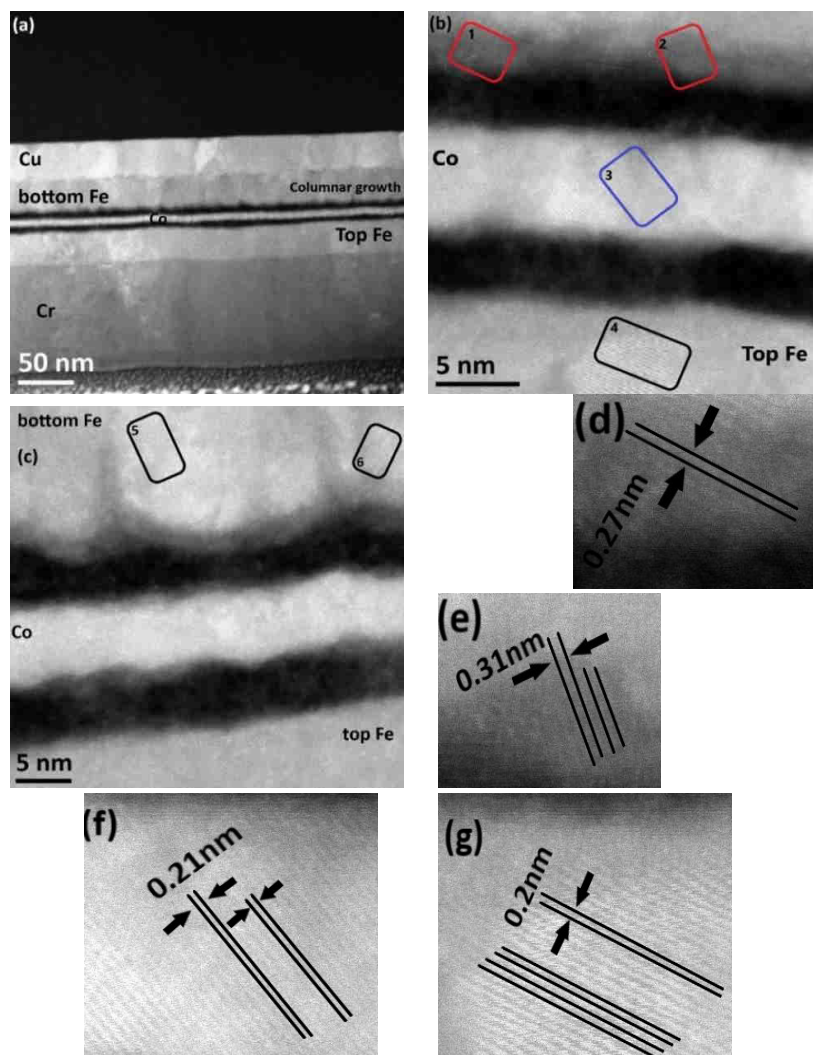


**Figure 16:** (a) (b) (c) Dark field STEM images for Fe/ZnTPP/Co/ZnTPP/Fe sandwich sample. Bottom iron shows columnar growth. Red rectangular boxes are for the fringes in the mixed iron-ZnTPP interface. Blue box for the fringes in the cobalt film while the black boxes corresponds to the fringes in top and bottom iron layers. (d) (e) (f) (g) inter-planar distances for the boxes marked as 1, 2, 3 and 4, respectively.

At last, EELS spectroscopy has been applied to have insights into the chemical composition of the heterostructure. The elemental line on which EELS was conducted is shown in figure 17. The line covers all the layers starting with the top Fe layer and goes all the way to bottom Fe layer. Extracting the EELS spectrum for each region will allow to track the elemental composition of the sample.

Figure 17 describes the evolution of the EELS spectra extracted from the line scan of the STEM survey image. The analysis is concentrated on the interfacial regions and deep inside the ZnTPP molecular film. As observed, when in region 1 i.e. top Fe interfacial area, the black spectrum shows  $L_{3,2}$  edges of iron, alongside the K-edges of carbon and oxygen.

Going into the ZnTPP film, precisely at the grey spot marked as region 2, the red spectrum shows a decrease in the intensity of iron L-edge (more than half of the intensity is diminished), increase in the intensity of carbon K-edge and a very small contribution from cobalt  $L_3$ -edge. Oxygen signature is still observed in this area. Reaching the top cobalt mixed interface (region 3), the blue spectrum indicates  $L_{3,2}$  edges of cobalt, K-edge of carbon and surprisingly a small signature of iron  $L_3$ -edge. The green spectrum of the bottom cobalt mixed interface reveals carbon K-edge and  $L_{3,2}$  edges of cobalt but no iron L-edge. The bottom ZnTPP molecular layer shows only  $L_{3,2}$  edges of iron, intense K-edge of carbon and K-edge of oxygen (purple spectrum). No cobalt contribution was observed in this region (region 5). At last, the spectrum of the bottom mixed iron interface shows profound  $L_{3,2}$  edges of iron and small contribution from the K-edge of carbon and K-edge of oxygen. There are no hints of cobalt in this zone.

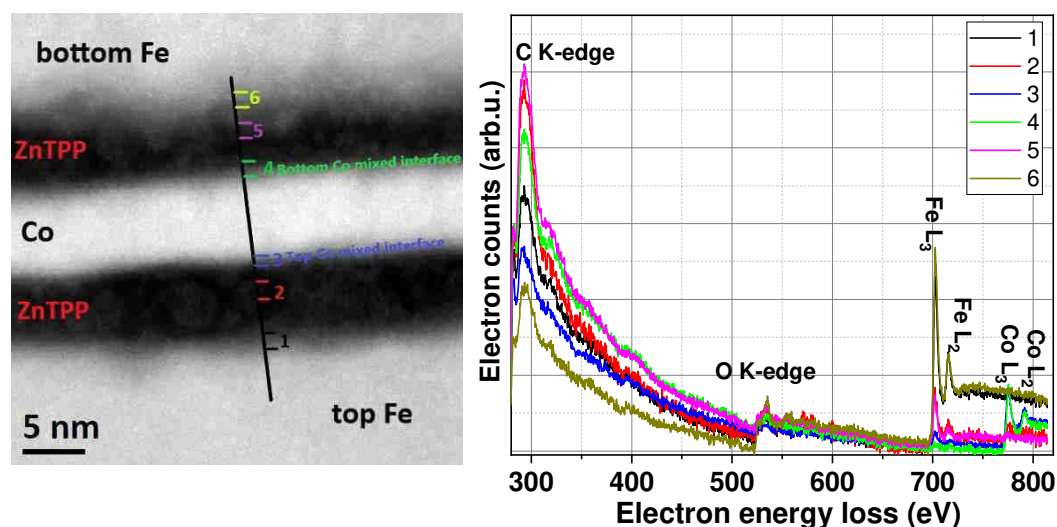


**Figure 17:** (left) Dark field STEM survey image for EELS spectroscopy. (right) EELS spectra acquired from the line profile of the survey image. Each spectrum corresponds to its number and color code, respectively.

From the spectra, one can deduce the following points:

- (i) Top and bottom Fe-ZnTPP interfaces are composed of iron, oxygen and ZnTPP molecules. As mentioned previously, the presence of oxygen could be the result of Fe oxidation post FIB sample preparation.
- (ii) The top Co interface is mainly composed of Co with small contributions from ZnTPP molecules and Fe atoms. Bottom Co interface shows only mixture of Co and ZnTPP molecules.
- (iii) Good fraction of Fe atoms are diffused in the top ZnTPP molecular film while Co atoms are found to be less in it, leaving few regions with pure ZnTPP molecules.
- (iv) Bottom ZnTPP molecular film has only Fe atoms diffused in it and no Co atoms are present within this molecular film.

### 11.1.3 Cu/ZnTPP/Co/Fe heterostructure

To finalize the TEM study, the Cu/ZnTPP(20ML)/Co(6nm)/Fe(30nm) sample has been used to prepare TEM thin specimen. As noticed, the sample has 20ML of ZnTPP which is above the threshold thickness (15ML) for obtaining continuous molecular films. More importantly, this sample includes the ZnTPP/Co kind of single interface that is built upon preparing the Co film on top of the molecular layer. It is in this sample that the FNR analyses showed a rougher ZnTPP/Co interface.

Figure 18 shows the dark field STEM images of the FIB prepared Cu/ZnTPP/Co/Fe sample acquired at different regions and different scales. In figure 18a, all the layers are clearly observed and are consistent with the deposited thicknesses. As mentioned on the image, the bottom-most layer is the Cu seed layer. On top of it, the black colored layer corresponds to the ZnTPP molecular film. Next in the stack comes the Co and Fe metallic films. Finally, the top-most layer that shows darker grey color contrast is the Cr capping layer. All the layers are separated by a black line to be differentiated from each other and to be observed clearly in the image.

Figures 18b and 18c represent the STEM images at a smaller scale and concentrates on the ZnTPP/Co interfacial region. It has been observed that in-between the ZnTPP molecular film and the Co layer there exists a region which has different color contrast compared to the black colored ZnTPP molecular film and the bright colored Co metallic film. In this region, there are some areas where lattice fringes have been observed. The computed distance between these fringes is of 0.26nm and above which is wider than the inter-planar distance of metallic Co planes that is around 0.19nm. The wide spacings and the different color contrast suggest that these mixed interfacial areas are not composed of pure metallic Co and might be a mixture of different atomic entities that do not have the structure of a metallic Co film. As mentioned previously, these mixed areas can be composed of Co-Zn alloys or even Co carbide.

The line profile of the mixed region at the ZnTPP/Co interface showed that this mixed region is rather thick and is in the order of 3.5nm.

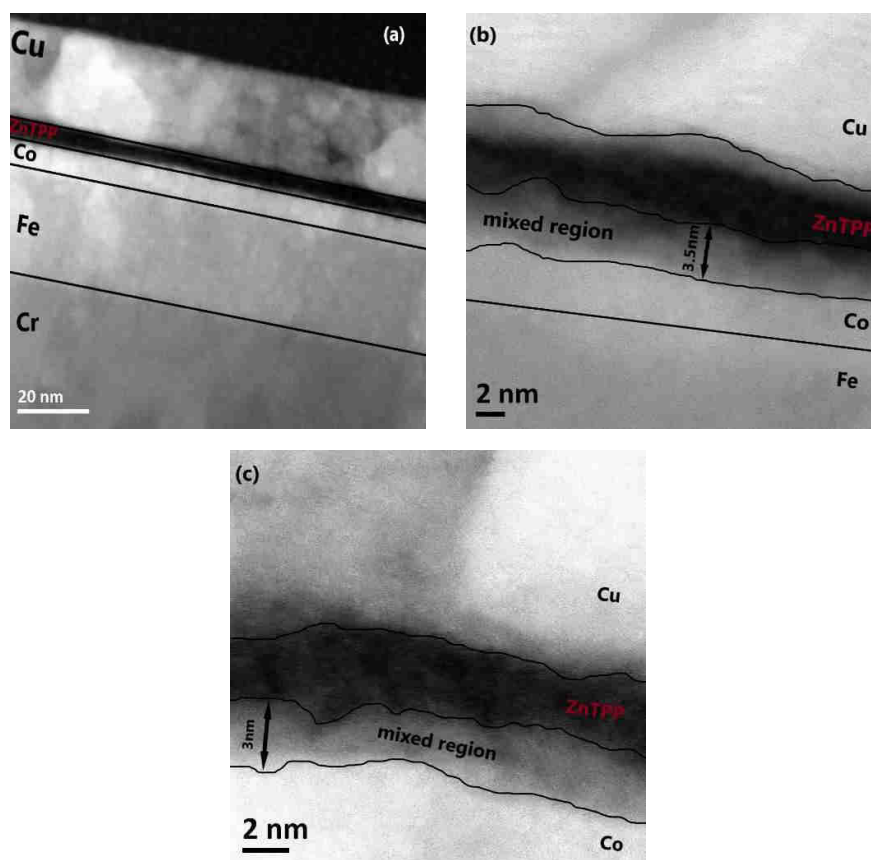


**Figure 18:** (a) (b) (c) Dark field STEM images for Cu/ZnTPP (20ML)/Co/Fe/Cr heterostructure. The different layers are separated by black contours for clarity. In (b) and (c) the imaging is focused on the ZnTPP/Co interfacial areas. Mixed regions are of 3nm-3.5nm thick, extended into the molecular film.

The FNR analysis of the ZnTPP/Co interface spectral line revealed that this interface has a rather diffusive and extended kind of morphology. In addition, it was explained that the amount of Co atoms involved in building up the interfaces is very large when the Co metallic atoms are deposited on top of the molecular film. Indeed, this is what has been observed in the images where the mixed ZnTPP/Co interfacial region extends up to 3.5 nm. Moreover, comparing the thickness of this region to the thickness of the mixed Co/ZnTPP area of Co/ZnTPP/Fe sample it can be seen that there is big difference between the two samples. In Co/ZnTPP interface (figure 14) the mixed regions had a thickness of 0.7nm which is much thinner than the mixed region in ZnTPP/Co interface (3.5nm).

To have further insight into the properties of the investigated sample EELS spectroscopy has been applied to it, to study the chemical composition of the layers and of the interfaces. The line profile on which EELS was conducted is shown in figure 19. The line starts from the Co metallic film and goes all the way through the molecular film reaching the Cu seed layer. The graph of figure 19 shows the evolution of the EELS spectra extracted from the line scan of the STEM survey image. The analysis is particularly concentrated on the interfacial regions and on the ZnTPP molecular film as they are the regions of most interest.

In the region 1 of metallic Co film the black spectrum shows profound  $L_{3,2}$  edges of cobalt and very weak carbon K-edge. Moving towards the molecular film and in the region 2 of the mixed region the spectrum (red) shows strong  $L_{3,2}$  cobalt edges, carbon K-edge and oxygen K-edge. Going further into the ZnTPP film precisely at the region 3 the spectrum (blue) shows an increase in the intensity of carbon K-edge and decrease in the intensities of  $L_{3,2}$  edges of cobalt and oxygen K-edge. Deep into the molecular film when passing the mixed regions (region 4) the spectrum shows only strong carbon K-edge with no hints of cobalt edge nor oxygen edge. Finally, at the bottom mixed area (region 5) the spectrum indicates the carbon K-edge and a very weak oxygen K-edge. No cobalt edge was observed in the spectrum.

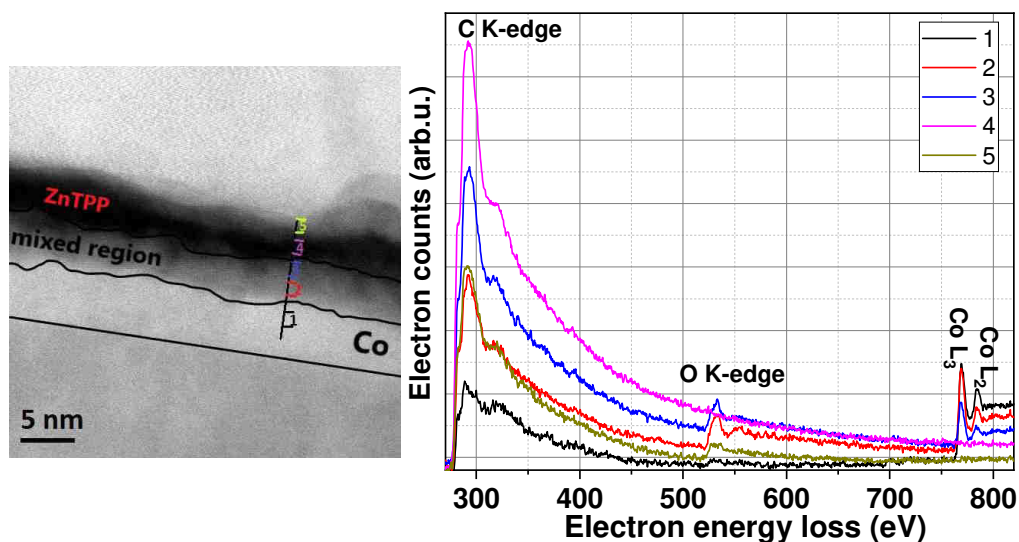


**Figure 19:** (left) Dark field STEM survey image for EELS spectroscopy. (right) EELS spectra acquired from the line profile of the survey image. Each spectrum corresponds to its number and color code, respectively.

Tracking the evolution of the spectra along the line it is observed that the mixed ZnTPP/Co interfacial regions are composed of cobalt, oxygen, and carbon. ZnTPP molecules are mostly composed of carbon atoms (44 carbon atoms, 4 nitrogen and 1 zinc) therefore, the observed strong carbon edge in the spectrum of these areas is attributed to ZnTPP molecules. The cobalt L-edge in the spectra of these mixed areas (extended up to 3.5nm) showed that indeed Co atoms are penetrating much deeper into the molecular film when they are deposited on top of the molecular film. In addition, the presence of the oxygen K-edge in the spectra is attributed to the sample contamination post FIB specimen preparation. Co atoms in this mixed region might be in the form of nano-particles so they will get oxidized faster than bulk Co, when exposed to air. However, it is only in this sample that the mixed Co interfacial regions showed signature of oxygen. This is because this sample has been kept outside for a very long time (longer than previous samples) and has been measured the latest due to events independent of our will. The presence of oxygen also suggests that it is possible that the fringes seen in these mixed regions might be the consequence of cobalt oxide structure. Interestingly, once deep into the molecular film the spectrum shows only carbon K-edge. This suggests that these areas are composed of ZnTPP molecules only with no hints of any cobalt atoms. This is opposite to what have been observed for Co/ZnTPP(15ML)/Fe structure where the top metallic atoms were diffused all the way in the molecular film and Fe atoms were present all over the molecular layer. This can be explained by the presence of 20ML of ZnTPP in the current Cu/ZnTPP/Co/Fe sample. The molecular thickness is 5ML thicker than the threshold thickness (15ML) for obtaining a continuous molecular layer. Therefore, the surface of the molecular film might be more continuous and contain less fractures thus decrease the possibilities for counter Co adatoms to penetrate through and migrate deep inside the thick molecular film.

### 11.2 Partial conclusion

In all of the heterostructures, Co and Fe films showed lattice fringes with an inter-planar distance of 0.2nm which means that the FM films have not lost their metallic nature during FIB sample preparation and measurement. Moreover, all the STEM images and EELS spectra showed that whenever metallic atoms (Co and Fe) are deposited on top of the ZnTPP molecular film, the migration of the atoms which also contributes to the mixed interfacial zones is stronger compared to when the molecules are deposited on top of the metallic films. For all the samples, top and bottom mixed interfacial zones of Fe-ZnTPP showed strong admixture of Fe atoms, oxygen atoms and ZnTPP molecules. These areas had fringes with wide inter-planar distance ( $>0.26\text{nm}$ ) therefore they are crystallized and most likely are composed of Fe-Zn alloys or iron oxide structures.

For Co/ZnTPP/Fe and Fe/ZnTPP/Co/ZnTPP/Fe samples, the Co/ZnTPP interfacial region is mainly composed of Co atoms with small portion of ZnTPP and Fe. Therefore, Fe atoms penetrate into the molecular film and reach to this mixed interfacial area. The ZnTPP/Co interfacial area of the same samples showed only Co atoms with small contents of ZnTPP molecules.

Finally, the ZnTPP/Co mixed region in Cu/ZnTPP/Co/Fe sample showed mixture of Co, oxygen and ZnTPP and fringes with wide inter-planar distance ( $>0.26\text{nm}$ ). The observed fringes are most probably the result of the cobalt-oxide structure.

### 11.3 General conclusions

NMR spectroscopy technique is not commonly applied to study ferromagnetic systems but when it is, FNR provides important structural and morphological information of thin films, multilayers, and even devices. The uniqueness of FNR lies in its original outputs that allows to study the chemical environment and the crystal structure of the probed Co atoms. Owing to these outputs, new FNR methodology has been developed that allowed to study the morphological properties of the organic hybrid heterostructures and of the embedded hybrid interfaces. In fact, it is the first time that FNR has been used to study in detail such organic hybrid systems.

FNR and TEM were able to provide important insights into the overall morphology of the different layers and of the hybrid interfaces of the studied organic heterostructures. It was shown that the extent of migration of the metallic atoms (Co and Fe) into the molecular film is much more important when the atoms are deposited on top of the ZnTPP molecular film compared to when the molecules are deposited on top of the FM metallic electrodes (Co and Fe). Moreover, it was shown that these migrations occur more often for heterostructures with 15ML of ZnTPP thickness compared to the heterostructures with 20ML. This proves that indeed 15ML is just at the limit of the threshold value of continuity and it is only after the 15<sup>th</sup> ML of ZnTPP that the Co and Fe electrodes would be fully isolated.

More importantly, it was concluded that FM/ZnTPP and ZnTPP/FM interfaces are asymmetric with completely different morphologies. The FM/ZnTPP interface is smoother and contains less contribution from the metallic atoms compared to the ZnTPP/FM interface that showed more metallic atoms involved in the interfacial regions leading to an extended and diffusive type of interface. These differences originate from the porous surface morphology of the molecular films which provides more spaces for the metallic adatoms first to fill these voids before forming continuous FM metallic films. These morphological properties of the interfaces are true for the two FM metallic atoms: Co and Fe.

FNR provided macroscopic information on the morphology of the heterostructures and TEM gave direct and local visualization into the morphology of the films. Combining these two techniques, it was possible to deliver a thorough description on the structure and the morphology of the hybrid interfaces of the organic heterostructures.



The newly developed FNR methodology is proven to be successful and very efficient in probing the morphological properties of the already grown organic molecular films in-between FM metallic electrodes. The FNR methodology can be used also in other organic hybrid systems where the organic molecular family is different than of MTPP molecules. In fact, the FNR methodology can be applied to any kind of spacer: metallic, insulating, semi-conducting and of course organic.





# **Part V**

## **General discussion, conclusions, and outlook**



## Part V: General discussion, conclusions, and outlook

### 1. General discussion

The general discussion of this part uses the morphological characteristics of the organic molecules and of the interfaces embedded in the hybrid organic heterostructures to correlate them to the magnetic properties of the heterostructures. The discussion is mainly focused on three different magnetic effects: molecular exchange bias effect, magnetic hardening effect, and indirect magnetic exchange coupling effect.

This thesis work is initiated with the study of molecular exchange bias in Au(25nm)/Co(6nm)/MTPP(30ML) hybrid systems. It is concluded that exchange bias in these hybrid systems is not an “spinterface” magnetic effect and appears only after the samples are aged. This tells that exchange bias in these systems most likely originates from air-driven partial oxidation of the Co films. Actually similar trends were observed even on the optimized organic heterostructures where the Au buffer layer is replaced with Cu and the Au capping layer is changed to Cr. The only difference is that while the original samples aged at the time scale of days the optimized samples aged at the time scale of one year. This is represented in figure 1, where the magnetization loops of the “freshly deposited” and one year aged Cu(25nm)/Co(6nm)/ZnTPP(24ML)/Fe(30nm) and Cu(25nm)/Co(6nm)/ZnTPP(60ML)/Fe(30nm) samples are displayed. Both samples have ZnTPP thickness larger than the threshold thickness for continuity (15ML) and are capped with 100nm of Cr.

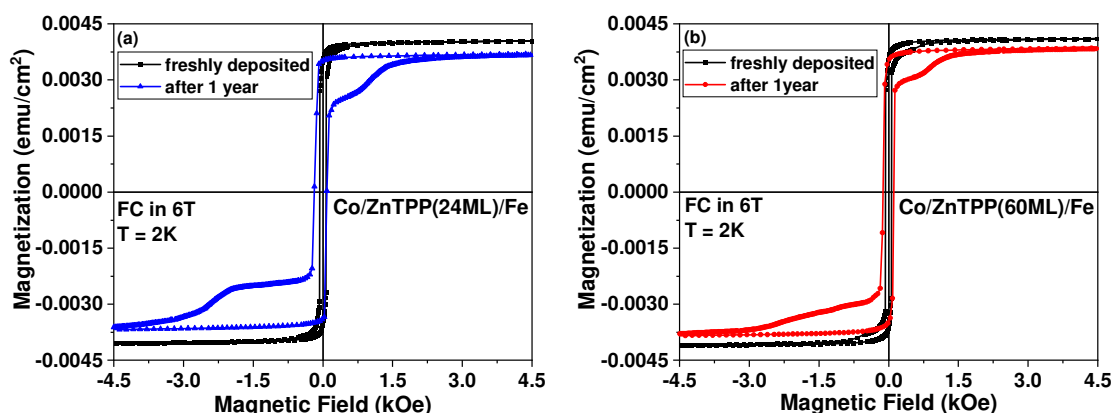


**Figure 1:** Magnetization loops of (a) Cu(25nm)/Co(6nm)/ZnTPP(24ML)/Fe(30nm) sample. Black loop: directly after growth, blue loop: measured again after 1-year (b) Cu(25nm)/Co(6nm)/ZnTPP(60ML)/Fe(30nm) sample. Black loop: directly after growth, red loop: measured again after 1-year. The two samples are capped with 100nm of Cr. All loops are measured at 2K after FC in an in-plane +6T external magnetic field.

While the freshly deposited samples did not show any exchange bias effect, after one year of sample exposure to air the onset of exchange bias appeared. During this 1-year interval of time the samples were kept in a desiccator which was opened and closed during working days hence the samples were exposed to air like any other sample of this work. This means that regardless the nature and thickness of the capping layer, extrinsic impurities manage to enter the heterostructures. Most likely, oxygen is able to penetrate and travel all the way through the capping layers and the molecular film and reach the buried Co film. As a result, part of the metallic Co film eventually is transformed to cobalt oxide ( $CoO_x$ ) structure that is well known to produce the exchange bias effect.

For explaining this oxidation process, one can consider the following mechanisms:

- i) Oxygen atoms migrate through the capping layer and the molecular film without reacting with the organic molecules and finally reach the underneath Co film. For this process to occur all the layers above the Co film should not be uniform. This was particularly the case for the Au capped Au(25nm)/Co(6nm)/MTPP(30ML) heterostructures.
- ii) Oxygen atoms penetrate through the capping layers reach the organic molecular films and react with the organic molecules. The reaction between oxygen atoms and the MTPP molecules are easily possible because MTPP molecules are considered to be highly reactive agents and good acceptor-donor of electrons. These reactions could occur either with the metallic site of the MTPP molecules or at their peripheries with the phenyl rings. If the reaction is at the metallic site, then the central metal ion (+2-oxidation state) of the molecule will lose an electron and transform to +3-oxidation state. In this case, the diamagnetic molecules will have a free spin that might pin the spin of Co surface atoms hence create the exchange bias effect. This is not the case in our studies because the XPS spectra of the hybrid samples did not show any signal that can be attributed to the +3-oxidation state of the molecule's central ion. The MTPP molecule's central ion (+2-oxidation state) peak was observed at the expected binding energy. In addition, it is observed that the first oxidation of Zn(II)TPP, Ni(II)TPP, and Co(II)TPP molecules occurs at the porphyrin macrocycle and not at the central metal ions [85]. This means that it is the porphyrin molecular orbital from which an electron is removed and not from the HOMO of the molecule's metallic ion. This feature further indicates that the Zn(II) and Ni(II) ions do not undergo changes in their electronic structure hence their orbitals would be still fully occupied. Moreover, in Co(II)TPP molecules when an electron is removed from the porphyrin ring then an internal redistribution of electrons will take place thus transferring an electron from the metallic site to the porphyrin ring. As a result, Co(II) will be transformed to Co(III) leading to closed shell configuration with  $3d^6$  orbital with no free spin. All these features rule out the possibility for Zn(II)TPP, Ni(II)TPP, and Co(II)TPP molecules to induce exchange bias to the Co metallic films when the molecules undergo changes in their oxidation state.

iii) Finally, it is still possible that with or without the reaction of the oxygen atoms with the metallic site and/or with the phenyl rings of the molecules, modifications of the morphology of the molecular films takes place with time. This is what has been observed on the free molecular surface. Actually it might even already occur during the in-situ UHV molecular growth and progress with time even once encapsulated. Such molecular deformations could alter the morphology of all the layers in the samples and especially the morphology of the capping layers. If the morphology of the capping layers is getting distorted due to these deformations, one can expect penetration of oxygen atoms from the atmosphere to the Co layers and hence the oxidation of the metallic Co films even if the fresh samples are efficiently capped.

From these discussions, it is concluded that MTPP molecules cannot induce the molecular exchange bias effect once adsorbed on Co FM metallic films, but the origin of the molecular deformations still remains an open question. It is not clear whether the degradation is an intrinsic effect or is initiated when the samples are exposed to air. These observations further stress the importance of the efficiency of the capping layer since the ingress of the oxygen atoms not only are oxidizing the buried Co film but also might be one of the reasons of the ageing of the molecular free surfaces.

After having discussed the origin of the molecular exchange bias and why the hybrid organic samples are getting aged the question is: what are the intrinsic magnetic properties of the non-aged organic heterostructures? Does the adsorption of MTPP molecules on top of the FM metallic films induce any magnetic effect? To answer these questions let us recall that the magnetization loops of the properly capped (Au or Cr capping layers) non-aged Au(25nm)/Co(6nm)/MTPP(30ML) samples showed well-defined hysteretic response with no shift i.e. no evidence of molecular exchange bias. Nevertheless, these hysteresis loops showed slow and high saturation field; higher than 4.5 Tesla (figure 2).



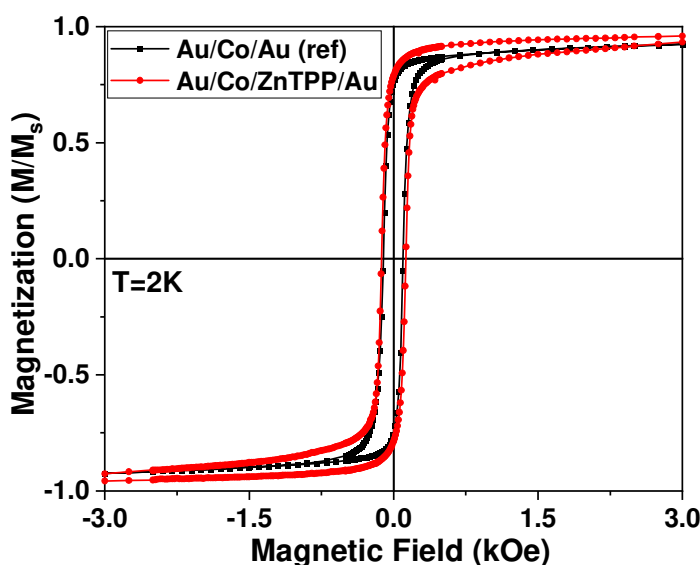


**Figure 2:** Black curve: Magnetization loop of Au(25nm)/Co(6nm)/Au(10nm) reference sample, FC in +3T magnetic field. Red curve: Magnetization loop of the “freshly deposited” non-aged Au(25nm)/Co(6nm)/ZnTPP(10nm)/Au(50nm) hybrid sample, FC in +6T magnetic field. The loops are acquired at  $T=2K$  and are normalized to saturation magnetization.

The only difference between these samples is the additional MTPP molecular films on top of the Co FM film while all other layers are similar to each other. Most likely, the insertion of the MTPP molecular layer is causing the differences observed in the magnetization loops. This could be the signature of some interface magnetic hardening effect. However, the STEM images of the optimized samples i.e. samples with Cu buffer layer, revealed that whenever ZnTPP molecules are deposited on top of the Co metallic films there is always migration of Co atoms up into the ZnTPP molecular film. These Co atoms most likely will exist in the form of small nanoparticles or grains. This is a rather strange mechanism especially in the optimized samples where the Co film is well-defined with very smooth surface morphology. If such mechanism is occurring in the optimized samples, it probably also happens in the samples with Au buffer that are much rougher. The migration of Co atoms is even probably stronger. Therefore, one can consider that the small coercive field is due to the intact part of the Co film while the high saturation field part of the non-aged Au/Co/MTPP hybrid samples originates from these diffused Co atoms forming nanoparticles.

The possibility of an interface magnetic hardening effect is further discussed using the optimized samples. Magnetic hardening effect is considered to be a “spinterface” magnetic effect and it is a phenomenon observed in other organic/inorganic hybrid systems [55,56,139]. To probe the existence

of a magnetic hardening effect FNR was used. This was possible because one of the unique kinds of information that FNR can provide is to measure the local, environment dependent, magnetic anisotropy of the samples. Indeed, the procedure used to establish the FNR spectra [136] also provides the so-called site dependent restoring field. In the investigated organic hybrid systems, the restoring field can be identified as the in-plane magnetic anisotropy of the organic heterostructures. In the previous part, samples with a specific architecture have been used to probe by FNR the morphology of the single Co/ZnTPP and ZnTPP/Co interfaces. Simultaneously the magnetic stiffness of these hybrid interfaces has been measured. Figure 3 represents the restoring fields obtained from Cu(25nm)/Fe(30nm)/Co(6nm)/ZnTPP(20ML) and Cu(25nm)/ZnTPP(20ML)/Co(6nm)/Fe(30nm) organic heterostructures, as a function of resonant radiofrequency.

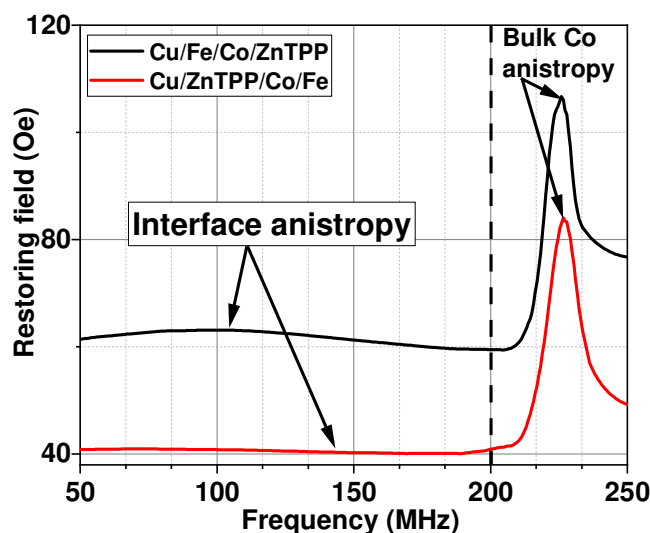


**Figure 3:** Frequency dependent restoring field. Graph shows the magnetic softness of the interfaces (< 200 MHz) and the magnetically stiffer cobalt in the bulk part of the cobalt films (> 200 MHz).

The two samples showed similar behaviour: higher restoring fields around 224-225 MHz that corresponds to the FM Co atoms inside the Co films and lower restoring fields corresponding to the single Co/ZnTPP (black spectrum) and ZnTPP/Co (red spectrum) interface anisotropy. The interface anisotropy is significantly lower (by about a factor 2) at both interfaces compared to the one corresponding to the Co atoms in the bulk part of the film which are situated far from the interfacial regions. Similar features (interface anisotropy lower than the bulk Co atoms' anisotropy) have also been seen in inorganic layered systems [135] and seems to be a general trend when the samples present some interfacial disorder. It is only when the samples show almost no interfacial disorder that the interface

anisotropy becomes similar to the one of the bulk part of the layer. Since the organic heterostructures under investigation present significant interfacial disorder it is therefore not surprising that the interfaces show a smaller anisotropy than the bulk part of the Co film. Nevertheless, one might notice in figure 3 that the sample with the sharper interface (ZnTPP on top of Co) presents an interface anisotropy that is a little bit larger relatively to the one of bulk Co: The bulk to interface restoring field ratio is 1.8 when ZnTPP is on top of Co and 2.1 when Co is on top of ZnTPP. It is consistent with the fact that the interface is sharper when ZnTPP is deposited on top of Co than when Co is deposited on top of ZnTPP. However, the differences cannot be attributed to any interface hardening effect. Real interface hardening would result in an interface restoring field significantly larger than the one of the bulk part of the film. Nevertheless, it is still possible that the hardening effect exists at a local scale, but the interfacial disorder would probably annihilate it. However, the structural and chemical analyses of the FNR spectra of all of the organic hybrid heterostructures confirmed previous works suggesting that Co atoms at the vicinity of the ZnTPP molecules do not form any strong chemical ionic and/or covalent bonds. The interactions between them are governed by weak and long-range van der Waals forces. Since the magnetic hardening effect occurs only when the adsorbed molecules show strong interactions with the interfacial atoms of the FM metallic substrate, it is consistent that no interface magnetic hardening is observed in the investigated organic hybrid systems.

With the knowledge acquired from the morphological and structural study reported in part 4 a study of the indirect exchange coupling, that might occur between two FM electrodes separated by a pin-hole free spacer layer was planned. Unluckily events independent of our will did not make this investigation possible therefore the magnetic study was concentrated on the samples prepared more specifically for the morphological and structural investigations. The SQUID magnetization loops obtained for the Cu(25nm)/Co(6nm)/ZnTPP(*t*)/Fe(30nm)/Cr(100nm) samples with  $1 \text{ ML} \leq \text{ZnTPP}(t) \leq 60 \text{ ML}$  are shown in figure 4. Figure 4a represents the magnetization curves of the heterostructures with ZnTPP thickness below the threshold value of continuity (15ML) while figure 4b shows the magnetization loops of the samples with ZnTPP thickness above the threshold value. The comparison of the saturation magnetization values of these heterostructures showed that all samples exhibit significant loss in their saturation magnetizations. For an ideal 6nm of Co film and 30nm of Fe the total saturation magnetization would be  $0.006 \text{ emu/cm}^2$  which is not the case for the Cu(25nm)/Co(6nm)/Fe(30nm)/Cr(100nm) reference sample that has  $0.0045 \text{ emu/cm}^2$ . This loss was ascribed to the dead layers at the Fe/Cr top interface.

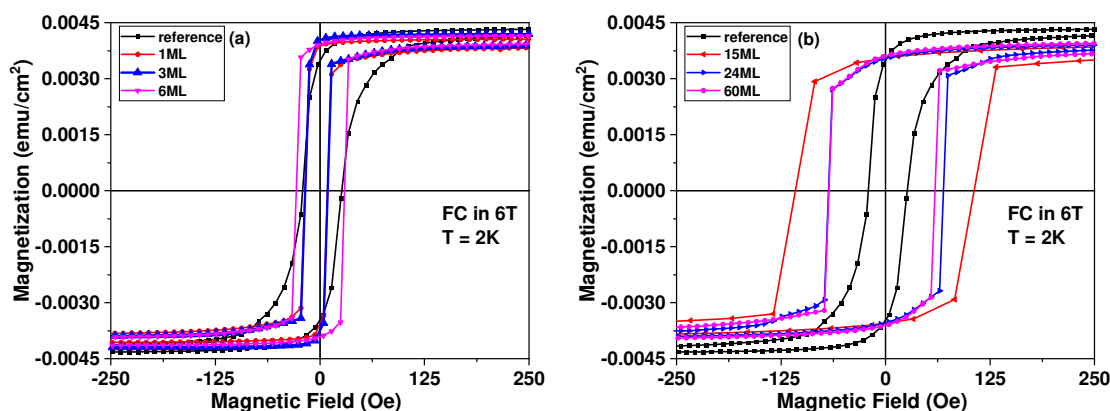


**Figure 4:** Magnetization loop of (a) Cu/Co(6nm)/Fe(30nm) reference sample (black curve) and Cu/Co(6nm)/ZnTPP(t)/Fe(30nm) heterostructures with ZnTPP thickness of 1ML, 3ML and 6ML (b) Cu/Co(6nm)/Fe(30nm) reference sample (black curve) and Cu/Co(6nm)/ZnTPP(t)/Fe(30nm) heterostructures with ZnTPP thickness 15ML, 24ML and 60ML. All the heterostructures are capped with 100nm of Cr. All loops are measured at 2K after FC in in-plane +6T external magnetic field.

Moreover, when ZnTPP molecules are introduced in-between Co and Fe layers the samples experienced further decrease in their saturation magnetization. In the previous parts of this manuscript the FNR quantitative analyses of these heterostructures revealed that diffusion/migration of the Co and Fe metallic atoms through the organic molecular layer does take place. In addition, the STEM images and EELS spectra unveiled that indeed there is a significant amount of Fe and Co atoms that migrated into the organic molecular film. The smallest of these isolated atoms or nanoclusters probably do not contribute to the saturation magnetization of the investigated systems. Therefore, the additional loss of the saturation magnetization is associated to the increase in the interface roughness at the ZnTPP interfaces and to the diffusion of Co and Fe metallic atoms into the molecular film.

A closer look at the shape of the magnetization curves revealed that the Cu(25nm)/Co(6nm)/Fe(30nm)/Cr(100nm) reference sample shows a low coercive field due to the large thickness of Fe and a high saturation field due to the magnetically stiffer Co layer. The samples with ZnTPP thickness below the threshold value i.e. 1ML, 3ML, and 6ML of ZnTPP, showed similar magnetic behaviour (figure 4a). Above the threshold thickness i.e. 15ML, 24ML, and 60ML of ZnTPP (figure 4b), the magnetization curves depart more significantly from the one of the reference sample.

The magnetization loops of the samples with 1ML, 3ML, and 6ML of ZnTPP showed a coercive field close to the one of the reference sample what is consistent with the fact that the Co and Fe layers are

directly coupled through the pin-holes in the organic film. On the contrary, the samples with 15ML, 24ML, and 60ML of ZnTPP showed magnetization curves having a two-step reversal process. Considering the magnitude of the magnetization reversals, the low field reversal can be attributed to the Fe layer whereas the second reversal at higher fields corresponds to the thinner and magnetically stiffer Co layer. Moreover, these samples showed a reversal field for Fe that is larger than the coercive fields of the samples with ZnTPP thickness smaller than the threshold value of continuity (15ML). The difference between the coercive fields could be due to a greater stiffness of the top Fe layer due to the increase in the ZnTPP/Fe interface roughness induced by the increase in ZnTPP thickness. The increasing roughness might result in additional magnetic pinning centres resulting in larger reversal fields. This would imply that the coercive fields of the samples would increase with the increase in ZnTPP thickness. This is not the case in these investigated samples since the coercive field of the samples is maximum for a ZnTPP thickness just above the threshold thickness (15 ML) and then decreases when the ZnTPP thickness is increased. Therefore, this explanation can be ruled out. The increased coercive fields could also originate from an indirect exchange coupling between the Co and Fe layers through the organic spacer layer. The coercive field of the soft Fe layer would be increased by a ferromagnetic coupling with the stiffer Co film. The highest increase of the coercive field would be for the thinnest pin-hole free organic spacer layer then the coercive field would start to gradually decrease with the increase in the organic spacer layer thickness. Indeed, indirect exchange coupling usually decreases with the increase of the spacer layer. This interpretation looks more convincing but remains an open question for further investigations.

To further dig into the magnetic behaviour of these organic hybrid systems, the optimized Cu(25nm)/Fe(30nm)/ZnTPP(20ML)/Co(5nm)/ZnTPP(20ML)/Fe(30nm) heterostructure has also been measured by SQUID. This heterostructure has 20ML of ZnTPP molecular film which is above the threshold thickness of continuity and most likely is not thick enough to induce high interface roughness at the FM metal-molecule contact. Figure 5 represents the magnetization loop at  $T=2K$  of the above-mentioned heterostructure where the in-plane external magnetic field is swept from 60 000 Oe to -60 000 Oe and back. It showed total saturation magnetization value in the order of  $0.01040 \text{ emu/cm}^2$  which is lower than the expected value ( $0.01098 \text{ emu/cm}^2$ ) of a 60nm Fe film and a 5nm of Co film. This loss can be attributed partly to the dead layers at the Fe/Cr interface and partly to the Co/ZnTPP and Fe/ZnTPP interfaces where diffusion of Co and Fe atoms were evidenced by FNR and TEM. The hysteresis loop showed three different reversals at different magnetic field ranges which suggests the presence of three different effective magnetic anisotropies. At this stage, it is difficult to attribute these reversals to the different FM layers of the sample as the architecture of the studied heterostructure itself is already complicated. Nevertheless, this complicated magnetic hysteresis loop confirms that the 20ML of ZnTPP molecular films are indeed continuous and pin-hole free. If the molecular layers had pin-

holes, all layers would be directly coupled and the magnetic behaviour of the heterostructure would be closer to that of a single FM layer.

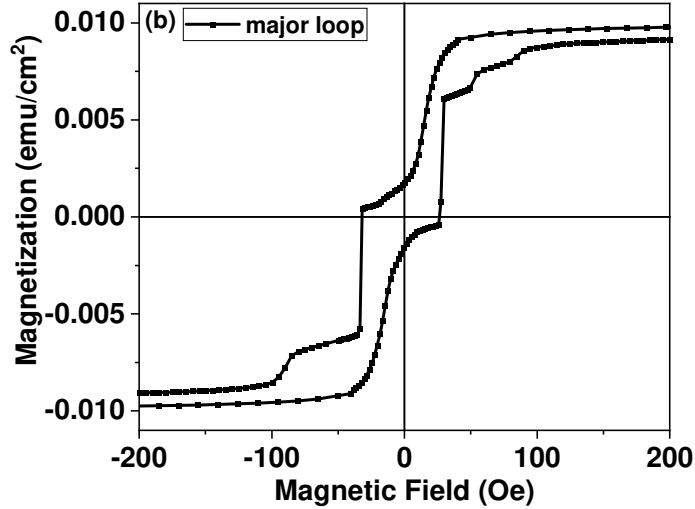


**Figure 5:** (a) Major magnetization loop at  $T=2\text{K}$  for the 100nm Cr capped  $\text{Cu}(25\text{nm})/\text{Fe}(30\text{nm})/\text{ZnTPP}(20\text{ML})/\text{Co}(5\text{nm})/\text{ZnTPP}(20\text{ML})/\text{Fe}(30\text{nm})$  heterostructure

Some particular feature can be noticed on the magnetization curve in Figure 5. The first reversal occurs at a positive field value and the magnetization decreases strongly even before reaching zero magnetic field. This is a rather unusual feature and might be a clue for the presence of an anti-ferromagnetic exchange coupling in the studied heterostructure. To unravel these unusual features and to better understand the magnetic behaviour of the heterostructure some minor magnetization loops have been measured. This is represented in figure 6. In the first minor loop denoted as minor 1 the field was cycled from 60 000 Oe to -3 Oe and back. As observed, when the field is swept from 60 000 Oe down to -3 Oe the magnetization of one of the FM layers is reversed and will be aligned along the negative field direction. On the contrary, the magnetization of the other FM layers is remained intact. The minor 1 magnetization loop showed a shift towards the positive field axis with an exchange field of +36 Oe. This positive shift indicates the presence of an anti-ferromagnetic indirect exchange coupling between the FM electrodes through the ZnTPP molecular film. The magnetization height of the minor 1 loop is around 43% of the total magnetization height of the major hysteresis loop. Considering the thickness of the different FM electrodes of the studied heterostructure i.e.  $\text{Fe}(30\text{nm})$ ,  $\text{Fe}(30\text{nm})$  and  $\text{Co}(6\text{nm})$ , this percentage is close to what a 30nm of Fe layer (46%) would contribute to the total magnetization height. Therefore, one can assume that the first reversal of the minor 1 loop corresponds to the reversal of one of the  $\text{Fe}(30\text{nm})$  films and that an indirect antiferromagnetic exchange coupling is experienced by this Fe layer.

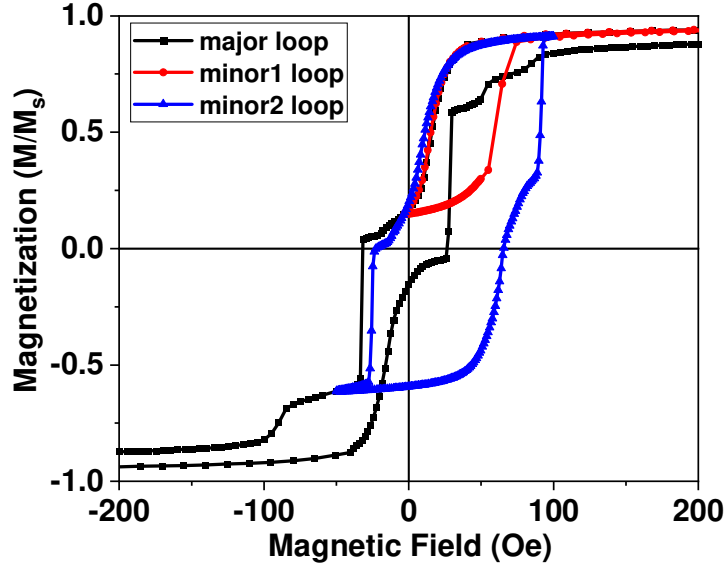


**Figure 6:** Major and minor magnetization loops for the 100nm Cr capped Cu(25nm)/Fe(30nm)/ZnTPP(20ML)/Co(5nm)/ZnTPP(20ML)/Fe(30nm) heterostructure. Both minor loops show a shift towards the positive field axis with an exchange field of +36 Oe. All loops are acquired at 2K. All magnetization loops are normalized to saturation magnetization value.

In a similar way, the minor 2 magnetization loop was measured by decreasing the applied field first from 60 000 Oe to -50 Oe and then sweeping it from -50 Oe to 100 Oe and back. With this process, it is observed that the magnetization of two FM layers reverse while the magnetization of the third FM film remains unchanged because the applied magnetic field does not exceed the coercive field of this third FM layer. The minor 2 magnetization loop showed also a positive shift along the magnetic field axis with an exchange field of +36 Oe. This is again the signature of an indirect anti-ferromagnetic exchange coupling. Moreover, the magnetization height of the minor 2 loop is approximately 81% of the total magnetization height of the major hysteresis loop. Considering that the two Fe(30nm) films together would contribute by around 92% to the total magnetization, it can be concluded that the reversals observed in the minor 2 magnetization curve correspond to the consecutive reversal of the two Fe(30nm) films.

At last, if the first reversal of the major loop at +15 Oe corresponds to the one of the Fe(30nm) films and the second reversal at -33 Oe corresponds to the other Fe(30nm) film, then the third reversal at the highest field (-90 Oe) can be attributed to the magnetically stiffer Co(5nm) film. The magnetization curve in figure 6 can therefore be explained by a magnetic three-layer system composed of two Fe

layers that are both antiferromagnetically coupled through the ZnTPP layers to the intermediate stiffer Co layer. Note, even though the two Fe layers are of the same thickness and deposited using the same deposition technique and conditions, they show coercive fields that are significantly different. These differences in their coercive fields could be due to their different morphologies. Indeed, it was observed in the STEM images of this heterostructure that the Fe film deposited on top of the Cu buffer layer showed a columnar growth with granular surface morphology which was not the case for the second Fe film deposited on top of the ZnTPP molecular film. But this is an hypotheses only.

The interpretation of the major and minor magnetization loops of the Cu(25nm)/Fe(30nm)/ZnTPP(20ML)/Co(5nm)/ZnTPP(20ML)/Fe(30nm) heterostructure was checked with magnetic simulations. Using a Stoner Wohlfarth model, the simulation considers two Fe(30nm) films coupled to a Co(5nm) layer by an indirect anti-ferromagnetic exchange coupling having the same coupling constant  $J_{AF}$ . To induce two different reversal fields for the two Fe layers, two different magnetic anisotropies have been used for the Fe layers. Both Fe anisotropies have been taken smaller than the magnetic anisotropy of the Co film.

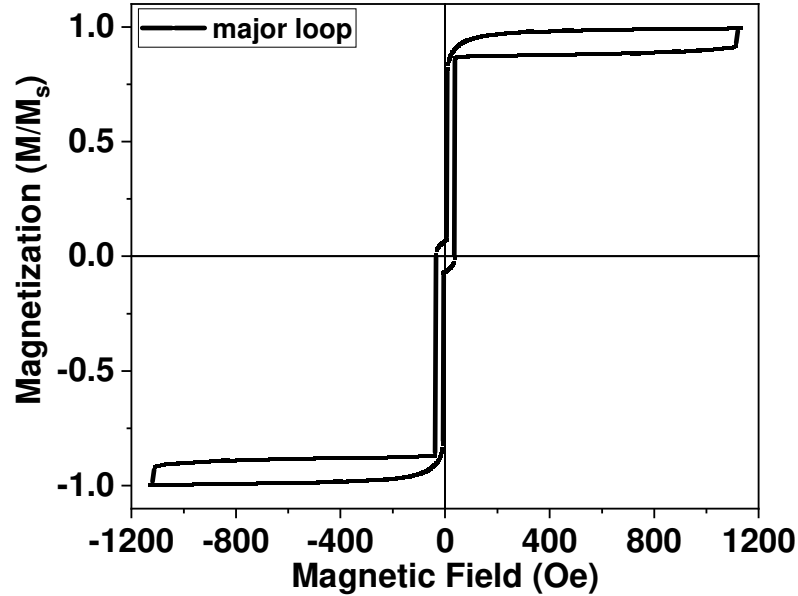


**Figure 7:** Magnetic simulation of the major hysteresis loop for Cu(25nm)/Fe(30nm)/ZnTPP(20ML)/Co(5nm)/ZnTPP(20ML)/Fe(30nm) heterostructure. It is calculated using the model described in the text. The magnetization curve is normalized to saturation magnetization.



Figure 7 represents the simulated magnetization loop of the above studied system. To obtain this type of magnetization loop the anisotropy energy of the Co film has to be larger than the coupling energy between the Co and Fe films. As observed, the major magnetization loop reproduces the three different reversals for different field ranges. The reversal fields as well as the magnitude of the reversals are qualitatively in good agreement with the experimental magnetization curve of figure 5. In addition, the two minor magnetization loops have been computed in figure 8 and are also in good agreement with the experimental data. These simulations confirm the interpretation of the experimental magnetization curves and show the presence of an anti-ferromagnetic coupling between ferromagnetic electrodes separated by 20 ML of ZnTPP.

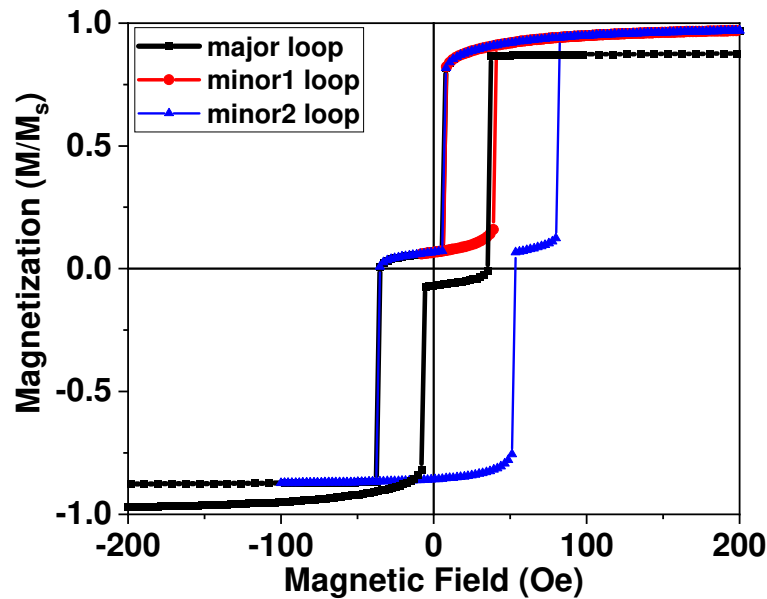


**Figure 8:** Magnetic simulations showing the major and minor magnetization loops for the Cu(25nm)/Fe(30nm)/ZnTPP(20ML)/Co(5nm)/ZnTPP(20ML)/Fe(30nm) hybrid system. Both minor magnetization loops show positive shift with an exchange field of +27 Oe. All magnetization loops are normalized to saturation magnetization.

To identify which Fe layer has the larger coercive field a sample in which the bottom Fe film is omitted has been measured: Cu(25nm)/ZnTPP(20ML)/Co(5nm)/ZnTPP(20ML)/Fe(30nm). As expected from the interpretation of the previous paragraph, figure 9 shows a magnetization loop with two different reversals at different field range. The Fe film magnetization reverses at around -40 Oe while the stiffer Co film shows a reversal at around -80 Oe. The reversal field of this Fe layer's magnetization is close to the reversal field (-33 Oe) seen in figure 5 which was attributed to one of the Fe layers in the

Fe(30nm)/ZnTPP(20ML)/Co(5nm)/ZnTPP(20ML)/Fe(30nm) heterostructure. Therefore, it can be concluded that the steep reversal in figure 5 is originating from the top Fe layer that is deposited on top of the molecular film while the first reversal at around +15 Oe corresponds to the bottom Fe film which is deposited on the Cu seed layer. Moreover, the minor magnetization loop in which the magnetic field is swept from 60 000 Oe to -50 Oe and back showed a shift towards the positive magnetic field axis with an exchange field of + 32 Oe. This confirms the presence of an indirect anti-ferromagnetic exchange coupling between the Fe and Co films.

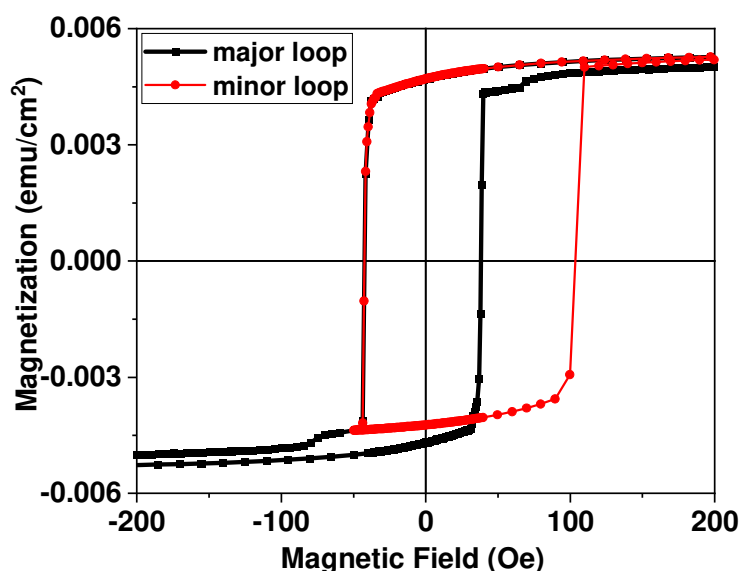


**Figure 9:** Major and minor magnetization loops for 100nm Cr capped Cu(25nm)/ZnTPP(20ML)/Co(5nm)/ZnTPP(20ML)/Fe(30nm) heterostructure. The minor loop shows a shift towards the positive field axis with an exchange field of 32 Oe. For all loops, the measurements are at 2K.

## 2. Conclusion and outlook

Hybrid organic heterostructures are the subject of immense research activities because they might play a big role for future computational nanotechnologies and electronic devices in general. However, their physical properties are still poorly understood and stay controversial. This is attributed to the complex morphological and chemical properties (e.g. roughness, chemical bonds, atomic diffusion etc.) of the hybrid organic/inorganic interfaces. Many kinds of defects can be found at the interfaces and can be at the origin of many effects observed in such heterostructures.

The first part of this experimental thesis focused on the molecular exchange bias effect and allowed the following conclusions:

- (i) Exchange bias in the studied Co/organic (MTPP and MPc) hybrid systems is not an “spinterface” effect. It is an experimental artefact resulting from the air-driven partial oxidation of the Co films due to the inefficient capping layers.

The second part introduced a newly developed original FNR methodology. FNR along with TEM allowed to probe in detail the morphology, the chemical, and the structural properties of the organic molecules and their respective hybrid interfaces embedded in the organic heterostructures. FNR and TEM allowed to highlight for the first time the following results:

- (ii) The growth morphology of the ZnTPP molecules strongly depends on the nature and on the structure of the metallic underlayer.
- (iii) A minimum of 15 monolayers of ZnTPP molecules are required to obtain organic heterostructures with continuous and pin-hole free molecular film.
- (iv) The Co/ZnTPP and ZnTPP/Co hybrid interfaces of the organic heterostructures are highly asymmetrical: Co/ZnTPP interface is sharper and smoother than the ZnTPP/Co interface which is rough and extended over large thickness.
- (v) The ZnTPP molecular films are rich in Co and Fe metallic atoms. The penetration of the metallic atoms is more important when they are deposited on top of the molecular film compared to when the molecules are deposited on top of the metallic film.
- (vi) The interactions between Co atoms and ZnTPP molecules at the hybrid interfaces are governed by weak and long-range van der Waals forces in the absence of strong chemical bonds.

After having obtained a deep understanding of the morphology of the organic heterostructures and of the interactions at the hybrid interfaces it was possible to probe the magnetic behaviour of these organic hybrid heterostructures. With FNR and SQUID the following new results can be mentioned:

- (vii) Magnetic hardening effect does not exist in the studied organic hybrid systems. Interfaces are relatively softer compared to the bulk of the FM layer.
- (viii) An indirect anti-ferromagnetic exchange coupling exists between the Co and Fe electrodes of the heterostructures through 20 ML of ZnTPP molecular spacer layer. An indirect ferromagnetic coupling might exist when the thickness of ZnTPP is reduced to 15 ML.

The results of the magnetic properties of the samples are very promising but require further investigations. This is the first perspective of this work. Indeed, our results suggest that an indirect exchange coupling takes place between the ferromagnetic electrodes through the ZnTPP organic film. This coupling should be studied (above the threshold thickness) versus the molecular layer thickness. An increment of 1 molecular layer per heterostructure would allow to better understand the nature of

this indirect exchange coupling. Above the TPP's threshold thickness value of continuity and taking advantage of the fact that Fe and Co reverse at different reversal fields a next step would be to study their magneto-transport properties. In compliment to these experimental measurements, it will be noteworthy to conduct theoretical DFT ab initio calculations to have deeper understanding of the physical mechanisms underlaying the magnetic and transport behaviour of the studied organic hybrid heterostructures.

One of the main points addressed in this work is the ageing of the samples. Investigating the free molecular surface's deformations would be of great interest to better understand this ageing process. This includes room temperature growth of MTPP molecules on top of the FM metallic surfaces followed by in-situ room and low temperature STM/AFM measurements to monitor the evolution of the molecule's surface morphology with time. This would allow to understand if the ageing of the samples is due to the ingress of oxygen or if the organic films tend to aggregate and therefore break the heterostructures even once properly encapsulated.

Since ageing as well as interface roughness and atom migration probably result from the mobility of the elements during the deposition process, a way to limit their mobility would be to drastically decrease the deposition temperature of the organic films. For example, preparing all the layers of the heterostructures at liquid nitrogen temperature might strongly limit the molecule mobility as well as the interdiffusion of the metallic atoms.

From a more general point of view it would be interesting to expand the FNR methodology established in this work to other molecular films (MTPP; M=Ni, Co, Mn, Fe etc. and other families of molecules) and study their structural and magnetic properties. In particular, it would be interesting to use different set of molecules which show strong interactions with the inorganic layers near the interface. Actually, the original FNR methodology that is introduced in the current manuscript can be applied to any kind of spacer layer. In addition, as the method can be applied on already grown samples it could be used on device's full architectures and can be implemented for the future development of organic based spintronic devices.

Organic spintronics has not truly taken advantage of the unique properties of the organic molecules: their different chemical functionalities and their response to different external stimuli e.g. optical, electrical, magnetic etc. In this direction, it could be interesting to integrate robust magnetic and functional molecules (chiral molecules, luminescent organic radicals, photo-switchable radicals) into spintronics structures to actively control the hybrid interfaces via the functionalized radicals of the molecules by controlling the strength of the hybridization. Then, the application of different external stimuli might allow changing the strength of this hybridization hence explore new interfacial physical and chemical properties.

Finally, organic molecules are mostly studied when they are deposited on top of metallic surfaces (magnetic and non-magnetic). It can be interesting to replace the metallic materials by transition metal oxides. Transition metal oxides have several degrees of freedom: spin, charge, orbital, etc, that can be triggered by different external stimuli like magnetic, electric, heat, light. Integrating these materials with organic molecules within spintronic heterostructures might create a wide avenue for new research as both materials can be triggered by large variety of external stimuli.

# Bibliography

- [1] M. N. Baibich, J. M. Broto, A. Fert, F. Nguyen Van Dau, F. Petroff, P. Etienne, G. Creuzet, A. Friederich, and J. Chazelas, *Phys. Rev. Lett.* **61**, 2472 (1988).
- [2] G. Binasch, P. Grünberg, F. Saurenbach, and W. Zinn, *Phys. Rev. B* **39**, 4828 (1989).
- [3] N. F. Mott, *Proc. R. Soc. London, Ser. A* **153**, 699 (1936).
- [4] A. Fert and I. A. Campbell, *Phys. Rev. Lett.* **21**, 1190 (1968).
- [5] A. Fert and I. A. Campbell, *J. Phys. (France)* **32**, C1-46 (1971).
- [6] A. Fert and I. A. Campbell, *J. Phys. F: Met. Phys.* **67**, 5680 (1976).
- [7] A. Fert, *Rev. Mod. Phys.* **80**, 1517 (2008).
- [8] C. Chappert, A. Fert, and F. Nguyen Van Dau. *Nat. Mater.* **6**, 813-823 (2007).
- [9] M. Julliere, *Phys. Lett. A*, **54**, (1975).
- [10] J. S. Moodera, L. R. Kinder, T. M. Wong and R. Meservey, *Phys. Rev. Lett.* **74**, 3273-3276, (1995).
- [11] T. Miyazaki and N. Tezuka, *J. Magn. Magn. Mater* **139(3)**, 231-234, (1995).
- [12] D. Wang, C. Nordman, J. M. Daughton, Z. Qian and J. Fink, *IEEE Trans. Magn.*, **40** (2004).
- [13] Stuart. S. P. Parkin, C. Kaiser, A. Panchula, P. M. Rice, B. Hughes, M. Samant, and S.-H. Yang, *Nat. Mater.* **3** (12) 862-867 (2004)
- [14] S. Yuasa, T. Nagahama, A. Fukushima, Y. Suzuki, and K. Ando, *Nat. Mater.* **3** (12) 868-871 (2004).
- [15] W. H. Butler, X.-G. Zhang, T. C. Schulthess, and J. M. MacLaren, *Phys. Rev. B.* **63(5)**: 054416 (2001).
- [16] X.-G. Zhang and W. H. Butler, *J. Condens. Matter Phys.* **15(41)**: R1603 (2003).
- [17] S. Ikeda, J. Hayakawa, Y. Ashizawa, Y. M. Lee, K. Miura, H. Hasegawa, M. Tsunoda, F. Matsukura, and H. Ohno, *Appl. Phys. Lett.* **93(8)**, 082508 (2008).
- [18] M. Bowen, M. Bibes, A. Barthélémy, J.-P. Contour, A. Anane, Y. Lemaitre, and A. Fert, *Appl. Phys. Lett.* **82(2)**, 233-235 (2003).
- [19] J.-G. Zhu and C. Park, “Magnetic tunnel junction”. *Materials Today*, **9**, 36-45 (2006).
- [20] E. I. Rashba, *Phys. Rev. B* **62**, R16267 (2000).
- [21] A. Fert, and H. Jaffrès, *Phys. Rev. B* **64**, 184420 (2001).
- [22] H. Ohno, A. Shen, F. Matsukura, A. Oiwa, A. Endo, S. Katsumoto and Y. Iye, *Appl. Phys. Lett.* **69**, 363 (1996).
- [23] M. Tanaka and Y. Higo, *Phys. Rev. Lett.* **87**, 026602 (2001).

- [24] P. P. Ruden and D. L. Smith, J. Appl. Phys., **95**:4898-4904, (2004).
- [25] C. B. Harris, R. L. Schlupp, and H. Schuch, Phys. Rev. Lett. **30**, 1019-1022, (1973).
- [26] V. I. Krinichnyi, S. D. Chemerisov, and Y. S. Lebedev, Phys. Rev. B **55** 16233-16244, (1997).
- [27] V. Dediu, M. Murgia, F. C. Maticotta, C. Taliani, and S. Barbanera, Solid State Commun, **122**(3-4):181-184, (2002).
- [28] Z. H. Xiong, D. Wu, Z. V. Vardeny and J. Shi, Nature **427**, 821-824 (2004).
- [29] S. Majumdar, H. S. Majumdar, R. Laiho, and R. Osterbacka, J. Alloys Compd. **423**, 169-171 (2006).
- [30] T. S. Santos, J. S. Lee, P. Migdal, I. C. Lekshmi, B. Satpati and J. S. Moodera, Phys. Rev. Lett. **98**, 016601 (2007).
- [31] J. H. Shim, K. V. Raman, Y. J. Park, T. S. Santos, G. X. Miao, B. Satpati, and J. S. Moodera, Phys. Rev. Lett. **100**, 226603 (2008).
- [32] C. Barraud, P. Seneor, R. Mattana, S. Fusil, K. Bouzehouane, C. Deranlot, P. Graziosi, L. Hueso, I. Bergenti, V. Dediu, F. Petroff and A. Fert, Nat. Phys. **6**, 615-620 (2010).
- [33] G. Szulcowski, S. Sanvito and J. M. D. Coey, Nat. Mater. **8**, 693-695 (2009).
- [34] S. Sanvito, the rise of spinterface science. Nat. Phys **6** 562 (2010).
- [35] H. Ishii, K. Sugiyama, E. Ito and K. Seki, Adv. Mater. **11**, 605-625 (1999).
- [36] X. -Y. Zhu, Surf. Sci. Rep. **56**, 1-83 (2004).
- [37] D. C. Langreth, B. I. Lundqvist, S. D. Chakarova-Käck, V. R. Cooper, M. Dion, P. Hyldgaard, A. Kelkkanen, J. Kleis, L. Kong, S. Li, P. G. Moses, E. Murray, A. Puzder, H. Rydberg, E. Schröder and T. Thonhauser, Phys. Cond. Mat. **21**, 84203 (2009).
- [38] J. B. Neaton, M. S. Hybertsen and S. G. Louie, Phys. Rev. Lett. **97**, 216405 (2006).
- [39] J. M. Garcia-Lastra, K. S. Thygesen, Phys. Rev. Lett. **106**, 187402 (2011).
- [40] J. K. Nørskov, Rep. Prog. Phys. **53**, 1253 (1990).
- [41] H. Harutyunian, M. Callsen, T. Allmers, V. Caciuc, S. Blügel, N. Atodiresei and D. Wegner, Chem. Commun. **49**, 5993 (2013).
- [42] M. C. Lennartz, V. Caciuc, N. Atodiresei, S. Karthäuser and S. Blügel, Phys. Rev. Lett. **105**, 066801 (2010).
- [43] M. Cinchetti, V. A. Dediu and L. E. Hueso, Nat. Matter., **16**, 507-515 (2017).
- [44] E. Pavarini, E. Koch, F. Anders, and M. Jarrell. Correlated Electrons: From Models to Materials. Chapter 7: Exchange mechanism. Forschungszentrum Jülich GmbH Institute for Advanced Simulation.
- [45] M. A. Ruderman, C. Kittel, Phys. Rev. **96**, 99 (1954).
- [46] T. Kasuya, Prog. Theoret. Phys. (Kyoto) **16**, 45 (1956).

- [47] K. Yosida, Phys. Rev. **106**, 983 (1957).
- [48] R. J. D. Tilley, Understanding solids: the science of materials. Chapter 12: Magnetic solids. John Wiley and sons, Ltd, The Atrium, Southern Gate, Chichester, West Sussex, England.
- [49] D. Chylarecka, T. K. Kim, K. Tarafder, K. Müller, K. Gödel, I. Czekaj, C. Wäckerlin, M. Cinchetti, Md. E. Ali, C. Piamonteze, F. Schmitt, J. P. Wüstenberg, C. Ziegler, F. Nolting, M. Aeschlimann, P. M. Oppeneer, N. Ballav and T. A. Jung, J. Phys. Chem. C, **115**, 1295–1301 (2011).
- [51] H. Wende, M. Bernien, J. Luo, C. Sorg, N. Ponpandian, J. Kurde, J. Miguel, M. Piantek, X. Xu, Ph. Eckhold, W. Kuch, K. Baberschke, P. M. Panchmatia, B. Sanyal, P. M. Oppeneer and O. Eriksson, Nat. Mater., **6**, 516–520 (2007).
- [51] J. Girovsky, K. Tarafder, C. Wäckerlin, J. Nowakowski, D. Siewert, T. Hählen, A. Wäckerlin, N. Ballav, T. A. Jung and P. M. Oppeneer, Phys. Rev. B **90**, 220404 (2014).
- [52] Q. Arnoux, C. Blouzon, D. Li, Y. J. Dappe, A. Smogunov, P. Bonville, L. Torteche and J. -B. Moussy, Phys. Rev. B **99**, 144405 (2019).
- [53] C. Blouzon, F. Ott, L. Torteche, D. Fichou and J. -B. Moussy, App. Phys. Lett. **103**, 042417 (2013).
- [54] F. Al Ma’Mari, T. Moorsom, G. Teobaldi, W. Deacon, T. Prokscha, H. Luetkens, S. Lee, G. E. Sterbinsky, D. A. Arena, D. A. MacLaren, M. Flokstra, M. Ali, C. Wheeler, G. Burnell, B. J. Hickey and O. Cespedes, Nature **524**, 69-73 (2015).
- [55] T. Moorsom, M. Wheeler, T. M. Khan, F. Al Ma’Mari, C. Kinane, S. Langridge, D. Ciudad, A. Bedoya-Pinto, L. Hueso, G. Teobaldi, V. K. Lazarov, D. Gilks, G. Burnell, B. J. Hickey and O. Cespedes, Phys. Rev. B **90**, 125311 (2014).
- [56] M. Callsen, V. Caciuc, N. Kiselev, N. Atodiresei and S. Blügel, Phys. Rev. Lett. **111**, 106806 (2013).
- [57] W. H. Meiklejohn and C. P. Bean, Phys. Rev. **102** (1956).
- [58] J Nogués and Ivan K Schuller, J. Magn. Magn. Mater, 192(2):203–232, (1999).
- [59] R. L. Stamps, J. Journal of Physics D, 33(23):R247, (2000).
- [60] J. Nogués, J. Sort, V. Langlais, V. Skumryev, S. Suriñach, J. S. Muñoz, and M. D. Baró, Physics Reports, 422(3):65–117, (2005).
- [61] M. Gruber, F. Ibrahim, S. Boukari, H. Isshiki, L. Joly, M. Peter, M. Studniarek, V. Da Costa, H. Jabbar, V. Davesne, U. Halisdemir, J. Chen, J. Arabski, E. Otero, F. Choueikani, K. Chen, P. Ohresser, W. Wulfschkel, F. Scheurer, M. Alouani, E. Beaurepaire, and M. Bowen, Nat. Mater. **14**, 981-984 (2015).
- [62] S. Boukari, H. Jabbar, F. Schleicher, M. Gruber, G. Avedissian, J. Arabski, V. Da Costa, G. Schmerber, P. Rengasamy, B. Vilen, W. Weber, M. Bowen, and E. Beaurepaire, Nano Lett. **18**, 4659-4663 (2018).



- [63] J. Jo, J. Byun, I. Oh, J. Park, M. J. Jin, B. C. Min, J. Lee, and J. W. Yoo, *ACS Nano*, **13**, 894-903 (2019).
- [64] J. Jo, J. Byun, J. Lee, D. Choe, I. Oh, J. Park, M. -J. Lee, J. Lee, and J. -W. Yoo, *Adv. Funct. Mater.* 1908499 (2020).
- [65] N. V. Bhagavan and C. -E. Ha, *Hemoglobin. Essentials of Medical Biochemistry* (2011).
- [66] D. Voet and J. Voet, *Biochemistry*, Wiley, New York, (1995).
- [67] P. S. Vincett, W. A. Barlow, R. A. Hann and G. G. Roberts, *Thin Solid Films* **94**, 171–183 (1982).
- [68] H. Tajima, K. Shimatani, T. Komino, S. Ikeda, M. Matsuda, Y. Ando and H. Akiyama, *Colloids and Surfaces A: Physiochem. Eng. Aspects* 284-285, 61-65 (2006).
- [69] K. Shimatani, H. Tajima, T. Komino, S. Ikeda, M. Matsuda, Y. Ando and H. Akiyama, *Chem. Lett.* **34**, 948–949 (2005).
- [70] H. Tajima, S. Ikeda, M. Matsuda, N. Hanasaki, J. Oh and H. Akiyama, *Solid Sates Commun.* **126**, 579–581 (2003).
- [71] H.-Y. Gu, A. -M. Yu and H. -Y. Chen, *J. Electroanal. Chem.* **516**, 119-126 (2001).
- [72] H. Ju, S. Liu, B. Ge, F. Lisdat and F. W. Scheller, *Electroanalysis* **14** (2), 141-147 (2002).
- [73] X. Zhao, Z. Mai, X. Kang, Z. Dai and X. Zou, *Electrochim. Acta.* **53**, 4732-4739 (2008).
- [74] B. M. L. Chen and A. Tulinsky, *J. Am. Chem. Soc.* **94**, 4144-4151 (1972).
- [75] M. Schallbach, H. H. Limbach, E. Bunnenberg, A. Y. L. Shu, B. R. Tolf and C. Djerassi, *J. Am. Chem. Soc.* **115**, 4554-4565 (1993).
- [76] M. Schallbach, B. Wehrle, H. Rumpel, J. Braun, G. Scherer and H. H. Limbach, *Ber. Bunsen Ges.* **96**, 821-833 (1992).
- [77] T. Wolfle, A. Görling and W. Hieringer, *Phys. Chem. Chem. Phys.* **10**, 5739-5742 (2008).
- [78] A. Rosa, G. Ricciardi and E. J. Baerends, *J. Phys. Chem. A* **110**, 5180-5190 (2006).
- [79] T. Higashino and H. Imahori, *Dalton Trans.*, **44**, 448-463 (2015).
- [80] Ö. Birel, S. Nadeem and H. Duman, *J. Fluoresc.*, **27**, 1075-1085 (2017).
- [81] I. Obraztsov, W. Kutner and F. D'Souza, *Solar RRL*, **1**, 1600002-n/a (2017).
- [82] J. Kesters, P. Verstappen, M. Kelchtermans, L. Lutsen, D. Vanderzande and W. Maes, *Adv. Energy Mater.*, **5**, 1500218-n/a (2015).
- [83] P. Hambright, in: K. M. Smith (Ed.), *Porphyrins and Metalloporphyrins*, Amsterdam, pp. 157-232 (1975).
- [84] M. Panighel, G. D. Santo, M. Caputo, C. Lal, B. Taleatu and A. Goldoni, *J. Phys. Conf. Series* 470, 012012 (2013).
- [85] M. -S. Liao and S. Scheiner, *J. Chem. Phys.* **117**, (2002).

- [86] A. Weber-Bargioni, W. Auwärter, F. Klappenberger, J. Reichert, S. Lefrancois, T. Strunskus, C. Wöll, A. Schiffrin, Y. Pennec and J. V. Barth, *Chem. Phys. Chem* **9**, 89-94 (2008).
- [87] T. Lukasczyk, K. Flechtner, L. R. Merte, N. Jux, F. Maier, J. M. Gottfried, and H. P. Steinrück, *J. Phys. Chem. C* **111**, 3090-3098 (2007).
- [88] W. Hieringer, K. Flechtner, A. Kretschmann, K. Seufert, W. Auwärter, J. V. Barth, A. Görling, H. P. Steinrück and J. M. Gottfried, *J. Am. Chem. Soc.* **133**, 6206-6222 (2011).
- [89] S. A. Krasnikov, N. N. Sergeeva, M. M. Brzhezinskaya, A. B. Proebrajenski, Y. N. Sergeeva, N. A. Vinogradov, A. A. Cafolla, M. O. Senge and A. S. Vinogradov, *J. Phys. - Condens. Matter* **20**, 235207 (2008).
- [90] M. Chen, X. F. Feng, L. Zhang, H. X. Ju, Q. Xu, J. F. Zhu, J. M. Gottfried, K. Ibrahim, H. J. Qian and J. O. Wang, *J. Phys. Chem. C* **114**, 9908-9916 (2010).
- [91] S. A. Krasnikov, N. N. Sergeeva, Y. N. Sergeeva, M. O. Senge and A. A. Cafolla, *Phys. Chem. Chem. Phys.* **12**, 6666-6671 (2010).
- [92] C. Castellarin-Cudia, P. Borghetti, G. Di Santo, M. Fanetti, R. Larciprete, C. Cepek, P. Vilmercati, L. Sangaletti, A. Verdini, A. Cossaro, L. Floreano, A. Morgante and A. Goldoni, *Chem. Phys. Chem.* **11**, 2248-2255 (2010).
- [93] W. Xu, G. J. Szulczewski, P. LeClair, I. Navarrete, R. Schad, G. Miao, H. Guo and A. Gupta, *App. Phys. Lett.* **90**, 072506 (2007).
- [94] J. G. Simmons, *J. Appl. Phys.* **34**, 1793 (1963).
- [95] MBE KOMPONENTEN, Dr. EBERL; [https://www.mbe-komponenten.de/glossary/hot-lip-filament-hl\\_110.php](https://www.mbe-komponenten.de/glossary/hot-lip-filament-hl_110.php)
- [96] M. Studniarek, Ph.D. thesis “Interface and Multifunctional Device Spintronics. Studies with Synchrotron Radiation”, University of Strasbourg 2016.
- [97] H. Jabbar, Ph.D. thesis “Ferromagnet/Phthalocyanines heterostructures for spintronic applications”, University of Strasbourg 2015.
- [98] I. Horcas, R. Fernandez, J. M. Gomez-Rodriguez, J. Colchero, and J. Gomez-Herrero, *Rev. Sci. Instrum.* **78**, 013705 (2007).
- [99] H. Hertz, *Annalen der Physik* **31**, p983 (1887).
- [100] A. Einstein, *Annalen der Physik* **17**, p132 (1905).
- [101] A. Kaech, *Introduction to Electron Microscopy Instrumentation, Imaging and Preparation*, University of Zurich (2013).
- [102] D.B. Williams, C.B. Carter, *Transmission Electron Microscopy: A Textbook for Materials Science* (Springer, New York, 2009).
- [103] F. Faupel, *Adv. Mater.* **2**, 266 (1990).
- [104] F. Faupel, R. Willecke, A. Thran, *Mater. Sci. Eng. R22* (1998) 1.

- [105] G. Philipp, C. Müller-Schwanneke, M. Burghard, S. Roth, K. von Klitzing, J. Appl. Phys. **85** 3374 (1999).
- [106] Andrew A. Herzing, Hyun Wook Ro, Christopher L. Soles and Dean M. DeLongchamp, ACS Nano, 7, 9, 7937-7944 (2013).
- [107] J. B. Gilchrist, S. Heutz and D. W. McComb, Curr. Opin. Solid State Mater. Sci (2017).
- [108] Gilchrist, T. H. Basey-Fisher, S. C'E. Chang, F. Scheltens, D. W. McComb and S. Heutz, Adv. Funct. Matter. **24**, 6473-6483 (2014).
- [109] C. Meny and P. Panissod. Modern magnetic resonance, 1-12 (2017).
- [110] G. Y. Guo and H. Ebert. Phys. Rev. B **53**, 2492 (1996).
- [111] C. Meny. Correlations between structure and physical properties of thin layers and ferromagnetic nanocomposites: Contribution of Nuclear Magnetic Resonance (Habilitation for research supervision in condensed matter physics) (2013).
- [112] C. Meny, E. Jedryka and P. Panissod, J. Phys.: Condens. Matter. **5**, 1547-1556 (1993).
- [113] P. Panissod and C. Meny., Appl. Magn. Reson. **19**, 447-460 (2000).
- [114] S. Rangan, C. Ruggieri, R. Bartynski, J. Ignacio Martínez, F. Flores, and J. Ortega, J. Phys. Chem. C. **120**, 4430-4437 (2016).
- [115] C. D. Wagner, W. M. Riggs, L. E. Davis, J. F. Moulder, and G. E. Muilenberg, Perkin Elmer Corp. Publisher, Eden Prairie, MN, (1979).
- [116] S. C. Petitto and M. A. Langell, J. Vac. Sci. Technol. A **22**(4) (2004).
- [117] T. J. Chuang, C. R. Brundle, and D. W. Rice, Surf. Sci. **59**, 413-429 (1976).
- [118] S. Xie, Y. Liu, J. Deng, J. Yang, X. Zhao, Z. Han, K. Zhang, and H. Dai, J. Catal. **352**, 282-292 (2017).
- [119] T. Lukasczyk, K. Flechtner, L. R. Merte, N. Jux, F. Maier, J. M. Gottfried, and H. P. Steinruck, J. Phys. Chem. C, **111**, 3090-3098 (2007).
- [120] L. Scudiero, D. E. Barlow, and K. W. Hipps, J. Phys. Chem. B, **104**, 11890-11905 (2000).
- [121] R. P. Gupta and S. K. Sen, Phys. Rev. B **12**, 15 (1975).
- [122] W. Hieringer, K. Flechtner, A. Kretschmann, K. Seufert, W. Auwärter, J. V. Barth, A. Gorling, H. P. Steinruck, and J. M. Gottfried, J. Am. Chem. Soc. **133**, 6206-6222 (2011).
- [123] T. E. Shubina, H. Marbach, K. Flechtner, A. Kretschmann, N. Jux, F. Buchner, H. P. Steinruck, T. Clark, and J. M. Gottfried, J. Am. Chem. Soc. **129**, 9476-9483 (2007).
- [124] J. L. Bubendorff, E. Beaupaire, C. Meny and J. P. Bucher, J. Appl. Phys. **83**, 7043-7045 (1998).
- [125] M. Vélez, C. Meny, S. M. Valvidares, J. Diaz, R. Morales, L. M. Alvarez-Prado, P. Panissod and J. M. Alameda, Eur. Phys. J. B **41**, 517-524 (2004).

- [126] A. Azizi, A. Sahari, M. L. Felloussia, G. Schmerber, C. Meny and A. Dinia, Appl. Surf. Sci. **228**, 320-325 (2004).
- [127] M. Wójcik, J. P. Jay, P. Panissod, E. Jedryka, J. Dekoster and G. Langouche. Zeitschrift für Physik B **103**, 5-12 (1997).
- [128] H. El Fanity, K. Rahmouni, M. Bouanani, A. Dinia, G. Schmerber, C. Meny, P. Panissod, A. Cziraki, F. Cherkaoui and A. Berrada. Thin Solid Films **318**, 227-230 (1998).
- [129] J. Dekoster, E. Jedryka, C. Meny and G. Langouche. J. Magn. Magn. Mater. **121**, 69-72 (1993).
- [130] K. Le Guen, M. -H. Hu, J. -M. Andre, S. K. Zhou, H. Ch. Li, J. T. Zhu, Z. S. Wang, C. Meny, A. Galtayries and P. Jonnard. Appl. Phys. Let. **98**, 251909 (2011).
- [131] E. Jedryka, M. Wójcik, S. Nadolski, D. Kubinski, M. Parsons and H. Holloway, J. Appl. Phys. **91**, 7191-7193 (2002).
- [132] M. Wójcik, C. Christides, E. Jedryka, S. Nadolski and I. Panagiotopoulos, Phys. Rev. B **63**, 012102 (2001).
- [133] M. Malinowska, C. Meny, E. Jedryka and P. Panissod, J. Phys.: Condens. Matter. **10**, 4919-4928 (1998).
- [134] Berlepsch, v. H., Böttcher, C., J. Phys. Chem. B **106**, 3146 (2002).
- [135] Kobayashi, T. J-Aggregates (World Scientific, Singapore, 1996).
- [136] P. Panissod and C. Meny, Appl. Magn. Reson. **19**, 447-460 (2000).
- [137] P. Panissod, C. Meny, M. Wojcik, E. Jedryka, Mater. Res. Soc. Symp. Proc. **475**, 157-168 (1997)
- [138] C. Meny, P. Panissod, P. Humbert, J. P. Nozieres, V. S. Speriosu, B. A. Gurney and R. Zehring, J. Magn. Magn. Mater. **121**, 406-408 (1993).
- [139] K. Bairagi, A. Bellec, V. Repain, C. Fourmental, C. Chacon, Y. Girard, J. Lagoute, S. Rousset, L. Le. Laurent, A. Smogunov and C. Barreteau, Phys. Rev. B. **98**, 085432 (2018).



## List of publications

- 1) G. Avedissian, J. Arabski, J. A. Wytko, J. Weiss, and C. Meny. Probing the growth of organic molecular films embedded in cobalt and iron electrodes: Ferromagnetic nuclear resonance approach. *Adv. Funct. Mater.* **30**, 2005605 (2020).
- 2) G. Avedissian, J. Arabski, J. A. Wytko, J. Weiss, and C. Meny. Revealing the morphology and the magnetic properties of single cobalt-ZnTPP hybrid interfaces by ferromagnetic nuclear resonance spectroscopy. *Phys. Rev. B* **102**, 184114 (2020).
- 3) S. Mohapatra, V. Da Costa, G. Avedissian, J. Arabski, W. Weber, M. Bowen, and S. Boukari. Robust ferroelectric properties of organic croconic acid films grown on spintronically relevant substrates. *Mater. Adv.* **1**, 415 (2020).
- 4) S. Boukari, H. Jabbar, F. Schleicher, M. Gruber, G. Avedissian, J. Arabski, V. Da Costa, G. Schmerber, P. Rengasamy, B. Vilen, W. Weber, M. Bowen, and E. Beaupre. Disentangling magnetic hardening and molecular spin chains contribution to exchange bias in ferromagnet/molecular bilayer. *Nano. Lett.* **18**, 4659-4663 (2018).

## List of Conferences

- 1) G. Avedissian, C. Meny, W. Jo, Y. Shin, S. L. Cho. Investigating the properties of functional nanostructures (Invited talk). The 11th International Conference on Advanced Materials and Devices (ICAMD); 10-13 Dec. 2019, Jeju, South Korea.
- 2) G. Avedissian, J. Arabski, J. A. Wytko, J. Weiss, V. Papaefthimiou, G. Rogez, E. Beaupre and C. Meny. Is Exchange bias at the hybrid organic/ferromagnet interface an interface effect (Oral presentation). The 65<sup>th</sup> Annual Conference on Magnetism and Magnetic Materials (MMM 2020, virtual conference); 2-6 Nov. 2020, Palm Beach, Florida.

- 3) G. Avedissian, J. Arabski, J. A. Wytko, J. Weiss, and C. Meny. Revealing the morphology and magnetic properties of single hybrid interfaces embedded in Co/ZnTPP and ZnTPP/Co by FNR (Oral presentation). The 65<sup>th</sup> Annual Conference on Magnetism and Magnetic Materials (MMM 2020, virtual conference); 2-6 Nov. 2020, Palm Beach, Florida.
- 4) G. Avedissian, J. Arabski, J. A. Wytko, J. Weiss, V. Papaefthimiou, G. Rogez, E. Beaurepaire and C. Meny. Is Exchange bias at the hybrid organic/ferromagnet interface an interface effect (Invited talk). The Joint European Magnetic Symposia (JEMS 2020, virtual conference) conference; 7-11 Dec. 2020, Lisbon, Portugal.
- 5) G. Avedissian, J. Arabski, J. A. Wytko, J. Weiss, and C. Meny. Probing the continuity of tetra-phenyl porphyrin organic layers embedded between cobalt and iron films by ferromagnetic nuclear resonance (poster presentation). The Joint European Magnetic Symposia (JEMS 2020, virtual conference) conference; 7-11 Dec. 2020, Lisbon, Portugal.





### Résumé

Dans un dispositif spintronique organique hybride, la région active est l'interface hybride. La première partie de cette thèse montre que le biais d'échange moléculaire des systèmes Co/MTPP et Co/CoPc n'est pas un effet d'interface mais provient de l'oxydation des films de Co. La deuxième partie introduit une nouvelle méthodologie en Résonance Nucléaire Ferromagnétique qui montre que 15 monocouches de ZnTPP sont nécessaires pour obtenir des films moléculaires continus et que leur morphologie dépend de la nature du substrat (Fe ou Co). De plus les interfaces sont asymétriques, l'interface Co/ZnTPP est abrupte alors que l'interface ZnTPP/Co est rugueuse et diffuse. Ces analyses ont été confirmées par TEM. De plus, la FNR n'a montré aucun effet de durcissement magnétique interfacial. C'est cohérent avec le fait que les interfaces Co/ZnTPP sont régies par des interactions faibles de type van der Waals et qu'aucune signature de liaison chimique forte entre les molécules et les atomes de Co n'ai été identifiée. Enfin, les mesures magnétiques ont révélé un couplage d'échange indirect antiferromagnétique entre les électrodes FM au travers des films organiques.

**Mots clés :** Organique, nanostructures, RMN a l'état solide, Résonance Nucléaire Ferromagnétique, anisotropie magnétique, morphologie, exchange bias, interface hybride.

### Summary

In hybrid organic spintronic devices, the active regions are essentially the hybrid interfaces. The first part of this thesis shows that molecular exchange bias in Co/MTPP and Co/CoPc systems is not an interface effect but originates from air-driven oxidation of the Co films. The second part introduces a new Ferromagnetic Nuclear Resonance methodology which showed that 15 monolayers of ZnTPP are required to obtain heterostructures with continuous molecular films and that their morphology depends on the nature of the underlayer (Co or Fe). In addition, the interfaces are asymmetrical with sharp Co/ZnTPP interface and rough ZnTPP/Co interface. These analyses have been confirmed by TEM. Moreover, FNR showed that no interfacial magnetic hardening effect exists in these systems. This is consistent with the fact that the Co/ZnTPP interfaces are governed by weak van der Waals interactions and that no signature of strong chemical bonds between interfacial ZnTPP molecules and Co atoms has been identified. Finally, the magnetic measurements suggest that an anti-ferromagnetic indirect exchange coupling takes place between the FM electrodes through the organic film.

**Key words:** Organics, nanostructures, solid-state NMR, Ferromagnetic nuclear resonance, magnetic anisotropy, morphology, exchange bias, hybrid interface.